# *Investigations on Clay Hybrids and Carbon based Nanostructures*

**A Thesis Submitted for the Degree of**

**Doctor of Philosophy**

**By**

*Kumara Ramanatha Datta K*


**Chemistry and Physics of Materials Unit**
**Jawaharlal Nehru Centre for Advanced Scientific Research**
**(A Deemed University)**
**Bangalore – 560 064**
**April 2011**

*Dedicated to amma and appa*

# DECLARATION

I hereby declare that the matter embodied in the thesis entitled "**Investigations on Clay Hybrids and Carbon based Nanostructures**" is the result of investigations carried out by me at the Chemistry and Physics of Materials Unit, Jawaharlal Nehru Centre for Advanced Scientific Research, India under the supervision of Prof. Muthusamy Eswaramoorthy and that it has not been submitted elsewhere for the award of any degree or diploma.

In keeping with the general practice in reporting the scientific observations, due acknowledgement has been made whenever the work described is based on the findings of other investigators. Any omission that might have occurred due to oversight or error in judgement is regretted.

Kumara Ramanatha Datta K

# CERTIFICATE

I hereby certify that the work described in this thesis entitled "**Investigations on Clay Hybrids and Carbon based Nanostructures**" has been carried out by Mr. Kumara Ramanatha Datta K under my supervision at the Chemistry and Physics of Materials Unit, Jawaharlal Nehru Centre for Advanced Scientific Research, India and that it has not been submitted elsewhere for the award of any degree or diploma.

Prof. Muthusamy Eswaramoorthy

(Research Supervisor)

# ACKNOWLEDGEMENTS

I wish to express my sincere gratitude to my research supervisor Prof. M. Eswaramoorthy for the kind support, guidance, criticism and invaluable suggestions he gave me all through the course of these investigations. He has been very kind and affectionate towards me on many occasions. I have learnt so much by interacting with him both professionally and personally. I am thankful to him for giving me an opportunity to work under his guidance.

I thank Prof. C. N. R Rao, FRS, who has been a constant source of inspiration for me. I am grateful to him for the interest that he had shown in my research work in the form of many valuable suggestions. I consider it an honor to have worked with him on one research problem. Also I thank him for selecting me for IJGS fellowship under JNCASR-NIMS graduate school program.

I am thankful Prof. Katsuhiko Ariga and Dr. Ajayan Vinu for guiding me in various research problems and invaluable discussions during my stay in National Institute for Materials Science (NIMS), Japan.

I thank the past and present chairmen of CPMU for allowing me to use the facilities of the centre.

I am thankful to the faculty members of JNCASR and the Chemical Sciences division at the Indian Institute of Science for the course that have been extremely beneficial to this study. In particular, I would like to thank Prof. G. Mugesh, Prof. U. Maitra, Prof. S. Ramashesha, Prof. D. D Sarma, Prof. B. Jagirdar, Prof. P. Balaram, Prof. N. Ravishankar, Prof. T. N. Guru Row, Prof. M. S. Hegde of IISc and Prof. A. Sundaresan, Prof. M. Eswaramoorthy, Prof. G. U. Kulkarni, Prof. Swapan. K. Pati of JNC for their courses.

I would like to sincerely thank Prof. H. Balaram (MBGU), Dr. S. George (NCU), Dr. T. K. Maji (CPMU), Dr. R. Datta (ICMS), Dr. S. Reddy (IICT) and Dr. S. Mandal (NIMS) for our fruitful collaborations.

I thank the timely help of the technical staff namely Mr. Basavaraj, Mrs. Usha, Mr. Anil, Mr. Vasu, Mr. Mahesh, Mr. Basavaraju and Mrs. Selvi in JNCASR and Dr. Uemura, Dr. Wada Dr. Nemato, Ms. Akada, Dr. Ri in NIMS for their help with the various characterization techniques.

I thank JNCASR Library, Complab, Hostel, Health Center, Academics and Administration staff for providing and maintaining the various facilities that have helped me immensely. Special thanks are due to IISc library and SERC for their facilities.

I also thank my wonderful lab mates Mr. Saikrishna, Dr. Dinesh, Dr. Kalyan, Mr. Piyush, Mr. Pawan, Ms. Josena and Mr. Amrit for their kind cooperation and help. Also I acknowledge all the visiting scientists and students (POCE and SRF) for their contributions.

I would like to thank administrative staff Mrs. Sukanya and Mrs. Sudha of JNCASR, Ms. Toshie, Mrs. Inoue and Mr. Koike of NIMS for their constant help. Special thanks to Mrs. Anna and Mrs. Wang for their care during my stay in NIMS.

My cordial thanks are due to my friends Madhu, Srinivas, Venky, Rak, Mohan, Pranab, Pavan, Gopal, Chaitanya, Srini, Reji, Sairam, Suidapta, Ashish, Anil, Mighfar, Claudy, Guru, Ayya, Sundaraya, Sandy, Matte, Ankita, Urmi, Basant, Shipra, Neenu, Kalyani, Ajmala, Gopal, Sabyasachi, Avinash, Gangaiah, Moses, Subbu, Jayram, Kanishka, Meenakshi, Anshuman, Sonai, Dhanu, Dinesh, Navya Logu, Chitra, Vinila, Ravi, Bala, Pranjal, Michael, Anupama, Satish, Hari, Ujjal Rajashree, Vinu, Ajay, Kiran, Basheer, Vinay, Anirban, Vijay, Sam, Abhi, Manoj,

Arun, JP, Naresh, Asha, Preetam, etc. Their support and encouragement have been an indispensable in my Ph D life.

Last but not least, my heartfelt thanks to amma, appa and my sister and for being there for me always. Their love and care has been the greatest strength for me. This thesis is a humble offering to my parents.

# PREFACE

Hybrid materials are receiving great attention in recent years owing to their application in medicine, energy, catalysis and reinforcements. In particular, hybrid materials having metal/semiconductor nanoparticles as one of their components are expected to have significant improvement in the properties of the resulting materials due to the size dependent optical, catalytic and electronic properties of the nanoparticles. Equally important are the carbon based nanostructures whose application in catalysis, adsorption and medicine reached new heights with the emergence of new forms of carbon. **Chapter 1** gives a brief overview on clay hybrids and carbon based nanostructures.

**Chapter 2** deals with (Part A) the synthesis of water soluble, metal nanoparticles embedded aminoclay layers of approximate composition $R_8Si_8Mg_6O_{16}(OH)_4$, where $R=CH_2CH_2NH_2$. These exfoliate clay layers were brought to the oil-water interface by the addition of long chain alkane thiols. Part B discusses the permselective nature of aminoclay in protecting air sensitive copper nanoparticles.

**Chapter 3** deals with the usage of naturally occurring biopolymer, agarose for the stabilization of metal and semi-conducting nanoparticles. Anti-bacterial studies were performed using Ag and Cu nanoparticles by this method on *Escherichia coli.*

**Chapter 4** involves the preparation of porous layered carbon with flexible framework templated by aminoclay showing mesoscale order-disorder transformation on application of shear (centrifugal) force.

**Chapter 5** deals with the encapsulation of gold nanoparticles in mesoporous carbon nitride and utilizing them as active catalyst in the synthesis of propargylamine.

**Chapter 6** describes the effect of carbonization temperature on the conductivity, nitrogen content and electrochemical performance of mesoporous carbon nitride.

**Chapter 7** investigates the adsorption behavior of nucleosides (Part A) and DNA intercalators (Part B) on various porous carbon supports (carbon nanocage, mesoporous carbon and activated carbon). Among the supports chosen, carbon nanocage displays pronounced selectivity between purine and pyrimidine-based nucleosides and high adsorption capacity towards DNA intercalators.

# TABLE OF CONTENTS

# LIST OF ABBREVIATIONS

**AAO**: Anodic Alumina Oxide

**BET**: Brunauer-Emmett-Teller

**CEC**: Cation Exchange Capacity

**CNT:** Carbon Nanotube

**CTAB:** Cetyltrimethylammonium bromide

**CV**: Cyclic Voltammetry

**DMFCs**: Direct Methanol Fuel Cells

**DNA:** Deoxyribonucleic acid

**ED**: Electron Diffraction

**EDLC**: Electrochemical Double-Layer Capacitor

**EDX/EDAX:** Energy Dispersive X-ray (analysis)

**FESEM:** Field Emission Scanning Electron Microscope

**FFT:** Fast Fourier Transform

**FTIR**: Fourier Transform Infra-Red

**GC**: Gas Chromatography

**ICP-MS**: Inductively Coupled Plasma Mass Spectroscopy

**MCN**: Mesoporous Carbon Nitride

**MCM**: Mobil Crystalline Material

**MOF**: Metal Organic Framework

**NHE**: Normal Hydrogen Electrode

**NLDFT**: Non-Local Density Functional Theory

**P123**: Pluronic 123 [(polyethelene oxide)$_{20}$-(polypropelene oxide)$_{70}$-(polyethelene oxide)$_{20}$]

**PEM**: Polymer Electrolyte Membrane

**PL**: Photoluminescence

**SBA-15**: Santa Barbara Amorphous-15

**TEM:** Transmission Electron Microscope

**TEOS:** Tetraethylorthosilicate

**TGA**: Thermogravimetric analysis

**TLC**: Thin Layer Chromatography

**UV-Vis:** Ultraviolet and Visible

**XRD:** X-Ray Diffraction

# Chapter 1

# Introduction to Clay Hybrids and Carbon based Nanostructures

# Part A: Clay-hybrids

## 1.1. Introduction:

Hybrid materials derived from organic and inorganic components are receiving enormous attention owing to their applications in the fields of biology, energy, catalysis, reinforcements, etc.[1] These materials are broadly defined as molecular or nanocomposites, with organic and inorganic components intimately mixed having at least one of the component domains in the range of few Å to several nanometers.[1,2] Though there is no clear-cut definition to differentiate between hybrids and nanocomposites, it is generally presumed that hybrid materials would have superior functions or properties compared to the traditional composites.[3]

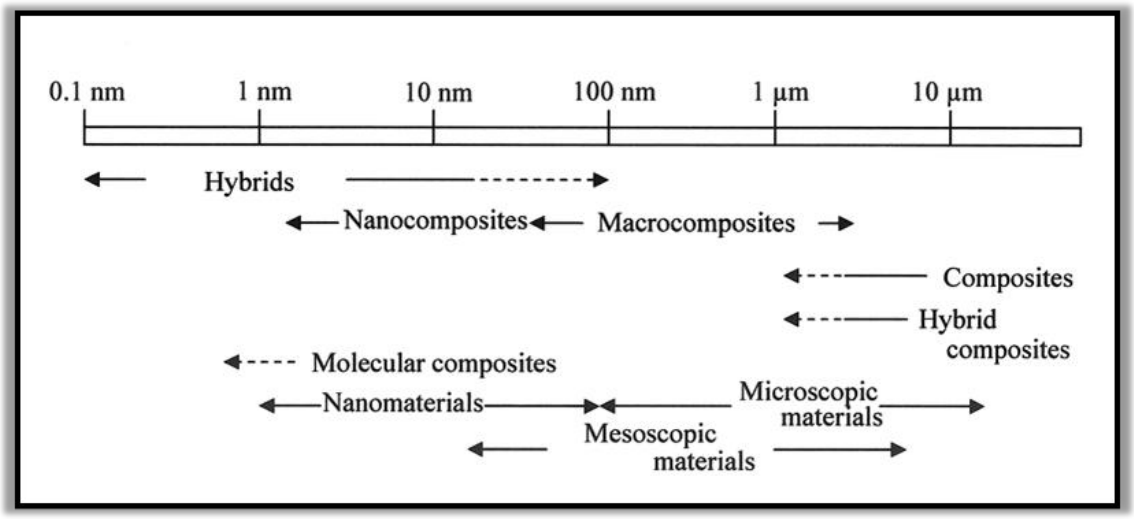


**Figure 1.** Classification of materials based on different length scale levels **(***Definitions and categories of hybrid materials*. *Azojomo,* **2009**, *6*, 10.2240).

Figure 1 shows a classification of materials by different scale levels, as proposed by the Materials Science Society of Japan.[3b,4] The size domain of hybrids overlaps with that of nanocomposites, molecular composites and nanomaterials.

**Composites, Solutions and Hybrids:**

In all the three cases such as composites, solutions and hybrids, two or more components are joined or mixed together. Table 1 gives a rough idea of the differences among them.

| *States* | *Component size* | *Character of the components* | *Examples* |
|---|---|---|---|
| Composite | ~µm (at least one of the components) | similar<br>dissimilar | porcelain, Pyroceram®<br>Carbon fiber-reinforced plastics (CFRP), bone cements |
| Solution(*) | atomic and molecular level | similar<br>dissimilar | gasoline, brass (CuZn), air, glass saline |
| Hybrids | atomic and molecular level | dissimilar | under development, involving molecular brush on substrate, oxide layer on metal |

***** Solid solution is an extreme form of hybridization.

**Table 1**. Mixtures under different names (*Hybrid materials*, **2006**, *Wiley-VCH*).

Carbon fiber-reinforced plastics are prepared by reinforcing carbon fibers into synthetic polymer matrix. The fibers are wound in lamellae, mimicking collagen fibrils in cortical bone (hard bone). The steel-belted automobile tyre is another example of a composite. Composites formed between ceramic particles and metallic particles are possible; they are cermets (cer + met). Porcelains consist of a number of crystalline particles (grains) of various oxides, bonded together by firing at high temperature (sintering). All the above mentioned examples are composites.

Polymers are made up of an infinite number of units of one kind. When two or more kinds of polymers are mixed together to yield polymeric solids, they are called polymer blends. Sometimes they are denoted as polymer alloys, but rarely are they called hybrids since the components are similar in both structure (almost infinite repetition of a monomer unit) and property (soft, tough, deforming well). When

chemical affinity of the component is low, they do not form a homogeneous mixture but an inhomogeneous one, where the molecules of each component get together but are also segregated (phase separation). The mixture looks like mayonnaise (emulsion), which consists of tiny isolated droplets of oil and water. A block copolymer material comprises repetition of oligomers of different kinds: $[—(A—)_m—(B—)_n—]_x$ where m and n are arbitrary, and x is practically infinite. Hence, a block copolymer is then probably one of the hybrid materials. Hybrids stand between composites and solutions. Hybrids are not only homogeneous solids but also atomic or molecular-level mixtures of individual components. Even though the components have different chemical properties, their integration gives rise to novel properties or at least those of each component at the same time. For e.g. a hybrid composed of organic and inorganic components, may behave either as an inorganic or organic solid, exhibiting the properties of both or either.

The requirement for considering a solid as an organic-inorganic hybrid material is that the combination between the two integrating parts should occur at the molecular level, i.e. at the nanometer scale.[1,4] The term hybrid material is used for many different systems spanning a wide area of diverse materials such as highly ordered, crystalline coordination polymers, amorphous sol-gel compounds, layered silicate (clay) hybrids, colloids, nanoporous materials, etc.[1b] Development of hybrid materials with extraordinary properties has attracted a lot of interest in recent years. Current challenges in this rapidly growing field include designing novel hybrid materials for applications in the fields of energy, reinforcements, biology, optics, electronics, packaging materials, etc.[2]

## 1.2. Development of hybrid materials:

The pursuit for more efficient energy related technologies demands the development of lightweight, high-performance structural materials with exceptional strength and toughness. Steel and other metal alloys have long been used for the fabrication of strong and flaw tolerant materials for structural applications. As opposed to metals, ceramic and polymeric materials do not exhibit the unique blending of high strength and flaw tolerance. Ceramics are typically strong but not tolerant to surface flaws and cracks, whereas most polymers are flaw-tolerant but deform extensively at rather low applied stresses. Unfortunately, these two properties (strength and toughness) tend to be mutually exclusive, and attaining optimal mechanical performance is always a compromise often achieved through the empirical design of microstructures. This necessitates the development of hybrid materials which can accomplish all technological desires for various applications. However, it should be noted that the origin of hybrid materials did not take place in a laboratory but in nature.

Nature has found its way around this dilemma by combining brittle minerals and organic molecules into hybrids with excellent fracture resistance and structural capabilities.[5] Materials like bone, calcified tendons, teeth, wood and nacre (abalone shell) with highly intricate structures have properties far exceed what could be expected from a simple mixture of their components.[5,6] For e.g., nacre, known as mother of pearl, formed by the organization of highly oriented crystalline calcium carbonate (aragonite 95 vol. %) cemented by a thin layer of organic material exhibits a toughness three orders of magnitude higher than that of pure calcium carbonate.[5b,7] Although substantial progress has been made on understanding their mechanical

response of such bio-hybrids, the manufacture of artificial hybrid materials that mimic nature designs remain a challenging goal.[8]

**(a) Maya blue: A Clay-Organic Hybrid Pigment**

As far as man-made hybrids are concerned, the possibility to combine properties of organic and inorganic components for materials design and processing is a very old challenge (Egyptian inks, green bodies of china ceramics, prehistoric frescos, etc). In 1946, at a site in eastern Chiapas (Mexico) known as Bonampak (painted walls) a surprising archaeological discovery was made. This ancient Maya site contained an impressive collection of fresco paintings characterized by bright blue and ochre colors that had been miraculously preserved (Figure 2). The striking feature of these wall paintings was their vivid blue hues, called Maya blue. This blue pigment is a beautiful example of a remarkable hybrid organic-inorganic material that combines the color of the organic pigment (natural blue indigo) and the resistance of the inorganic clay palygorskite.[9]

Durability was the most remarkable feature of this particular pigment. It had withstood more than twelve centuries of a harsh jungle environment looking almost as fresh as when it was used in the eighth century. Maya blue is indeed a robust pigment, not only resisting biodegradation, but showing also unprecedented stability when exposed to acids, alkalis and organic solvents.

**(b) Clay hybrids: From Ancient Tradition to 21st Century Materials**

The addition of fillers and reinforcements has played a key role in the polymer industry.[10] Of the various fillers introduced in polymers to provide a synergistic improvement to processability and properties like tensile strength, heat distortion temperatures, thermal and electrical conductivities and enhanced gas

barrier properties,[11] clays/layered silicates/nanoclays have gained tremendous interest in both academic and industrial research.[12]

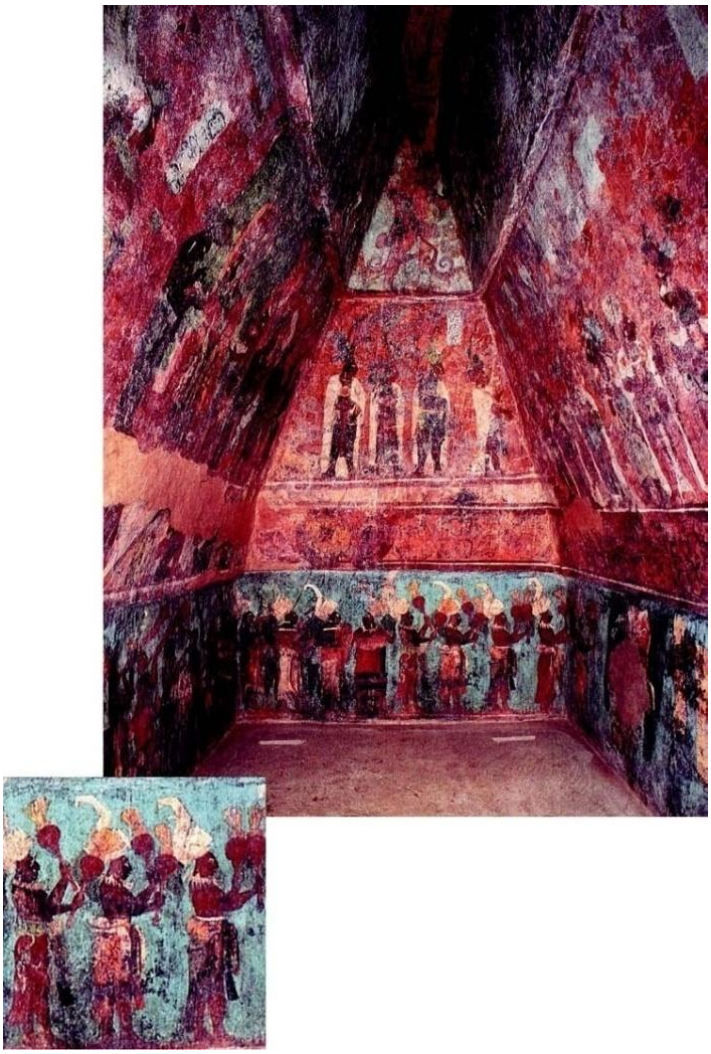

**Figure 2.** Mayan wall paintings at Bonampak which are twelve centuries old (*Functional Hybrid Materials*. **2004**, *Wiley VCH*).

Layered silicates like clays serve as an efficient inorganic component for the design of nanocomposites due to their lamellar elements that possess high in plane strength, stiffness and high aspect ratio.[13] To get a detailed overview of the processing and applications of clay hybrids, it is important to understand the structural aspects, nature, classification and modification of clays.

## 1.3. Clay:

Clay minerals are ubiquitous on our planet in geologic deposits, terrestrial biogeochemical cycles, in the buffering capacity of the oceans and in the containment of toxic waste materials.[14] They are also used as lubricants in petroleum extraction, fillers for the preparation of polymer-nanocomposites and as industrial catalysts for the synthesis of various organic compounds.[15] These applications derive fundamentally from the colloidal size and permanent charge of the clay minerals. Clay is defined as a naturally occurring layer-type alumino/magnesium silicates (phyllosilicates) composed primarily of fine-grained minerals which are generally plastic at appropriate water contents and will harden when dried or fired.[15,16]

**(a) Structure of Clay:**

Clays and clay minerals belong to a subtype of phyllosilicates with characteristic layered atomic structures. Two basic structural modular units are important in the formation of the clay structure: the tetrahedra (T) formed by silicon and oxygen atoms and the octahedra (O) formed by aluminium/magnesium and oxygen atoms as shown in Figure 3. The tetrahedra are linked through their corners, forming a tetrahedral sheet, whereas the octahedra are edge-linked, resulting in an octahedral sheet. The structural framework of the clays are basically composed of these two kinds of sheets joined together to form layers. Commonly, one tetrahedral sheet is attached to an octahedral sheet, forming a 1:1 (TO) layer (e.g. kaolinite) (Figure 4a). In other case, one octahedral sheet is sandwiched between two tetrahedral sheets forming a 2:1 (TOT) layer (chlorites and smectites) as shown in Figure 4b. For most of the clays, the layers are stacked parallel to each other, forming the characteristic layered structure.

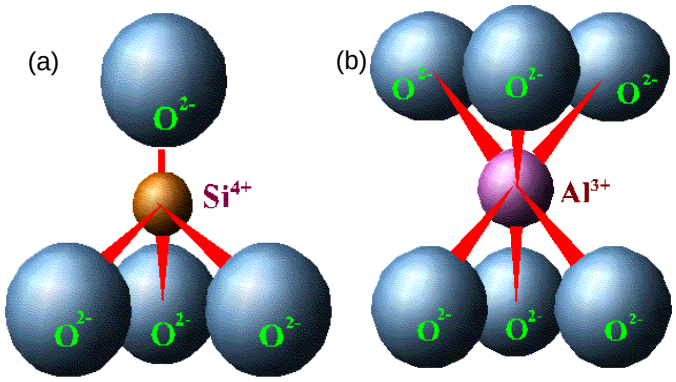


**Figure 3**. Building blocks of clay (a) silica tetrahedra, (b) aluminium octahedra.

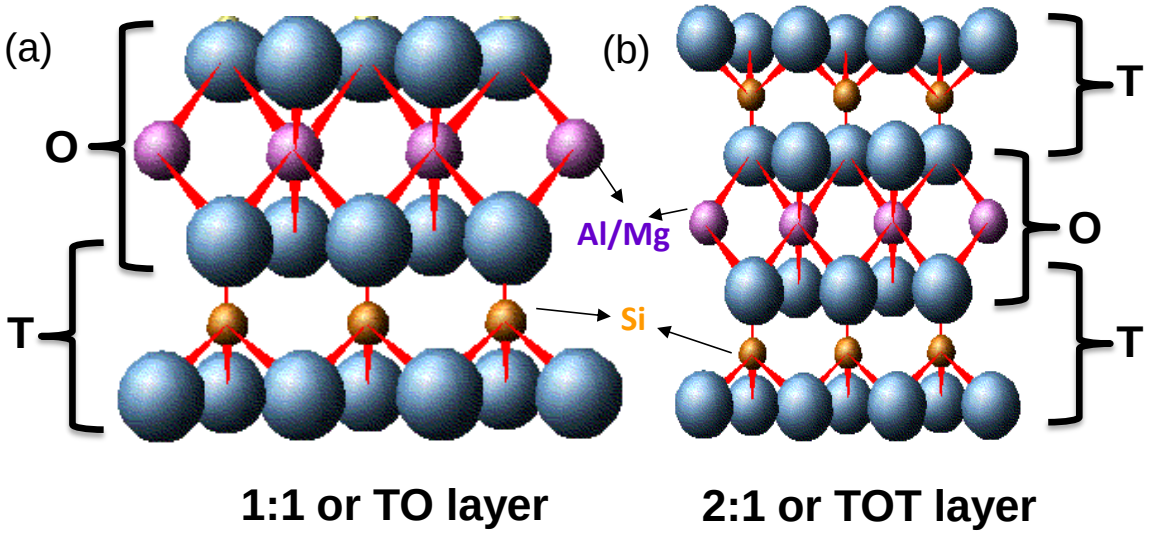


**Figure 4**. Cartoon illustrating the crystal structure of a) 1:1 and b) 2:1 layer type clay minerals (blue spheres represent oxygen atoms).

Natural minerals made up of only octahedral sheets include gibbsite $Al(OH)_3$ and brucite $Mg(OH)_2$. In the former case, just two-thirds of the octahedral are filled with Al atoms. Clay derivatives of gibbsite are therefore referred to as dioctahedral. Brucite and its clay derivatives, on the other hand, are referred to as trioctahedral because all of the octahedra are filled with Mg atoms. Clay layers carry negative charges due to the replacement of some Si (IV) in the tetrahedral sheets, or some Al (III) in the octahedral sheets. Usually, $Si^{4+}$ ions (in the tetrahedral sheet) are replaced

by $Al^{3+}$ and/or $Fe^{3+}$ cations, whereas $Al^{3+}$ ions (in the octahedral sheet) are replaced by $Mg^{2+}$ and/or $Fe^{2+}$ cations. These substitutions[15,16] are considered isomorphous and do not cause significant distortions in the structure of the clays because the sizes of the replacing cations are comparable to the original ones. To compensate the negative charges formed in this way, $Na^{+}$ or $Ca^{2+}$ cations are usually present in the interlayer region. Cations and anions may also be present on the crystal edges due to the break of valence bonds of the crystal along the c-axis. When the clays are dispersed in aqueous suspension, these charge-compensating cations can be exchanged and replaced by others present in the bulk of the suspension. The total amount of the exchangeable cations is known as the Cation Exchange Capacity (CEC) and is commonly expressed in milliequivalents per 100 g of clay (mEq/100 g clay).[17]

**(b) Groups and Subgroups**:

The major clay mineral groups according to layer type and layer charge, are classified into layer types of 1:1 (T:O) and 2:1 (T:O:T), along with ideal structural chemical compositions is presented in Table 2. The extensive variety of clays found in nature occurs due to the myriad substitutions that can occur in T or O sites. The most typical clay structures correspond to kaolinites, illites, chlorites, attapulgites and smectites. Among various clay minerals, smectite clays are widely studied and used for scientific and technological purposes. This is due to its unique combination of swelling, intercalation and ion exchange properties that make them valuable nanomaterials in diverse fields.[15-17] Montmorillonite (hydrated alumina-silicate) is the most common mineral of this group (smectite), it is named for its location in Montmorillon, France. The crystal structure of montmorillonite is shown in Figure 5 and the exchangeable cations are marked blue.

| Structure type | Charge per unit cell | Group | Mineral examples | Ideal composition | Notes |
|---|---|---|---|---|---|
| 1 : 1 (TO) | 0 | Kaolin-serpentine | Kaolinite, dickite, nacrite | $Al_4Si_4O_{10}(OH)_8$ | Kaolin subgroup, dioctahedral, nonswelling |
| | | | Chrysotile, antigorite, lizardite | $Mg_6Si_4O_{10}(OH)_8$ | Serpentine subgroup, trioctahedral, nonswelling |
| 2 : 1 (TOT) | 0 | Pyrophyllite-talc | Pyrophyllite | $Al_4Si_8O_{20}(OH)_4$ | Dioctahedral, nonswelling |
| | | | Talc | $Mg_6Si_8O_{20}(OH)_4$ | Trioctahedral, nonswelling |
| | 0.5-1.2 | Smectite | Beidellite | $[(Al_4)(Si_{7.5-6.8}Al_{0.5-1.2})O_{20}(OH)_4]Ex_{0.5-1.2}$ | Dioctahedral, swelling |
| | | | Montmorillonite | $[(Al_{3.5-2.8}Mg_{0.5-1.2})(Si_8)O_{20}(OH)_4]Ex_{0.5-1.2}$ | |
| | | | Saponite | $[(Mg_6)(Si_{7.5-6.8}Al_{0.5-1.2})O_{20}(OH)_4]Ex_{0.5-1.2}$ | Trioctahedral, swelling |
| | 1.2-1.8 | Vermiculite | Vermiculite | $[(Al_4)(Si_{6.8-6.2}Al_{1.2-1.8})O_{20}(OH)_4]Ex_{1.2-1.8}$ | Dioctahedral, swelling |
| | | | Vermiculite | $[(Mg_6)(Si_{6.8-6.2}Al_{1.2-1.8})O_{20}(OH)_4]Ex_{1.2-1.8}$ | Trioctahedral, swelling |
| | | Illite | Illite | $[(Al_4)(Si_{7.5-6.5}Al_{0.5-1.5})O_{20}(OH)_4]K_{0.5-1.5}$ | Dioctahedral, nonswelling |
| | 2 | Mica | Muscovite | $[(Al_4)(Si_6Al_2)O_{20}(OH,F)_4]K_2$ | Dioctahedral, nonswelling |
| | | | Taenolite | $[(Li_2Mg_4)(Si_8)O_{20}(OH,F)_4]K_2$ | Trioctahedral, lithium mica |
| | 4 | Brittle mica | Margarite | $[(Al_4)(Si_4Al_4)O_{20}(OH,F)_4]Ca_2$ | Dioctahedral, nonswelling |
| 2 : 1 channels or inverted ribbons | Variable | Palygorskite-sepiolite | Palygorskite | $[(Mg,Al)_4(Si_{7.5-7.75}Al_{0.5-0.25})O_{20}(OH)_2(OH_2)_4]Ex_{var}$ | Dioctahedral, nonswelling |
| | | | Sepiolite | $[(Mg,M)_8(Si,M')_{12}O_{30}(OH)_4(OH)_2)_4]Ex_{var}$ | Trioctahedral (M = Al, Fe(III); M = Fe(II), Fe(III), Mn(II) |
| 2 : 1:1 | Variable | Chlorite | Clinochlore | | [TOT]O[TOT] structure |

**Table 2**. Classification scheme of phyllosilicate clay minerals (T=tetrahedral, O= octahedral) (*Handbook of Layered Materials*. **2004**, *Marcel Dekker*)

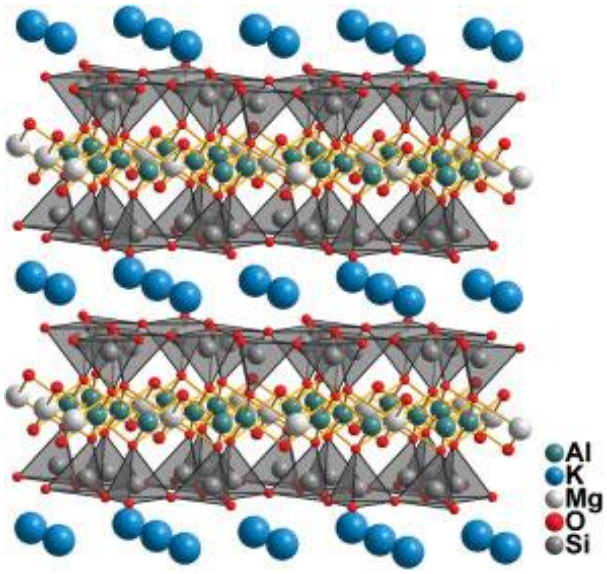


**Figure 5**. Crystal structure of montmorillonite (*Hybrid materials*. **2006**, *Wiley-VCH*).

Although smectite type of clays have significant potential applications in multidisciplinary fields, in many cases these materials suffer from heterogeneous composition and poor swelling ability in polar/non polar solvents that often hamper their exploitation.[18] Thus it is highly essential to tailor the property of clay by using appropriate organic functional groups for dispersing in aqueous/organic solvents[18a] for the design of novel hybrids.

**(c) Organic modification of clay:**

As discussed above clay layers often carry a net negative charge due to the isomorphic substitution of one element for another in both octahedral ($Mg^{2+}$ for $Al^{3+}$) and tetrahedral ($Al^{3+}$ or $Fe^{3+}$ for $Si^{4+}$) sheets. This negative charge must be balanced by a corresponding positive charge at some location. The cations that are present in gallery space like sodium, potassium (naturally occurring) balances the negative charge of clay (Figure 5). Furthermore, the hydrophilic nature of the clay surfaces hinders homogeneous dispersion in the organic polymers.[8] To overcome this problem, it is usually necessary to render the surface organophilic prior to its use.

Three methods have been used commonly for organic modification of the clay.[1a]

- Exchange of gallery cation ($Na^+$ or $K^+$) with quaternary organic cations, such as ammonium and phosphonium salts.
- Directly modifying the clay layers using organic coupling agents, such as silane coupling agents.
- Using crown ether to complex the clay cations.

The obtained organically modified clays can be homogeneously dispersed in aqueous/organic solvents depending on the nature of the reaction. The role of the organic compounds in the organoclay is to reduce the surface energy of the clay[8b], thereby improving the wetting characteristics by the polymer. The organic modification can be done either by ex-situ or in-situ approach. In the former case, the organic moiety is grafted with the clay (e.g. ion exchange of the sodium cation for the quaternary ammonium cation or reaction of the external Al-OH surfaces of imogolite with aminopropyl triethoxy silane under hydrolysis conditions),[19] whereas the later approach uses direct addition of organic moiety during the synthesis of clay. In-situ approach is advantageous compared to ex-situ method since the linkage or organic components via covalent bonds enable a durable immobilization of the reactive organic groups, preventing their leaching in the surrounding medium when the modified clay materials are to be used in solutions. The modification of the surface characteristics of silica or alumina/magnesium silicates is typically done by the reaction of silane derivatives such as chlorosilane, alkoxysilane, or organosilanes with silanol groups accessible on the surface.[20] Thus, organoclays based on smectites have been extensively studied for industrial and environmental applications, such as rheology controlling agents in paints, greases and cosmetics,[16] nanofillers in the preparation of polymer-clay nanocomposites (PNCs),[12] adsorbents for poorly water

soluble species,[21] hosts for electrochemical reactions,[22] as matrices for photofunctional species and catalytically active species,[23a] as well as in the so-called environmentally-oriented pesticide formulations that avoid or reduce the loss of bioactivity due to volatility or photodegradation of insecticides and herbicides.[23a, 24]

## 1.4. Clay-polymer nanocomposites (hybrids):

Hybrid organic-inorganic nanocomposites of polymer and clay nanoplatelets have received special attention for various scientific and industrial applications.[8,13] Three main properties of polymer-clay hybrids have been commercially exploited: improvement of mechanical properties of polymers, gas barrier performance and fire/heat resistance. Consequently markets concerned with clay based polymer hybrids are mainly automotive and food/beverage packaging.[2] In general the properties of the resulting nanocomposites depend upon the interaction between the clay and polymer (compatibility).

The compatibility between organic polymers and organoclays resulting in polymer-clay hybrids are classified in two idealized morphologies (intercalated or exfoliated). The classification is based upon the registry of the silicate layers in the polymer matrix (Figure 6). In the intercalated structure, the organic component is inserted between the layers of the clay in such a way that the inter-layer spacing is expanded, but the layers still bear a well defined spatial relationship to each other (Figure 6a). In an exfoliated structure, the layers of the clay have been completely separated and the individual layers are distributed throughout the organic matrix (Figure 6b). A third possible morphology is the immiscible mixing of clay and polymer, also known as a microcomposite, in which the clay is not well-dispersed and is behaving as conventional filler. Exfoliated hybrids exhibit superior

mechanical and barrier properties compared to intercalated systems and are quite challenging to obtain these hybrids.

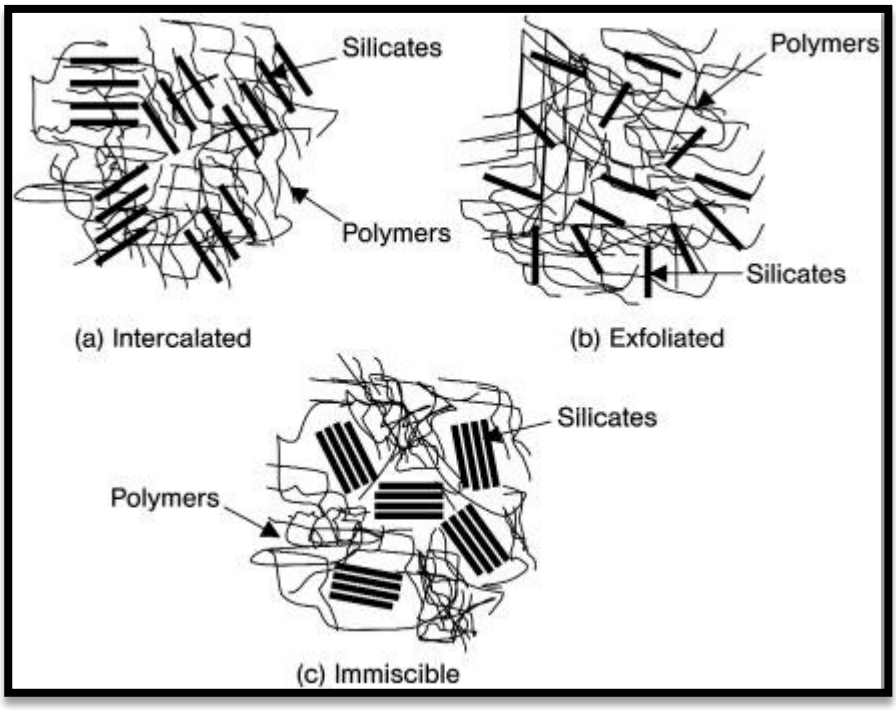


**Figure 6**. Scheme showing possible clay-polymer nanostructures (*Hybrid materials*. **2006**, *Wiley-VCH*).

## 1.5. Aminopropyl functionalized Mg phyllosilicate:

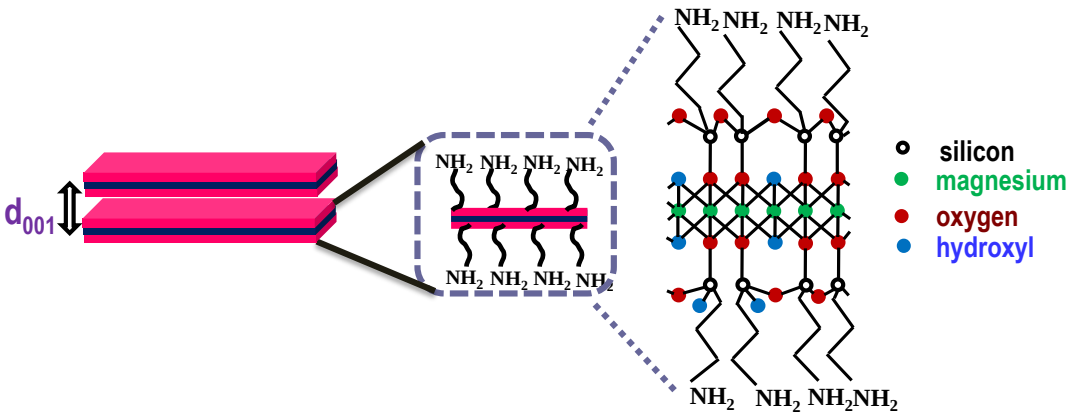


**Figure 7.** Two dimensional structural representation of amine functionalized magnesium phyllosilicate.

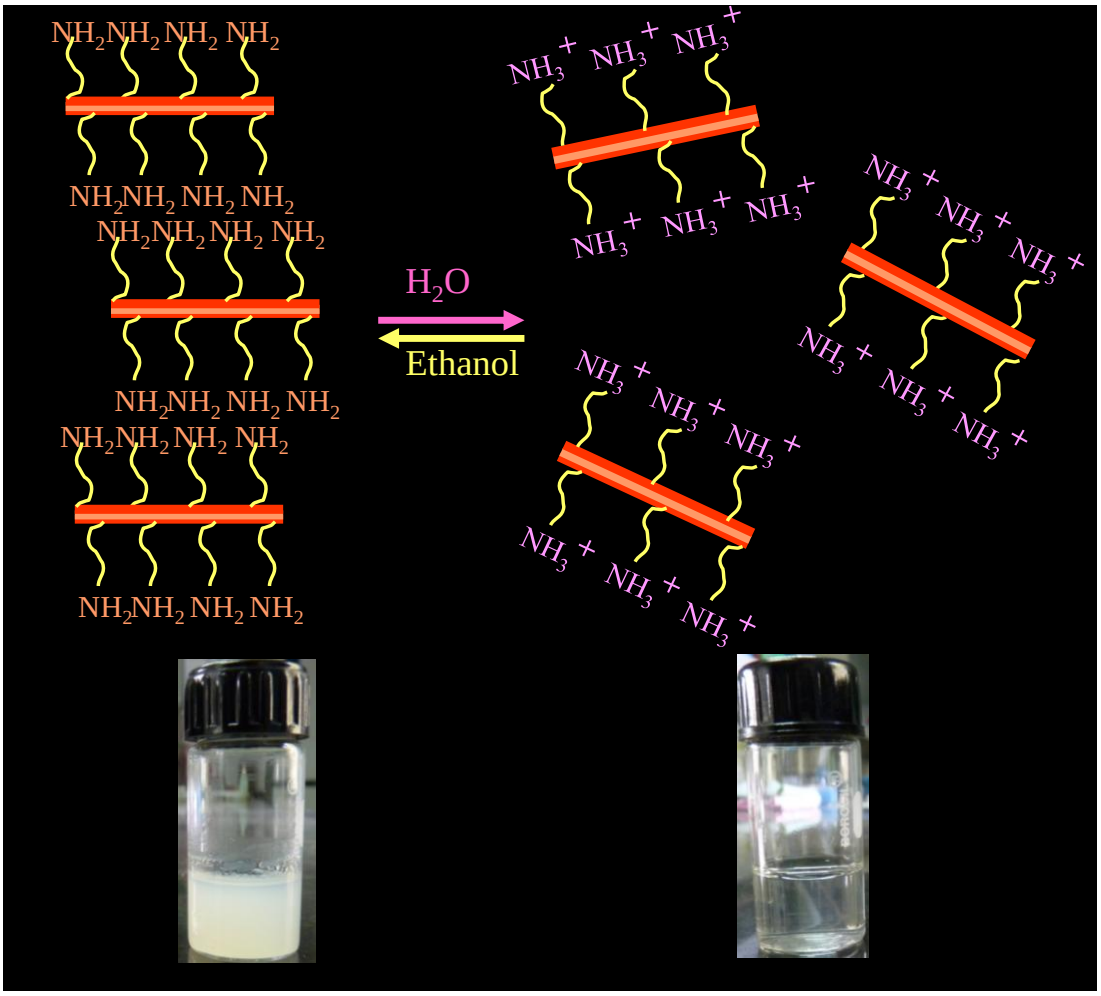


**Figure 8.** *Top*: Schematic showing disorder-order arrangement of aminoclay in water and ethanol respectively, *bottom*: corresponding optical images.

Traditionally, organoclays which are not easily dispersible in water are used as fillers in the preparation of polymer-nanocomposites. However, for various biological and environmental related applications organically functionalized clays with high water dispersiblity are very much advantageous.[23] One such organoclay which has received enormous attention in the recent years is aminopropyl modified magnesium phyllosilicate (Figure 7).[25] The approximate unit cell composition of this organoclay is $R_8Si_8Mg_6O_{16}(OH)_4$ (in which $R=CH_2CH_2NH_2$) and consisted of octahedrally coordinated MgO/OH sheets (brucite) overlaid on both sides with a tetrahedrally coordinated aminopropyl-functionalized silicate network.[18] The as-

synthesized aminoclay exhibits a basal distance ($d_{001}$) of 1.6 nm, which is nearly double to that of talc ($d_{001}$= 0.9 nm)[26] indicating that the propylamine functionalities are present within the interlayer spaces. One important feature of aminoclay is its free exfoliation in water by the protonation of amine groups in water which can be restacked by the addition of ethanol (Figure 8).

The positively charged aminoclay was used to prepare bio-hybirds composed of negatively charged biomolecules such as DNA, proteins, etc (Figure. 9).[27,25,28] Furthermore, aminoclay has been successfully utilized for the confinement and controlled release of pharmaceutically important guest molecules such as the anti-inflammatory drug, ibuprofen and the antioxidant polyphenol extracted from green tea, epigallocatechin (EGCG), which has the ability to inhibit the growth of cancer cells.[27, 29]

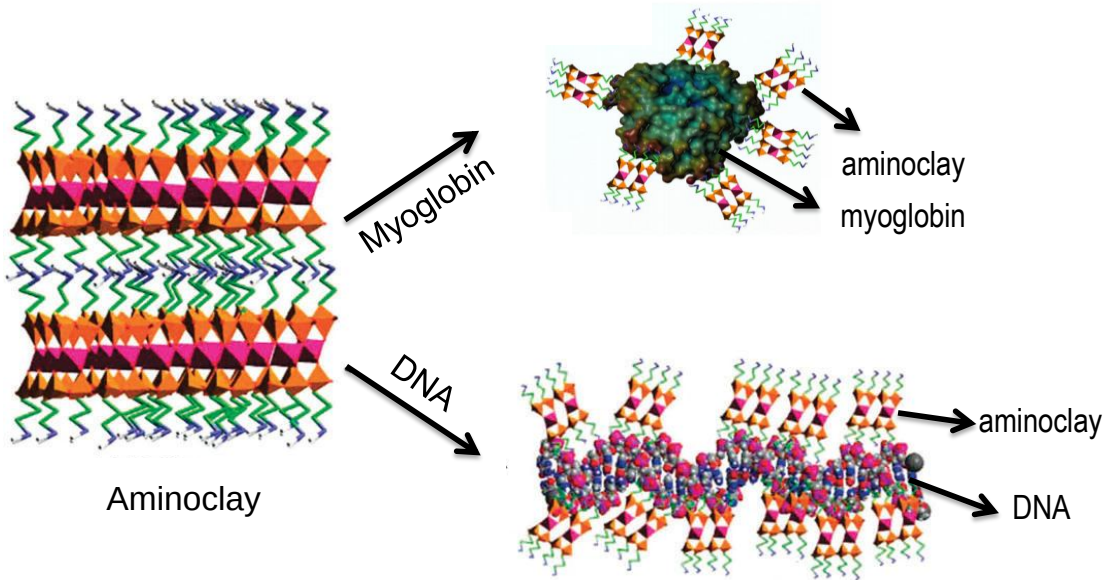


**Figure 9.** Scheme showing the protocol involving aminoclay (left), in the preparation of biohybrids with negatively charged biomolecules (Myoglobin: *Angew. Chem. Int. Ed*. **2004**, *43*, 4928 and *DNA: Nano Lett*. **2007**, *7*, 2660).

## 1.6. Conclusions:

Organically modified phyllosilicates are emerging as powerful candidates in the fields of chemistry, biology, materials, catalysis, etc. The exfoliation/restacking ability of organoclays in various solvents can be utilized in delivery of guest molecules and designing smart materials. The functional groups of organoclays can be utilized in stabilizing noble-metal nanostructures. This is advantageous because the coupling of size dependent optical, catalytic and electronic properties of nanoparticles with clay materials lead to the development of novel clay-nanoparticle hybrids. The nanoscopic voids provided by the clay layers could be used to prepare various layered nanostructures.

## 1.7. References:


1. a) G. Kickelbick, *Hybrid materials*. **2006**, *Wiley-VCH*, b) *P. G-Romero, C. Sanchez Functional Hybrid Materials*. **2004**, *Wiley VCH*, c) Y. Chujo**,** KONA. **2007**, *25*, 255.
2. C. Sanchez, P. Belleville, M. Popall, L. Nicole, *Chem. Soc. Rev*. **2011**, *40*, 696.
3. a) Y. Hagiwara, H. Suzuki, **2000**, 135 *Fracture Mechanics*, Ohmsha, Tokyo, Japan, b) Nanko M. **2009**, *6*, *Definitions and categories of hybrid materials*. *Azojomo*, 10.2240.
4. Materials Science Society of Japan, *Molecular Hybridization and Hybrid Materials, Composite System in Materials*, **1993**, *Shokabo Publishing Co*, 336.
5. a) G. Mayer, *Science*. **2005**, *310*, 1144, b) M. A. Meyers, P. Y. Chen, A. Y. M. Lin, Y. Seki, *Prog. Mater. Sci*. **2008**, *53*, 1, c) C. Ortiz, M. C. Boyce, *Science.* **2008**, *319*, 1053.
6. a) J. Aizenberg, J. C. Weaver, M. S. Thanawala, V. C. Sundar, D. E. Morse, P. Fratzl, *Science.* **2005**, *309*, 275, b) F. Barthelat, H. D. Espinosa, *Exp. Mech*. **2007**, *47*, 311, c) R. K. Nalla, J. H. Kinney, R. O. Ritchie, *Biomaterials*. **2003**, *24*, 3955, d) R. K. Nalla, J. J. Kruzic, J. H. Kinney, R. O. Ritchie, *Biomaterials*. **2005**, *26*, 217.
7. E. R-Hitzky, M. Darder, P. Aranda, *J. Mater. Chem*. **2005**, *15*, 3650.
8. a) E. Munch, M. E. Launey, D. H. Alsem, E. Saiz, A. P. Tomsia, R. O. Ritchie, *Science.* **2008**, *322*, 1516, b) L. J. Bonderer, A. R. Studart, L. J. Gauckler, *Science.* **2008**, *319*, 1069,
9. H. V. Olphen, *Science*. **1966**, *154*, 645

10. E. P. Giannelis, *Appl. Organometal. Chem.* **2001**, *12*, 675.
11. a) Y.T. Lim, O.O. Park, *Rheol. Acta.* **2001**, *40*, 220, b) A. C. Balazs, T. Emrick, T. P. Russell, *Science.* **2006**, *314*, 1107.
12. a) H. R. Dennis, D.L. Hunter, D. Chang, S. Kim, J. L. White, J. W. Cho, D. R. Paul, *Polymer*. **2001**, *42*, 9513, b) R. Krishnamoorti, A. S. Silva, **2000**, in *Polymer-clay Nanocomposites*, T. J. Pinnavaia, G.W. Beall (Eds.), *John Wiley and Sons*, 315, c) G. Johnsy, K. K. R. Datta, S. Vallayil, S. Shanmugam, B. Amarinder, M. Eswaramoorthy, *ACS Applied Materials & Interfaces***. 2009**, *1*, 2796.
13. a) O. L. Manevitch, G. C. Rutledge, *J. Phys. Chem. B.* **2004**, *108*, 1428, b) R. K. Gupta, S. N. Bhattacharya, *Indian. Chem. Eng*. **2008**, *50*, 242
14. a) L. Pauling, *PNAS.* **1930**, *16*, 123, b) L. Pauling, *PNAS.* **1930**, *16*, 578, c) S. B. Hendricks, W. H. Fry, *Soil. Sci.* **1930**, *29*, 457.
15. G. Sposito, N. T. Skipper, R. Sutton, S-H. Park, A. K. Soper, J. A. Greathouse, *PNAS.* **1999**, *96*, 3358
16. S. M. Auerbach, K. A. Carrado, P. K. Dutta, *Handbook of Layered Materials*, **2004**, *Marcel Dekker*
17. M. G. Neumann, C. C. Schmitt, F. Gessner, *Encycl. Surf. Colloid Sci.* **2006**, *1*, 389.
18. a) B. Lebeau, J. Brendle, C. Marichal, A. J. Patil, E. Muthuswamy, S. Mann, *J Nanosci. Nanotechnol.* **2006**, *6*, 352, b) N. T. Whilton, S. L. Burkett, S. Mann, *J. Mater. Chem*. **1998**, *8*, 1927, c) S. L. Burkett, A. Press, S. Mann, *Chem. Mater*. **1997**, *9*, 1071.
19. a) L. M. Johnson, T. J. Pinnavaia, *Langmuir*. **1990**, *6*, 307, b) L. M. Johnson, T. J. Pinnavaia, *Langmuir.* **1991**, *7*, 2636.

20. a) I. K. Tonlé, T. Diaco, E. Ngameni, C. Detellier, *Chem. Mater.* **2007**, *19*, 6629, b) N. R. E. N. Impens, P. van der Voort, E. F. Vansant, *Microporous Mesoporous Mater.* **1999**, *28*, 217.
21. a) Y. H. Shen, *Colloids Surf. A.* **2004**, *232*, 143, b) G. Sheng, T. C. Johnston, B. J. Teppen, S. A. Boyd, *J. Agric. Food Chem.* **2001**, 49, 2899.
22. I. K. Tonlé, E. Ngameni, H. L. Tcheumi, V. Tchiéda, C. Carteret, A. Walcarius, *Talanta*. **2008,** *74*, 489
23. a) E. R-Hitzky, P. Aranda, M. Darder, G. Rytwo, *J. Mater. Chem.* **2010**, *20*, 9306, b) E. R-Hitzky, P. Aranda, M. Darder, M. Ogawa, *Chem. Soc. Rev.* **2011**, *40*, 801.
24. Q. Huang, P. M. Huang, A. Violante, Soil Mineral-Microbe-Organic Interaction*s: Theories and Applications*, **2008**, 145, *Springer-Verlag Berlin*.
25. A. J. Patil, E. Muthusamy, S. Mann, *Angew. Chem., Int. Ed*. **2004**, *43*, 4928
26. JCPDS Card Number 13-0558.
27. a) A. J. Patil, S. Mann, *J. Mater. Chem*. **2008**, *18*, 4605, b) A. J. Patil, E. Muthusamy, S. Mann, *J. Mater. Chem*. **2005**, *15*, 3838.
28. A. J. Patil, M. Li, E. Dujardin, S. Mann, *Nano Lett*. **2007**, *7*, 2660.
29. Z. Hou, S. Sang, H. You, M. J. Lee, J. Hing, K. V- Chin, C. S. Yang, *Cancer Res*. **2005**, *65*, 8049.

# Part B: Carbon based Nanostructures

## 1.1. Introduction:

The element carbon provides the basis for life on Earth. Its high natural abundance, low specific weight, catenation property as well as the chemical and thermal robustness has resulted in carbon components being increasingly utilized in inexpensive, lightweight and durable high performance materials over the past two decades.[1] In particular, carbon nanostructures such as fullerenes, carbon nanotubes, graphenes and carbon fibers have been used in a broad range of technological applications, such as novel energy sources, efficient energy storage, sustainable chemical technology, high-performance construction materials and organic electronic materials.[2-4]

Nanoporous carbons, another class of non-oxidic porous materials,[5] are of great scientific and technological importance due to the applications in areas of water and air purification, templates, separation, gas storage, electrochemistry, biology and catalysis.[6] The widespread use of porous carbons results from their remarkable properties like high surface area, chemical inertness, thermal stability, good mechanical stability, biocompatibility, etc.[7] These porous carbon materials are classified according to their pore diameters as microporous (pore size < 2nm), mesoporous (2nm < pore size < 50 nm) and macroporous (pore size > 50 nm). The pore size can be tuned by choosing various templating techniques which are discussed below.[5]

### 1.2. Synthesis of porous carbons:

Synthesis of hierarchical carbon structures with designed porosity often based on the hard and soft-templating approaches.[8-10] The general concept of hard templating procedure, which is essentially similar as that used to fabricate a ceramic

jar, but scaled down to the nanometer regime is shown in Figure 10. To make a jar, a piece of wood with the desired shape is first carved, and then clay is applied to the surface of the wood. Through heating at approximately1000 °C under air, the clay is transformed to ceramic and the wood is simultaneously burnt to generate the empty space inside the jar. The general template synthetic procedure for porous carbons is as follows: 1) preparation of the carbon precursor/inorganic template composite, 2) carbonization and 3) removal of the inorganic template. Various inorganic materials, including silica nanoparticles (silica sol), zeolites, anodic alumina membranes and mesoporous silica materials have been used as hard templates. Precursors such as sucrose, glucose, (solids) furfuryl alcohol, acetonitrile, (liquids), ethylene, propylene (gases) are generally used as carbon sources.[8]

The synthesis of microporous, mesoporous and macroporous carbons using zeolite, mesoporous silica and synthetic silica opal as hard templates is shown in Figure 10b to 10d. Figure 10e shows the synthesis of carbon nanotubes (CNTs) using an anodic alumina membrane template. By choosing appropriate template, it is possible to control both the internal (pore engineering) and external (spheres, rods, etc) structures of the porous carbons.

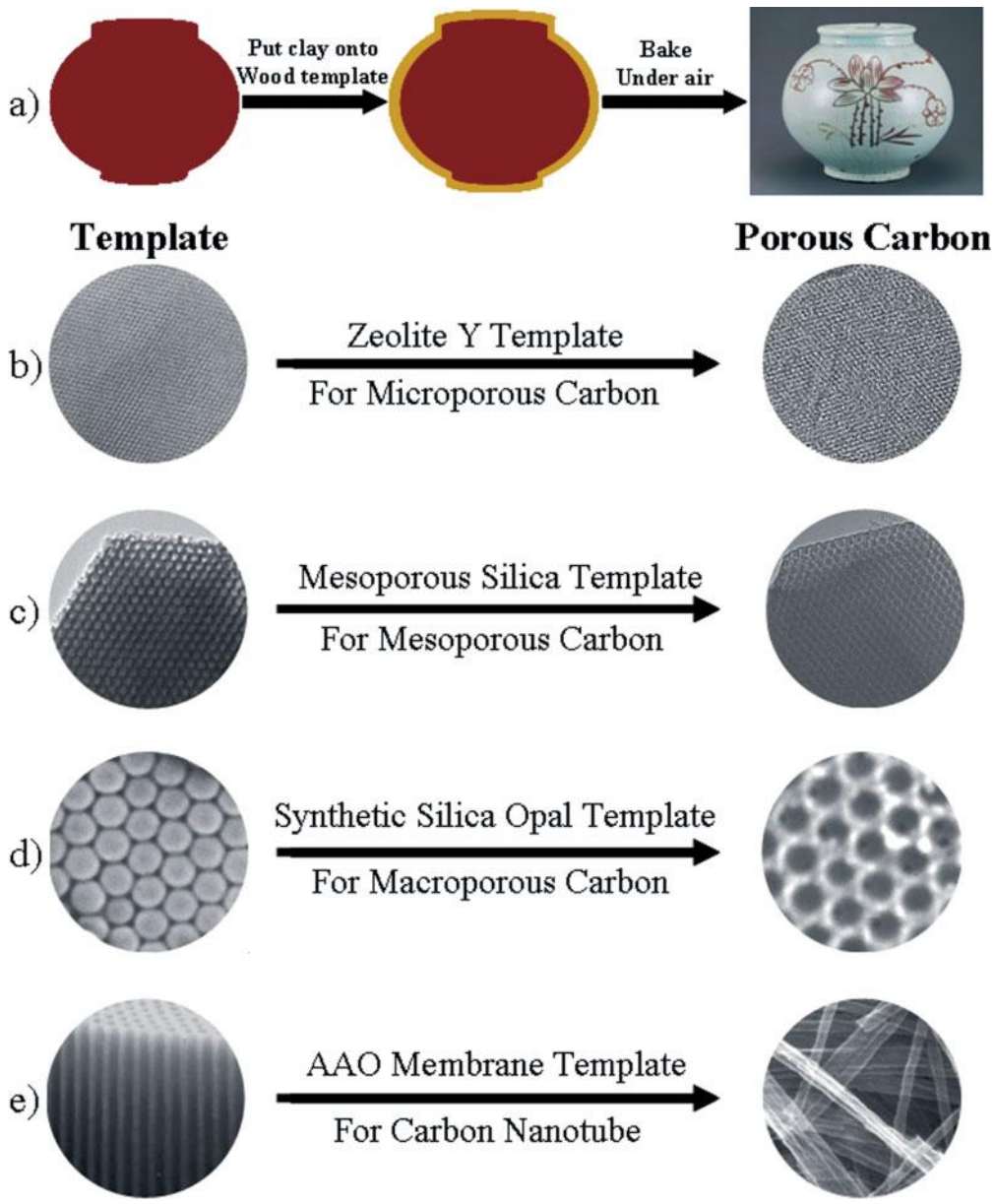


**Figure 10.** a) Schematic representation showing the concept of template synthesis. b) Microporous, c) mesoporous, and d) macroporous carbon materials, and e) carbon nanotubes were synthesized using zeolite, mesoporous silica, a synthetic silica opal, and an AAO membrane as templates respectively (*Adv. Mater.* **2006**, *18*, 2073).

**Soft-templating route:**

Recently, considerable progress has been made on the direct synthesis of ordered mesoporous carbon materials by self-assembly of copolymer molecular arrays and carbon precursors. This opens a new way for the preparation of ordered

mesoporous carbon materials with fewer synthesis steps. The self-assembly of organic-organic species via soft templating represents a breakthrough allowing the efficient synthesis of mesoporous polymers and mesoporous carbons with controlled pore structures. Zhao and co-workers have made major progress in the soft template synthesis of mesoporous carbons. They reported the self-assembly of the triblock copolymer (PEO-PPO-PEO) templates and resol (phenol-formaldehyde resin) mixtures and successful removal of the templates including Pluronic F127, F108 and P123 to produce mesoporous polymer and carbon materials.[11] Figure 11 illustrates the five-step synthesis procedure adopted by Zhao's group to synthesize mesoporous carbons.

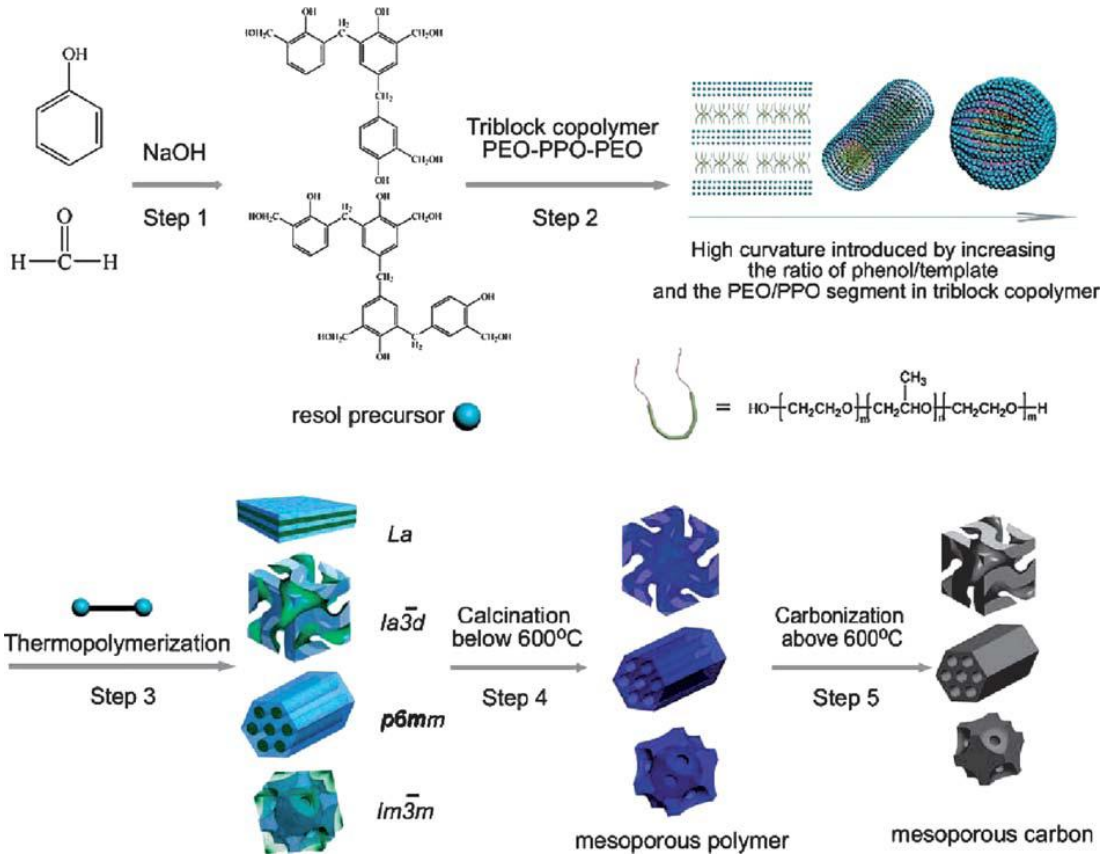


**Figure 11.** Scheme illustrating the preparation of ordered mesoporous polymer resins and carbon frameworks (*Chem. Mater*. **2006**, *18*, 4447).

However, there are still plenty of challenges ahead in the synthesis of porous carbons. For example, unlike mesoporous carbons that can be prepared with various pore sizes via either hard or soft template methods, microporous carbons with tunable pore diameter and narrow pore size distribution remain a major challenge. This is because the wall thickness of zeolite templates is too rigid to adjust. Preparation of highly ordered (well defined pore diameter) and high surface area microporous carbons via direct routes is a challenge[11e] that will continue to attract attention due to the fact that such microporous carbons are of great importance for energy applications such as gas storage.

To date, block copolymers have dominated as soft templates for the synthesis of mesoporous carbons and only hydrogen bonding has been explored as the self-assembly driving force. It is desirable to investigate other driving forces and other surfactants or templates to synthesise porous carbon materials. In particular, the synthesis of microporous carbon via soft template strategies is of great interest. The further development of new hierarchical materials that possess not only mesopores and macropores, but also micropores will be desirable for new applications involving smaller molecules. Furthermore, functionalizing porous carbon through direct incorporation of heteroatoms in the carbon synthesis, surface oxidation and activation, halogenation, sulfonation, grafting, attachment of nanoparticles and surface coating with polymers are ongoing projects in this field.[12]

## 1.3. Hetero atom doping and nitrides of mesoporous carbons:

There has been great deal of interest generated among various researchers to study the doping effects of hetero atoms such as nitrogen and boron onto porous carbons.[13] The important properties that originate due to the hetero atom doping onto carbonaceous nanostructures are extreme hardness, conduction, storage, field

emission, oxidation resistance and chemical inertness. Nitrogen doped mesoporous carbons and mesoporous carbon nitride (MCN) are the most studied materials with a wide range of applications. In particular, MCN is an attractive material for various applications such as photocatalysis for water splitting, metal-free activation of $CO_2$, templating ternary metal nitrides, fabrication of low dielectric devices, hydrogen storage, etc.[14]

## 1.4. Applications of Nanoporous Carbon Materials:

Properties like chemical stability, electronic conductivity, intercalation ability of electrochemically active species and sorption capabilities make porous carbons an interesting class of materials for a range of applications related to biomolecule adsorption, catalysis, storage and sorption.[6,8,12] Many of these applications have previously benefited from other forms of carbon, including glassy carbon and graphitic carbon for electrodes and activated carbons for catalysis and sorption. However, the new carbon materials with designer porosity can provide significant benefits related to tunable surface areas, pore-size distribution and pore access. Even more advantages can be derived by modifying the carbon wall or surface composition.[12]

**(a) Sensors:**

The important properties such as high electrical conductivity, large surface areas and pore volumes of porous graphitic carbons make them suitable candidates for sensor substrates. For e.g. mesocellular carbon foam (MSU-F-C) was used as an immobilization host for glucose oxidase (GOx) [molecular dimensions: 5.2 nm× 6.0 nm× 7.7 nm].[15] Due to its large pore size high amounts of GOx ((39.1±0.7) wt %) is adsorbed than for graphite, activated carbon and mesoporous carbon CMK-3. To use this material as a glucose sensor, MSU-F-C was combined with Nafion and coated

onto a glassy-carbon electrode, followed by immobilization of GOx. This sensor exhibited high sensitivity as well as fast glucose response (Figure 12). Current challenges in this area include preparation of novel forms of porous carbons and nitrogen containing porous carbons with excellent sensing abilities towards heavy metal ions, toxic dyes, biomolecules, etc.

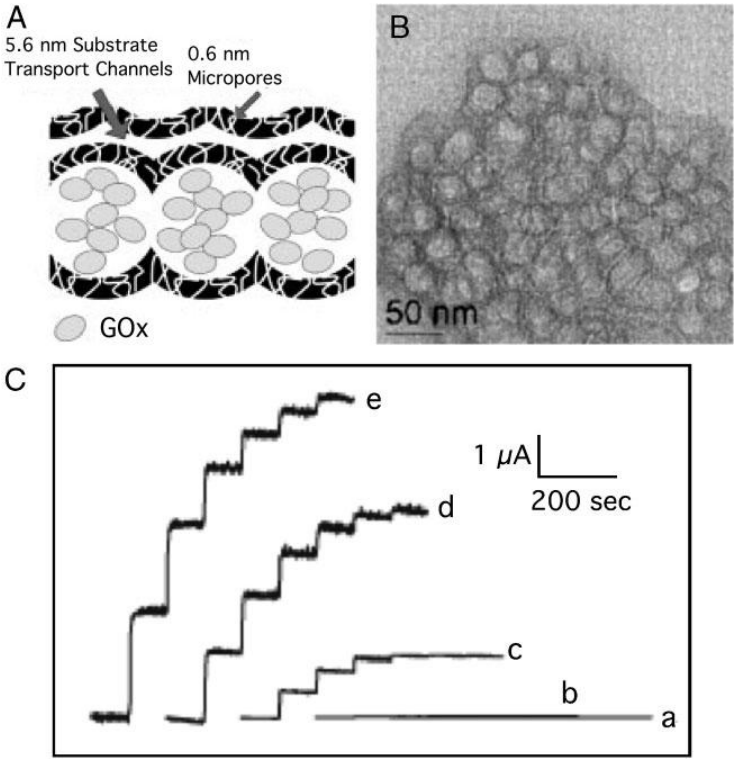


**Figure 12.** A) Schematic representation of an MSU-F-C/glucose oxidase composite, showing effective retention of enzymes within large mesopores and the role of small pores in the facile transport of a substrate. B) TEM image of MSU-F-C. C) Current response of the glucose biosensor prepared with different MSU-F-C contents on successive additions of 1 M glucose aliquots (10 μL each). The MSU-F-C contents are: a) 0, b) 0.5, c) 1.0, d) 2.0 and e) 3.0 mg/ $mL^{-1}$ in Nafion solution (*Adv. Mater*. **2005**, *17*, 2828).

**(b) Electrochemistry:**

Crystalline forms of carbons especially graphite, have been thoroughly investigated for lithium-ion battery anode materials, due to their ability to intercalate lithium ions.[16] Recently, graphitic porous carbons have gained interest as anode

materials. Even without further functionalization, mesoporous carbons can have large capacities. Because of their high surface areas, they display large capacity losses in the first cycle, due to electrolyte decomposition at the carbon surface. High surface areas and porous structure also enhance lithium-ion transfer which makes them useful candidates where quick charge and discharge are required.[12]

Templated nanoporous carbons (TNCs) having tunable surface textures, electronic conductivity and low density serve as ideal candidates for electrode materials in capacitors. Current research in porous carbon-based capacitors is primarily concerned on the area of electrochemical capacitors and super-capacitors, in which charge is stored within the double layers at the interfaces between the carbon electrodes and the electrolyte. This type of charge-storage device is also referred an electrochemical double-layer capacitor (EDLC). This electrochemical design provides two advantages: 1) very high specific surface areas are easily obtained in TNCs; 2) the electric double layer is extremely thin (few nm) in comparison to conventional physical capacitors, in which electrodes are separated by solid dielectric materials. Both these factors contribute to the high specific capacitance of EDLC, as the capacitance increases with better overlapping area and shorter distance between two electrodes. EDLCs are being studied widely due to their increasing demand for new energy-storage media with high specific power and improved durability.[17] Due to their high power densities and relatively high energy densities (compared to conventional capacitors), EDLCs are of great interest for hybrid power sources for electrical vehicles, digital telecommunications systems, uninterruptible power supplies for computers and pulse-laser generators.[12]

**(c) Fuel Cells:**

An electrochemical cell that converts energy from a fuel into electrical energy is called fuel cell. These are promising alternatives to the existing fossil-based energy generation technologies. Among various types of fuel cells, direct methanol fuel cells (DMFCs) have drawn much interest, as they can be built with small dimensions, ideal as continuous power supplies for portable electronic devices including cell phones, personal digital assistants (PDAs) and laptops. The essential unit of a DMFC is a membrane-electrode assembly, which is composed of two electrodes, one proton exchangeable (but not electrically conductive) membrane and one bipolar plate for current collection and feeding of methanol and air/oxygen. The core parts of DMFCs are the electrodes consisting of a cathode for oxygen reduction, typically composed of a porous carbon support decorated with dispersed Pt nanoclusters and an anode for methanol oxidation, composed of another porous carbon support loaded with highly dispersed Pt-Ru nanoclusters.[12]

For efficient functioning of DMFCs, high surface area and accessible porosity of the carbon supports are vital. Conventional catalytic supports include deposition of Pt onto carbon gels or activated carbon.[6b] In these cases Pt is dispersed on the external surface of the matrix due to their low accessible porosity and majority of micropores, which requires a high loading of Pt there by increasing the cost of the electrodes. As a result, designing novel porous carbon supports with large and accessible pores is highly essential. Current research include the designing of new cathode and anode materials comprising of novel mesoporous carbons, in particular developing nonprecious-metal and metal-free catalysts for cathode materials.[18]

**(d) Hydrogen Storage:**

Developing better, safe and efficient hydrogen storage materials remains one of the challenging problems in the contemporary research. Various forms of carbon are among the options of materials considered for hydrogen storage.[19] In particular, nanoporous carbons merit examination for hydrogen storage applications because of their high surface areas and pore volumes, low densities and tunable pore structures. For enhanced hydrogen-storage in porous carbons, physisorption should be combined with chemisorption.[12,19] In this regard, development of functionalization methods and porous carbon materials help to pave the path to the desired target.[20] Moreover, the presence of metal clusters well within the pores of carbon facilitates increase the hydrogen uptake via the spillover effect (catalyzed formation of monatomic hydrogen followed by migration to the surface of the support).[21]

**(e) Catalysis:**

Properties such as chemical inertness, high oxidation resistance, mechanical resistance and high surface area necessitate carbon supports as highly active catalytic materials. Indeed allocation of pores is most important in catalytic reactions involving large molecules, where accessible mesopores are preferred over micropores. Studies concerning the functionalization of mesoporous carbons followed by loading of metal nanoclusters for various organic transformations are investigated in detail during the last few years.[22]

In addition to being an efficient metal-catalyst support, synthetic carbon is a useful support for acid catalysis such as esterification of diacids, liquid phase acylation of alcohols, etc. Beyond acting as supports for metal and acid catalysis, porous carbons also provide a platform for biocatalysts, such as enzymes.[12]

**(f) Adsorbents:**

The best attraction of mesoporous and macroporous carbons with designed porosity is their ability to accommodate relatively large guests, such as enzymes and other biomolecules.[23] Adsorption of enzymes on porous carbon is of interest for potential applications in biosensing, enzymatic catalysis, biotechnology, medical technology and food processing. Mesoporous carbons, in particular, provide an opportunity for selective adsorption of proteins and other biomolecules with specific molecular sizes, because their textural parameters are readily tunable.[23]

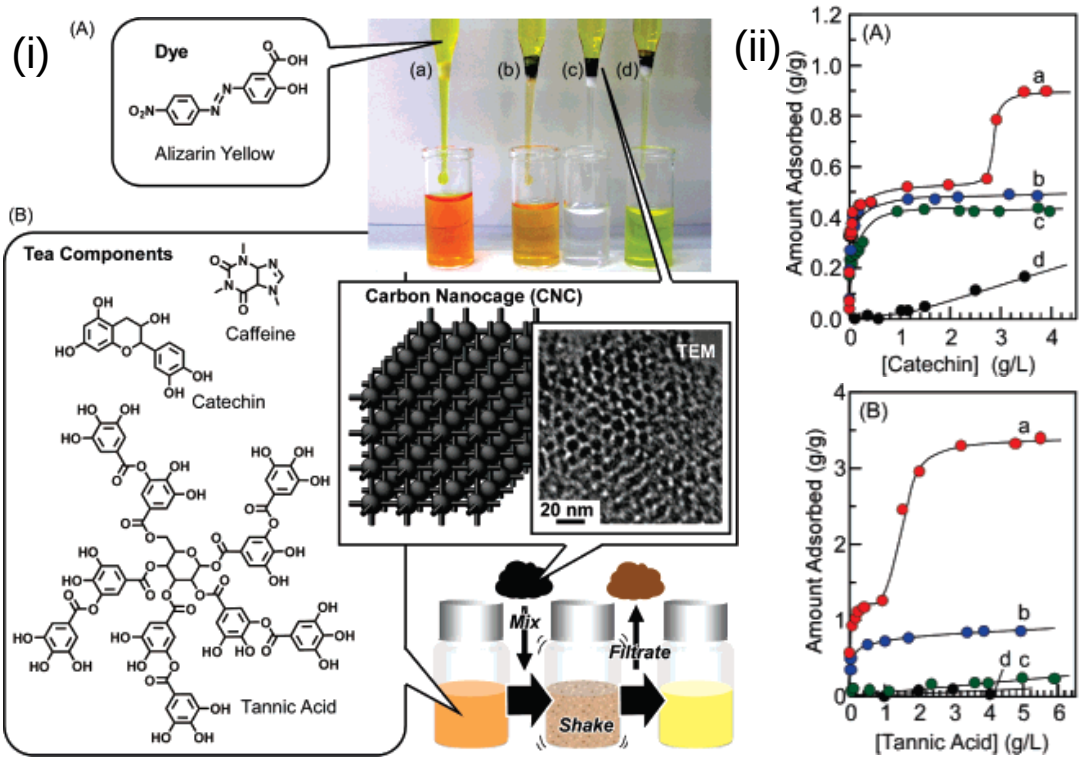


**Figure 13. (i)** (A) Filtration of Alizarin Yellow by carbon adsorbents: (a) none; (b) AC; (c) CNC; (d) CMK-3. (B) Outline of tea component adsorption experiment with formula of guests structure of CNC. (ii) Adsorption isotherms of (A) catechin and (B) tannic acid: (a) CNC; (b) CMK-3; (c) AC; (d) SBA-15 ( *J. Am. Chem. Soc.* **2007**, *129* 11022).

Functionalized and non-functionalized mesoporous carbons are also being considered for sorption applications. For example, a mesoporous carbon impregnated with ferrous chloride and oxidized with sodium hypochlorite was used as a sorbent for removing arsenic from drinking water.[24]

Furthermore, these porous carbon materials exhibit very high affinities towards aromatic organic compounds. For e.g. carbon nanocage shows very high selectivity for adsorption of tea components (tannic acid and catechin)[26] through a simple one-pot process (Figure 13).

## 1.5. Conclusions:

The remarkable features of nanoporous carbons make them as versatile materials in the fields of material science, biology, catalysis and storage. There is still a plenty of scope to improve and invent new properties to the porous carbon materials. For example, designing mesoporous carbons with inbuilt functionalites (mesoporous carbon nitride) would easily facilitate in stabilizing metal/metal oxide nanoparticles. The effect of heat treatment on textural parameters like specific surface area, specific pore volume and conductivity of the mesoporous carbon nitrides is of interest in electrode materials. Similarly, developing porous carbon supports for selective adsorption of biomolecules and hazardous molecules would have tremendous application in the fields of biology and environment.

## 1.6. References:


1. E. H. L. Falcao, F. Wudl, *J. Chem. Technol. Biotechnol*. **2007**, *82*, 524.
2. T. N. Hoheisel, S. Schrettl, R. Szilluweit, H. Frauenrath, *Angew. Chem. Int. Ed.* **2010**. *49*, 6496.
3. a) C. Popov, NATO *Sci. Ser. Ser. II.* **2006**, *223*, 387, b) E. Dervishi, Z. Li, Y. Xu, V. Saini, A. R. Biris, D. Lupu, A. S. Biris, *Part. Sci. Technol*. **2009**, *27*, 107.
4. a) R. V. Noorden, *Nature*. **2011**, *469*, 14, b) A. Hirsch, *Nat. Mat*, **2010**, *9*, 868, c) Y. H. Hu, O. A. Shenderova, Z. Hu, C. W. Padgett, D. W. Brenner, *Rep. Prog. Phys*. **2006**, *69*, 1847
5. R. Ryoo, S. H. Joo, M. Kruk, M. Jaroniec, *Adv. Mater*. **2001**, *13*, 677.
6. a) F. Schüth, *Angew. Chem. Int. Ed.* **2003**, *42*, 3604, b) S. H. Joo, S. J. Choi, I. Oh, J. Kwak, Z. Liu, O. Terasaki, R. Ryoo, *Nature*. **2001**, *412*, 169, c) T. Yu, Y. H. Deng, L. Wang, R. L. Liu, L. J. Zhang, B. Tu and D. Y. Zhao, *Adv. Mater*. **2007**, *19*, 2301, d) A. H. Lu, W. Schmidt, N. Matoussevitch, H. Bonnemann, B. Spliethoff, B. Tesche, E. Bill, W. Kiefer, F. Schüth, *Angew. Chem. Int. Ed*. **2004**, *43*, 4303, e) J. Lee, S. M. Jin, Y. Hwang, J. G. Park, H. M. Park, T. Hyeon, *Carbon*. **2005**, *43*, 2536, f) P. Gao, A. Q. Wang, X. D. Wang, T. Zhang, *Chem. Mater*. **2008**, *20*, 1881, g) C. Liang, Z. Li, S. Dai, *Angew. Chem. Int. Ed*. **2008**, *47*, 3696.
7. E. C. de Oliveira, C. T. G. V. M. T. Pires, H. O. Pastore, *J. Braz. Chem. Soc.* **2006**, *17*, 16.
8. J. Lee, J. Kim, T. Hyeon, *Adv. Mater*. **2006**, *18*, 2073
9. Y. Xia, Z. Yang, R. Mokaya, *Nanoscale*. **2010**, *2*, 639 and references therein

10. Y. Meng, D. Gu, F. Zhang, Y. Shi, L. Cheng, D. Feng, Z. Wu, Z. Chen, Y. Wan, A. Stein, D. Zhao, *Chem. Mater*. **2006**, *18*, 4447.
11. a) F. Zhang, Y. Meng, D. Gu, Y. Yan, C. Yu, B. Tu, D. Zhao, *J. Am. Chem. Soc*. **2005**, *127*, 13508, b) Y. Meng, D. Gu, F. Zhang, Y. Shi, H. Yang, Z. Li, C. Yu, B. Tu, D. Zhao, *Angew. Chem, Int. Ed*. **2005**, *44*, 7053, c) Y. Meng, D. Gu, F. Zhang, Y. Shi, L. Cheng, D. Feng, Z. Wu, Z. Chen, Y. Wan, A. Stein, D. Zhao, *Chem. Mater*. **2006**, *18*, 4447, d) Y. Huang, H. Q. Cai, T. Yu, F. Q. Zhang, F. Zhang, Y. Meng, D. Gu, Y. Wan, X. L. Sun, B. Tu, D. Y. Zhao, *Angew. Chem*. *Int. Ed*. **2007**, *46*, 1089, e) T. Kyotani, *Carbon*. **2000**, *38*, 269.
12. A. Stein, Z. Wang, M. A. Fierke, *Adv. Mater.* **2009**, *21*, 265
13. a) T. Kwon, H. Nishihara, H. Itoi, Q-H. Yang, T. Kyotani, *Langmuir*. **2009**, *25*, 11961, b) H. Nishihara, H. Itoi, T. Kogure, P-X. Hou, H. Touhara, F. Okino, T. Kyotani, *Chem. Eur. J.* **2009**, *15*, 5355, c) R. Liu, D. Wu, X. Feng, K. Müllen, *Angew. Chem. Int. Ed*. **2010**, *49*, 2565.
14. A. Thomas, A. Fischer, F. Goettmann, M. Antonietti, J.-O. Müller, R. Schlögl, J. M. Carlsson, *J. Mater. Chem*. **2008**, *18*, 4893.
15. D. Lee, J. Lee, J. Kim, J. Kim, H. B. Na, B. Kim, C-H. Shin, J. H. Kwak, A. Dohnalkova, J. W. Grate, T. Hyeon, H-S. Kim, *Adv. Mater*. **2005**, *17*, 2828.
16. M. Wissler, *J. Power Sources*. **2006**, *156*, 142.
17. H. Li, H. A. Xi, S. Zhu, Z. Wen, R. Wang, *Microporous Mesoporous Mater*. **2006**, *96*, 357.
18. a) B. Lim, M. J. Jiang, P. H. C. Camargo, E. C. Cho, J. Tao, X. M. Lu, Y. M. Zhu, Y. N. Xia, *Science.* **2009**, *324*, 1302, b) M. Lefèvre, E. Proietti, F. Jaouen, J.-P. Dodelet, *Science*. **2009**, *324*, 71.

19. a) H. Wang, Q. Gao, J. Hu, *J. Am. Chem. Soc*. **2009**, *131*, 7016, b) M. J-Beneyto, F. S -García, D. L-Castelló, D. C-Amorós, A. L-Solano, *Carbon*. **2007**, *45*, 293.
20. L. Wang, Ralph T. Yang, *J. Phys. Chem. C*. **2009**, *113*, 21883.
21. a) Z. Wang, R. T. Yang, *J. Phys. Chem. C*. **2010**, *114*, 5956, b) N. R. Stuckert, L. Wang, R. T. Yang, *Langmuir*. **2010**, *26*, 11963.
22. H. I. Lee, S. H. Joo, J. H. Kim, D. J. You, J. M. Kim, J-N Park, H. Chang, C. Pak, *J. Mater. Chem*. **2009**, *19*, 5934.
23. a) A. Vinu, M. Miyahara, V. Sivamurugan, T. Mori, K. Ariga, *J. Mater. Chem*. **2005**, *15*, 5122, b) A. Vinu, C. Streb, V. Murugesan, M. Hartmann, *J. Phys. Chem. B*. **2003**, *107*, 8297.
24. a) D. D. Asouhidou, K. S. Triantafyllidis, N. K. Lazaridis, K. A. Matis, S-Su Kim, T. J. Pinnavaia, *Microporous Mesoporous Mater*. **2009**, *117*, 257, b) H. Tamai, T. Kakii, Y. Hirota, T. Kumamoto, H. Yasuda, *Chem. Mater.* **1996**, *8*, 454.
25. Z. Gu, B. Deng, *Environ. Eng. Sci*. **2007**, *24*, 113.
26. K. Ariga, A. Vinu, M. Miyahara, J. P. Hill, T. Mori, *J. Am. Chem. Soc.* **2007**, *129*, 11022.

# Chapter 2

## Part A

# Water-Solubilized Aminoclay-Metal Nanoparticle Composites and their Novel Properties

## Summary

This chapter deals with facile synthesis and characterization of water dispersible aminoclay-metal nanoparticles composites. Nanoparticles of metals such as Au, Ag, Pd and Pt embedded in exfoliated layers of aminoclays of the type $R_8Si_8Mg_6O_{16}(OH)_4$,where R = $CH_2CH_2NH_2$, are entirely water dispersible. The obtained metal nanoparticles composites were characterized by UV-Vis absorption spectroscopy, transmission electron microscopy and X-ray diffraction methods. The metal nanoparticles decorated aminoclay layers can be stabilized at the oil-water interface on interaction of metal nanoparticles with long chain alkane thiols.

A paper based on this study has been published in *J. Mater. Chem*. **2007**, *17*, 613-615.

## 2.1. Introduction:

Metals at the nanosize regime often display fascinating optical, chemical and electronic properties that are distinctly different from those of bulk.[1] In an ever expanding field of nanomaterials research, noble-metal nanoparticles have received particular interest because of their remarkable properties and potential applications in areas such as catalysis, sensors, storage, optical, electronics and biology.[2-4] Although various synthetic strategies (bottom-up) are reported in the literature to obtain noble-metal nanostructures of different shape and size, the most commonly used one being the chemical reduction of metal precursor in presence of a capping agent.[5-6] Typical capping agents used in stabilizing these metal nanoparticles include thiols,[7] polymers,[8] surfactants,[9] amine-borane complexes[10] and dendrimers.[11]

However, for catalytic applications, these nanoparticles preferably dispersed on a support like as silica, alumina, carbon, clay and zeolite.[12] For example, noble metal nanoparticles dispersed in clay matrices are widely used as heterogeneous catalysts for hydrogenation, coupling, oxidation and dye degradation reactions.[13] However, the usage of such catalysts for biphasic reactions is limited by their poor dispersibility in aqueous/organic medium.[14] In such reactions, dispersion of catalysts at the oil-water interface would be advantageous to obtain high conversion. Biphasic reactions, such as biocatalytic transformations of a variety of water-insoluble compounds, including epoxides and steroids are of significant commercial interest for the synthesis of pharmaceuticals and fine chemicals.[15,16]

The synthesis of metal nanoparticle-clay composites which would be stabilized at the oil/water interface is therefore essential to improve the catalytic efficiency of the biphasic reactions. To our knowledge till date there are no reports to stabilize clay

sheets at the oil/water interface. In the present work we use aminoclay to stabilize metal nanoparticles and bring them to air-water interface.

## 2.2. Scope of the present study:

Our current investigation involves the synthesis of aminoclay belonging to 2:1 trioctahedral smectite structure. It consists of a central brucite sheet of octahedrally coordinated MgO/OH chains overlaid on both sides with an aminopropyl-functionalized silicate network to give an approximate unit cell composition of $[H_2N(CH_2)_3]_8Si_8Mg_6O_{16}(OH)_4$.[17] Protonation of the amino groups in water results in the exfoliation of the organoclay layers.[18] Addition of ethanol (less polar solvent as compared to that of water) to the aqueous dispersion containing exfoliated clay layers induces stacking, leading to its precipitation. Amine molecules are known for their excellent reducing and stabilizing nature towards metal nanoparticles.[10,19] Since our tailor made clay, magnesium-phyllo(organo) silicate contains pendant amino groups, this can also be utilized for stabilizing various metal nanoparticles. Furthermore, nanoparticle embedded clay layers can successfully be brought to and stabilized at the oil-water interface by the addition of long chain alkane thiol.

## 2.3. Experimental and related aspects:

**(a) Materials:**

3-aminopropyltriethoxysilane, $MgCl_2.6H_2O$, $Mg(NO_3)_2$, $HAuCl_4$, $AgNO_3$, $H_2PtCl_6$, $PdCl_2$, $NaBH_4$ and hexadecane thiol were purchased at an analytical pure grade and were used without any further purification. Millipore water and ethanol were used wherever essential.

**(b) Synthesis of aminoclay:**

The aminoclay was prepared by the method reported in the literature.[18] Typically, an aminopropyl-functionalized magnesium (organo) phyllosilicate clay was prepared at room temperature by dropwise addition of 3-aminopropyltriethoxysilane (1.3 mL, 5.85 mmol) to an ethanolic solution (20 g) of magnesium chloride (0.84 g, 3.62 mmol). The white slurry obtained after 5 min was stirred overnight and the precipitate was isolated by centrifugation, washed with ethanol (50 mL) and dried at 40 ºC.

**(c) Preparation of aminoclay-metal nanocomposite** (*Ex-situ synthesis*)

Exfoliation of aminoclay was done by dispersing 20 mg of clay in 2 mL of Millipore water by sonication for 2 minutes. To this transparent clay suspension, 2 mL of 1 mM metal precursor solution was added followed by the addition of 2 mL of 0.1M $NaBH_4$ solution. In the case of Ag nanoparticles, the aminoclay was prepared using Mg $(NO_3)_2$ as the Mg source to avoid precipitation of AgCl.

**(d) In-situ synthesis**

In-situ synthesis of the clay stabilized Au nanoparticles was also carried out by dissolving 1.68 g of $MgCl_2$ .$6H_2O$ (8.26 mmol) in 20 mL of 3.8 mM solution of $HAuCl_4$ followed by the addition of 2 mL of 3-aminopropyltrimethoxysilane. The yellow slurry obtained was stirred overnight at room temperature and then kept at 75 ºC for 24 h. It slowly turned pink in color due to the formation of gold nanoparticles by thermal reduction. The pink transparent film obtained was washed with ethanol and then dried again. In the case of Ag nanoparticles, $Mg(NO_3)_2$ was used and the obtained film was brown-orange color. $PdCl_2$ and $H_2PtCl_6$ were taken as metal precursors to get Pd and Pt nanoparticles-clay composites.

## 2.4. Characterization techniques:

**X-ray Diffraction**: X-ray diffraction (XRD) patterns of the aminoclay and Au-aminoclay composite were recorded using Cu Kα radiation on a Rich-Siefert XRD-3000-TT and Bruker DS discover diffractometer.

**Transmission electron microscopy**: Transmission electron microscope (TEM) images were obtained with a JEOL JEM 3010, operating with an accelerating voltage of 300 kV. The aqueous clay suspension was first precipitated by the addition of ethanol and redispersed in ethanol by sonication before drop casting on a carbon-coated copper grid.

**UV-Vis absorption spectroscopy**: UV-Vis absorption spectroscopic measurements of metal nanoparticles-clay aqueous dispersions were performed with Perkin Elmer Lambda 900.

## 2.5. Results and Discussion:

XRD pattern of the as-synthesized aminoclay shows a low-angle reflection with a $d_{001}$ interlayer spacing of 1.6 nm corresponding to the bilayer arrangement of propylamino groups Figure 1 (a). The broad in-plane reflections at higher angles ($d_{020,110}$ = 0.41 nm, $d_{130,200}$ = 0.238 nm) and the characteristic (060) reflection at 0.15 nm confirm the formation of 2:1 trioctahedral Mg-phyllosilicate clay with talc-like structure.[17, 20] The XRD pattern of the metal nanoparticles-clay composite did not show the low angle peak confirming the complete exfoliation of clay (Figure 1 (b)).

Figure 2 shows the optical images of aminoclay and aminoclay-metal nanoparticles composite solutions. The pure aminoclay on exfoliation is colorless and transparent, whereas, the clay stabilized Au and Ag nanoparticles display a transparent pink and yellow color while dark brown in the case of both Pt and Pd

nanoparticles respectively. The reddish-brown color observed for Au-clay nanoparticles composite immediately after the addition of $NaBH_4$ changed to pink with time.

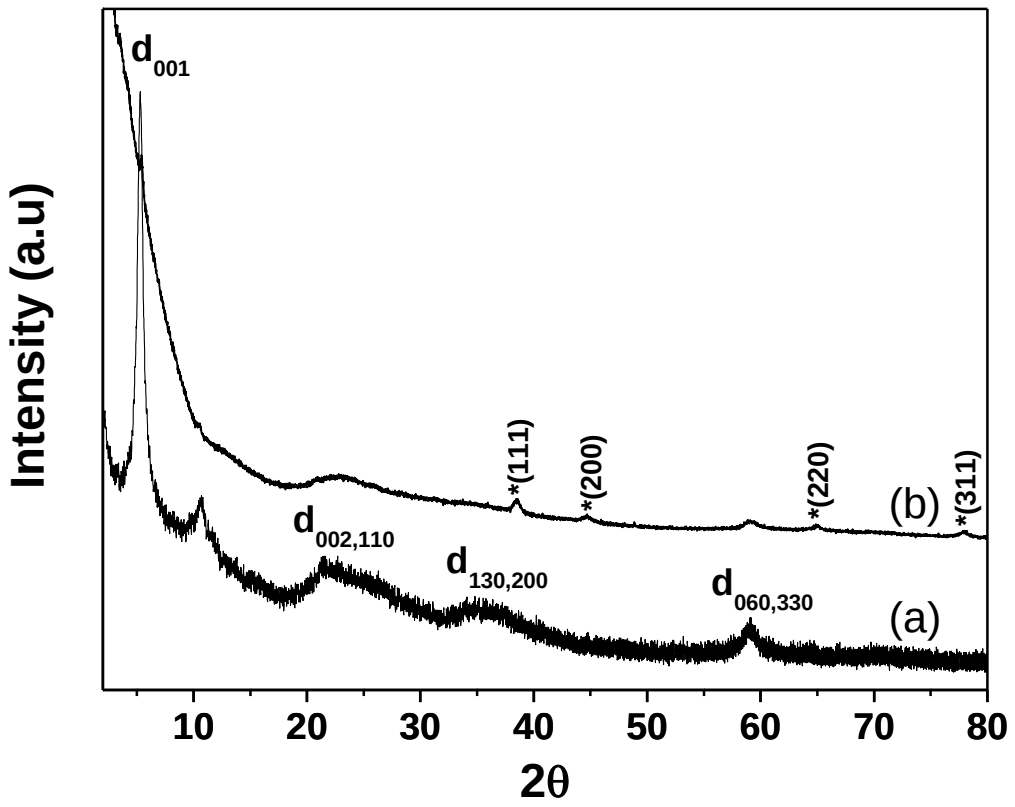


**Figure 1.** X-ray diffraction patterns of the (a) as-synthesized aminoclay and (b) the Au-aminoclay composite. Pattern (a) shows a low-angle reflection with $d_{001}$ spacing of 1.6 nm corresponding to the bilayer arrangement of propylamino groups. * indicates the peaks corresponding to Au nanoparticles.

The presence of Au and Ag metal particles at the nano-dimensions is manifested from the appearance of characteristic plasmon resonance bands for the Au and Ag-clay suspension in UV spectra at 513 nm and 410 nm respectively (Figure 3).[21, 22] The decrease in intensity of the Pt and Pd precursors peak at around 260 to 280 nm[23, 24] and the appearance of broad featureless absorption at visible region for the $NaBH_4$ treated Pt and Pd clay suspension confirms the presence of nanometer sized Pt and Pd particles (Figure 3).

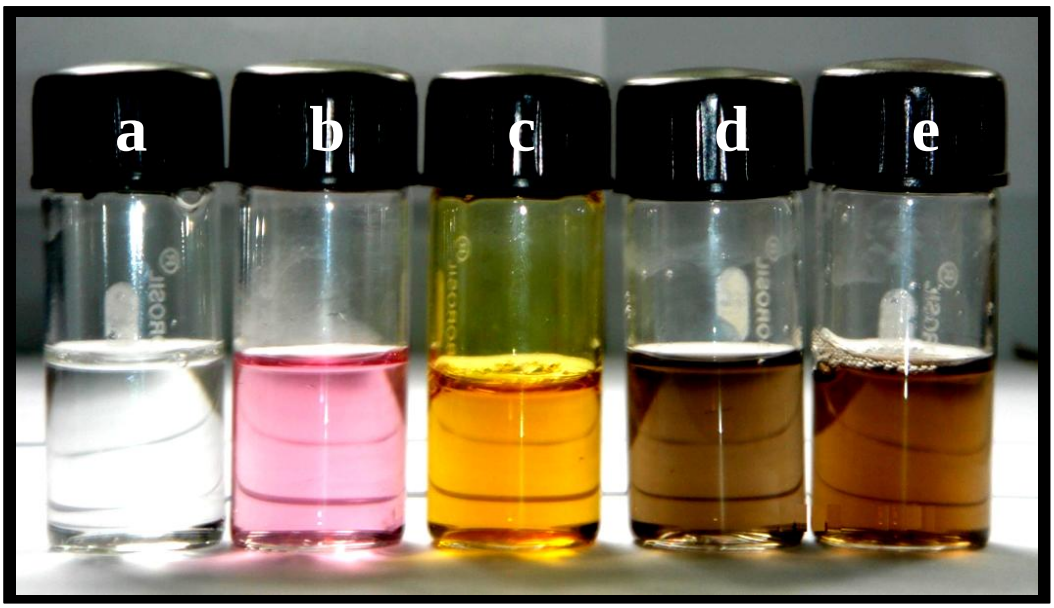


**Figure 2.** Optical images of aminoclay-metal nanoparticle composites forming clear transparent solutions in water. (a) aminoclay solution and aminoclay with (b) Au, (c) Ag, (d) Pt and (e) Pd nanoparticles.

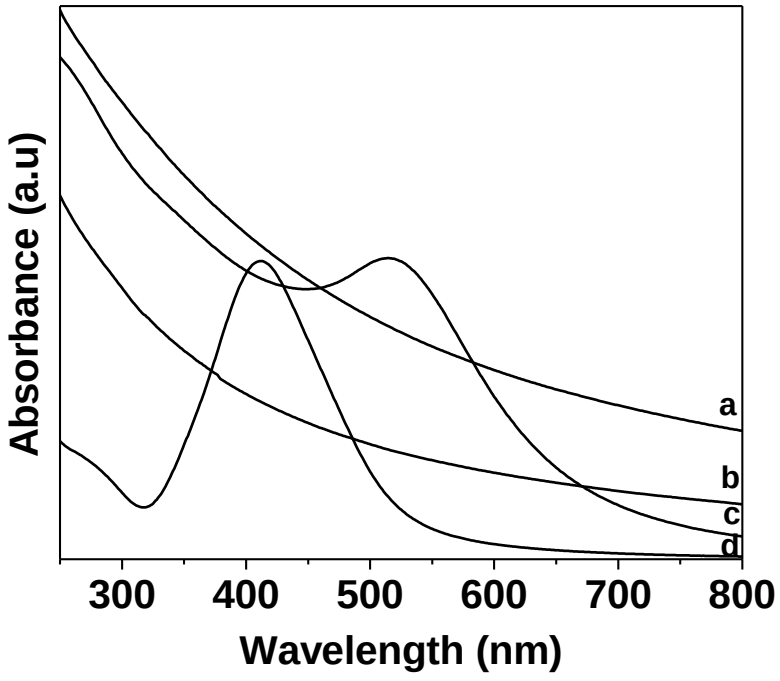


**Figure 3.** UV-Vis absorption spectra of a) Pd, b) Pt, c) Au and d) Ag metal nanoparticles.

Transmission electron microscope (TEM) images of the aminoclay-metal nanoparticles composites deposited on a carbon coated copper grid are shown in Figure 4 (a-d). TEM images show regions of organized nanoparticles (black spherical dots), probably stabilized by the clay oligomers as observed for aminoclay stabilized proteins.[18] The histograms show the average particle sizes to be around 3.5 and 5 nm respectively in the case of Au and Ag nanoparticles.

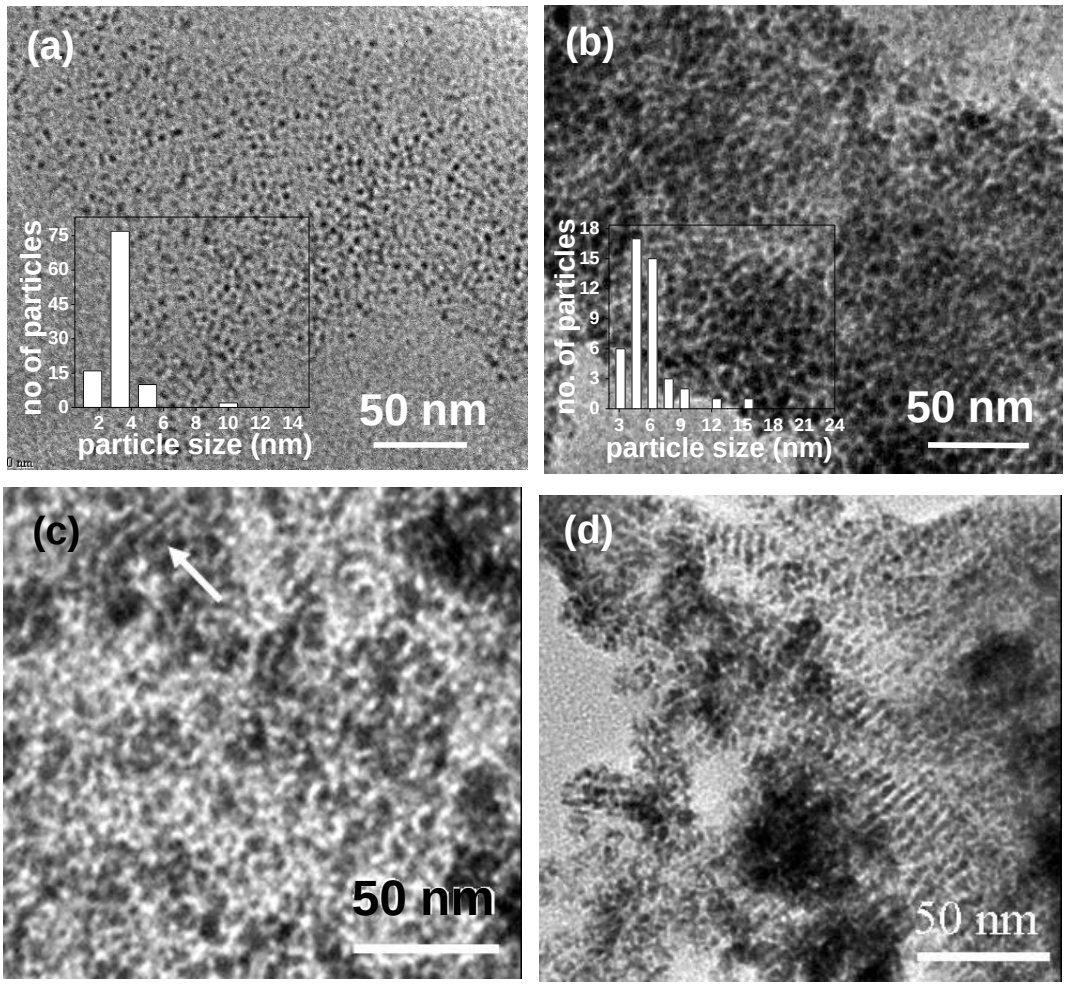


**Figure 4.** TEM images of (a) Au-clay nanoparticles composite. Inset: histogram of Au nanoparticles. (b) Ag-clay nanoparticles composite. Insets (bottom left) histogram of Ag nanoparticles (c) Pd nanoparticles show layered arrangement indicated by an arrow. (d) Pt nanoparticles assembling into layered structure.

We could observe the assembly of metal nanoparticles in the form of layered arrangements with the interspacing of 1.6 nm commensurate with the bilayer arrangement of aminoclay. The layered arrangement is more pronounced in the case of Pt and Pd nanoparticles as compared to that of Au and Ag nanoparticles.

The aminoclay-Au nanoparticle composite was also prepared by an *in-situ* procedure, wherein the reduction was carried out thermally without the use of $NaBH_4$. The clay composite so prepared can be readily dispersed in water and shows the characteristic plasmon band at 530 nm. The plasmon band is slightly red shifted to one that is prepared by *ex-situ* method. The TEM image of the *in-situ* prepared aminoclay-Au nanoparticles is shown in Figure 5. The size of the Au nanoparticles are around 10-15 nm and in some regions the particles are randomly organized as shown in Figure 5 (a).

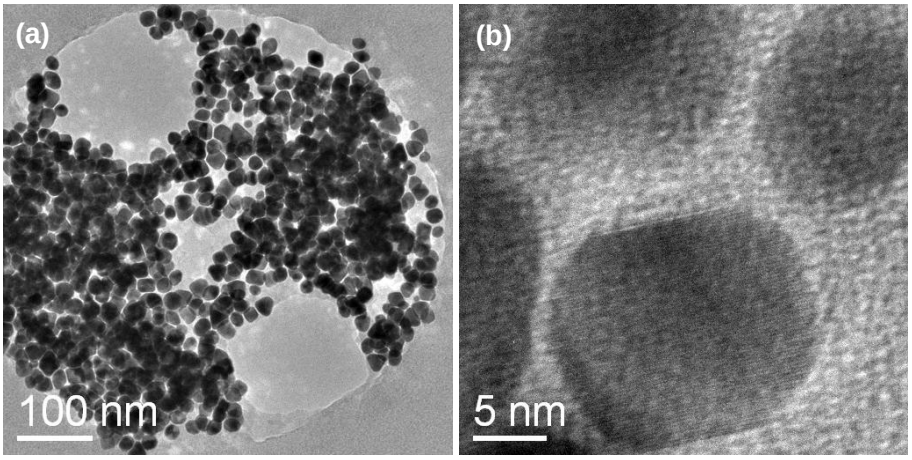


**Figure 5.** (a) TEM image of Au nanoparticle-aminoclay composite synthesized by in-situ method, (b) corresponding HRTEM showing the lattice planes of Au.

It is quite understandable that the addition of $NaBH_4$ in the *ex-situ* synthesis creates more nucleation centers resulting in small nanoparticles. The distance between the particles are about 1.6 nm as shown in Figure 5 (b**)** which suggests that the particles

would be surrounded by the disintegrated aminoclay oligomers**.** This aminoclay-Au nanoparticle composite is dispersible in water and can be re-precipitated by adding excess ethanol as shown in the Figure 6.

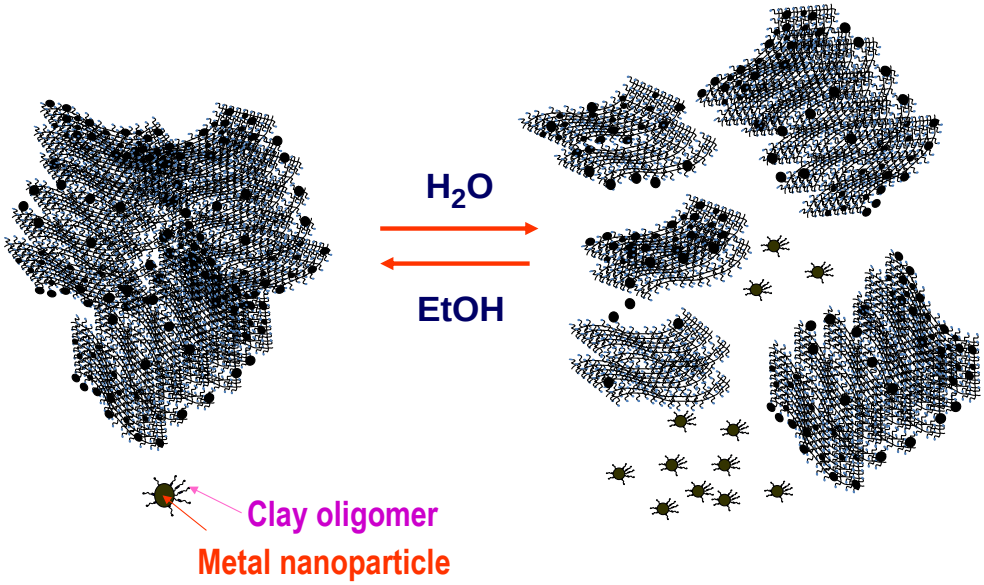


**Figure 6.** Scheme illustrating exfoliation and re-precipitation of aminoclay-metal nanoparticles composite in water and ethanol respectively.

## 2.6. Novel properties:

The effect of addition of hexadecanethiol to an aqueous solution of the aminoclay-Au nanoparticles composite was examined and the result is shown in Figure 7 (a). Immediately after the addition, the hexadecanethiol forms a clear non-aqueous layer on top of the pink aqueous layer. After several hours, the thiol interacts with Au nanoparticles embedded in the aminoclay and brings the sheets of composite to the aqueous/organic interface as seen in Figure 7 a (ii).

The binding strength of the Au nanoparticles by the aminoclay is so strong that hexadecanethiol, which is known to have a strong affinity to Au by its thiol bond

formation could not isolate the Au nanoparticles from the clay surface on mixing with the aqueous clay suspension. The compromise between the hydrophobic alkyl chain of hexadecanethiol and the hydrophilic aminoclay sheets with its gravitational pull towards the water resulted in stabilizing the nanoparticles decorated clay sheets at the oil-water interface.

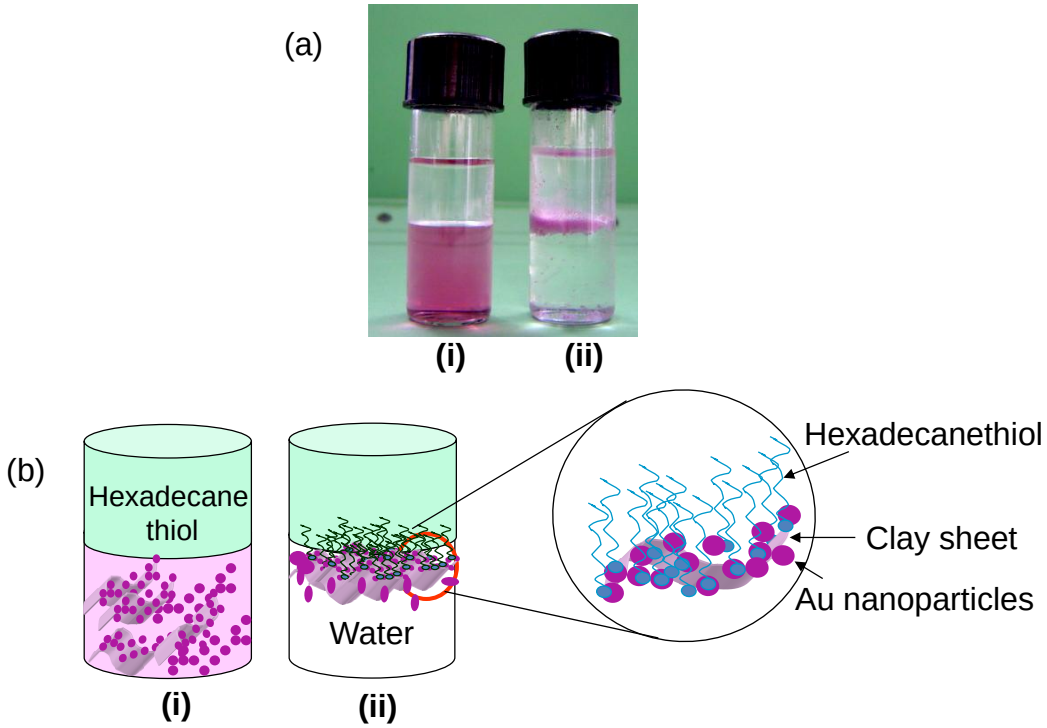


**Figure 7.** (a) Optical image of aqueous Au-clay composite on addition of hexadecane thiol (i) at the time of addition (the top transparent layer is the oil phase and the bottom pink layer is the aqueous phase) (ii) after 14 days. (b) Corresponding schematic diagram.

The presence of all the exfoliated aminoclay at the interface was confirmed by ensuring the absence of any clay in the aqueous layer. Replacing hexadecanethiol by other organic solvents such as benzene or toluene still retains the composite particles at the interface. We show the process of formation of the clay-Au nanoparticles composite schematically in Figure 7 (b).

This process occurs with all metal nanoparticles studied, but more effectively in the case of Ag and Au. Thus we show a simplistic design of aqueous-organic interface by using metal nanoparticles encapsulated in aminoclay matrix.

## 2.7. Conclusions:

In conclusion, we have used the exfoliated sheets of Mg-phyllo(organo)silicates containing the pendant amino groups to stabilize the Au, Ag, Pd and Pt nanoparticles. The nanoparticles-decorated clay sheets can be easily dispersible in water. The nanoparticles obtained by this methodology are highly stable. Further *in-situ* synthesis of clay stabilized metal nanoparticles has been prepared without the use of any external reducing agent. These metal nanoparticles can be used to lift the clay sheets to the oil-water interface with the help of an alkanethiol. Since clays are good hosts for proteins and enzymes, stabilizing them at the oil/water interface could be useful for hosting various biocatalytic transformations. Furthermore we are evaluating the catalytic activity of Pd nanoparticles encapsulated on aminoclay matrix for Suzuki-coupling and hydrogenation reactions. Also we are using metal nanoparticles encapsulated aminoclay nanocomposite as a reusable catalyst for azo-dye degradation. Although we have worked here with a family of aminoclays, other suitably functionalized clays may also exhibit similar properties.

## 2.8. References:


1. a) C. N. R. Rao, G. U. Kulkarni, P. J. Thomas, P. P. Edwards, *Chem. Eur. J.* **2002**, *8*, 28, b) E. Roduner, *Chem. Soc. Rev*. **2006**, *35*, 583.
2. a) H. Goesmann, C. Feldmann, *Angew. Chem. Int. Ed*. **2010**, *49*, 1362, b) P. K. Jain, X. Huang, I. H. El-Sayed, M. A. El-Sayed, *Acc. Chem. Res*. **2008**, *41*, 1578, c) B. H. Lipshutz, Y. Yamamoto, *Chem. Rev.* **2008**, *108*, 2793, d) A. J. Nozik**,** *Nano Lett.* **2010**, *10*, 2735, e) D. A. Giljohann, D. S. Seferos, W. L. Daniel, M. D. Massich, P. C. Patel, C. A. Mirkin, *Angew. Chem. Int. Ed.* **2010**, *49*, 3280, f) M. C. Daniel, D. Astruc, *Chem. Rev.* **2004**, *104*, 293.
3. M. A. El-Sayed, *Acc. Chem. Res*. **2001**, *34*, 257.
4. a) S. Eustis, M. A. El-Sayed, *Chem. Soc. Rev*, **2006**, *35*, 209, b) J. Homola, *Chem. Rev*, **2008**, *108*, 462.
5. a) A. Halder, P. Kundu, B. Viswanath, N. Ravishankar, *J. Mater. Chem.* **2010**, *20*, 4763, b) Y. Xia, Y. Xiong, B. Lim, S. E. Skrabalak, *Angew. Chem. Int. Ed.* **2009**, *48*, 60.
6. G. Schmid, *Nanoparticles: From Theory to Applications*, **2004**, *Wiley-VCH*.
7. a) M. Brust, M. Walker, D. Bethell, D. J. Schiffrin, R. Whyman, *J. Chem. Soc, Chem. Commun*. **1994**, 801, b) K. V. Sarathy, G. U. Kulkarni, C. N. R. Rao, *Chem. Commun*. **1997**, 537.
8. a) M. K. Corbierre, N. S. Cameron, M. Sutton, S. G. J. Mochrie, L. B. Lurio, A. Ruhm, R. B. Lennox, *J. Am. Chem. Soc.* **2001**, *123*, 10411, b) S. Porel, S. Singh, S. S. Harsha, D. N. Rao, T. P. Radhakrishnan, *Chem. Mater*. **2005**, *17*, 9, c) S. W. Kim, S. Kim, J. B. Tracy, A. Jasanoff, M. G. Bawendi, *J. Am. Chem. Soc*. **2005**, *127*, 4556.

9. J. Liu, P. Raveendran, Z. Shervani, Y. Ikushima, Y. Hakuta, *Chem. Eur. J.* **2005**, *11*, 1854.
10. N. Zheng, J. Fan, G. D. Stucky, *J. Am. Chem. Soc.* **2006**, *128*, 6550.
11. R. W. J. Scott, O. M. Wilson, R. M. Crooks, *J. Phys. Chem. B.* **2005**, *109*, 692.
12. a) N. Zheng, G. D. Stucky, *J. Am. Chem. Soc.* **2006**, *128*, 14278, b) S. Ayyappan, G. N. Subbanna, R. S. Gopalan, C. N. R. Rao, *Solid State Ionic*. **1996**, *84*, 271, c) S. Mandal, D. Roy, R. V. Chaudhari, M. Sastry, *Chem. Mater.* **2004,** *16*, 3714.
13. a) H. Firouzabadi, N. Iranpoor, A. Ghaderi, M. Ghavami, S. J. Hoseini, *Bull. Chem. Soc. Jpn*. **2011**, *84*, 100, b) J. C. A. A. Roelofs, Peter H. Berben, *Chem. Commun.* **2004**, 970, c) K. K. R. Datta, J. Kumar, M. Eswaramoorthy, *manuscript under preparation*.
14. a) P. Asuri, S. S. Karajanagi, J. S. Dordick, R. S. Kane, *J. Am. Chem. Soc*. **2006**, *128*, 1046, b) R. S. Ghadge, S. B. Sawant, J. B. Joshi, *Chem. Eng. Sci*. **2003**, *58*, 5125.
15. A. Schmid, J. S. Dordick, B. Hauer, A. Kiener, M. Wubbolts, B. Witholt, *Nature*. **2001**, *409*, 258.
16. K. M. Koeller, C. H. Wong, *Nature*. **2001**, *409*, 232.
17. N. T. Whilton, S. L. Burkett, S. Mann, *J. Mater. Chem*. **1998**, *8*, 1927.
18. A. J. Patil, E. Muthusamy, S. Mann, *Angew. Chem. Int. Ed.* **2004**, *43*, 4928.
19. M. Aslam, L. Fu, M. Su, K. Vijayamohanan, V. P. Dravid, *J. Mater. Chem*. **2004**, *14*, 1795.
20. a) S. L. Burkett, A. Press, S. Mann, *Chem. Mater.* **1997,** *9*, 1071, b) E. Muthusamy, D. Walsh, S. Mann, *Adv. Mater*. **2002**, *14*, 969.

21. J. A. Creighton, D. G. Eadon, *J. Chem. Soc., Faraday Trans*. **1991**, *87*, 3881.

22. S. Eustis, M. A. El-Sayed, *Chem. Soc. Rev*. **2006**, *35*, 209.

23. A. M. Choudary, S. Madhi, N. S. Chowdari, M. L. Kantam, B. Sreedhar, *J. Am. Chem. Soc.* **2002**, *124*, 14127.

24. D. G. Duff, P. P. Edwards, J. Evans, J. T. Gauntlett, D. A. Jefferson, B. F. G. Johnson, A. I. Kirkland, D. J. Smith, *Angew. Chem. Int. Ed.* **1989**, *28*, 59019.

# Chapter 2

## Part B

# Aminoclay: A Permselective Matrix to Stabilize Copper Nanoparticles

## Summary

Air sensitive copper nanoparticles have been stabilized using a water dispersible aminoclay matrix. The aminoclay shows remarkable permselective behaviour allowing only the ionic species to diffuse through it and react with copper nanoparticles. It blocks the neutral molecule oxygen, thereby stabilizing the copper nanoparticles against oxidation for a longer period. Copper nanoparticles protected by aminoclay matrix selectively allow the permeation of chalcogenide ions and are readily converted into copper chalcogenide nanoparticles. Furthermore, the obtained Cu nanoparticles are catalytically active in reducing the toxic pollutant p-nitrophenol to p-aminophenol in the presence of sodium borohydride.



A paper based on this study has been published as in *Chem. Commun*. **2010**, *46*, 616–618.

## 2.1. Introduction:

Metal nanoparticles have gained tremendous impact in the field of nanoscience and nanotechnology owing to its size dependant electronic, optical and magnetic properties. High surface energies, superior surface to volume ratio and advanced density of surface defects are the key parameters which emerge out as the size of metals tend to approach nano-regime. The unique size and shape dependant properties of these nanosized metals find applications in the fields of optics, sensors, storage, microelectronics and catalysis.[1-3] Numerous researchers are extensively involved in designing various shapes and sizes of nanomaterials for specific applications. Experimentalists are involved in controlling the shape and size of these nanostructures, theorists are involved in understanding and elucidation of the intricate mechanisms that are involved in the formation of these nano-systems and finally technologists use these novel nanomaterials for various applications such as catalyzing organic transformations, biology and medicine. However, stabilizing them in the metallic state at the nanometer size regime for long term applications is not an easy task in materials synthesis.

One such metal which has attracted lot of attention due to its high electrical and thermal conductivity is copper. The metal's low cost and abundance have been extensively utilized in the fields of electronics, optics, catalysis, storage and biology. Elemental copper is highly sensitive to air, particularly oxygen (oxophilic nature) necessitates it to form thin coating of surface oxide. Air sensitivity of the copper upon exposure to ambient laboratory conditions forms cuprous oxide which on subsequent exposure forms cupric oxide quickly. In particular, stabilizing copper nanoparticles, a sought-after nanomaterial in catalysis, [4] optics [5] and sensors [6] in their

metallic state, is one of the challenging tasks as they undergo rapid oxidation in air or aqueous media.[7] It oxidizes so fast that the observation of electron diffraction pattern for copper oxide in transmission electron microscope (TEM) is unavoidable unless it is prepared and transported in an inert environment.[8] Even in aqueous medium the dissolved oxygen will be sufficient to oxidize the Cu nanoparticles.

There are many physical and chemical methods for the synthesis of copper nanoparticles. Physical methods include sonochemical reduction, electrochemical, sono-electrochemical, thermal reduction, radiolytic reduction, solid-liquid phase arc-discharge, flow-levitation method, spray pyrolysis, UV radiation, photochemical and vacuum vapour deposition.[9] Bottom-up methods typically comprise reduction of copper ions in the presence of stabilizer to generate copper nanoparticles. Typical molecules that are employed for capping copper nanoparticles are, octyl amine, sulfobetaine, alkanethiolate, macromolecules such as dendrimers and surfactants such as CTAB.[10] Though there are many physical[9] and chemical methods[10] available in the literature to make copper nanoparticles, their high reactivity towards oxygen necessitates not only their synthesis but also their storage in a stringent inert environment. Thus it would be a challenging task to protect copper nanoparticles and stabilize them for long term devoid of using inert conditions.

## 2.2. Scope of the present investigation:

Herein, we develop a simple route to stabilize the Cu nanoparticles for an extended period of time using an aminoclay, a phyllosilicate family of molecular formula $R_8Si_8Mg_6O_{16}(OH)_4$, where R = $CH_2CH_2NH_2$ as the water dispersible support. The protonation of amino groups in water resulted in exfoliation of the organoclay layers.[11] Previous studies have shown that the water-dispersible

aminoclay has a strong interaction with air-stable Ag, Au, Pt nanoparticles which are being used to stabilize the clay at the oil-water interface.[12] However, use of these aminoclay in stabilizing the air-sensitive copper nanoparticles has not been explored so far.

Firstly we stabilize air-sensitive copper nanoparticles by using water dispersible aminoclay matrix. In this study, we also demonstrated the selective permeation towards ionic species exhibited by protonated aminoclay stabilized copper nanoparticles, while passive nature to molecular species (air, oxygen). The former principle is utilized in synthesizing copper chalcogenide nanoparticles from copper nanoparticles by choosing appropriate chalcogenide precursor (ionic form). The latter principle is exploited in long term stability of copper nanoparticles effectively against air oxidation. Furthermore the obtained Cu nanoparticles are catalytically active in reducing the toxic pollutant p-nitrophenol to p-aminophenol in the presence of sodium borohydride.

## 2.3. Experimental Section:

### (a) Materials:

3-aminopropyltriethoxysilane, $MgCl_2.6H_2O$, hydrazine hydrate, $CuSO_4.5H_2O$, $Na_2S$, Se powder, p-nitrophenol and $NaBH_4$ were purchased at an analytical pure grade and were used without any further purification. Millipore water and ethanol were used wherever essential.

### (b) Synthesis of aminoclay:

The aminoclay was prepared by the method reported in the literature.[11] Typical synthesis involves room temperature drop wise addition of 3-

aminopropyltriethoxysilane (1.3 mL, 5.85 mmol) to an ethanolic solution of magnesium chloride (0.84 g, 3.62 mmol). The white slurry obtained after 5 min was stirred overnight and the precipitate isolated by centrifugation was washed with ethanol (50 mL) and dried at 40 °C.

**(c) Synthesis of aminoclay stabilized Cu nanoparticles:**

$CuSO_4.5H_2O$ was used as the metal precursor for Cu nanoparticles synthesis. The aminoclay-Cu nanoparticles composite was prepared as follows. The aminoclay was first exfoliated by dispersing 20 mg of clay in 2 mL millipore water by sonication. To this transparent clay suspension, 500 µL of 10 mM copper sulphate solution was added followed by the drop wise addition of 1 mL of 1 M hydrazine hydrate solution.

**(d) Synthesis of Cu chalcogenide nanoparticles from Cu nanoparticles:**

**(i) Synthesis of $Cu_2S$ nanoparticles:**

A known volume of freshly prepared Cu-aminoclay solution was mixed with an equal volume of 10 mM $Na_2S$ solution followed by sonication for 5 minutes. The wine-red color of Cu-aminoclay solution changed in 5 minutes to greenish-brown colour indicative of formation of $Cu_2S$ nanoparticles.

**(ii) Synthesis of $CuSe_2$ nanoparticles:**

A known volume of freshly prepared Cu-aminoclay solution was mixed with an equal volume of 1 mM NaHSe solution followed by sonication for 5 minutes. The wine-red color of Cu-aminoclay solution changed in 5 minutes to dark orange-red colour due to the formation of $CuSe_2$ nanoparticles.

**(e) Estimation of undissociated hydrazine hydrate present in water and aminoclay**:

20 mg of aminoclay was first exfoliated in 3 mL millipore water by sonication. 1 mL of 1 M hydrazine hydrate was added to this aminoclay solution. In a separate vial 1 mL of 1M hydrazine hydrate was added to 3 mL millipore water for comparison. Both the samples were kept for 8 days exposed to air. For the estimation of residual hydrazine hydrate present in pure water and aminoclay, the following quantitative titration was performed. Equal volumes of 0.05 M $K_3Fe(CN)_6$ solution and 0.05 M KOH solution were mixed in a conical flask and titrated against hydrazine hydrate to give light brown coloured solution as an end point. The reaction is shown below.[13]

$$4\ K_3Fe(CN)_6 + 4\ KOH + N_2H_4\ H_2O \longrightarrow 4\ K_4Fe(CN)_6 + N_2 + 5\ H_2O$$

## 2.4. Characterization techniques:

**X-ray Diffraction**: For XRD analysis, the Cu-aminoclay solution prepared was precipitated by the addition of excess ethanol which further on drying yields copper powder. The XRD patterns of the samples were recorded using Cu Kα radiation on a Rich-Siefert XRD-3000-TT and Bruker DS discover diffractometer.

**Transmission electron microscopy**: For TEM analysis, the aqueous clay copper nanoparticle-suspension was first precipitated by the addition of excess ethanol and then redispersed it in ethanol by sonication before drop casting on a carbon-coated copper grid. TEM images were recorded with a JEOL JEM 3010 instrument (Japan) operated at an accelerating voltage of 300 kV.

**UV-Vis absorption spectroscopy**: UV-Vis absorption spectroscopic measurements of Cu, Cu chalcogenide nanoparticles and catalytic reduction of p-nitro phenol were performed with Perkin-Elmer instruments Lambda 900 UV/Vis/NIR spectrometer. The reduction of p-nitro phenol was quantitatively monitored with a time gap of 20 seconds in a scanning range of 200-700 nm at room temperature of 25 $^0$C with scan speed of 250 nm per minute.

## 2.5. Results and discussion:

**Figure 1.** Optical image of aminoclay and Cu-aminoclay solution at different ageing times. From left to right; aminoclay in water, freshly prepared Cu-aminoclay solution (wine-red color) and Cu-aminoclay solution kept for 14 days (brick-red color).

Copper nanoparticles are prepared by using aminoclay as a stabilizing agent, copper sulphate as the metal precursor and hydrazine hydrate as the reducing agent. Addition of hydrazine hydrate to the blue coloured $CuSO_4$-aminoclay mixture immediately gives a golden-brown colored solution which was then transformed to wine-red coloured solution within five minutes indicating the formation of copper nanoparticles. This suggests that the reduction of $Cu^{2+}$ ions to $Cu^0$ (wine red color) occurs through $Cu^+$ intermediate (golden-brown color). Figure 1 shows the optical image of aminoclay dispersion and Cu-

aminoclay solution at different ageing time. The pure aminoclay solution is colorless and optically transparent, while the freshly prepared Cu-aminoclay solution shows wine red color. Ageing the solution in open air for 14 more days slowly changes the color from transparent wine red solution to brick red precipitate. On sonication, the brick red precipate forms a stable and transparent dispersion. The UV-Vis absorption spectra of freshly prepared Cu-aminoclay solution shows characteristic plasmon band at 570 nm for copper nanoparticles associated with the excitation plasma resonance or interband transition.[14] A red shift in the plasmon band from 570 to 593 nm was observed for the samples kept for a longer period of time probably due to increase in particle sizes (Figure 2).

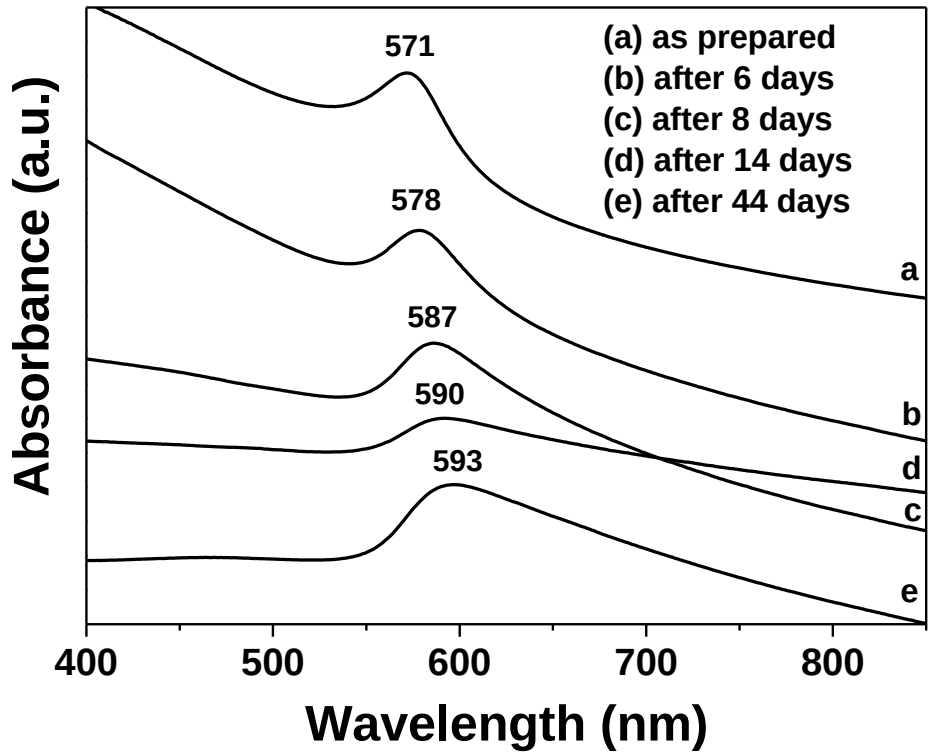


**Figure 2.** UV-Vis absorption spectra of Cu-aminoclay solution aged at different time intervals.

When copper nanoparticles are surrounded by oxide layers, in addition to the plasmon peak at 566 nm, a residual absorption characteristic of copper oxide was reported at 800 nm.[7d] However, we did not observe a residual peak at 800 nm suggesting the formation of highly stable copper nanoparticles despite prolonged ageing (more than 44 days).

Transmission electron microscope (TEM) image (Figure 3) also confirms the increase in particle size when the Cu-aminoclay solution was kept for a longer time. For example, the TEM image of freshly prepared sample shows the copper particles of size less than 10 nm on the backdrop of clay sheets whereas, the sample aged for 14 days shows sizes between 25 and 50 nm.

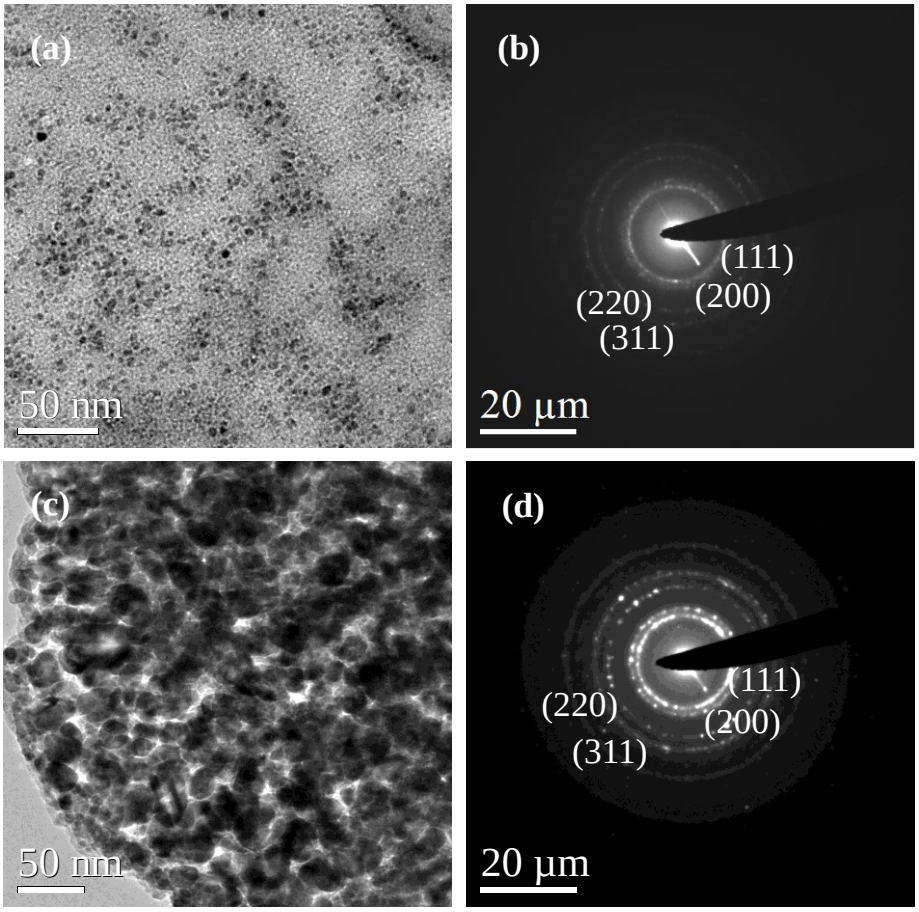


**Figure 3.** TEM images of (a) freshly prepared Cu-aminoclay solution, (b) corresponding electron diffraction pattern, (c) Cu-aminoclay solution aged for 14 days, (d) corresponding electron diffraction pattern.

The selected area diffraction pattern (SAED) shows four rings related to the (111), (200), (220) and (311) lattice planes corresponding to face centered cubic structure of copper nanoparticles (Figure 3).[8] The increase in particle size of copper with ageing can be attributed to either coarsening or extended reduction or growth of copper ions from the solution by hydrazine hydrate. In a separate experiment, we arrested the growth of copper nanoparticles by seperating out the Cu-aminoclay composite from the freshly prepared solution by precipitation and repeated washing with ethanol. The separated sample shows particle size of copper less than 10 nm even after keeping the powder in air for two months (Figure 4).

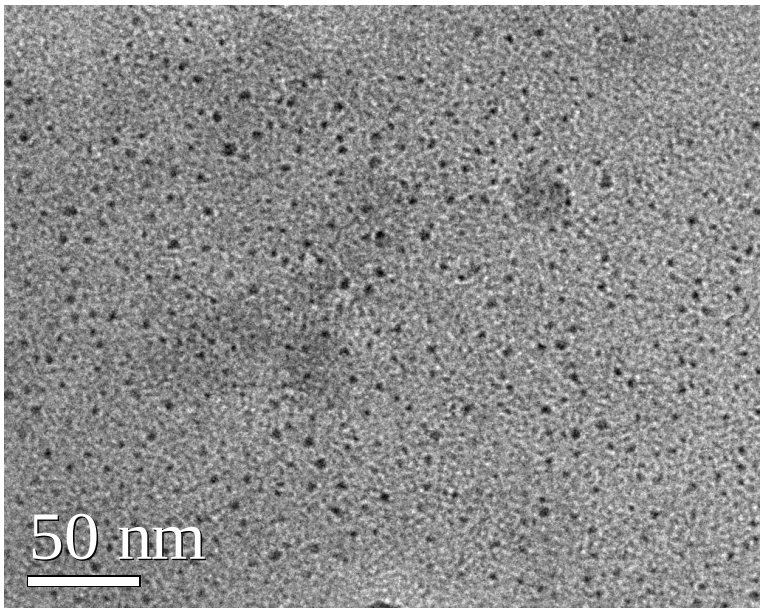


**Figure 4.** TEM image of Cu powder (obtained by precipitating freshly prepared Cu-aminoclay solution) kept in air for two months.

This suggests that the increase of Cu nanoparticles size in solution is mainly associated with the excess reduction of copper ions over a long period of time. The extended reduction of copper ions is possible only if the hydrazine hydrate dissociation is controlled in clay solution for a longer time. Time dependent

quantitative analysis of undissociated hydrazine hydrate (by ferricyanide to ferrocyanide reduction process) present in pure water and aminoclay solution after mixing them with a known amount of hydrazine hydrate confirmed that its dissociation is significantly slowed down in presence of aminoclay.[15] The possibility that copper nanoparticles catalyzing the decomposition of hydrazine hydrate is also ruled out since copper nanoparticles are not that efficient in activating the dissociation of hydrazine hydrate.[16] These results suggest that in addition to the prolonged reduction of copper ions in Cu-aminoclay solution, the nitrogen coming out from the slow dissociation of hydrazine hydrate provides an oxygen free environment to the copper nanoparticles. Further, the quick oxidation of copper nanoparticles in air when copper sulphate solution was reduced with hydrazine hydrate (in absence of aminoclay) supports the oxygen barrier property provided by the clay nanosheets.

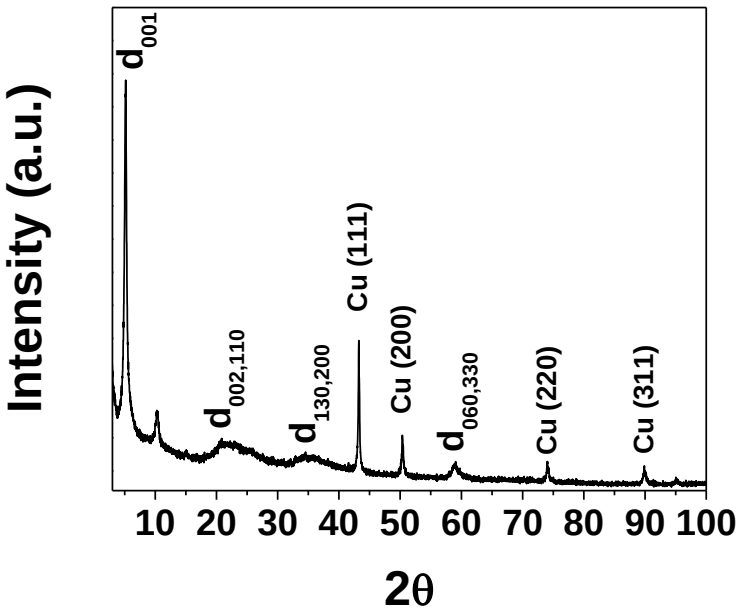


**Figure 5.** Wide angle XRD pattern of Cu-aminoclay composite kept in air for two months. Low-angle reflection with $d_{001}$ spacing of 1.7 nm corresponding to the bilayer arrangement of propylamino groups of aminoclay. The in-plane reflections with $d_{020,110}$ = 0.42 nm, $d_{130,200}$ = 0.26 nm and $d_{060}$ = 0.156 nm are associated with clay. [17]

Powder XRD pattern of the Cu-aminoclay composite kept for two months in air (obtained by precipitation from freshly prepared Cu-aminoclay solution) (Figure 5) shows peaks corresponding to (111), (200), (220) and (311) planes associated with the face centered cubic (fcc) structure of copper. The absence of any noticeable peaks corresponding to $Cu_2O$ and CuO phases in XRD signifies the importance of clay in stabilizing the copper nanoparticles against the air oxidation. The observation of low-angle peak corresponding to the interlayer spacing (~1.7 nm) of aminoclay suggest the possible coexistence of staked nanostructures made up of few layers of aminoclay.

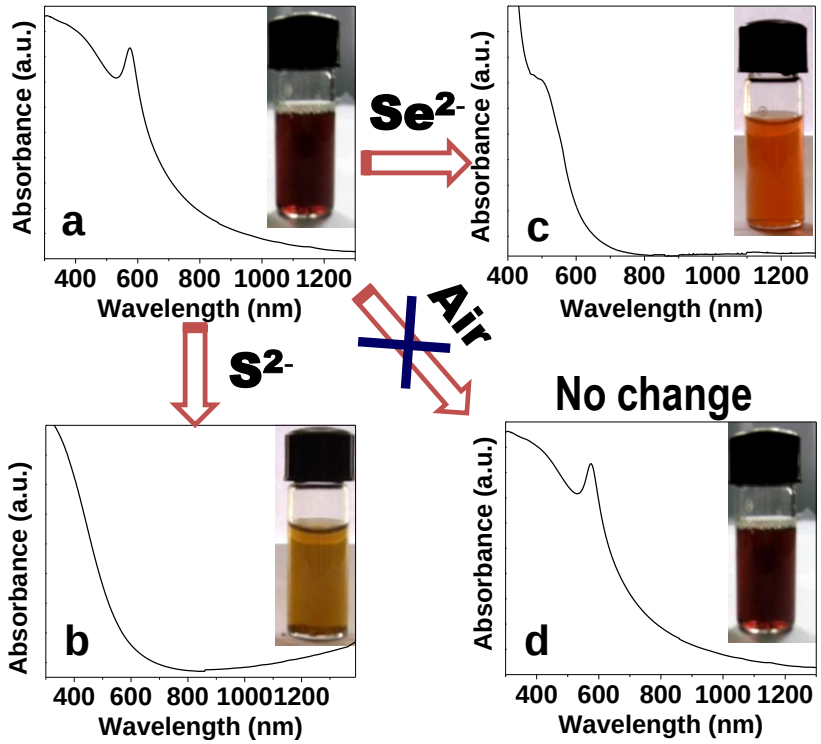


**Figure 6.** UV-Vis absorption spectra of (a) freshly prepared Cu-aminoclay solution, (b) Cu-aminoclay solution after the addition of $Na_2S$ solution, (c) Cu-aminoclay solution after the addition of NaHSe solution, (d) Cu-aminoclay solution aged for 6 days in air. Inset shows the corresponding optical images.

The optical image in Figure 6 shows the wine red color for the freshly prepared Cu-aminoclay solution. The solution remains in wine red color even after keeping it for 6 days in air. However, it slowly changed to brick red color after 14

days (Figure 1). The corresponding UV-Vis absorption spectrum shows no change in the plasmon band observed for copper nanoparticles with respect to ageing or any other band for copper oxide particles. The XRD pattern (Figure 5) also did not show any reflections for copper oxides even after ageing in air for a longer time. This underlines the stability provided by the clay matrix by being impermeable to the oxygen molecules.

On the other hand, when the Cu-aminoclay solution was treated with sodium sulfide solution the color changed immediately to greenish brown (Figure 6b). The disappearance of plasmon band at 578 nm and the emergence of a strong absorption for $Cu_2S$ nanoparticles in the near-IR region in the UV-Vis absorption spectrum confirm the transformation of copper nanoparticles to $Cu_2S$ nanoparticles.[18] Similarly, addition of sodium hydrogen selenide to the Cu-aminoclay solution gives rise to orange red colour (Figure 6c) due to the formation of $CuSe_2$ nanoparticles. Again the disappearance of copper plasmon band at 578 nm and the appearance of a new band at 485 nm in the UV-Vis absorption spectrum clearly support the conversion of copper nanoparticles to $CuSe_2$ nanoparticles.[19]

However, these copper chalcogenides are prone to undergo reduction in the reduced environment provided by the amine groups as well as the hydrazine hydrate trapped within the clay matrix. Keeping the solution for 3 more days reduces most of the $Cu_2S$ and $CuSe_2$ nanoparticles to copper nanoparticles. The UV-Vis absorption spectra (Figure 8) and the XRD patterns (Figure 7) obtained for these samples also show evidence for the presence of copper nanoparticles. It is to be noted that the formation of $Cu_2S$/Cu or $CuSe_2$/Cu core-shell nanoparticles by surface reduction of copper chalcogenides cannot be ruled out under this conditions.

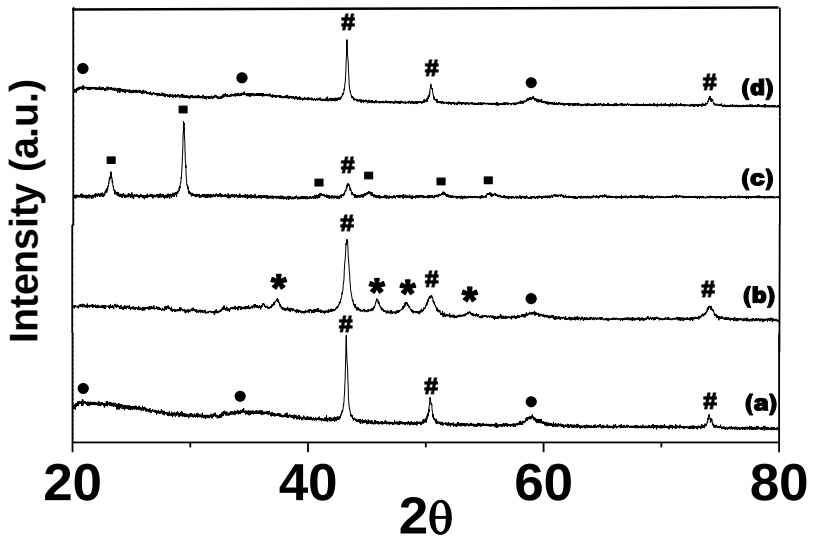


**Figure 7.** Wide angle XRD pattern of (a) freshly prepared Cu-aminoclay composite, (b) $Cu_2S$-aminoclay composite, (c) $CuSe_2$-aminoclay composite, (d) Cu-aminoclay composite aged for 6 days in air. Symbols denote [#] Cu, [*] $Cu_2S$, [■ ] $CuSe_2$ and [●] aminoclay respectively.

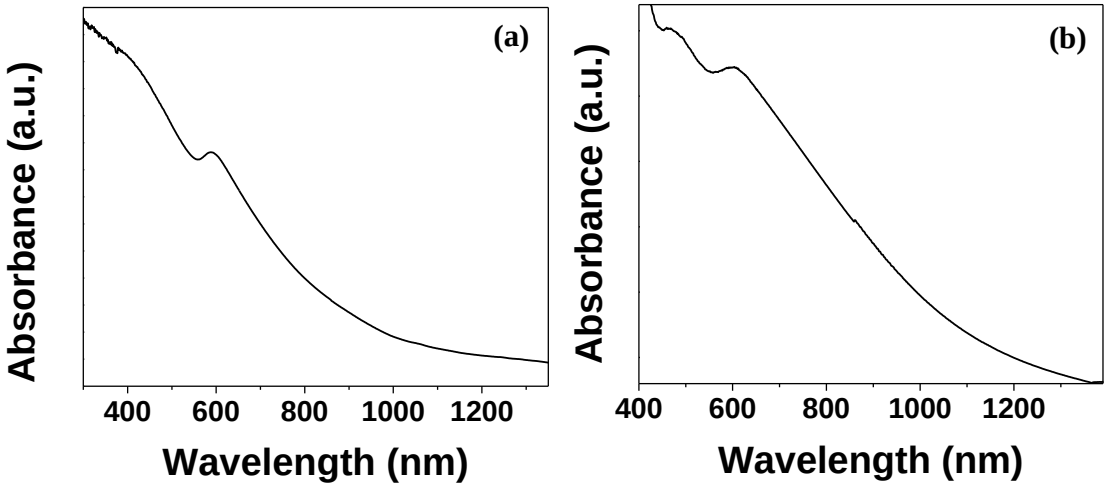


**Figure 8.** UV-Vis absorption spectra of Cu chalcogenides in aminoclay solution kept for 3 days (a) $Cu_2S$-aminoclay solution, (b) $CuSe_2$-aminoclay solution (both the cases copper plasmon band is seen).

In contrast to oxygen molecules which are very reactive towards copper nanoparticles but unable to permeate the clay galleries effectively, sulfide and selenide ions easily diffuse through it and react with the copper nanoparticles (Figure 9). It is evident that the protonated form of aminoclay is facilitating the diffusion of charged species within the galleries compared to the neutral molecules like oxygen.

Importantly, aminoclay provides an inert, reducing environment at the microlevel by controlling the dissociation of hydrazine hydrate (a reducing agent as well as an oxygen scavenger)[20] for a longer period of time which is conducive for the stabilization of copper nanoparticles against the air oxidation.

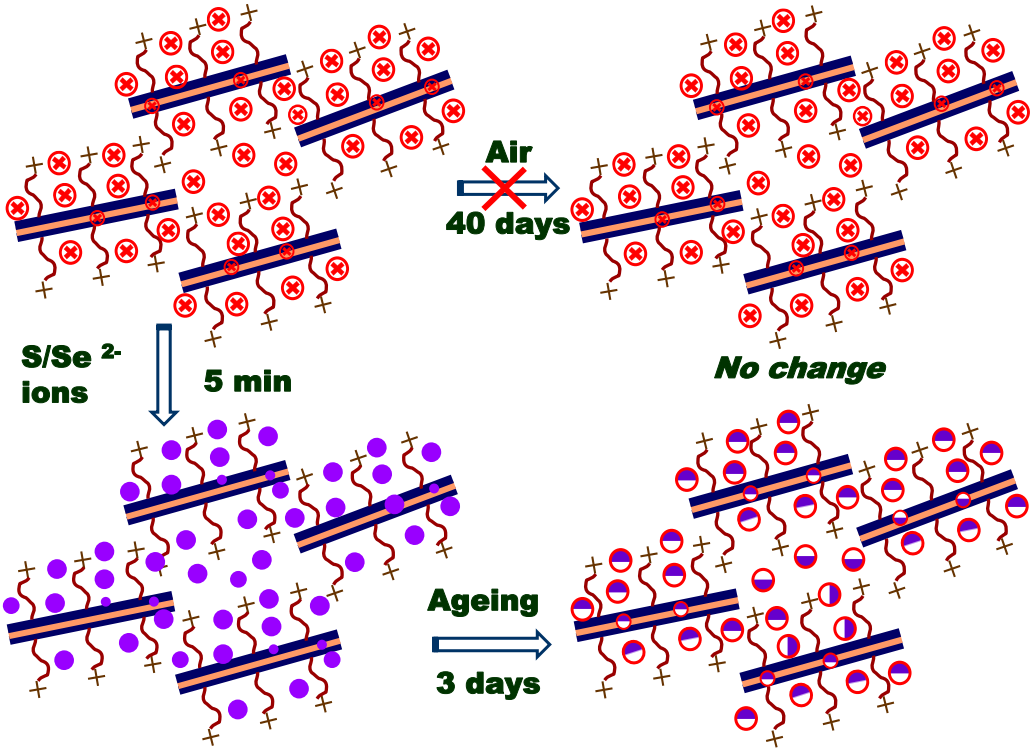


**Figure 9.** Schematic showing the permselective behaviour of aminoclay. [⊗] denotes Cu, [●] $Cu_2S$ or $CuSe_2$ and [◒] mixed phase of Cu and Cu chalcogenides.

**Reduction of p-nitrophenol by Cu nanoparticle-aminoclay composite:**

p-nitrophenol is a phenolic compound that has nitro group at the opposite position of the hydroxy group on the benzene ring. It is mainly used as fungicide. There are plenty of disadvantages that are associated with this compound. It irritates eyes, skin, respiratory tract, and may cause the inflammation of those parts. It has a delayed interaction with blood and forms methaemoglobin which is responsible for

methemoglobinemia, potentially causing cyanosis, confusion and unconsciousness. When ingested, it causes abdominal pain and vomiting. Prolonged contact with skin may cause allergic response.[21] Thus it is highly imperative to convert p-nitrophenol into useful forms (such as p-aminophenol used in the synthesis of paracetamol) which are relatively less toxic and are of industrial importance.

One way to address this problem would be the reduction of p-nitrophenol to p-aminophenol by using appropriate reducing agent such as $NaBH_4$. Reduction of 4-nitrophenol by $NaBH_4$ is a thermodynamically allowed reaction, since the reduction potential of 4-nitrophenol to 4-aminophenol is 0.76 V, while for borate-borohydride ($H_3BO_3/BH_4^-$) it is -1.33 V; both potentials were measured versus Normal Hydrogen Electrode (NHE). This reaction is kinetically very slow in the absence of a catalyst (it takes two days).[22] This reduction reaction proceeds in the presence of colloidal nanoparticles as a catalyst.[23-24] Therefore, the reduction of 4-nitrophenol to 4-aminophenol using $NaBH_4$ has become a model reaction for the evaluation of catalytic activity of metals (Au, Ag, Pt, Pd and Ni).[23-25] We herein, illustrate the catalytic action of aminoclay stabilized copper nanoparticles by carrying out the reduction of p-nitrophenol to p-aminophenol.

The reduction of p-nitrophenol was monitored using UV-Vis absorption spectroscopy. 1 mL of 15 mM $NaBH_4$ (aqueous solution) was mixed with 1.7 mL of 0.2 mM 4-nitrophenol (aqueous solution) in a quartz cell. The light yellow colour of p-nitrophenol changes to yellow-green upon mixing of sodium borohydride solution. The reduction of p-nitrophenol to p-aminophenol was very slow in presence of $NaBH_4$ alone (without the aid of Cu nanoparticles).

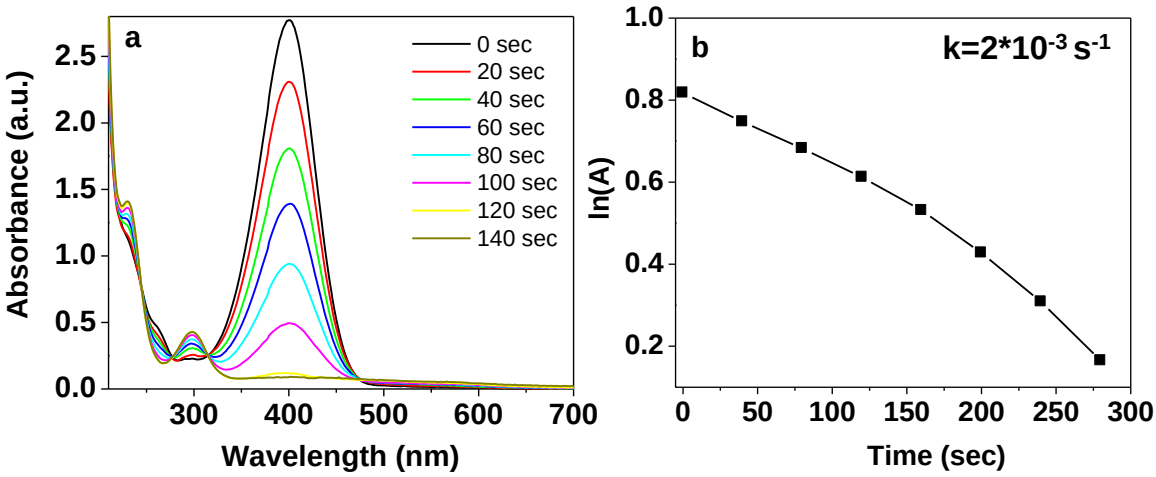


**Figure 10.** (a) UV-Vis absorption spectra for the reduction of 0.2 mM p-nitro phenol by 15 mM $NaBH_4$ in the presence of Cu-aminoclay solution; (b) Plot of ln (A) vs time for the reduction of p-nitrophenol.

Aqueous p-nitrophenol shows a peak maximum around 317 nm, which on addition of $NaBH_4$ red-shifted to 401 nm. In the absence of copper nanoparticles this peak remains unaltered. Addition of 100 μL of Cu-aminoclay solution (100 μL contains 63.5 μg of copper) to the above mixture gradually decolourises the solution due to the formation of p-aminophenol (Figure 10 a). The decrease in intensity of the peak at 401 nm was monitored for the reduction of p-nitrophenol (or the increase in intensity of the peak at 300 nm corresponding to p-aminophenol) using UV-Vis absorption spectroscopy. The rate constant was calculated by measuring the absorbance (at 401 nm) at regular intervals of every 20 sec. The rate constant derived by plotting $\ln(A_{max})$ vs. time was around $2*10^{-3}$ $sec^{-1}$ which follows first order kinetics as shown in Figure 10 (b). This value is comparable to other nanoparticle catalysts used for the reduction of p-nitrophenol in the presence of $NaBH_4$.[22-25]

## 2.6. Conclusions

In conclusion, we have demonstrated the permselective nature of aminoclay in protecting copper nanoparticles. The aminoclay acts as a barrier to the neutral oxygen molecules, but facilitates the ionic species to diffuse through the galleries. Copper nanoparticles stabilized with aminoclay remain passive towards neutral molecules like oxygen for prolonged time while forms copper chalcogenides immediately on reaction with sulfide/selenide ions. The selective protection provided by the water dispersible aminoclay can be exploited to stabilize many metal nanoparticles which are air sensitive and difficult to handle. These copper nanoparticles are also active in reducing the p-nitrophenol to p-aminophenol in the presence of $NaBH_4$.

## 2.7. References:


1. a) M. Schwartzberg, J. Z. Zhang, *J. Phys. Chem. C*. **2008**, *112*, 10323, b) P. V. Kamat, *J. Phys. Chem. B.* **2002**, *106*, 7729, c) E. Roduner, *Chem. Soc. Rev*. **2006,** *35*, 583.
2. M. E. Stewart, C. R. Anderton, L. B. Thompson, J. Maria, S. K. Gray, J. A. Rogers, R. G. Nuzzo, *Chem. Rev.* **2008**, *108*, 494.
3. a) M. Turner, V. B. Golovko, O. P. H. Vaughan, P. Abdulkin, A. B- Murcia, M. S. Tikhov, B. F. G. Johnson, R. M. Lambert, *Nature.* **2008**, *454*, 981, b) J. D. Aiken, R. G. Finke, *J. Mol. Catal. A: Chem.* **1999**, *145*, 1, c) A. Corma, H. Garcia, *Chem. Soc. Rev*. **2008**, *37*, 2096, d) A. S. K. Hashmi, M. Rudolph, *Chem. Soc. Rev*. **2008**, *37*, 1766, e) R. M. Crooks, M. Zhao, L. Sun, V. Chechik, L. K. Yeung, *Acc. Chem. Res.* **2001**, *34*, 181, e) D. T. Thompson, *Nanotoday.* **2007**, *2*, 40.
4. M. Kidwai, V. Bansal, A. Saxena, S. Aerry, S. Mozumdar, *Tetrahedron Letters.* **2006**, *47*, 8049.
5. a) G. H. Chan, J. Zhao, E. M. Hicks, G. C. Schatz, R. P. Van Duyne, *Nano Lett*. **2007**, *7*, 1947, b) H. H. Huang, F. Q. Yan, Y. M. Kek, C. H. Chew, G. Q. Xu, W. Ji, P. S. Oh, S. H. Tang, *Langmuir*. **1997,** *13*, 172, c) Y. Zhang, K. Aslan, M. J. R. Previte, C. D. Geddes, *Appl. Phys Lett.* **2007**, *90***,** 173116.
6. a) E. K. Athanassiou, R. N. Grass, W. J. Stark, *Nanotechnology*. **2006**, *17*, 1668, b) D. N. Muraviev, J. Macanás, M. Farre, M. Muñoz, S. Alegret, *Sensors and Actuators B.* **2006,** *118*, 408.
7. a) R. Nakamura, D. Tokozakura, H. Nakajima, J.-G. Lee, H. Mori, *J. Appl. Phys.* **2007,** *101*, 074303, b) A. C. Curtis, D. G. Duff, P. P. Edwards, D. A. Jefferson, B. F. G. Johnson, A. I. Kirkland, A. S. Wallace, *J. Phys. Chem.*

**1988**, *92*, 2270, c) J. H. Kim, S. H. Ehrman, T. A. Germer, *Appl. Phys Lett.* **2004**, *84*, 1278, d) A. Yanase, H. Komiyama, *Surface Science.* **1991,** *248*, 11.

8. J. Hambrock, R. Becker, A. Birkner, J. Weiß, R. A. Fischer, *Chem. Commun.* **2002**, 68.
9. a) I. Haas, S. Shanmugam, A. Gedanken, *Chem. Eur. J.* **2008**, *14*, 4696, b) N. A. Dhas, C. P. Raj, A. Gedanken, *Chem. Mater.* **1998,** *10*, 1446, c) Y. Yu, Y. Shi, C-H Chen, C. Wang, *J. Phys. Chem. C.* **2008**, *112*, 4176, d) A. Henglein, *J. Phys. Chem. B.* **2000**, *104*, 1206, e) W-T. Yao, S-H. Yu, Y. Zhou, J. Jiang, Q-S. Wu, L. Zhang, and J. Jiang, *J. Phys. Chem. B.* **2005**, *109*, 14011, f) J. H. Kim, T. A. Germer, G. W. Mulholland, S. H. Ehrman, *Adv. Mater*. **2002**, *14*, 518, g) S. Giuffrida, G. G. Condorelli, L. L. Costanzo, I. L. Fragala, G. Ventimiglia, G. Vecchio, *Chem. Mater*. **2004**, *16*, 1260, h) S. Kapoor, T. Mukherjee, *Chemical Physics Letters*. **2003**, *370*, 83, h) Z. Liu, Y. Bando, *Adv Mater*. **2003**, *15*, 303.
10. a) S. Panigrahi, S. Kundu, S. Basu, S. Praharaj, S. Jana, S. Pande, S. K. Ghosh, A. Pal, T. Pal, *J. Phys. Chem. C.* **2007**, *111*, 1612, b) B. K. Park, S. Jeong, D. Kim, J. Moon, S. Lim, J. S. Kim, *Journal of Colloid and Interface Science.* **2007**, *311*, 417, c) S. D. Bunge, T. J. Boyle, T. J. Headley, *Nano Lett.* **2003**, *3*, 901, d) Y. Song, E. E. Doomes, J. Prindle, R. Tittsworth, J. Hormes, C. S. S. R. Kumar, *J. Phys. Chem. B.* **2005**, *109*, 9330, e) S. Chen, J. M. Sommers, *J. Phys. Chem. B.* **2001**, *105*, 8816, f) L. Balogh, D. A. Tomalia, *J. Am. Chem. Soc.* **1998**, *120*, 7355, g) S-H. Wu, D-H. Chen, *Journal of Colloid and Interface Science.* **2004**, *273*, 165, h) M. P. Pileni, *J. Phys. Chem. C.* **2007**, *111*, 9019, i) K. K. R. Datta, B. Srinivasan, H. Balaram, M. Eswaramoorthy, *J. Chem. Sci*. **2008**, *120*, 579.

11. A. J. Patil, E. Muthusamy, S. Mann, *Angew. Chem. Int. Ed*. **2004**, *43*, 4928.
12. K. K. R. Datta, M. Eswaramoorthy, C. N. R. Rao, *J. Mater. Chem.* **2007**, *17*, 613.
13. P. J. Durrant, B. Durrant, *Introduction to Advanced Inorganic Chemistry*. **1962**, 703-704.
14. a) I. Lisiecki, M. P. Pileni, *J. Am. Chem. Soc.* **1993**,*115*, 3887, b) J. A. Creighton, D. G. Eadon, *Faraday Trans.* **1991**, *87*, 3881.
15. The undissociated hydrazine hydrate present in the aminoclay solution and pure water after 8 days was titrated against potassium ferricyanide in alkaline media. Results showed that aminoclay solution and the pure water retains 53 % and 23 % of the hydrazine hydrate respectively. (Experimental section)
16. S. K. Singh, X-B. Zhang, Q. Xu, *J. Am. Chem. Soc*. **2009**, *131*, 9894.
17. S. L. Burkett, A. Press, S. Mann, *Chem. Mater*. **1997**, *9*, 1071.
18. E. J. Silvester, F. Grieser, B. A. Sexton, T. W. Healy, *Langmuir*. **1991**, *7*, 2917.
19. X. Zheng, Q. Hu, *Appl Phys A*. **2009**, *94*, 805.
20. S. Basak, K. S. Rane, P. Biswas, *Chem. Mater*. **2008**, *20*, 4906.
21. http://en.wikipedia.org/wiki/4-Nitrophenol
22. S. Saha, A. Pal, S. Kundu, S. Basu, T. Pal, *Langmuir*. **2010**, *26*, 2885.
23. N. Pradhan, A. Pal, T. Pal, *Colloids Surf. A.* **2002**, *196*, 247.
24. S. K. Ghosh, M. Mandal, S. Kundu, S. Nath, T. Pal, *Appl. Catal. A.* **2004**, *268*, 61.
25. a) M. A. Mahmoud, B. Snyder, M. A. El-Sayed, *J. Phys. Chem. Lett.* **2010**, *1*, 28, b) J. Zeng, Q. Zhang, J. Y. Chen, Y. N. Xia, *Nano Lett.* **2010**, *10*, 30.

# Chapter 3

## Synthesis of Agarose-Metal/Semiconductor Nanoparticles having Superior Bacteriocidal Activity and their Simple Conversion to Catalytic Metal-Carbon Composites

## Summary

The chapter details with the stabilization of metal, semi-conductor nanoparticles by using naturally occurring biopolymer agarose. The gel forming ability of agarose is exploited to make metal/semiconducting nanoparticle composite transparent films. The rich functional groups are the key to necessitate the stabilization/reduction of metal nanoparticles. Furthermore, Au and Ag nanoparticle composite films are prepared by employing green chemical methods without using any external reducing agent. Ag and Cu nanoparticles stabilized in agarose matrix show excellent anti-bacterial activity against *Escherichia coli (E.coli)* bacteria. Metal nanoparticle composite films carbonized under inert conditions can be readily converted to metal nanoparticle-carbon composites which are of catalytic importance.

A paper based on this work has been published in *J. Chem. Sci*. **2008**, *120*, 579-586.

## 3.1. Introduction

Nanosized precious metals such as platinum, gold, silver and palladium display fascinating size-dependant properties.[1-2] The important applications of the nanosized metals are in the fields of catalysis, optics and biology. However, metal nanoparticles often tend to agglomerate due to their high surface activity. Thus surface passivation of metal nanoparticles is highly desirable for long term applications. One such approach to tackle this problem is by immobilization of nanoparticles on matrix materials such as porous carbon, silica and alumina.[3] Metal nanoparticles encapsulated within these systems cannot be fabricated into transparent films which are essential in optical and food packaging materials. Recently, polymers are gaining increasing interest as matrix materials due to their ability to control particle growth as well as to stabilize the resulting particles.[4] Metal nanoparticle-polymer composites are receiving tremendous interest in recent years owing to their numerous properties and various applications in opto-electronics,[5] nonlinear optical devices[6] and color filters.[7]

The size dependent electronic and optical properties of the nanoparticles coupled with the optical transparency and mechanical stability of the polymer films signify their importance in many applications.[5-7] Among the wide variety of polymer matrices, biopolymers become the preferred choice as they are readily available, inexpensive, environmentally green and more amenable to scale up. Moreover, the oxygen rich functionalities of the biopolymers and their affinity towards metals make them ideal candidates for the stabilization of nanoparticles.[8] Though biopolymers such as cellulose,[9] starch,[10] and alginic acid[11] have been used for the stabilization of nanoparticles, another natural polymer in that series, agarose, has not been fully exploited despite its ability to form a transparent gel and films which can

be used for packaging and separation purposes. Agarose is an oxygen rich naturally occurring polysaccharide extracted from seaweed. It is a sub-fraction of a mixture referred to as agar, well-known for its use in microbiology. Agar consists of alternating 1,3-linked β-D-galactose and 1,4-linked 3,6-anhydro-α-L-galactose and is known for its gelation property, finds application in gel electrophoresis as a cell culture media.[12] Gel formation occurs when cooling the hot aqueous agarose solution to room temperature which is stable over a wide range of pH from 3 to 9 and has high mechanical resistivity even at low agarose concentration, less than 6 wt%.[13] Caruso et al.[14] used the porous, agarose polymer matrix as a sacrificial template to prepare macroporous metal oxides. Kattumuri et al.[15] reduced the Au ions in presence of agarose matrix using trimeric alanine phosphine conjugates and used it for the surface-enhanced Raman spectroscopic detection of DNA nucleosides. Indeed, a general and simple route to make biopolymer-metal/semiconductor composite films would be advantageous given their potential application in many areas.

**Bacteriocidal activity:**

Microbial contaminations and deteriorations induced by micro-organisms are spreading to various fields such as foodstuffs, plastic materials, building materials, petroleum products, electronic equipments, optical instruments and textile industries.[16] Infection and contamination in the medical treatment become serious problems. To deal these problems effectively, new pasteurization and anti-bacterial technologies are required. Recently metal nanoparticles are sought after for these applications, especially silver, which has a strong growth inhibitory effect for *Escherichia coli and Pseudomonas aeruginosa*.[16] Silver has attracted particular attention because of its broad efficacy against bacteria and other organisms and its

relatively low toxicity to humans.[17-18] As the nanotechnology field is blossoming, the rational design of multifunctional nanomaterials is receiving tremendous attention. Furthermore looking for an alternative low cost metal to replace Ag would be highly desirable for industrial scale process.

## 3.2. Scope of the present investigation:

Although the oxygen rich functionalities of agarose are well exploited in biology, its ability to stabilize metal and semiconducting nanoparticles has not been explored much. In the present work agarose-metal nanoparticle gels are prepared by the introduction of metal precursor solution followed by the addition of reducing agent. These polymer-nanoparticle gels on drying yield hybrid films. The obtained Ag and Cu-polymer composite was tested for its antimicrobial activity against *Escherichia coli* bacteria. For various catalytic organic transformations dispersion of metal nanoparticles supported over carbon matrix (Metal@Carbon) is highly desirable. In order to achieve such catalytically important materials carbonization of agarose-metal nanoparticles composite films in presence of nitrogen atmosphere is performed. The versatility of the method is extended to the synthesis of semiconductor nanoparticle composite films by choosing appropriate metal and chalcogenide precursors.

## 3.3. Experimental Section:

### (a) Materials:

Agarose (Type I), $HAuCl_4$, $AgNO_3$, $H_2PtCl_6$, $PdCl_2$, $CuSO_4$ $5H_2O$, $NaBH_4$, hydrazine hydrate, glucose, $Cd(NO_3)_2$, $Pb(NO_3)_2$, $Zn(NO_3)_2$, $Na_2S$ were purchased at

an analytical pure grade and were used without any further purification. Millipore water and ethanol were used wherever essential.

**(b) Synthesis of metal nanoparticles-agarose composite:**

Agarose stabilized metal nanoparticles were prepared by introducing the metal precursors in the aqueous solution of agarose. In a typical synthesis, 0.1 g of agarose (Type I) powder was added to a 10 mL of Milli-Q$^{TM}$ (Millipore, USA) purified water kept at 80 $^{0}$C with constant stirring. After 2 minutes a clear viscous solution was obtained. To this 1 mL of 1 mM $AgNO_3$ solution was added followed by 200 µl of 10 mM $NaBH_4$ solution. The resulting yellow colored, transparent solution is indicative of the formation of Ag nanoparticles. On cooling to room temperature a yellow colored, transparent gel was obtained which was then transformed to a transparent, yellow colour film on drying. Similar procedure was repeated for the synthesis of Au, Pt and Pd nanoparticles. $HAuCl_4$, $H_2PtCl_6$ and $PdCl_2$ were chosen as metal precursors. Correspondingly, we obtained red, light brown, brown films for Au, Pt and Pd nanoparticles loaded agarose composites. For copper-agarose composite, 1 mL of 10 mM $CuSO_4$ solution was reduced with 500 µl of 1M $N_2H_4$ hydrate solution. The evolution of nitrogen when hydrazine hydrate was used as the reducing agent provides an inert environment that stabilizes the copper nanoparticles in the agarose matrix for a longer period of time against immediate air oxidation.

**(c) Glucose reduction of Au and Ag nanoparticles:**

10 ml of Milli-pore water was taken in a beaker and heated at around 80 $^{0}$C. To this 0.1 g of agarose (Type I) powder was added with constant stirring. After 2 minutes a clear viscous solution was obtained. To this 200 µL of 10 mM $HAuCl_4$ solution was added followed by 300 µL of 1 M glucose solution. After 5 minutes the

viscous solution turned to violet color indicative of formation of Au nanoparticles. The obtained viscous solution was poured into a Petri dish and after 5 minutes a transparent violet colored gel was obtained. This gel on further drying at room temperature for 2 days leads to a transparent composite film.

Similar procedure was adopted for the synthesis of Ag nanoparticles by taking $AgNO_3$ as the metal precursor. In this case 200 µl of 0.1 M $AgNO_3$ was added followed by the addition of 1M 300 µl glucose solution. Here we observed orange color indicating the formation of Ag nanoparticles.

**(d) Synthesis of semi-conducting nanoparticles-agarose composite:**

For the synthesis of CdS, PbS and ZnS-agarose composite films, $Cd(NO_3)_2$, Pb $(NO_3)_2$, and $Zn(NO_3)_2$ were used as the metal precursors. $Na_2S$ was taken as the sulphide precursor. To the 10 mL of Milli-Q water kept at 80 $^0$C, 0.1 g of agarose (Type I) powder was added with constant stirring until it dissolves. To this solution 500 µl of 0.1 M metal nitrate was added followed by the equal volume of 0.1 M $Na_2S$. The clear mixture was then cooled to room temperature to obtain the semiconductor nanoparticle incorporated agarose gel which was then converted into a film on drying at room temperature.

**(e) Synthesis of LB-agarose-nanoparticles (Ag and Cu) composites for assessment of antibacterial activity:**

A slight modification of the protocol for the synthesis of nanoparticles was done to assess their antibacterial activity. The nanoparticles were synthesized in Luria-Bertani (LB) medium rather than in Milli-Q purified water. All apparatus used for nanoparticle film preparation were autoclaved prior to use. All reactions were performed in a laminar hood, with high efficiency particulate air filter system, to

ensure sterility. LB broth was prepared by addition of 0.5 g of yeast extract, 1 g of Type I casein enzyme hydrolysate, 1 g of sodium chloride and 20 µl of 5 N NaOH to 100 mL of distilled water.

0.1 g agarose (Type I) was dissolved in a 10 mL of LB broth kept at 80 $^0$C with constant stirring. To this 50 µL of 0.01 M $AgNO_3$ (about 5 µg of Ag per mL of LB broth) was added followed by the addition of 10 µL of 0.1 M $NaBH_4$ solution. A dark orange color appears within 5 minutes due to the formation of Ag nanoparticles that becomes faint upon solidification and gets masked due to the components of LB broth. Another batch containing higher concentration of silver nanoparticles (about 10 µg of Ag per mL of LB broth) was also prepared by adding 100 µL 0.01 M $AgNO_3$ solution followed by the addition of 25 µL of 0.1 M $NaBH_4$. The same protocol was used to synthesize agarose composite gels containing copper nanoparticles (from copper sulphate precursor) at two different concentrations (about 3 µg and 6 µg of Cu per mL of LB broth) using hydrazine hydrate as the reducing agent. Immediate appearance of wine red color was observed indicating the formation of copper nanoparticles which becomes faint upon solidification and gets masked due to the components of LB broth. The nanoparticles were trapped in the LB agarose matrix, which were then employed to check the antibacterial activity without further modification. The plates, with the nanoparticles embedded in the matrix, were left aside for 45 minutes before plating bacteria. The pH of the various solutions was maintained at 7 to rule out the possibility of bacterial growth inhibition due to pH effect.

**(f) Analysis of antibacterial activity of LB-agarose containing Ag and Cu nanoparticles:**

Glycerol stock of *E. coli* strain DH5α, stored at -80ºC, was inoculated in 5 mL of Luria-Bertani (LB) broth and allowed to grow for 12 hours at 37 ºC in a shaker incubator. The grown bacterial cells were reinoculated into 10 mL of fresh LB broth and allowed to grow till the optical density reached 1.0 at 600 nm. Bacteria cells were harvested by centrifugation at 6000 rpm for 15 minutes and resuspended in 200 µL LB broth. The resuspended bacteria were spread onto LB agar plates containing varied concentrations of silver and copper nanoparticles. The spread plated LB agar plates were incubated at 37 °C for 12 hours. Appropriate control experiments were included to rule out the possibility of other components being anti-bacterial.

**(g) Synthesis of carbon-metal nanoparticles composites**

To obtain the carbon-metal nanoparticles composites, the agarose-metal nanoparticles composite films were carbonized in an inert atmosphere (nitrogen gas) at 400 °C for 30 min and then slowly cooled to room temperature.

## 3.4. Characterization techniques:

**Transmission electron microscopy**: The agarose-metal nanoparticle composite film was probe sonicated for 2 minutes in ethanol. The obtained dispersion was drop casted on a carbon-coated copper grid. TEM images were recorded with a JEOL JEM 3010 instrument (Japan) operated at an accelerating voltage of 300 kV.

**Field Emission Scanning Electron Microscopy:** The dispersion of metal nanoparticles embedded inside carbon matrix was examined by a Field Emission Scanning Electron Microscope (FESEM, FEI Nova-Nano SEM-600, Netherlands).

**UV-Visible and Photoluminescence spectroscopy**: The films obtained after drying agarose-nanoparticle gel were checked for UV-Vis absorption spectroscopic measurements. UV-Vis absorption spectroscopic measurements were performed with Perkin-Elmer instruments Lambda 900 UV/Vis/NIR spectrometer. Photoluminescence studies were done by using Perkin Elmer LS 50B instrument using a Xe lamp source.

## 3.5. Results and Discussion

The optical images of the transparent, agarose-stabilized metal nanoparticles gels are given in Figure 1. It shows a light brown colour for Pt and Pd, turmeric yellow for Ag, bright red for Au and a wine red colour for Cu nanoparticles stabilized by the agarose polymer. The uniform distribution of pink, yellow and wine red colour throughout the Au, Ag and Cu loaded composite films further indicates that the nanoparticles were spread evenly in the agarose matrix. Prolonged drying for 48 hours at room temperature allows these gels to become transparent composite films with a slight reduction in the intensity of the original colour (Figure 1B).

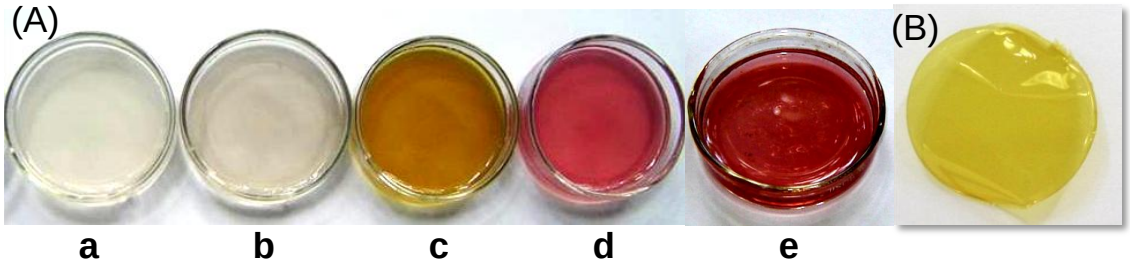


**Figure 1**. A) Optical images of nanoparticles embedded in an agarose matrix. a) Pd nanoparticles, b) Pt nanoparticles, c) Ag nanoparticles, d) Au nanoparticles, and e) Cu nanoparticles. B) Ag nanoparticles-agarose composite film after drying.

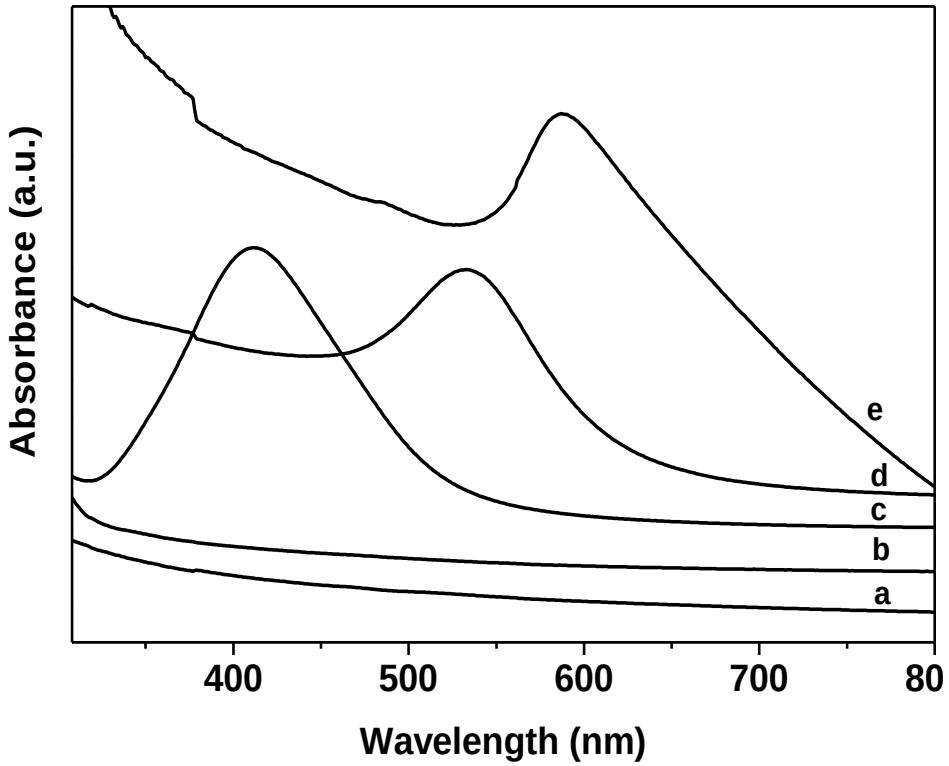


**Figure 2**. UV-Vis absorption spectra of metal nanoparticles embedded in agarose matrix. a) Pd nanoparticles, b) Pt nanoparticles, c) Ag nanoparticles, d) Au nanoparticles, and e) Cu nanoparticles.

In the case of agarose-copper composite gel, the wine red colour slowly transformed to pale green on drying due to partial oxidation of copper in air. The UV-Vis absorption spectra of the dried films show plasmonic bands in the visible region at 420, 520 and 585 nm respectively for Ag, Au and Cu nanoparticles loaded composites (Figure 2). On the other hand, the Pt and Pd nanoparticles composite films do not show any sharp plasmon band and the absorption is spread over the entire visible region.[19]

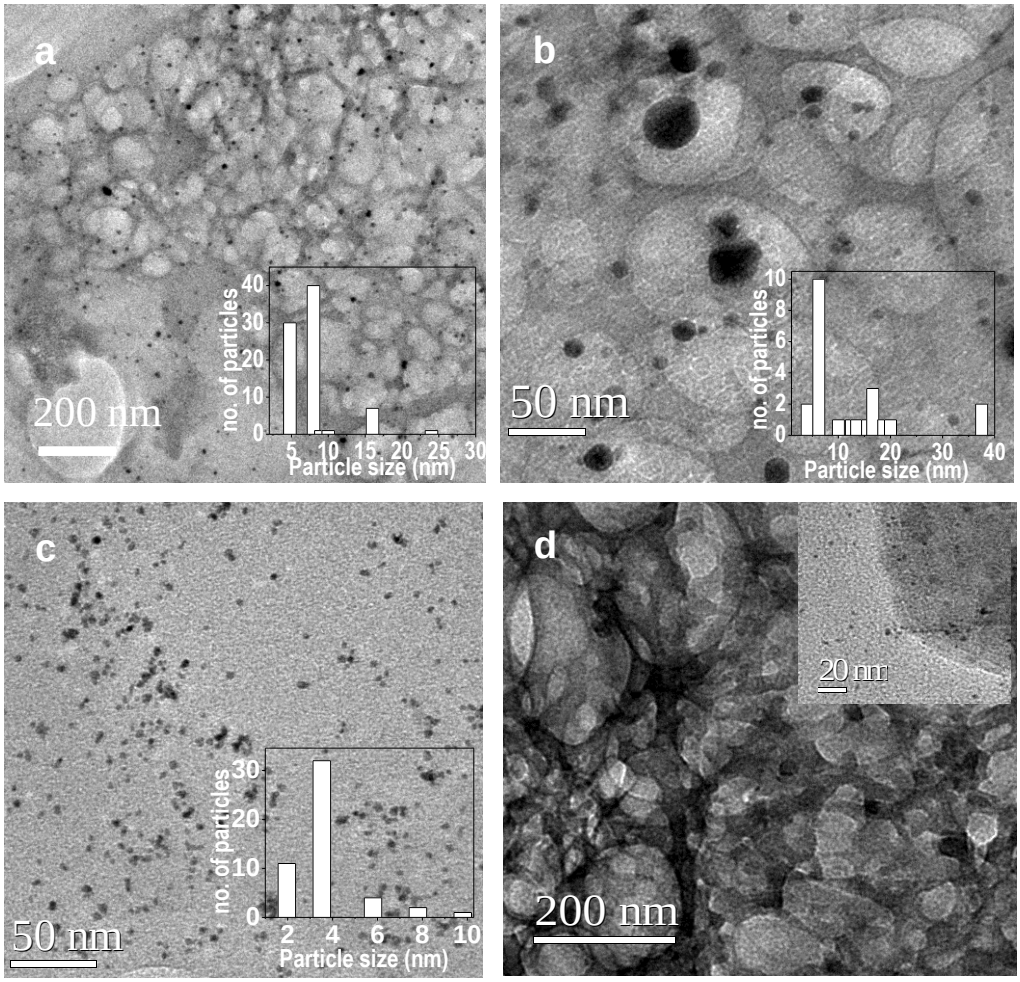


**Figure 3**. TEM images (a) Au nanoparticles, (b) Ag nanoparticles, (c) Pt nanoparticles, (d) Cu nanoparticles in agarose matrix. (a-c) Insets (bottom right) histogram of Au, Ag, and Pt nanoparticles, (d) (top right) higher magnification image of Cu nanoparticles.

The fine dispersion of metal nanoparticles throughout the agarose matrix is evident from the transmission electron microscope (TEM) images of the composite films shown in Figure 3. The agarose matrix that appears in light contrast in comparison to the electron dense metal nanoparticles is highly porous in nature and the sizes of the macropores are in the range of 50 to 200 nm. Au and Ag nanoparticles of sizes less than 10 nm are well dispersed inside the agarose matrix. Occasionally, few silver nanoparticles of size around 30 nm are seen in the larger pores of agarose network. In the case of copper, the particles size fall far below 5 nm

and are evenly distributed in the agarose network seen from the uniform dark contrast in the TEM image. These findings suggest that the presence of functional groups such as hydroxyl and ether linkages in the agarose network effectively help in passivating the surface of metal nanoparticles**.**

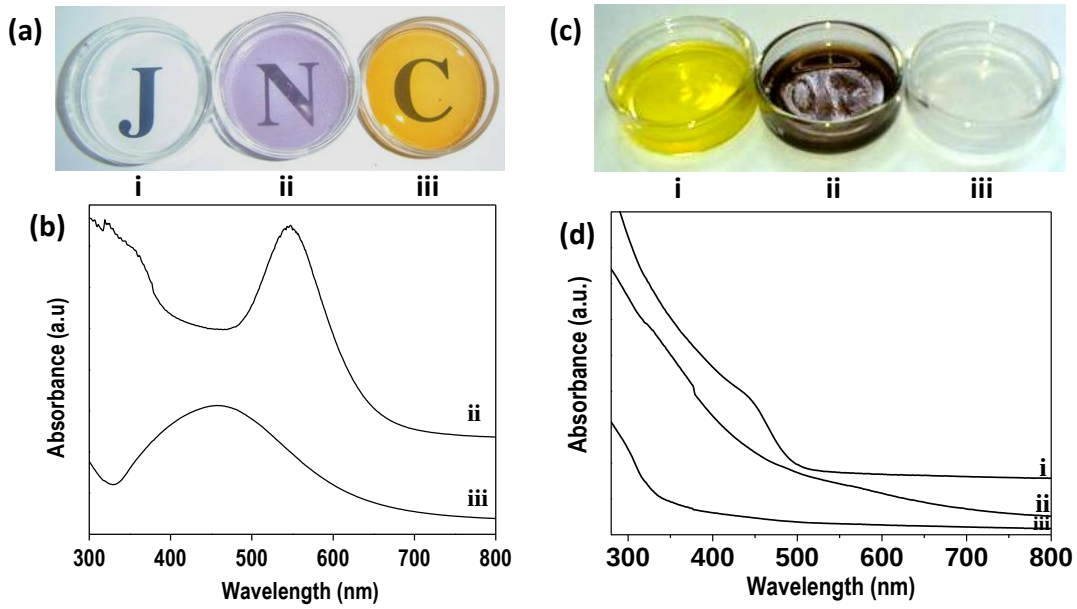


**Figure 4**. (a) Optical images of i) agarose gel, ii) Au nanoparticles in agarose, and iii) Ag nanoparticles in agarose and, (b) corresponding UV-Vis absorption spectra. (c) Optical images of (i) CdS, (ii) PbS, and (iii) ZnS nanoparticles in agarose matrix and (d), corresponding UV-Vis absorption spectra.

Interestingly, reduction of Ag and Au ions using glucose within the agarose medium gives bright yellow and violet coloured Ag, and Au-agarose composites (Figure 4a). The corresponding plasmon bands in the UV-Vis absorption spectra shifted to longer wavelengths (nearly 30 nm, Figure 4b) compared to the composites prepared using sodium borohydride as the reducing agent. This shift in the plasmon band for higher wavelength is associated with the larger particle sizes obtained by the slow diffusion of reducing agent, glucose, compared to $NaBH_4$ inside the agarose matrix.[20]

The gel forming ability and the oxygen-based functional groups of agarose polymer are not only used to stabilize metal nanoparticles but also the semiconducting metal sulphide nanoparticles. The optical image of the semiconducting PbS, CdS and ZnS nanoparticles encapsulated in agarose matrix is shown in Figure 4c. The CdS and PbS nanoparticles impart yellow and dark-brown colours respectively to the agarose matrix whereas, the ZnS nanoparticle impart no colour to the gel. The transparent nature of the composite films confirms the presence of metal sulphide particles in the nanosize regime. The UV-Vis absorption spectra of the agarose-semiconductor nanoparticles composites are shown in Figure 4d. The CdS-agarose composite film obtained after drying the gel in air at 30 ºC shows a characteristic absorption band edge at around 450 nm.[21] The PbS-agarose composite film also shows a broad absorption all through the visible region in addition to a strong absorption below 380 nm. On the other hand, ZnS-agarose composite didn't show any absorption in the visible region but only in the UV region below 320 nm.

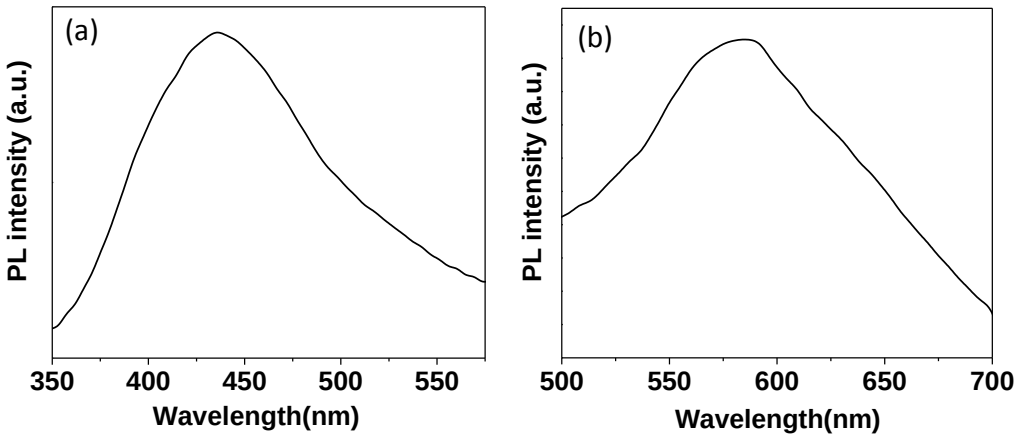


**Figure 5**. Photoluminescence spectra of agarose-semiconducting nanoparticle films (a) ZnS nanoparticles excited at 300 nm and (b) CdS nanoparticles excited at 390 nm.

The photoluminescence spectra of agarose-semiconducting nanoparticle films are presented in Figure 5. ZnS-agarose film on excitation at 300 nm resulted in blue emission at 435 nm (Figure 5a). In the CdS-agarose film (CdS particle size around 2 nm, TEM image is shown in Figure 6) excited at 390 nm shows a broad yellow-orange emission with the peak maximum at 580 nm associated with the CdS nanoparticles (Figure 5b). The transparent nature of the agarose-metal sulphide composite films coupled with their strong absorption in the UV and visible region would find application in UV and colour filters.[22]

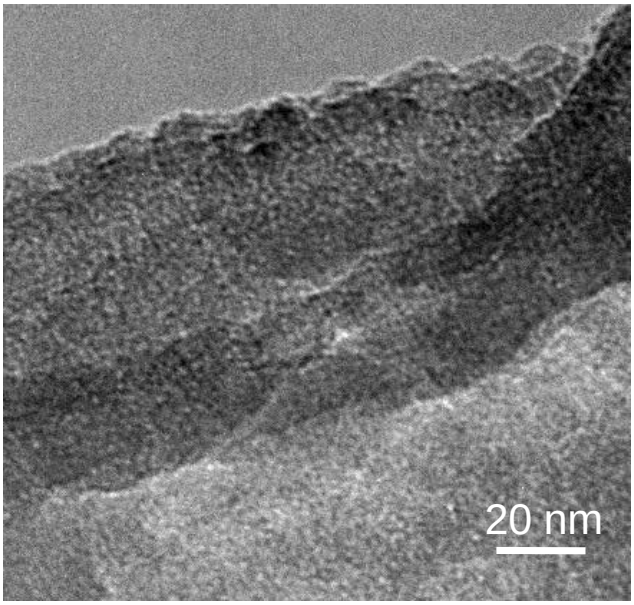


**Figure 6.** TEM image of CdS nanoparticles encapsulated in agarose matrix.

**Bacteriocidal activity of Ag and Cu nanoparticles:**

The antibacterial activity of silver and copper nanoparticles in the agarose matrix was tested on the bacteria *E. coli*. The antibacterial activity of silver nanoparticles is attributed to the increased chemical reactivity owing to their higher surface area to volume ratio.[23] The changes in the local electronic structure of the surfaces of the

smaller particles leads to the enhancement of their chemical reactivity leading to bacteriocidal effect.[24] Various mechanisms, through which silver nanoparticles kill bacteria, have been proposed. They are known to destabilize the plasma membrane potential leading to the depletion in the levels of intracellular adenosine triphosphate (ATP) bringing about cell death. They are also known to act through the formation of complexes with biomolecules containing sulfur, oxygen and nitrogen, such as thiols, carboxylates, amides, imidazoles, indoles and hydroxylates in proteins.[25] Silver nanoparticles are also shown to display affinity towards phosphorous containing compounds. Peroxide and free radical generation by silver nanoparticles is yet another mode by which they kill bacteria.[26] The excellent property of conformational entropy displayed by silver nanoparticles in polyvalent binding makes it easier for them to attach to flexible polymeric chains.[27] These observations assume significance in the light of the increasing antibiotic resistance displayed by bacteria. Similarly, copper ions, either alone or in copper complexes, are known as antimicrobial agents.[28-31] However, there are only a few reports on the antibacterial activity of copper nanoparticles.[32-35]

This study utilizes the *E. coli* strain DH5α for checking the antibacterial action of silver and copper nanoparticles dispersed in the porous agarose matrix. *E. coli* is a gram negative, facultative anaerobic, non-sporulating, motile, rod shaped bacterium commonly found in the lower intestine of warm-blooded animals. Figure 6 shows the antibacterial potency of silver and copper nanoparticles at two different concentrations stabilized by LB-agarose. Both silver and copper nanoparticles showed effective inhibition as shown in the Figure 7 a and b.

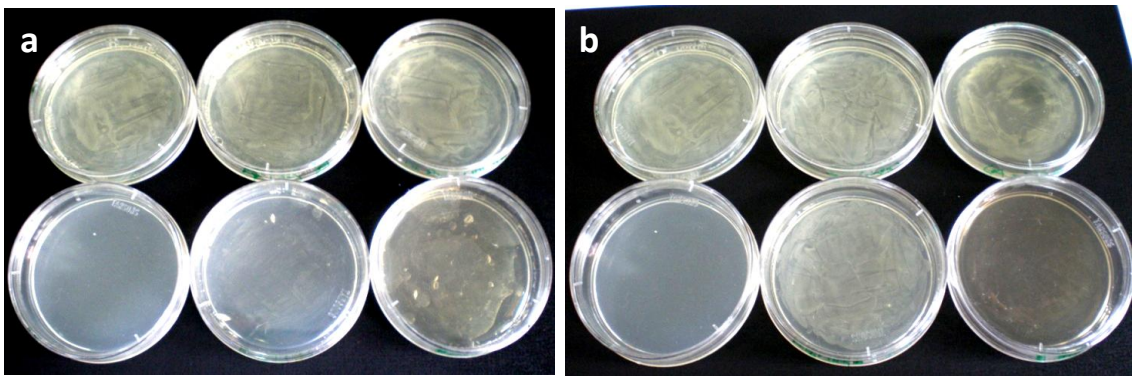


**Figure 7**. Antibacterial activity assay for silver and copper nanoparticles. The nanoparticles were synthesized in LB agarose and bacteria were plated on them.

a) upper left, agarose (0 μg $mL^{-1}$ copper nanoparticle) and bacteria; upper middle, agarose (only hydrazine hydrate) and bacteria; upper right, agarose (only copper sulphate) and bacteria; bottom left, agarose without bacterial inoculation; bottom middle, agarose (3.16 μg $mL^{-1}$ copper nanoparticle) and bacteria; bottom right, agarose (6.32 μg $mL^{-1}$ copper nanoparticle) and bacteria.

b) upper left, agarose (0 μg $mL^{-1}$ silver nanoparticle) and bacteria; upper middle, agarose (only $NaBH_4$) and bacteria; upper right, agarose (only silver nitrate) and bacteria; bottom left, agarose without bacterial inoculation; bottom middle, agarose (5.28 μg $mL^{-1}$ silver nanoparticle) and bacteria; bottom right, agarose (10.56 μg $mL^{-1}$ silver nanoparticle) and bacteria.

Two types of bacterial inhibition namely, bacteriocidal or bacteriostatic are known in using the nanoparticles. In bacteriocidal effect, the nanoparticles kill the bacteria and hence, prevent their growth in any fresh medium whereas, in bacteriostatic effect, they keep the bacteria dormant, giving room for their rejuvenation latter in a suitable medium. In our case, both Ag and Cu nanoparticles show complete bacteriocidal effect as seen when the surface of the LB agar plate was scarped and restreaked onto a fresh plate, without nanoparticles, after three days. The absence of any colony growth on restreaking confirms the bacteriocidal effect of the Ag and Cu nanoparticles. The LB/agarose stabilized silver nanoparticles prepared with lower concentration of silver (about 5 μg of Ag per gram of composite gel) showed nearly 50 % inhibition of bacterial growth while doubling the concentration

(about 10 μg of Ag per gram of composite gel) displayed complete inhibition (Figure 7a). In the case of copper, complete inhibition was observed even at lower concentration (at about 3 μg of Cu per gram of composite gel) indicating the superior bacteriocidal activity of copper nanoparticles over silver nanoparticles (Figure 7b). This is particularly significant when we compare the concentration of Ag nanoparticles used in other studies. For example, Kumar et al.[36] used nearly 3000 μg of Ag (in the form of nanoparticles) per gram of alkyd paint and 4000 μg of Au (in the form of nanoparticles) per mL of vegetable oil for antimicrobial coatings. Similarly, Morones et al.[23] reported silver nanoparticles solution containing 75 μg of Ag/mL showing good antimicrobial activity. Silver nanoparticles of size less than 15 nm are known to have effective bacteriocidal activity[23, 37-39] contributed by $Ag^{+}$ and $Ag^{0}$. The agarose matrix in our study plays a dual role for the exhibition of high antibacterial activity of nanoparticles even at very low metal concentration. It not only helps to stabilize the Ag and Cu nanoparticles of very small sizes by their functional -OH groups but also facilitates the full exposure of these nanoparticles to the microorganism due to their large porous network.

**Metal nanoparticles encapsulated in a carbon matrix:**

Metal nanoparticles supported on solid matrices especially carbon-based materials including amorphous and graphitic carbons are particularly interesting and important. Agarose-metal nanoparticles composite films can be readily converted to carbon-metal nanoparticles composite by carbonizing the films at 400 $^{o}$C for 30 min in presence of nitrogen atmosphere. A much shrunk, deformed carbon-metal nanoparticles residue was formed. Metal nanoparticles catalyze the carbonization

processes which effectively dehydrate agarose without predominant formation of gaseous carbon compounds.

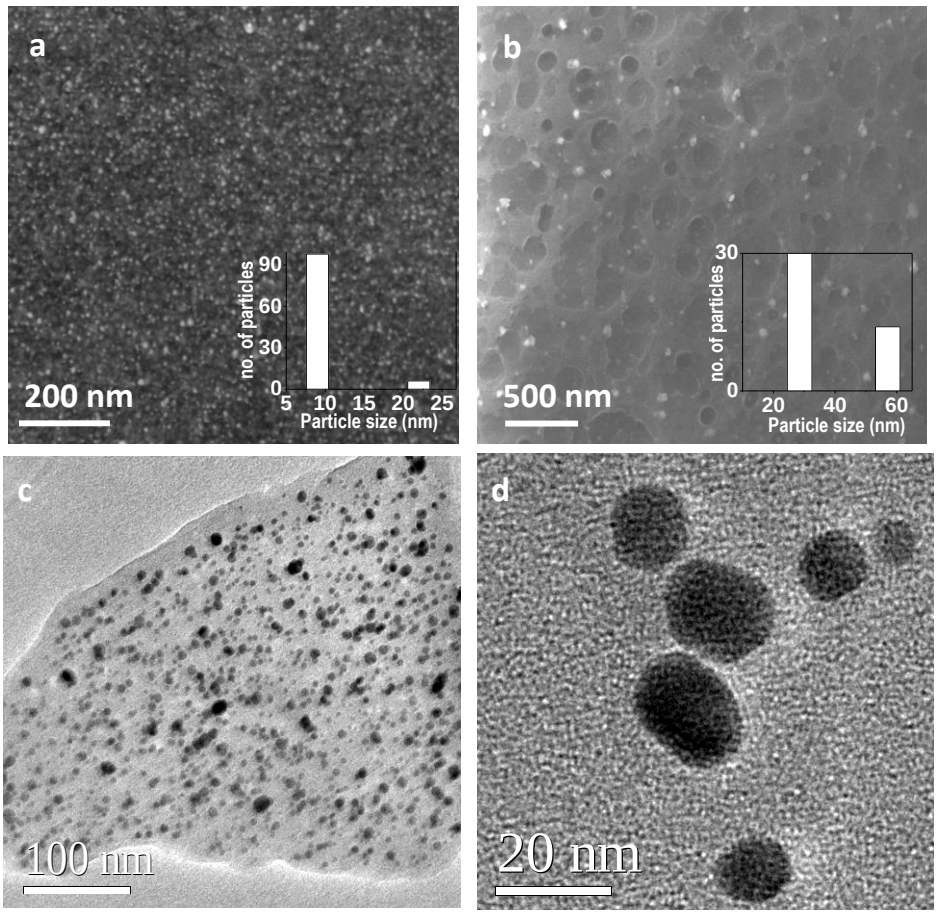


**Figure 8**. FESEM images of a) Au and b) Ag nanoparticle carbon composite after carbonization. Insets (bottom right) showing the histogram of a) Au and b) Ag nanoparticles embedded within carbon matrix. TEM images of c) Au and d) Ag nanoparticles carbon composite.

Figure 8 shows the field emission electron microscope images of carbonized Au and Ag agarose composite films. High concentrations of gold nanoparticles are uniformly dispersed within the carbon matrix (Figure 8a and 8c) respectively. The average particle size of gold nanoparticles is around 5-10 nm. In the case of silver nanoparticles we observe slight increase in particle size with less dispersion as compared to that of gold. The average particle size of silver nanoparticles is around 20-60 nm. Figure 8d shows a thin shell of carbon coating over Ag nanoparticles.

Similarly this approach can be extended in designing Pt and Pd nanoparticles embedded within carbon matrix.These metal nanoparticles encapsulated over carbon matrix can be utilized for various organic catalytic transformations and electrode materials.[40]

## 3.5. Conclusions

In conclusion, transparent agarose-metal/semiconducting nanoparticles composite films were fabricated by a simple route without compromising the optical properties of the nanoparticles. The high level antimicrobial activity of the Ag and Cu nanoparticles stabilized in the porous agarose matrix can be utilized in food packaging, sanitation and fabrics. More importantly, the agarose-metal nanoparticles films can be readily converted into carbon-metal nanoparticles composites by carbonizing the films in nitrogen environment at 400 ºC for 30 minutes. The obtained composites show fine distribution of metal nanoparticles (average particles size of 9 nm and 30 nm for Au and Ag respectively, on carbon matrix whose applications in catalysis are well known.[40]

## 3.6. References


1. C. N. R. Rao, A. Muller, A. K. Cheetham, *Chemistry of Nanomaterials*, **2004**, *Wiley-VCH*.
2. C. N. R. Rao, P. J. Thomas, G. U. Kulkarni, *Nanocrystals: Synthesis, Properties and Applications*, **2007,** *Springer-Verlag*.
3. a) N. Zheng, G. D. Stucky, *J. Am. Chem. Soc*. **2006**, *128*, 14278, b) S. H. Joo, S. Jae Choi, I. Oh, J. Kwak, Z. Liu, O. Terasaki, R. Ryoo, *Nature*. **2001**, *412*, 169.
4. E. Guibal, *Prog. Polym. Sci.* **2005**, *30*, 71.
5. S. Korchev, M. J. Bozack, B. L. Slaten, G. Mills, *J. Am. Chem. Soc.* **2004**, *126*, 10.
6. H. Inouye, K. Tanaka, I. Tanahashi, T. Hattori, H. Nakatsuka, *Jpn. J. Appl. Phys*. **2000**, *39*, 5132.
7. Y. Dirix, C. Bastiaansen, W. Caseri, P. Smith, *Adv. Mater.* **1999**, *11*, 223.
8. a) J. C. Liu, F. He, E. Durham, D. Zhao, C. B. Roberts, *Langmuir*. **2008**, *24*, 328, b) J. Cai, S. Kimura, M. Wada, S. Kuga, *Biomacromolecules*. **2009**, *10*, 87, c) M. J. Laudenslager, J. D. Schiffman, C. L. Schauer, *Biomacromolecules*, **2008,** *9*, 2682, d) S. Padalkar, J. R. Capadona, S. J. Rowan, C. Weder, Yu-Ho Won, L. A. Stanciu R. J. Moon, *Langmuir*, **2010**, *26*,8497.
9. J. He, T. Kunitake, A. Nakao, *Chem. Mater.* **2003,** *15*, 4401.
10. P. Raveendran, J. Fu, S. L. Wallen, *J. Am. Chem. Soc.* **2003**, *125*, 13940.
11. R. Brayner, M-J. Vaulay, F. Fiévet, T. Coradin, *Chem. Mater.* **2007**, *19*, 1190.
12. P. Serwer, *Electrophoresis.* **1983,** *4***,** 375.

13. J. A. Gavira, J. M. García-Ruiz, *Acta Crystallogr.* **2002**, *D58*, 1653.

14. J. Zhou, M. Zhou, R. A. Caruso, *Langmuir.* **2006,** *22*, 3332.

15. V. Kattumuri, M. Chandrasekhar, S. Guha, K. Raghuraman, K. V. Katti, K. Ghosh, R. J. Patel, *Appl. Phys. Lett.* **2006**, *88*, 153114.

16. a) S. Miyanaga, A. Hiwara, H. Yasuda, *Science and Technology of Advanced Materials*. **2002**, *3*, 103, b) A. Travan, C. Pelillo, I. Donati, E. Marsich, M. Benincasa, T. Scarpa, S. Semeraro, G. Turco, R. Gennaro, S. Paoletti, *Biomacromolecules.* **2009,** *10*, 1429.

17. a) S. Y. Liau, D. C. Read, W. J. Pugh, J. R. Furr, A. D. Russell, *Lett Appl Microbiol*. **1997**, *25*, 279, b) R. M. Slawson, H. Lee, J. T. Trevors, *Biol Metals*, **1990**, *3*, 151.

18. J. Jain, S. Arora, J. M. Rajwade, P. Omray, S. Khandelwal, K. M. Paknikar, *Mol. Pharmaceutics*. **2009**, *6*, 1388.

19. K. K. R. Datta, M. Eswaramoorthy, C. N. R. Rao, *J. Mater. Chem.* **2007**, *17*, 613.

20. P. Raveendran, J. Fua, S. L. Wallen, *Green Chem*. **2006**, *8*, 34.

21. D. Fan, P. J. Thomas, P. O'. Brien, *J. Mater. Chem.* **2007**, *17*, 1381.

22. S. Li, M. S. Toprak, Y. S. Jo, J. Dobson, D. K. Kim, M. Muhammed, *Adv. Mater.* **2007**, *19*, 4347.

23. J. R. Morones, J. L. Elechiguerra, A. Camacho, K. Holt, J. B. Kouri, J. T. Ramrez, M. J. Yacaman, *Nanotechnology.* **2005,** *16*, 2346.

24. J. Thiel, L. Pakstis, S. Buzby, M. Raffi, C. Ni, D. J. Pochan, S. I. Shah, *Small.* **2007**, *3*, 799.

25. F. Zeng, C. Hou, S. Wu, X. Liu, Z. Tong, S. Yu, *Nanotechnology*. **2007**, *18* 055605.

26. J. S. Kim, E. Kuk, K. N. Yu, J-H. Kim, S. J. Park, H. J. Lee, S. H. Kim, Y. K. Park, Y. H. Park, C-Y. Hwang, Y-K. Kim, Y-S. Lee, D. H. Jeong, M-H. Cho *Nanomedicine: Nanotechnology, Biology and Medicine.* **2007**, *3* 95.
27. P. Li, J. Li, C. Wu, Q. Wu, J. Li, *Nanotechnology*. **2005**, *16* 1912.
28. B. Gadi, G. Jeffrey, *Current medicinal chemistry.* **2005**, *12*, 2163.
29. B. Gadi, G. Jeffrey, **2004** *The FASEB Journal express.*
30. G. Faúndez, M. Troncoso, P. Navarrete, G. Figueroa, *BMC Microbiology*, **2004**, *4* 19.
31. C. C. Trapalis, M. Kokkoris, G. Perdikakis, G. Kordas, *Journal of sol-gel science and technology*. **2004**, *26*, 1213.
32. K-Y. Yoon, J. H. Byeon, J-H. Park, J. Hwang, *Science of the total environment*. **2007**, *373*, 572.
33. N. Cioffi, N. Ditaranto, L. Torsi, R. A. Picca, E. D. Giglio, L. Sabbatini, L. Novello, G. Tantillo, T.B-Zacheo, P. G. Zambonin, *Anal. Bioanal. Chem*. **2005**, *382* 1912.
34. C. Gu, B. Sun, W. Wu, F. Wang, M. Zhu, *Macromol. Symp.* **2007**, *254*, 160.
35. L. Qi, Z. Xu, X. Jiang, C. Hu, X. Zou, *Carbohydrate research*. **2004**, *339* 2693.
36. A. Kumar, P. K. Vemula, P. M. Ajayan, G. John, *Nature Materials.* **2008**, *7* 236.
37. K. Sudhir, *Langmuir*. **1998**, *14*, 1021.
38. G. S. Kumar, P. Gopinath, P. Anumita, A. Ramesh, S. S. Ghosh, A. Chattopadhyay, *Langmuir*. **2006**, *22*, 9322.
39. S. Pallab, A. Murugadoss, P. V. D. Prasad, S. S. Ghosh, A. Chattopadhyay, *International Journal of Food Microbiology.* **2008**, *124* 142.

40. N. A. Dhas, H. Cohen, A. Gedanken, *J. Phys. Chem. B.* **1997**, *101*, 6834.

# Chapter 4

# Observation of Pore-switching Behaviour in Porous Layered Carbon through a Mesoscale Order-Disorder Transformation

## Summary

Biomacromolecules known for their flexible nature and have the ability to alter their structures reversibly in response to external stimuli. Bringing such softness to porous solids has huge implications in areas such as separation, selective sensing, facile delivery and on-off switches. However, achieving flexibility in the rigid porous materials like zeolites and carbons is a difficult task. Here, we synthesize a porous layered carbon (PLC), containing nanographene domains by graphitizing glucose within the nanoscopic voids of aminoclay template. The obtained PLC shows a flexible pore size associated with the mesoscale order-disorder transformation brought out by an applied mechanical force (centrifugation). The pore flexibility has been exploited for size selective separation of dye molecules. The new form of carbon material with switchable pores would facilitate the development of selective screening of smaller biomolecules and toxic components that are distinct from those of rigid porous carbons.



A paper based on this study has been published in *Angew. Chem. Int. Ed.* **2011**, *50*, 3929.

## 4.1. Introduction:

The presence of structural flexibility (softness) in biomacromolecules is a fascinating phenomenon in nature.[1] For example enzymes efficiently change their tertiary structures which in turn reversibly modify their channels and cavities in order to accommodate guest molecules. The high specificity of enzymes in biologically important reactions is primarily attributed to their ability to change their structures in response to external stimuli. On the other hand, porous crystalline materials such as zeolites and aluminophosphates are rigid solids which are extensively used in separation, catalysis and adsorption.[2] The structural rigidity with regular porous nature of these materials have important role in sorting various guest species depending on their size and shape. Softness or flexibility hardly exists in such systems due to the compact arrangement making the overall structure rigid and condensed.[3]

Designing a new class of materials possessing integrated attributes of both crystallinity and flexibility would provide zeolite like regularity and enzyme-like specificity producing intelligent host materials that are responsive to guests under appropriate conditions. These structurally flexible porous inorganic materials could find enormous applications in catalysis, separation, sensors, fuel cells and gas storage owing to their unique properties and functions.[4-6] Recently metal organic frameworks (MOF) which consist of metal ions and organic linkers were shown to modify their framework structure in response to chemical or physical stimuli.[3,5,7-8] However, such a soft rearrangement of structure is not possible in rigid inorganic porous solids like zeolites, activated charcoal and mesoporous silica.[3] Considering their industrial significance structural flexibility in such porous materials would be

very advantageous for size selective separation of molecules or switching properties of the material itself.

Porous carbons are versatile and fascinating materials that can be used in number of scientific and technological processes as compared to other inorganic porous solids.[9-10] In particular due to their remarkable properties such as high surface area, large pore volume, uniform pore architecture, chemical inertness, good mechanical stability and biocompatibility these materials are attractive in the areas of adsorption, catalysis, electrochemistry, hydrogen storage, dye disposal and templating matrix for the fabrication of inorganic metal oxide with mesoporous structure.[11-14] Mesoporous silica such as MCM-48 and SBA-15 were often used as templates and sucrose as carbon precursor to obtain mesostructured carbons having high surface areas. However, the resulting carbon obtained by this synthetic route is often amorphous in nature having rigid pores replicating the template.[15e,f] Also layered materials like clays and layered double hydroxides due to their rich intercalation chemistry and swelling abilities served as efficient candidates for the fabrication of high surface area porous carbons.[16-17] Though clay galleries in the past have been used to make structurally rigid, porous carbons containing nanographene domains, they failed to show any mesoscale, long range order replicating the stacked clay layer structure.[16-17] Designing mesoscopically ordered porous graphitic carbons with flexible pores by employing clays will be advantageous in numerous applications.

## 4.2. Scope of the present investigation:

In the past, clays and mesoporous silica have been used as hard templates for the synthesis of porous carbons with rigid pores. In this study we use aminoclay[18-19] as the template to prepare flexible, porous layered carbon (PLC). Aminoclay is an

organophyllosilicate of approximate composition [$R_8Si_8Mg_6O_{16}(OH)_4$,where R = $CH_2CH_2NH_2$] consisting of octahedrally coordinated MgO/OH sheets (brucite) overlaid on both the sides with a tetrahedrally coordinated aminopropyl functionalized silicate network.[18-19] Since the amine groups get protonated in water, the clay layers can be easily exfoliated due to charge repulsion between the layers.[20-21] The exfoliated clay in water consists of a single layer or bundles containing few layers (nano bundles). The dispersed layers can be restacked by the addition of ethanol which immediately appears as a milky, white precipitate. In the present work, we first mixed glucose solution with the transparent aminoclay dispersion then induced stacking of clay layers/nanobundles by adding ethanol (Experimental section, Scheme 1). During the precipitation glucose molecules get trapped in between the layers as well as the space between the nanobundles. The composite after carbonization and subsequent etching of clay followed by filtration leaves behind the porous layered carbon (PLC).

## 4.3. Experimental Section:

### (a) Materials:

3-aminopropyltriethoxysilane, $MgCl_2$ $6H_2O$, glucose, HCl, HF, Congo red, alizarine yellow, $CuSO_4$ $5H_2O$, sodium potassium tartrate, NaOH and activated charcoal were purchased at an analytical pure grade and were used without any further purification. Millipore water and ethanol were used wherever essential.

### (b) Synthesis of aminoclay:

The aminoclay was prepared by the method reported in the literature.[20] Typical synthesis involves room temperature, drop wise addition of 3-aminopropyltriethoxysilane (1.3 mL, 5.85 mmol) to an ethanolic solution of

magnesium chloride (0.84 g, 3.62 mmol). The white slurry obtained after 5 min was stirred overnight and the precipitate isolated by centrifugation was washed with ethanol (50 mL) and dried at 40 °C.

**(c) Synthesis of aminoclay-glucose composite and porous layered carbon:**

1 g of aminoclay was exfoliated in 10 mL of water and 3 g of glucose was added to it. The solution was aged for 12 h and then re-precipitated with ethanol. The obtained precipitate was then dried at 50 $^{0}$C and finally a brown colored powder was observed. The obtained clay-glucose composite was taken in a clean silica boat and then carbonized for 600 $^{0}$C in $N_2$ atmosphere for 6 h with a heating rate of 5 $^{0}$C min$^{-1}$.

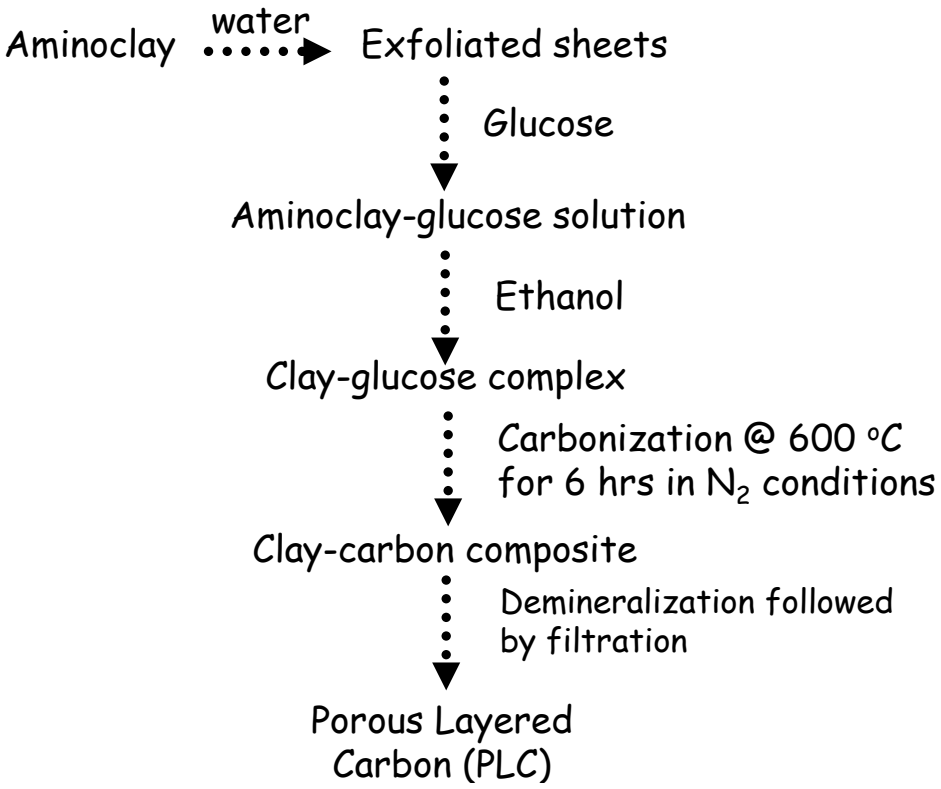


**Scheme 1.** Flowchart showing detailed synthetic methodology of porous layered carbon.

**(d) Dye sorption:**

Dye adsorption studies for each material were carried out by the following method. A stock solution of the dye of concentration 1.2 g/L was prepared by dissolving the dyes (Congo red and alizarin yellow) in 10 mL of water. In each experiment, 10 mg of the different adsorbents like porous layered carbon (PLC), porous layered carbon centrifuged (PLC-C) and activated charcoal (AC) were suspended in 2 g of the stock solution. Similarly for selective dye sorption, equal volumes of identical concentrations (1.2 g/L) of Congo red and alizarin yellow were mixed. To this mixture, 10 mg of different porous adsorbents PLC and PLC-C were added. These mixtures was allowed to stand for 12 h at 298 K and then centrifuged. The residual dye concentration in the supernatant was measured by UV-Vis spectrophotometer.

**(e) Estimation of glucose present in clay-glucose composite by Fehling's method**

**Preparation of Fehling's solution**:

**Solution A:** 6.9 g of $CuSO_4$ $5H_2O$ was dissolved in minimum amount of water by sonication and made up to 100 mL in a standard flask.

**Solution B:** 36.5 g of sodium potassium tartrate (Rochelle salt, $C_2H_4O_6NaK$ $H_2O$) and 15 g of NaOH are dissolved in minimum amount of water by sonication. Both the solutions are mixed and made up to 100 mL standard flask.

**Estimation of glucose**:

5 mL of Fehling A and Fehling B solutions were mixed in a conical flask and heated to 90 $^oC$ in an oil bath. The supernatant of clay-glucose composite is taken in

a burette and added drop wise to the conical flask until blue colored solution disappears and red precipitates of cuprous oxide starts forming.

**(f) Calculation of centrifugal acceleration and centrifugal force acting on PLC:**

The centrifugal acceleration and centrifugal force acting on PLC are calculated as follows.

*Centrifugal acceleration = $\omega^2$*R, where $\omega$ is angular velocity (radians per second), R is rotation radius (in meters).*

1 g of PLC sample is taken in a centrifuge tube. The rotation radius is 4.5 cm and the angular velocity is 6000 rpm respectively.

**Step 1***: The centrifugal acceleration experienced by the sample is given by = $\omega^2$*R (m/s$^2$)*

= $(6000*2\pi/60)^2*0.045$ = 17747.28 m/s$^2$ or 1811 g, where g is acceleration due to gravity.

**Step 2***: Centrifugal (shear) force is calculated by multiplying mass with centrifugal acceleration* = $1*10^{-3}*17747.28$= 17.74 N (Kg m/s$^{-2}$).

## 4.4. Characterization Techniques:

**X-ray Diffraction:**

The X-ray diffraction (XRD) patterns of the aminoclay, clay-glucose composite and porous layered carbons (PLC and PLC-C) were recorded on Bruker D8 discover X-ray diffractometer using CuKα radiation.

**Nitrogen adsorption and desorption isotherms:**

Nitrogen adsorption and desorption isotherms were carried out at 77 K under liquid nitrogen bath on a Quantachrome Autosorb 1 sorption analyzer. Before measurements the samples were degassed at 200 $^oC$ for more than 5 h. The Brunauer-Emmett-Teller (BET) method was used to calculate the specific surface

areas. The pore size distribution was determined by non-local density functional theory (NLDFT) calculations. In the NLDFT calculations, the equilibrium model of carbon slit pores was used.

**Transmission electron microscopy:**

For TEM measurements, the samples were prepared by dispersing the powder products in ethanol by sonication before drop casting on a carbon-coated copper grid. TEM studies were carried with a FEI TITAN (cube) operating at an accelerating voltage of 300 kV and a JEOL JEM 3010 instrument operating at an accelerating voltage of 300 kV.

**Thermogravimetric analysis:**

Thermogravimetric (TGA) analysis was performed using Mettler Toledo 850 from 30 to 900 $^{o}$C in oxygen flow at a heating rate of 5$^{o}$C per minute.

**Elemental analysis (CHN):**

Elemental analysis of PLC was carried out using a Perkin Elmer 2400 CHN analyzer.

**Computational details**:

The molecular sizes of Congo red and alizarin yellow were obtained using VMD (Visual Molecular dynamics).[22] The geometry optimizations were done using Gaussian-03 software.[23] The level of theory used was DFT, B3LYP hybrid functional with 6-31g basis set.

## 4.5. Results and Discussion:

We have used aminoclay as the template to synthesize porous layered carbon. The detailed experimental procedure is presented in experimental Scheme 1.

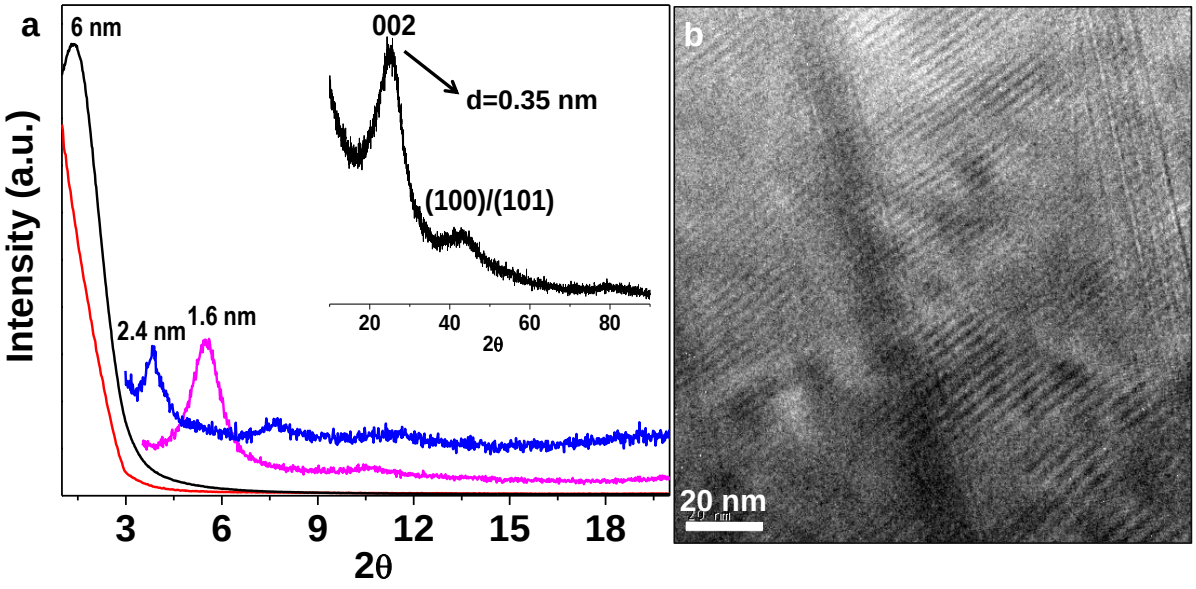


**Figure 1.** (a) XRD patterns (low angle) of aminoclay (magenta), clay-glucose composite before carbonization (blue), clay-glucose composite after carbonization (red) and clay-glucose composite after carbonization followed by etching of clay (black) yielding porous layered carbon (PLC), Inset showing wide angle XRD pattern of PLC, (b) HRTEM image of porous layered carbon.

The powder X-ray diffraction (PXRD) pattern of the resulting PLC is shown in Figure 1a. The low angle diffraction peak at $2\theta = 1.3^{o}$ corresponding to a basal distance of 6 nm confirms the existence of mesostructural order in the carbon after the removal of clay. Considering the basal distance of clay-glucose composite which is of 2.5 nm (and is lost on carbonization), it is unlikely that the individual clay layers would have acted as the template to get this large d-spacing of 6 nm. The amount of glucose that is present in clay-glucose composite estimated by Fehling's method comes nearly 65 % (See Experimental Section). The PLC with large d-spacing (6 nm) is therefore, originated from the carbonization of glucose mostly

trapped between the clay nanobundles of 2 to 3 layers thick during the precipitation. The peak broadening at $2\theta=25^{o}$, the characteristic $d_{002}$ graphitic peak in the higher angle XRD pattern signifies that the PLC is composed of nanocrystals of graphite. The crystallites width (perpendicular to the basal plane) calculated from the Scherrer formula is around 2.0 nm and are probably made up of 5 to 7 layers of graphene.[24]

The transmission electron microscope (TEM) image of PLC sample obtained using FEI TITAN$^{3TM}$ transmission electron microscope clearly shows the existence of layered structure with the spacing between the layers is about 2.5 nm (Figure 1b) and the wall thickness around 3 nm. Occasionally, we have also observed regions where the wall thickness was found to be in the range of 3 to 4 nm and the spacing between the layers varied from 2 to 4 nm which is typical of flexible layered structure (Figure 2). The low magnification TEM image (top view) shows the porous nature of the layers composed of interconnected nanoparticles of size 1 to 3 nm (Figure 3). The voids between the interconnected particles are well below 1.5 nm. Interestingly, the electron diffraction (ED) pattern observed for this region shows a single crystalline behaviour indicating the crystallographically well-oriented mesoscopic arrangement of the nanocrystallites. The high resolution TEM image of a layered surface clearly confirms such an orientation as the lattice fringes observed for the hexagonal carbon was continuous over a long distance (approximately. 50 nm).[25-27]

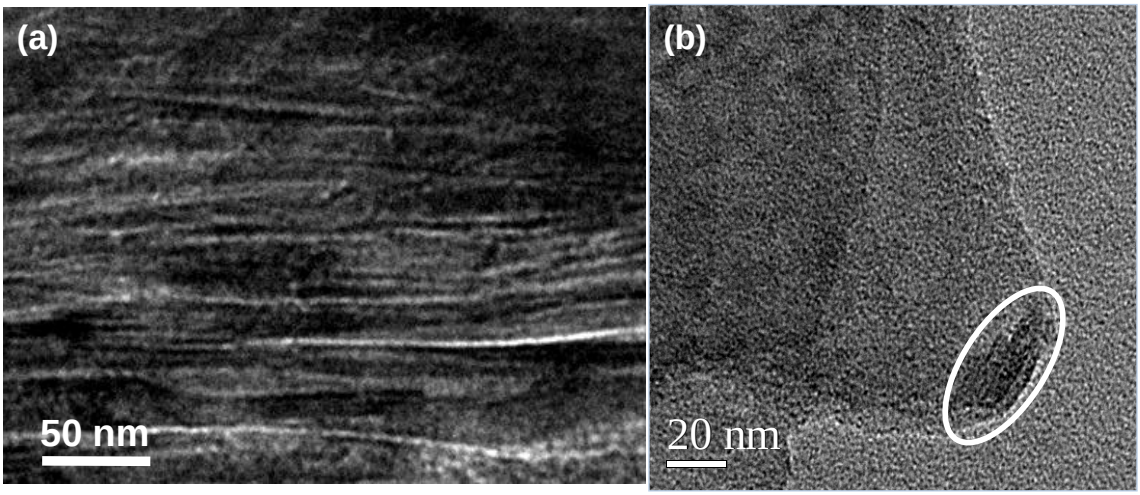


**Figure 2.** TEM images of PLC (a) showing flexible layered structure, (b) showing layered structure folded at the edge (highlighted by white circle); inset (top right) showing corresponding electron diffraction pattern.

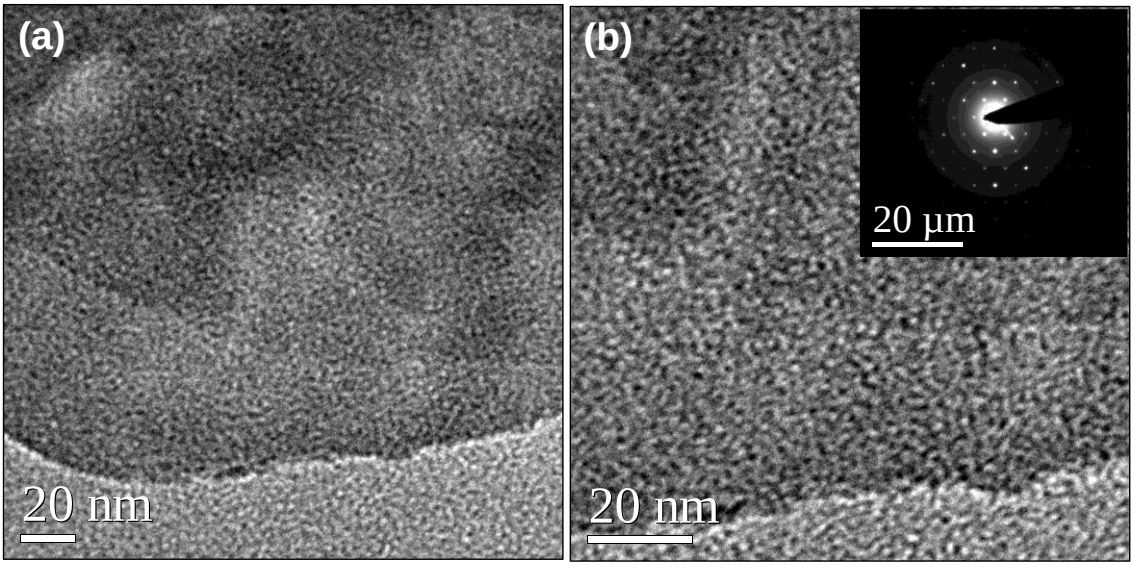


**Figure 3**. TEM images of (a) porous layered carbon (b) magnified portion of PLC showing sheet like nature, inset showing corresponding electron diffraction pattern.

Noticeably, we have found a significant number of dark contrast regions each one measuring about 3 nm in size likely to be originated from the pillar-like structures present between the layers (Figure 4). It is important to note that most of

these pillars are crystallographically oriented with the nanocrystals present in the layer.

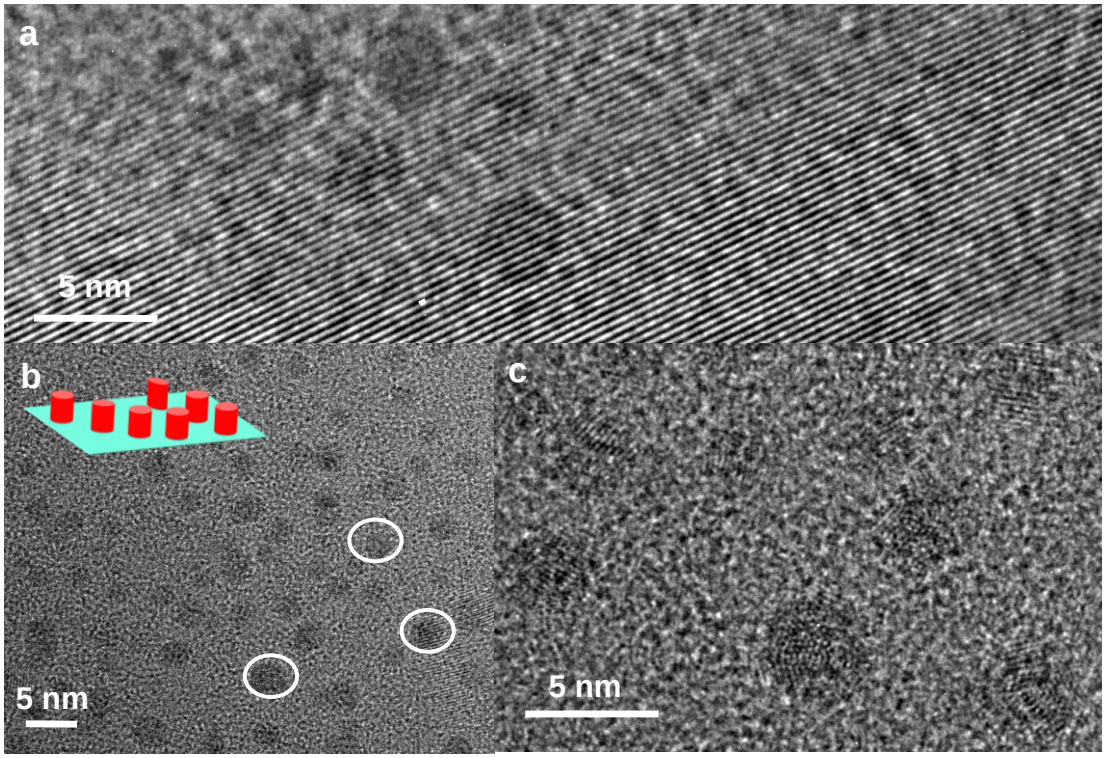


**Figure 4.** (a-c) HRTEM images of PLC showing pillar like structures (highlighted by white circles), Inset in (b) shows model of pillars (red).

It is important to note that most of these pillars are crystallographically oriented with the nanocrystals present in the layer. The PLC was found to be less stable under electron beam probably, due to the presence of large number of defects. This observation is also consistent with the nanographenes reported in the literature wherein the instability is caused due to the presence of pores that introduce defects along the edges.[28] Nevertheless, thermogravimetric analysis (TGA) shows that the thermal stability of PLC is comparable to that of multi-walled carbon nanotubes (Figure 5).[29]

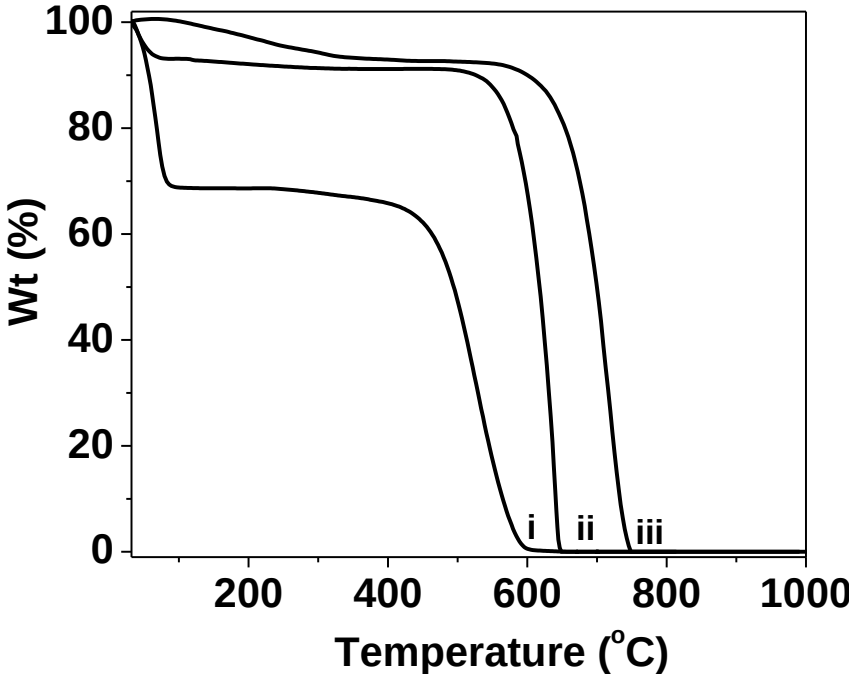


**Figure 5.** (a) TGA curves for the PLC (i), MWCNT (ii) and graphite (iii) in presence of oxygen gas. The heating rate was $5^{o}C\ min^{-1}$.

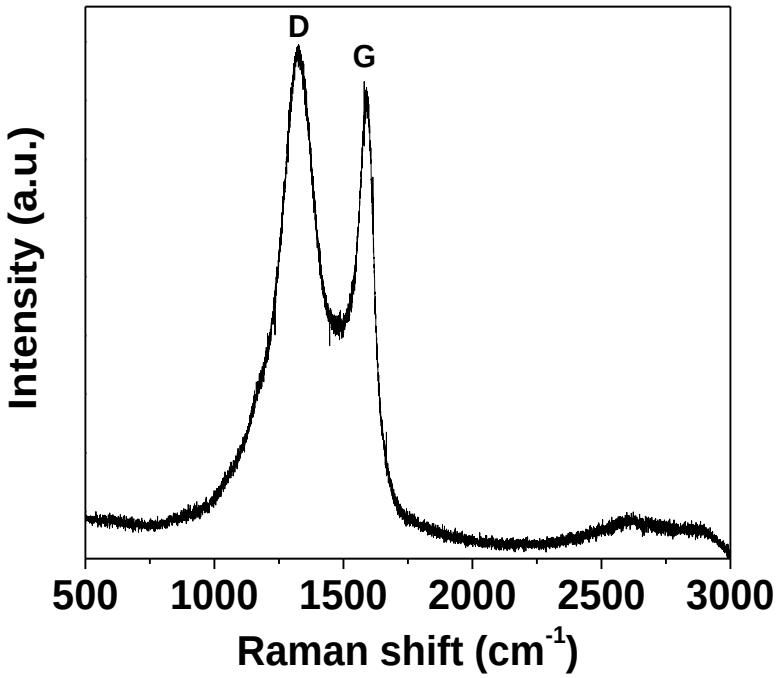


**Figure 6.** Raman spectrum showing D and G signatures of PLC.

Raman spectroscopy has been the most absolute valuable probe for graphitic carbon based materials till date. Raman analysis of PLC shows the appearance of an equally strong D-band (at 1325 $cm^{-1}$for the defect $sp^3$ carbon) in addition to the G-band (graphitic band at 1590 $cm^{-1}$) which is quite understandable considering the nature of defects associated with such a porous structure made of nanocrystallites (Figure 6).[30-31]

**Adsorptive properties of PLC:**

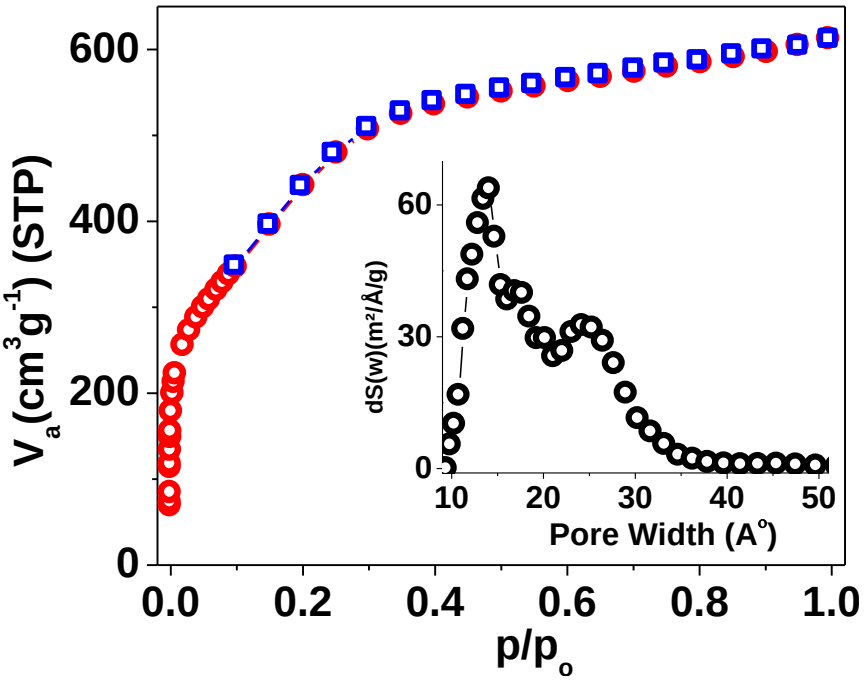


**Figure 7**. $N_2$ adsorption (red)-desorption (blue) isotherms of porous layered carbon, inset showing corresponding pore size distribution.

The nitrogen adsorption-desorption isotherms obtained for the PLC at liquid nitrogen temperature (77 K) shows mostly of type I behaviour with a two-step rise in adsorption at low p/po with no hysteresis (Figure 7). Indeed, type I and type II isotherms obtained for spherical or plate-like particles usually would not show any hysteresis. The initial steep rise in the adsorption isotherm at very low p/po (less than 0.1) can be accounted for the existence of micropores which are originated from

within the layers (as it is composed of interconnected nanoparticles). The second rise in the adsorption in the p/po range 0.1 to 0.4, bordering the mesopore region, but is not prominent like the one observed for MCM type materials, may be associated with the capillary condensation between the plate-like layered structures.[32] The pore size calculated from the non-local density functional theory (NLDFT) method shows two type of pores one at 1.4 nm in the micropore region and the other at 2.4 nm in the mesopore region (inset in Figure 3b). The specific surface area calculated by Brunauer-Emmett-Teller (BET) is about 1628 $m^2/g$ and the pore volume calculated at p/po = 0.95 is 0.95 cc/g. However, it is to be mentioned that caution must be exercised when measuring the surface area of the materials containing micropore regions. [33]

Materials with good $CO_2$ adsorption capacity are of importance from both environmental and industrial points of view. The capture and storage of $CO_2$ emitted from industrial processes are global challenges.[34] PLC shows remarkably high $CO_2$ uptake of 81 wt% at 195 K at 1 atm. Adsorption-desorption isotherms of $CO_2$ on PLC follow exactly the same path and do not reach saturation at p/po=1 (Figure 8a). Furthermore, carbon materials have attracted much interest owing to the possibility of adsorbing $H_2$ in a reversible way, without experiencing high-energy loss for fuel release.[35-36] Materials with good $H_2$ uptake have potential as clean energy alternatives. The hydrogen sorption capacity of porous carbons generally increases with surface area. We have examined $H_2$ adsorption on PLC at 77 K and found an uptake of 1.57 wt%, which is comparable to the capacity of mesoporous carbons template by mesoporous silica of similar surface area.[35a] Both the adsorption and desorption of $H_2$ follow a same path showing complete reversible adsorption and no

hysteresis as shown in Figure 8b. $H_2$ uptake on PLC does not increase with increasing pressure.

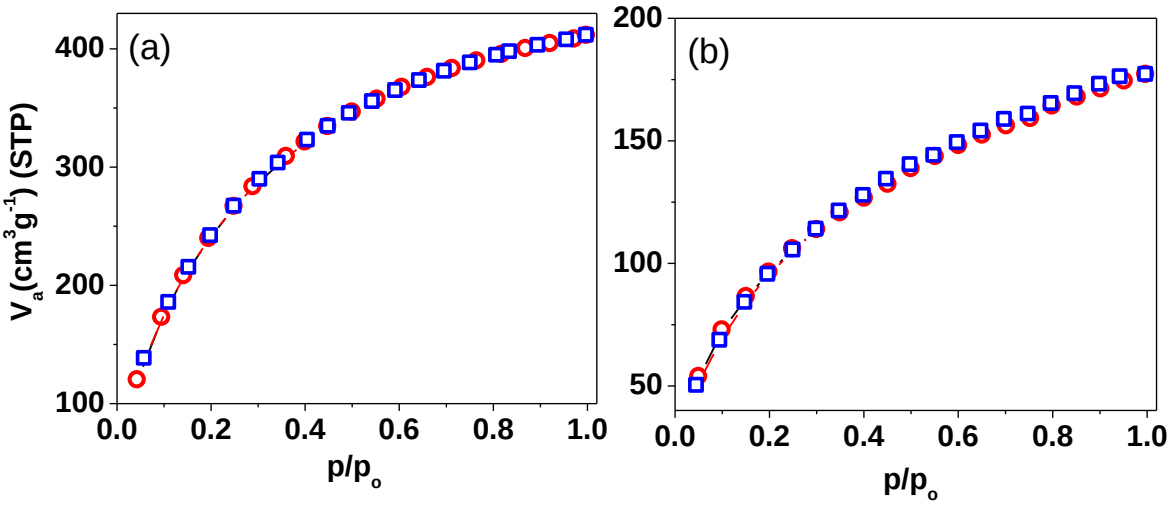


**Figure 8**. Isotherms curves of PLC showing adsorption (red)-desorption (blue) of (a) $CO_2$ and (b) $H_2$.

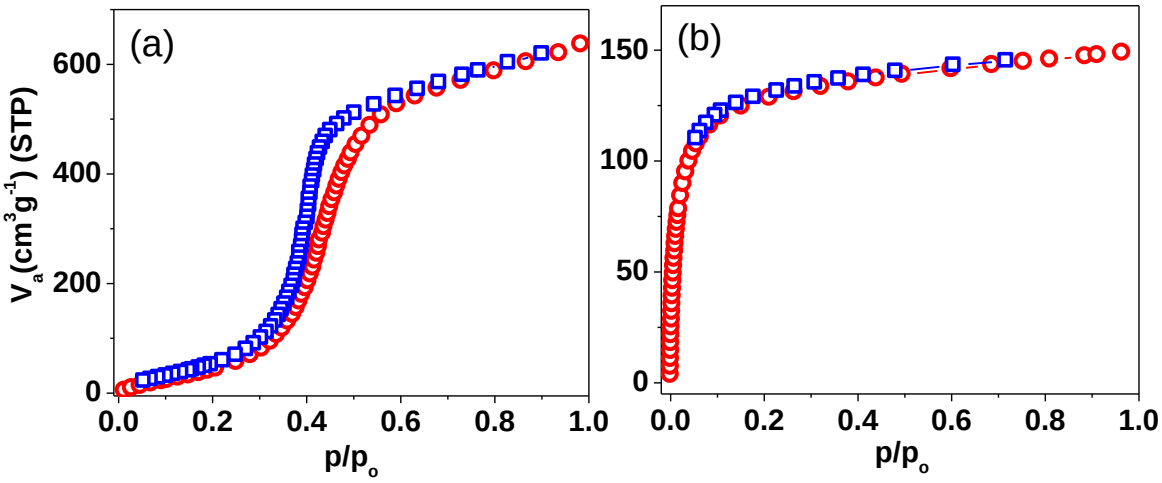


**Figure 9**. Vapour sorption isotherms for PLC, (a) $H_2O$ (298 K) and (b) $C_6H_6$ (298 K) respectively.

Vapour sorption experiments shows no significant uptake for water at lower $p/p_0$ region but shows a steep rise in adsorption with increase of pressure ($p/p_0 \sim 0.4$) (Figure 9a). On the other hand, benzene adsorption shows type I behaviour with strong uptake at very low $p/p_0$ (Figure 9b). This variation in adsorption behaviour for

water and benzene at low p/po indicates that the PLC, because of its graphitic structure can interact well with non-polar molecules like benzene. At the same time, it can also interact with polar molecules due to the presence of oxygen containing edges at the nanocrystallites.

Indeed, elemental analysis (CHN) of PLC showed nearly 15% oxygen and 5% nitrogen in addition to 60% carbon. Furthermore, Fourier transform infra-red (FTIR) spectrum analysis on PLC also showed bands corresponding to C-H stretch, C-O, C=C and O-H stretches (Figure10).

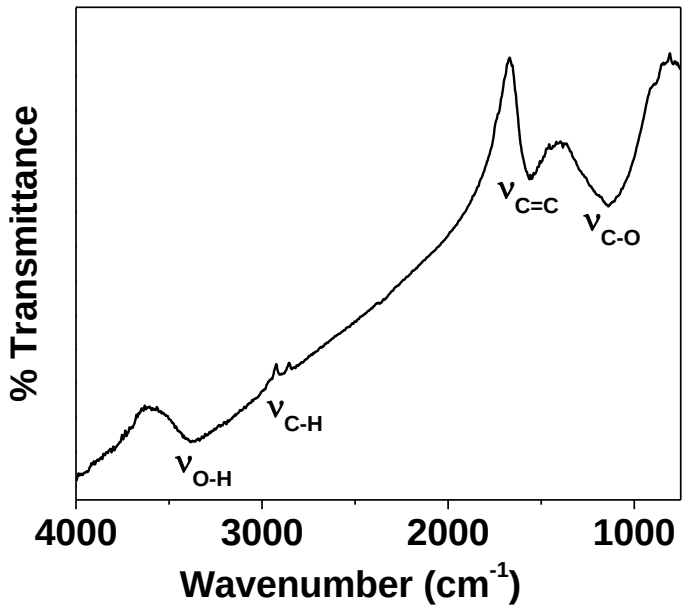


**Figure 10.** Infra-red spectrum of porous layered carbon.

**Mesoscale Order-Disorder Transformation:**

Interestingly, when PLC was dispersed in water and then centrifuged, the mesoscale order was lost as can be seen from the absence of low angle peak in the XRD pattern (Figure 11a). The $N_2$ adsorption-desorption isotherm clearly displays type I behaviour for this sample with BET specific surface 1,543 $m^2/g$ (Figure 11b and Table 1).

| Sample | Specific surface area ($m^2/g$) BET [a] | BET [b] | Pore volume ($cm^3/g$) $V_{micro}$ $N_2$ [c] | $V_{meso}$ $N_2$ [d] | Pore sizes [e] (nm) |
|---|---|---|---|---|---|
| PLC | 1345 | 1628 | 0.6 | 0.3 | 1.4 & 2.4 |
| PLC-C | 1634 | 1543 | 0.7 | - | 1.4 |

[a] *Determined using the data at p/po = 0.01-0.05.*
[b] *From the data at p/po = 0.05-0.3.*
[c] *From Dubinin-Radushkevich (DR) equation using $N_2$ isotherm.*
[d] *By subtracting the micropore volume (obtained from the $N_2$ isotherm) from the volume of $N_2$ adsorbed at p/po = 0.95.*
[e] *Pore size distribution was determined by non-local density functional theory (NLDFT) method.*

**Table 1**. Textural parameters of the PLC and PLC-C samples.

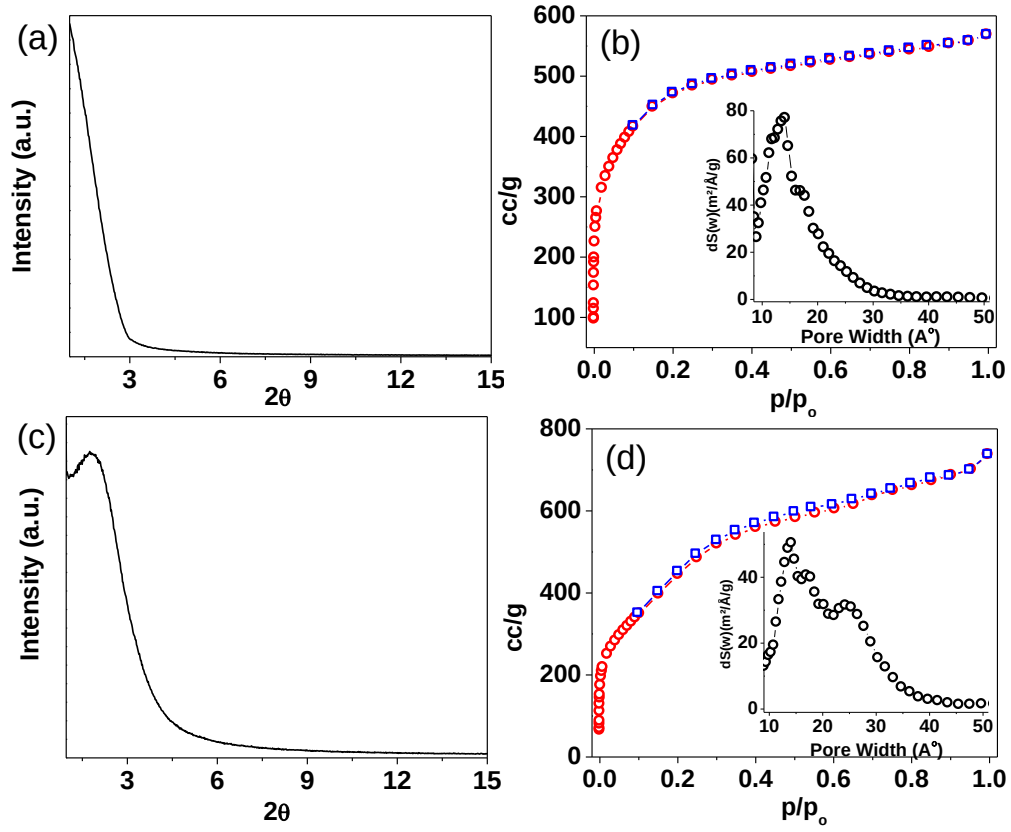


**Figure 11.** Low angle XRD patterns showing reversible nature of porous layered carbon (a) PLC soaked in water followed by centrifugation (PLC-C), (b) soaking of the sample (a) in water followed by filtration, (c, d) corresponding $N_2$ adsorption (red)-desorption (blue) isotherms at 77 K for (a) and (b), and inset showing pore-size distribution.

The pore size calculated from NLDFT method is around 1.4 nm (Table 1) and importantly, it did not show any mesopores perhaps, due to the collapse of space between the layers by centrifugal force. The centrifugal (shear) force required to cause this collapse was found to be 17 N for 1 g of sample (See Experimental section). However, we didn't observe any control in the degree of buckling by reducing the centrifugal (shear) force below 17 N. Since the micropores are mainly derived from the interconnected crystallites within the layer, it did not show any appreciable variation. To our surprise, the mesoscale order reverts back when the sample was again dispersed in water and allowed to settle on its own or separate it out by filtration (Figure 11c and Figure 13).

In commensurate with the reversible changes in structure, the adsorption behaviour also reappears with the existence of two types of pore sizes (Figure 11d). Though there is a slight variation in the resulting isotherms, as the structure of PLC is not as rigid as zeolites, the appearance and disappearance of mesopore region due to order-disorder transformation is clearly noticed. This process was reversible and reproducible (Figure 12). Indeed, if the porous layered carbon was obtained by etching out the clay followed by centrifugation (PLC-C) in the synthesis step (rather than filtration), the mesoscale order will not be observed (Figure 12a).The adsorption isotherm exhibits type I behaviour with the pore size around 1.4 nm (Figure 12d). But, when the same sample is dispersed in water and then allowed to settle or filtered, the resulting product shows the mesoscale order in the low angle XRD pattern and the pore size derived from the associated isotherm displays two types of pores one at around 1.4 nm and the other at 2.5 nm (Figure 12 b, e).

Dispersion of the sample again in water followed by centrifugation leads to the disappearance of the mesoscale order, also the mesopores (Figure12 c, f).

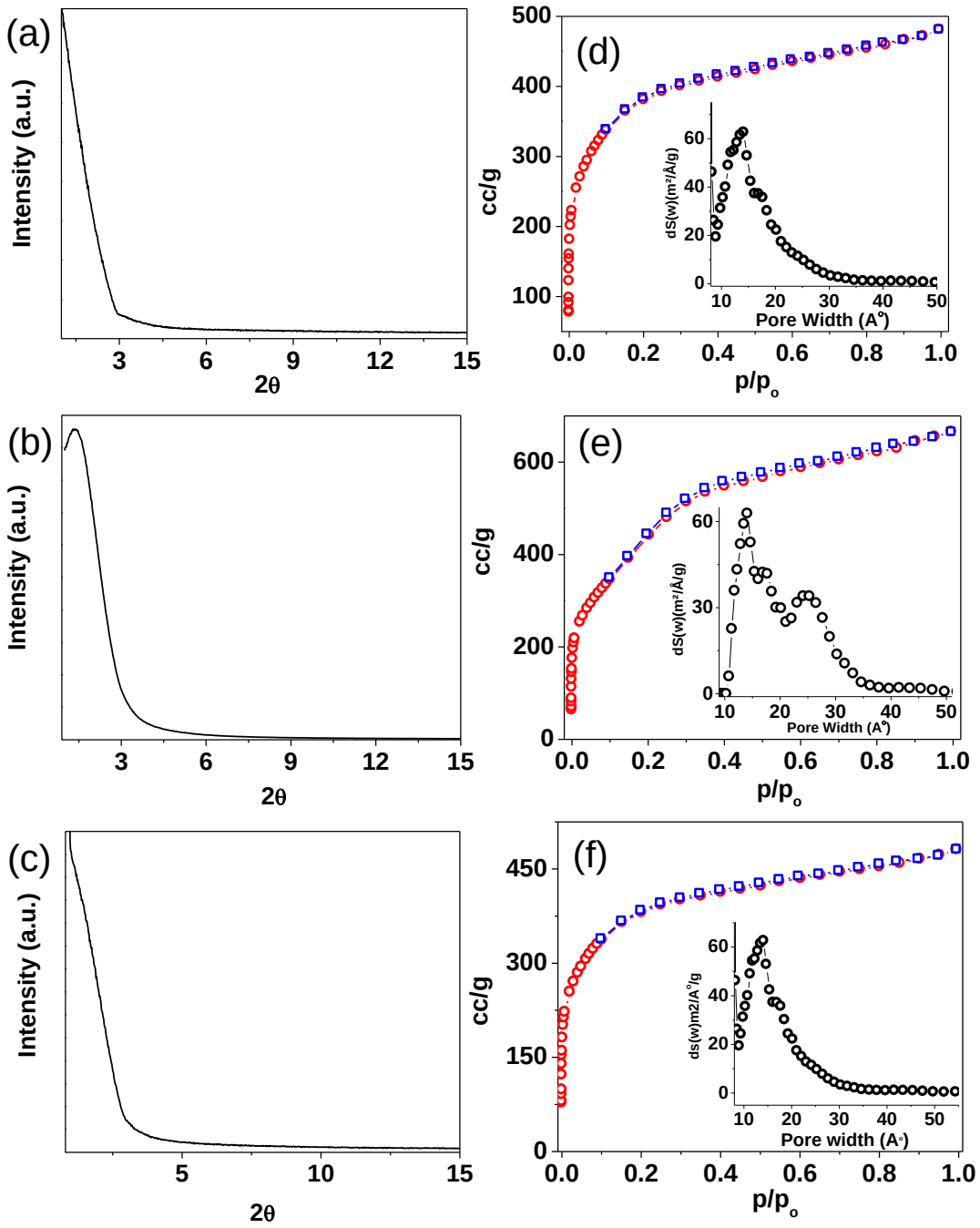


**Figure 12**. XRD patterns (a) porous layered carbon directly obtained by etching of clay in the synthesis step itself followed by centrifugation (PLC-C), (b) soaking of the sample (a), (PLC-C), in water followed by filtration, (c) dispersion of sample (b) in water followed by centrifugation, corresponding $N_2$ adsorption (red)-desorption (blue) isotherms (d, e, f) of (a, b, c) at 77 K and pore size distribution (inset).

The structural reversibility of PLC between the mesoscale order-disorder induced by filtration and centrifugation clearly shows the existence of flexibility in the layered stacking. Such an arrangement can be envisaged if the carbon interlayers are loosely held by pillar like structure. Formation of such pillars is possible in our case, since the glucose molecules trapped in space (in the stacking direction) between the clay nanobundles during the precipitation could provide pillar-like carbon structure on carbonization which could hold the carbon layers from collapsing (Figure 13).

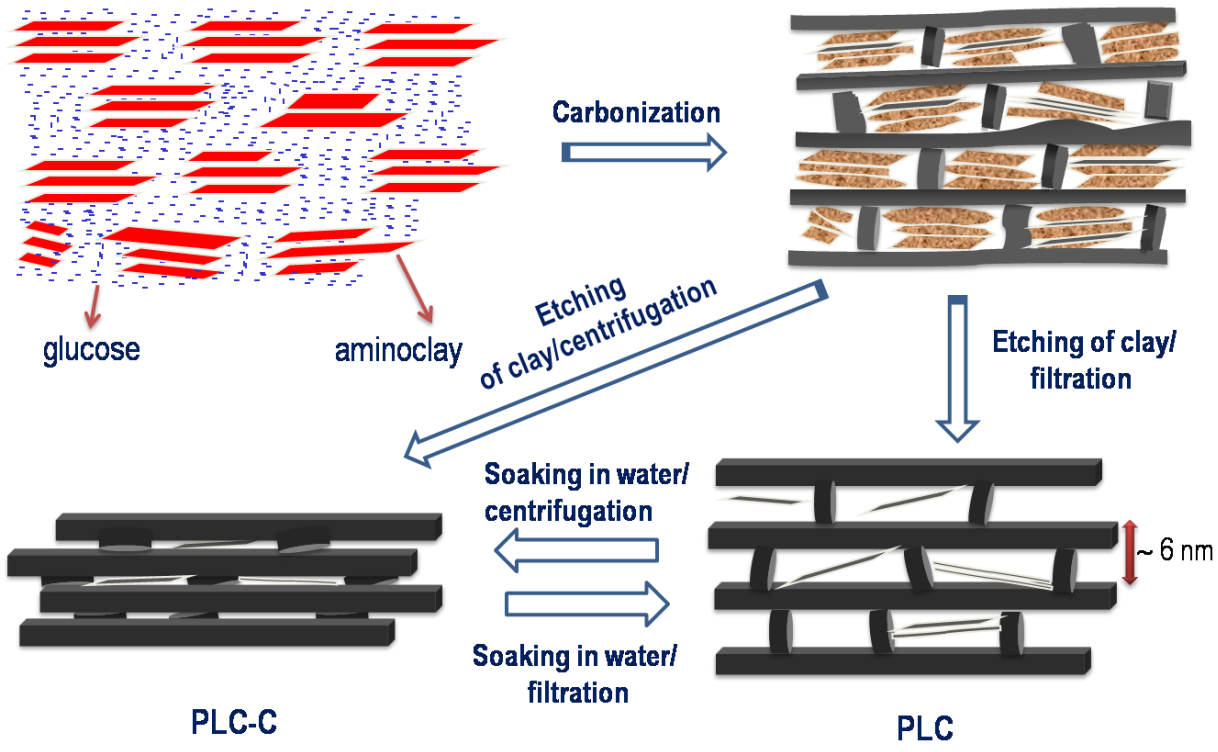


**Figure 13.** Schematic showing the step-wise formation of ordered and disordered layered flexible carbons.

The exact nature of chemical bonding connecting the pillars with the carbon layers is difficult to ascertain. We believe that the oxygen and nitrogen containing functional groups however play an important role in the loose connection of the pillar-like structures with the layers. The absence of pore-switching behaviour on

removal of the functional groups by high temperature heat treatment (above 700 $^{o}$C in $N_2$ environment or above 400 $^{o}$C for 6 h in $H_2$ environment) signifies the importance of the functional groups in the pore-switching behaviour. When there is no centrifugal force and the PLC was allowed to settle on its own in water, the layers can have a breathing space between them supported by the pillars and the water molecules in between. Similarly when the PLC-C sample is soaked in water the buckled, pillar-like carbon structures revert back to the original shape. TGA measurements show PLC holds about 10 wt% more water than the PLC-C (weight loss below 150$^{o}$C; Figure 14) which suggest that the interaction of water would be essential to reorient the pillar structures. However, when the centrifugal force (or shear force) is applied, the layers slide one over the other by buckling of the pillars which could squeeze out water between them.

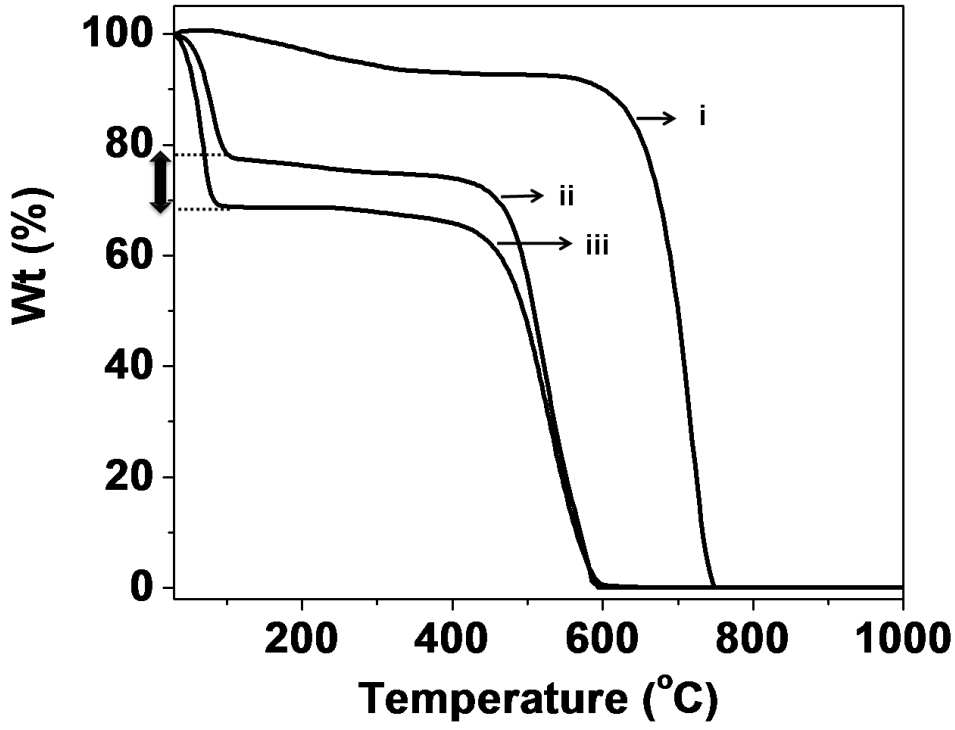


**Figure 14.** TGA curves for the graphite (i), PLC-C (ii) and PLC (iii) in presence of $O_2$ atmosphere.

**Dye Sorption experiment:**

The variation in pore size due to structural changes was demonstrated by the selective sorption of dye molecules of different molecular sizes (Congo red, alizarine yellow). The sizes of Congo red and alizarine yellow (Figure 15) were calculated to be 2.6 and 1.3 nm respectively (Experimental section, Computational details).

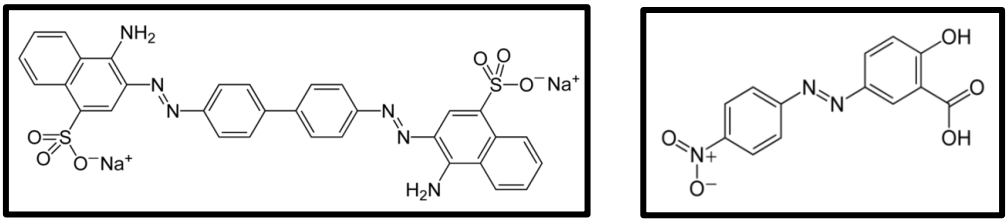


**Figure 15**. Chemical structures of Congo red (left) and alizarine yellow (right) respectively.

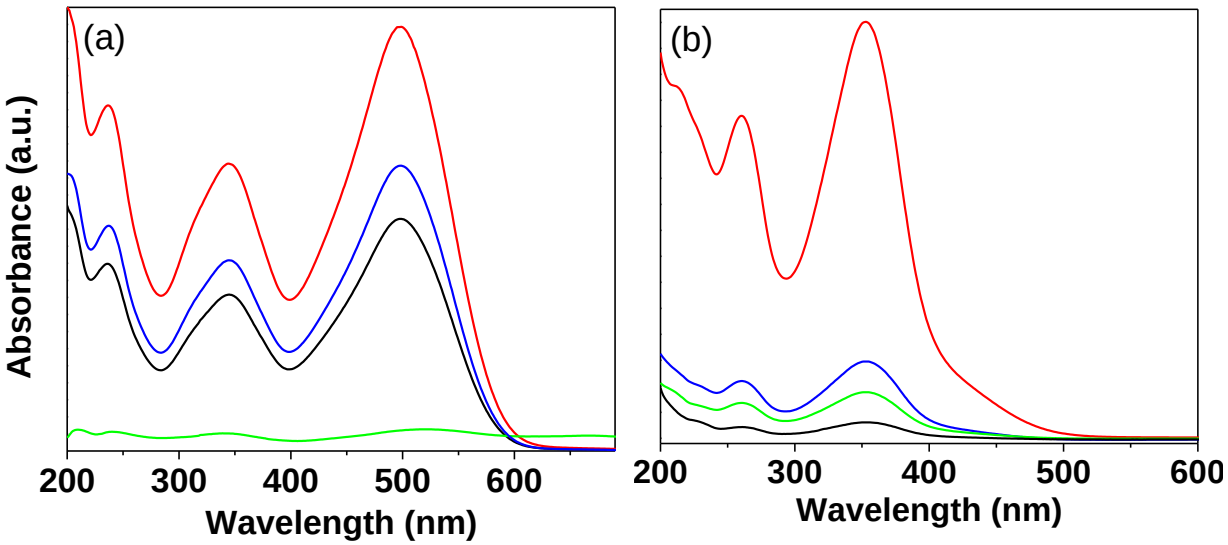


**Figure 16.** UV-Vis absorption spectra showing sorption of (a) Congo red (CR) and (b) alizarine yellow (AY) on various supports, PLC-C (blue), activated charcoal (black), PLC (green) and pure dye solution without support (red).

The as prepared PLC, PLC centrifuged (PLC-C) and an activated charcoal (AC) was compared for the dye sorption studies. The samples were soaked in the dye

solution for a period of 12 h and the extent of sorption was compared from the intensity of the absorption maxima of the remaining dye in the supernatant (Experimental Section).

The results are presented in Figure 16. The strong decrease in the absorption intensity of the Congo red solution for PLC compared to the PLC-C and AC samples clearly supports the presence of large pores (2.5 nm) which helps to maximize its sorption for Congo red. Since PLC-C and AC contain pores (only micropores) smaller than the size of the Congo red, they show poor sorption. On the other hand, alizarine yellow (1.3 nm), which is nearly half the size of Congo red molecule shows almost equal sorption (strong reduction in absorption intensity at 353 nm) for all the three samples.

As the sorption experiments on PLC and PLC-C were performed in aqueous medium there is a chance of reorientation of carbon pillars due to which PLC-C can be transformed into ordered structure (PLC). In order to validate this point, the following experiments were carried out. In the first case, PLC-C was directly soaked in Congo red solution, while in the second case PLC-C was soaked in water for 12 h followed by the addition of Congo red solution. The corresponding sorption profiles are presented in Figure 17. PLC-C directly soaked in Congo red solution shows a poor sorption capacity due to its microporous nature. While the same material PLC-C when soaked in water for 12 h followed by the addition of Congo red clearly shows more adsorption. The XRD pattern (not shown) for the same sample on filtration retains the mesoscale features in the low angle. Whereas, the PLC-C directly soaked in Congo-red solution for 12 h did not show any change in the low angle suggests that the Congo red adsorbed on the edges/surfaces of the PLC-C preventing the reorientation of the layers.

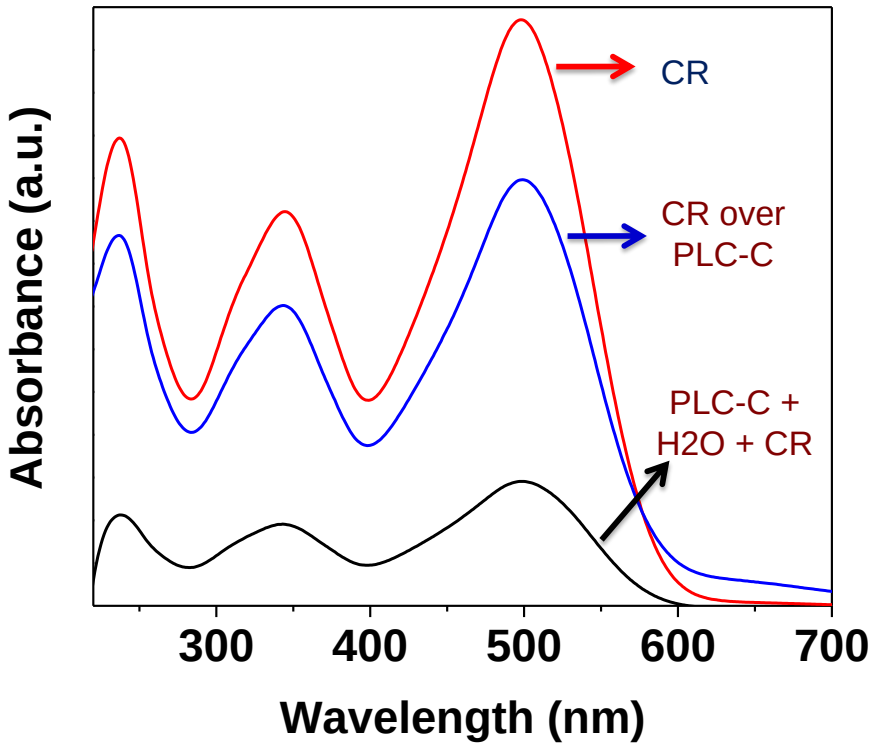


**Figure 17.** UV-Vis absorption spectra of pure Congo red (red) without porous support, Congo red over PLC-C (blue) and PLC-C soaked in water for 12 h followed by the addition of Congo red (black).

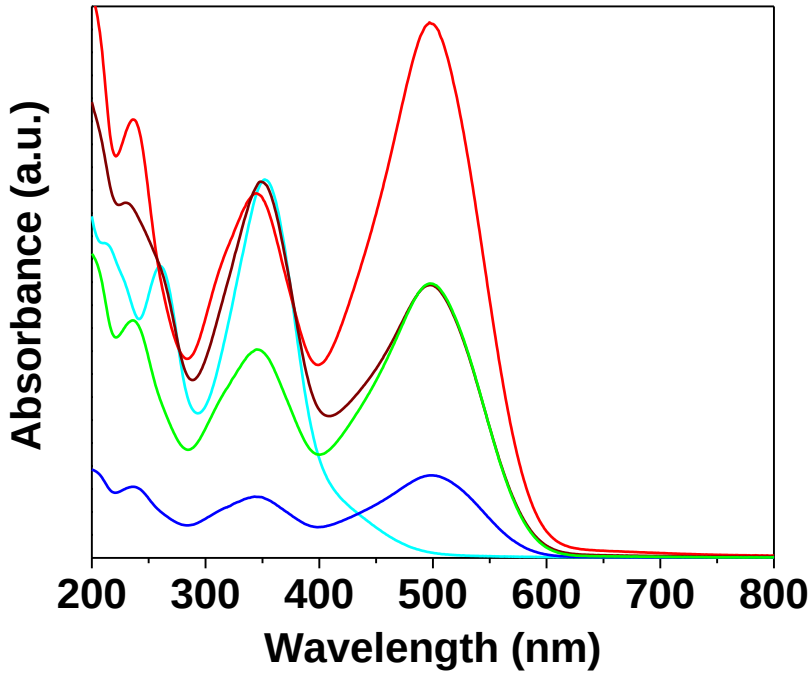


**Figure 18.** UV-Vis absorption spectra showing sorption of pure Congo red (red), pure alizarin yellow (cyan), mixed dye (brown) without porous support, mixed dyes in presence of PLC-C (green) and PLC (blue) supports.

Furthermore, the sorption behaviour of PLC and PLC-C in a mixed dye solution was performed by soaking each of them in a solution containing both Congo red and alizarin yellow. As expected, Congo red was selectively sorbed (absorbance at 499 nm) over PLC, while no sorption was observed in the case of PLC-C. Reasonable sorption was detected for smaller sized alizarin yellow molecule (absorbance at 350 nm) in both PLC and PLC-C, though PLC shows comparatively higher sorption behaviour for this smaller dye (Figure 18).

## 4.6. Conclusions:

In conclusion, we have shown a new synthetic route to obtain porous layered carbon (PLC) composed of nanographenes using aminoclay as the template. Carbonization of glucose within the aminoclay template leaves pillared carbon with flexible framework showing dynamic alteration for mesostructured periodicity. PLC shows remarkable hydrogen and carbon dioxide adsorptive properties due to its high surface area and high pore volume. The pore switching behaviour of PLC with respect to mechanical force (centrifugal force) was demonstrated by size selective sorption of dye molecules. We further envisage a possible use of these dynamic pores for selective screening of smaller biomolecules, dyes, toxic gases, etc.

## 4.7. References:


1. D. L. Nelson, M. M. Cox, *Lehninger Principles of Biochemistry*. **2000,** Chapter. 6 *Macmillan Press*.
2. M. E. Davis, *Nature*. **2002**, *417*, 813.
3. S. Horike, S. Shimomura, S. Kitagawa, *Nature Chemistry*. **2009**, *1*, 695.
4. a) J. Rabone, Y-F. Yue, S. Y. Chong, K. C. Stylianou, J. Bacsa, D. Bradshaw, G. R. Darling, N. G. Berry, Y. Z. Khimyak, A. Y. Ganin, P. Wiper, J. B. Claridge, M. J. Rosseinsky, *Science*. **2010**, *329*, 1053; b)A. Ziv, A. Grego, S. Kopilevich, L. Zeiri, P. Miro, C. Bo, A. Müller, I. A. Weinstock, *J. Am. Chem. Soc*. **2009**, *131*, 6380.
5. C. Serre, C. M-Draznieks, S. Surblé, N. Audebrand, Y. Filinchuk, G. Férey, *Science*. **2007**, *315*, 1828.
6. Y-J. Zhang, T. Liu, S. Kanegawa, O. Sato, *J. Am. Chem. Soc*. **2010**, *132*, 912.
7. S. K. Ghosh, W. Kaneko, D. Kiriya, M. Ohba, S. Kitagawa, *Angew. Chem. Int. Ed*. **2008**, *47*, 8843.
8. S. Bureekaew, S. Shimomura, S. Kitagawa, *Sci. Technol. Adv. Mater*. **2008**, *9*, 014108.
9. R. Ryoo, S. H. Joo, M. Kruk, M. Jaroniec, *Adv. Mater*.**2001**,*13*, 677.
10. F. Schüth, *Angew. Chem. Int. Ed*. **2003**, *42*, 3604.
11. M. S. Mauter, M. Elimelech, *Environ. Sci. Technol*, **2008**, *42*, 5843.
12. E. C. d. Oliveira, C. T. G. V. M. T. Pires, H. O. Pastore, *J. Braz. Chem. Soc.* **2006**, *17*, 16.
13. E. H. Falcao, F. Wudl, *J Chem Technol Biotechnol.* **2007**, *82*, 524.
14. T. Kyotani, *Carbon.* **2000**, *38*, 269.

15. a) J. S. Yu, S. Kang, S. B. Yoon, G. Chai, *J. Am. Chem. Soc.* **2002**, *124*, 9382, b) N. Yoshzawa, Y. Yamada, T. Furuta, M. Shiraishi, *Energy Fuels*. **1997**, *11*, 327, c) R. Leboda, H. S-Zieba, V. I. Bogillo, *Langmuir,* **1997**, *13*, 1211, d) H. Tamai, T. Kakii, Y. Hirota, T. Kumamoto, H. Yasuda, *Chem. Mater*. **1996**, *8,* 454, e) R. Ryoo, S. H. Joo, S. Jun, *J. Phys. Chem. B.* **1999**, *103*, 7743, f) S. Jun, S. H. Joo, R. Ryoo, M. Kruk, M. Jaroniec, Z. Liu, T. Ohsuna, O. Terasaki, *J. Am. Chem. Soc.* **2000**, *122,* 10712.
16. A. Bakandritsos, T. Steriotis, D. Petridis. *Chem. Mater.* **2004**, *16,* 1551, and references therein.
17. Y. Xia, Z. Yang, R. Mokaya, *Nanoscale*. **2010**, *2*, 639.
18. S. L. Burkett, A. Press,S. Mann, *Chem. Mater.* **1997**, *9,* 1071.
19. N. T. Whilton, S. L. Burkett, S. Mann, *J. Mater. Chem*. **1998**, *8*, 1927.
20. J. Patil, E. Muthusamy, S. Mann, *Angew. Chem. Int. Ed.* **2004**, *43*, 4928.
21. K. K. R. Datta, C. Kulkarni, M. Eswaramoorthy, *Chem. Commun*. **2010**, *46*, 616.
22. W. Humphrey, A. Dalke, K. Schulten, "*VMD - Visual Molecular Dynamics*", *J. Molec. Graphics*, **1996**, *14*, 33.
23. Frisch M. J. et al. **2003** *GAUSSIAN03*, Rev. A.1. Gaussian, Inc., Pittsburgh, PA.
24. C. N. R. Rao, K. Biswas, K. S. Subrahmanyam, A. Govindaraj, *J. Mater. Chem*. **2009**, *19*, 2457.
25. C. Ferrari, J. C. Meyer, V. Scardaci, C. Casiraghi, M. Lazzeri, F. Mauri, S. Piscanec, D. Jiang, K. S. Novoselov, S. Roth, A. K. Geim, *Phys. Rev. Lett*. **2006**, *97*, 187401.

26. A. Dato, V. Radmilovic, Z. Lee, J. Phillips, M. Frenklach, *Nano. Lett*. **2008**, *8*, 2012.
27. J. C-Delgado, J. M. R-Herrera, X. Jia, D. A. Cullen, H. Muramatsu, Y. A. Kim, T. Hayashi, Z. Ren, D. J. Smith, Y. Okuno, T. Ohba, H. Kanoh, K. Kaneko, M. Endo, H. Terrones, M. S. Dresselhaus, M. Terrones, *Nano. Lett*. **2008**, *8*, 2773.
28. D. Teweldebrhan, A. A. Balandin, *Appl. Phys. Lett*. **2009**, *94*, 013101.
29. D. Bom, R. Andrews, D. Jacques, J. Anthony, B. Chen, M. S. Meier, J. P. Selegue, *Nano. Lett*. **2002**, *2*, 615.
30. Ferrari. A. C, *Solid State Communications*.**2007**, *143*, 47.
31. a) M. S. Dresselhaus, A. Jorio, M. Hofmann, G. Dresselhaus, R. Saito, *Nano Lett.* 2010, *10*, 751; b) T. Enoki, K. Takai, V. Osipov, M. Baidakova, A. Vul, *Chem. Asian J*. **2009**, 4, 796.
32. J. C. Groen, L. A. A. Peffer, J. Pérez-Ramírez, *Microporous and Mesoporous Materials.* **2003**, *60*, 1.
33. K. Matsuoka, Y. Yamagishi, T. Yamazaki, N. Setoyama, A. Tomita, T. Kyotani, *Carbon.***2005**, *43*, 876.
34. R. Vaidhyanathan, S. S. Iremonger, G. K. H. Shimizu, P. G. Boyd, S. Alavi, T. K. Woo, *Science.* **2010**, *330*, 650**.**
35. a) E. Terrés, B. Panella, T. Hayashi, Y.A. Kim, M. Endo, J.M. Dominguez, M. Hirscher, H. Terrones, M. Terrones, *Chemical Physics Letters,* **2005,** *403,* 363, b) J. Burress, M. Kraus, M. Beckner, R. Cepel, G. Suppes, C. Wexler, P. Pfeifer, *Nanotechnology,***2009**, *20*, 204026, c) Z. Yang, Y. Xia, R. Mokaya, *J. Am. Chem. Soc*. **2007**, *129*, 1673.

36. a) M. G. Nijkamp, J. E. M. J. Raaymakers, A. J. van Dillen, K. P. de Jong, *Appl. Phys. A.* **2001**, *72*, 619, b) H. G. Schimmel, G. J. Kearley, M. G. Nijkamp, C. T. Visser, K. P. de Jong, F. M. Mulder, *Chem. Eur. J.* **2003**, *9*, 4764, c) M. Rzepka, P. Lamp, M. A. de la Casa-Lillo, *J. Phys. Chem. B*, **1998**, *102*, 10894, d) P. Sudan, A. Züttel, Ph. Mauron, Ch. Emmenegger, P. Wenger, L. Schlappbach, *Carbon*, **2003**, *41*, 2377.
37. D. Kamel, A. Sihem, C. Halima, S. Tahar, *Desalination*, **2009**, *250*, 76.

# Chapter 5

# Gold Nanoparticles Embedded in Mesoporous Carbon Nitride Stabilizer for Highly Efficient Three Component Coupling Reaction

## Summary

A simple methodology has been developed for the first time in fabricating highly dispersed Au nanoparticles with a size less than 7 nm on the surface of the mesoporous carbon nitride (MCN) support. The functionally rich MCN acts as stabilizing and size controlling agent without the need for any external agent or modification on the wall surface. We also demonstrate that the Au nanoparticles embedded on MCN are highly active, selective and recyclable catalysts for the three component coupling reaction of benzaldehyde, piperidine and phenyl acetylene for the synthesis of propargylamine.



A paper based on this study has been published in *Angew. Chem. Int. Ed.* **2010**, *49*, 5961-5965.

## 5.1. Introduction:

Engineering of controlled nanocomposite (hybrid) systems constitutes one of the most active and exciting fields combining biomimetics, self-assembly, soft chemistry and biology. During the past decades, the creativity of chemists and materials scientists provided a means for developing a wide variety of nanostructured materials with unprecedented functional properties.The rational design of these materials hold promise for obtaining small integrated chemical and physical devices for applications ranging from optical components to sensors or bioimplants.[1,2]

Numerous matrices have recently been used in order to confine metallic inclusions for applications in electrocatalysis, surface-enhanced Raman scattering (SERS), catalysis, separation, magnetism, optoelectronics and microelectronics.[3-11] However, the overall performance of these metal nanoparticles is dependent on the size, shape, crystal structure and the textural parameters.[12] Several methods including hydrogen reduction, porous support matrix, self-assembly and surfactant assisted process have been used for controlling the size and shape of the nanoparticles.[13-20] Among the methods used, the fabrication of the nanoparticles on the surface of porous support with a high surface area, especially nanoporous matrix, with different pore diameter and structure is quite attractive as they offer well-ordered pores with controllable size, high surface area and large pore volume.[21] The ordered nanopores dictate the size and shape of the nanoparticles as they are formed in the confined matrix whereas, the high surface area and large pore volume help the formation of high degree of homogenously dispersed nanoparticles on the surface of the support. Although the size of the nanoparticle can be controlled by nanoporous support

strategy, the stabilization and the reduction of the nanoparticles on the porous surface after their formation is quite challenging.

Generally, organic functional groups which are anchored or grafted on the surface of porous matrix are used for the stabilization and the reduction of the nanoparticles.[15] The derivatization of mesoporous materials with well-defined organic moieties represents a unique tool for designing hybrid mesoporous assemblies. However, the functionalization of the mesoporous support involves multiple-steps which is a time consuming process, in turn poisoning the catalytic active sites of both the support and the particles and sometimes even damage the structure and the textural properties of the supports. Thus, it is highly imperative to look for an alternative mesoporous support with inbuilt functional groups and excellent textural characteristics for the fabrication of highly stable nanoparticles.

Recently, Vinu et al.[22] reported the synthesis of mesoporous carbon nitride (MCN) with ordered pores and controlled textural parameters through a simple polymerization reaction between carbon tetrachloride and ethylene diamine by using mesoporous silica (SBA-15) as sacrificial template. The resultant 2D ordered hexagonal array of mesoporous carbon nitride possesses inbuilt $-NH_2$ and -NH groups on the mesoporous walls which in principle can be an ideal scaffold for stabilizing metal nanoparticles.

**Importance of $A^3$-coupling reactions:**

Demands for facile and efficient generation of complex and diverse drug like small molecules, continue to stimulate the design and development of conceptually innovative strategies in the synthetic community.[23] One-pot multi component coupling reactions are an attractive strategy in organic synthesis and are highly

valued among synthetic methodologies, as several elements of diversity can be introduced in a single step into a molecule.[24]

Propargylamines are major skeletons[25] or synthetically versatile and key intermediates [26] for the preparation of many nitrogen containing biologically active compounds such as $\beta$-lactams, oxotremorine analogues, confirmationally restricted peptides, isosteres and important structural elements of natural products and therapeutics drug molecules.[26] These compounds have traditionally been synthesized by nucleophilic attack of lithium acetylides, butyllithium, lithium diisopropylamide (LDA), organomagnesium reagents or their derivatives.[25-27]An alternative atom-economical approach to their synthesis is to perform this type of reaction by a catalytic coupling of alkyne, aldehyde and amine ($A^3$ coupling) by C-H activation, where water is the only theoretical by-product by employing various transition metal catalysts under homogenous conditions.[28]

However, this process becomes less attractive because of the need of stoichiometric quantities of the reagents and their high moisture sensitivity. Recently metal nanoparticles, especially gold which exhibit a high alkynophilicity and offer high surface to volume ratio, have been exploited to activate the C-H bond of the terminal alkyne.[28] Nevertheless, the metal nanoparticles in its pure form tend to agglomerate which limit their efficiency in the catalytic process. Thus, encapsulation of metal nanoparticles onto high surface area mesoporous hosts can be effective in preventing the agglomeration in turn high activity.

## 5.2. Scope of the present investigation:

The basic sites of mesoporous carbon nitride are comprehensively explored by various research groups for applications in the fields of catalysis (basic catalyst and photocatalyst for water splitting), metal free activation of $CO_2$, hydrogen storage

and fuel cells.[29] Nevertheless the powerful capping ability of MCN stabilizer towards the fabrication of metal nanoparticles is not investigated, which is the driving motivation for the present work. MCN possessing inbuilt -$NH_2$ and -NH groups on the mesoporous walls served as a perfect host for the creation of Au nanoparticles. We demonstrate the fabrication of highly dispersed Au nanoparticles with a size less than 7 nm on the surface of the MCN support which acts as stabilizing, size controlling and reducing agent without the need for any external agent and the surface modification (Figure 1). The hybrid material containing Au nanoparticles encapsulated in MCN stabilizer show retention of mesostructural order which is supported unambiguously by various characterization techniques. Furthermore, the Au nanoparticles embedded on MCN are highly active, selective and recyclable catalyst in the three component coupling reaction of benzaldehyde, piperidine and phenyl acetylene for the synthesis of propargylamine which is an intermediate for the construction of nitrogen containing biologically active molecules and for the synthesis of polyfunctional amino derivatives.[27]

## 5.3. Experimental Section:

### (a) Materials:

Pluronic P123, HCl, HF, tetraethylorthosilicate (TEOS), ethylene diamine, carbon tetrachloride, $HAuCl_4$, $NaBH_4$, benzaldehyde, p-nitrobenzaldehyde, p-chlorobenzaldehyde, piperidine and phenyl acetylene were purchased at an analytical pure grade and were used without any further purification. Millipore water and ethanol were used wherever essential.

**(b) Synthesis of SBA-15-150:**

In a typical synthesis, 4 g of pluronic P123 was added to 30 g of water. After stirring for a few hours, a clear solution was obtained. Thereafter, 120 g of 2 M HCl was added and the solution was stirred for another 2 h. Then, 9 g of tetraethylorthosilicate was added and the resulting mixture was stirred for 24 h at 40 $^{o}$C, and subsequently heated for 48 h at 150 $^{o}$C hydrothermally. The solid product was recovered by filtration, washed several times with water and dried overnight at 100 $^{o}$C. Finally, the product was calcined at 540 $^{o}$C to remove the template.

**(c) Preparation of the MCN:**

MCN material was prepared by the following method. In a typical synthesis the calcined SBA-15-150 (0.5 g) prepared at a synthesis temperature of 150 °C, was added to a mixture of ethylene diamine, EDA (1.75 g) and carbon tetrachloride, CTC (2.99 g). The resultant mixture was refluxed and stirred at 90 °C for 6 h. Then, the obtained dark-brown-colored solid mixture was placed in a drying oven for 12 h and ground into fine powder. The template-carbon nitride polymer composite were then heat treated in a nitrogen flow of 100 mL per minute at 600 °C with a heating rate of 5 °C per minute for 5 h to carbonize the polymer. The MCN was recovered after dissolution of the silicaframework in 5 wt% hydrofluoric acid, by filtration, repetitive washing with ethanol and drying at 100 °C.

**(d) Preparation of Au nanoparticles within MCN:**

$HAuCl_4$ was used as metallic salt precursor for the preparation of Au nanoparticles. Typically 20 mg of MCN is dispersed in 2 ml of water by mild sonication for 2 minutes. To this 1.5 ml of 2 mM $HAuCl_4$ solution was added

followed by the addition of 1 ml of 0.l M $NaBH_4$. The obtained mixture was washed thoroughly with distilled water and finally dried in vacuum oven at 60 °C.

**(e) Control experiment with nanoporous carbon:**

20 mg of CMK-3 150 was taken in a sample vial followed by the addition of 2 ml distilled water under sonication for 5 minutes. To this 1.5 ml of 2 mM $HAuCl_4$ solution was added followed by the addition of 1 ml of 0.l M $NaBH_4$. The obtained mixture was washed thoroughly with distilled water and finally dried in vacuum oven at 60 °C.

**(f) Catalysis with Au nanoparticles encapsulated MCN ($A^3$-coupling reaction):**

In a typical experiment, 50 mg of Au nanoparticles encapsulated MCN was added to a mixture of aldehyde (1 mmol), amine (1.2 mmol) and alkyne (1.3 mmol) in 2 mL of toluene. The resulting mixture was allowed to stir in toluene at 100 °C over a period of 12-24 h (Scheme 2). After complete disappearance of aldehyde as monitored by thin layer chromatography (TLC), the mixture was diluted with toluene and centrifuged to obtain clear solution, which was analyzed by GC. The desired product was isolated by silica gel column chromatography using a gradient mixture of ethyl acetate/*n*-hexane (1:9) as eluent. The product thus obtained was characterized by $^1$H NMR spectroscopy.

## 5.4. Characterization Techniques:

**X-ray Diffraction:**

X-ray diffraction (XRD) patterns of the mesoporous carbon nitride materials were collected on a Rigaku diffractometer using Cu Kα (λ = 0.154 nm) radiation. The diffractograms were recorded in a 2θ range from 0.8 to 10º with a 2θ step size of 0.01 and a step time of 1 s.

**Nitrogen adsorption and desorption isotherms:**

$N_2$ adsorption and desorption isotherms were measured at 77K on a Quantachrome Autosorb1sorption analyzer. All samples were outgassed at 250 ºC for 5 h prior to the nitrogen-adsorption measurements. The specific surface area was calculated using the Brunauer-Emmett-Teller (BET) method. The pore size was obtained from the adsorption branch of the nitrogen isotherms using the Barrett-Joyner-Halenda method.

**Field emission scanning electron microscopy:**

The morphology of the materials prepared at different synthesis conditions was observed on a Hitachi S-4800 field emission scanning electron microscope using an accelerating voltage of 5.0 kV.

**Transmission electron microscopy:**

The TEM images were obtained using a JEOL-3000F and a JEOL-3100FEF field emission high-resolution transmission electron microscope equipped with a Gatan-766 electron energy-loss spectrometer. The preparation of the samples for TEM analysis involved sonication in ethanol for 2 to 5 min and deposition on a copper grid. The accelerating voltage of the electron beam was 200 kV.

## 5.5. Results and Discussion:

The preparation of mesoporous carbon nitride from mesoporous silica (SBA-15-150) and fabrication of nanosize gold nanoparticles on the nanoporous structure of carbon nitride matrix without any stabilizing agent is illustrated in Figure 1a. Firstly, mesoporous carbon nitride is prepared by the simple polymerization reaction between ethylene diamine and carbon tetrachloride within the pores of mesoporous silica. The wall structure provides (Figure 1a) a uniform distribution of nitrogen atoms throughout the carbon matrix (functional centers) which can host platform for

the generation of metal and metal oxide nanoparticles. Secondly, the nanopore directed growth of Au nanoparticle with the help of support with inbuilt groups acting as a stabilizing agent is quite unique in controlling the size, shape and avoiding the agglomeration of the nanoparticles.

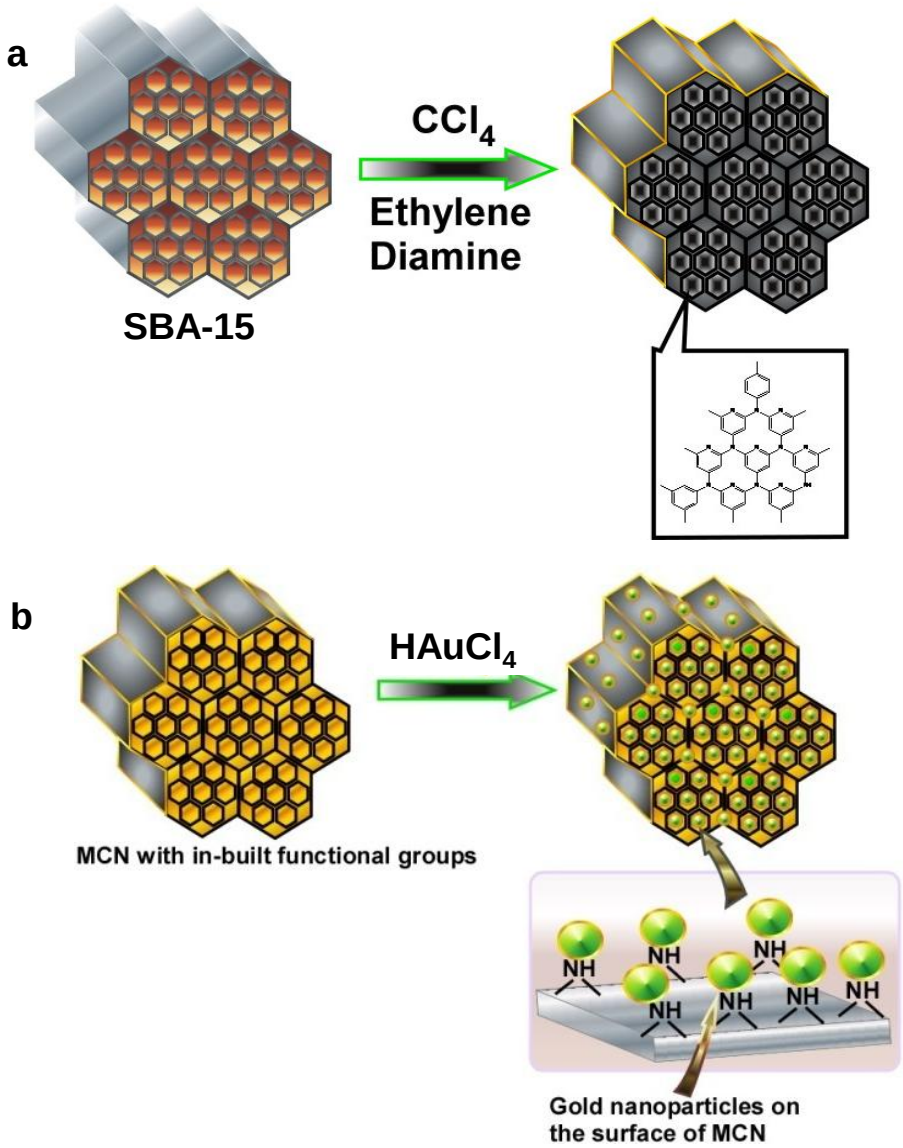


**Figure 1**. a) Scheme illustrating the preparation of mesoporous carbon nitride using SBA-15 templateand b) encapsulation of gold nanoparticles over MCN with in-built functional groups without any external stabilizing agent.

As can be seen in Figure 1b, the auric chloride ions can be adsorbed within the pores of MCN by means of sonication. The nanopores of the carbon nitride could control the size of the Au nanoparticles as they grow within the restricted environment of the pore channels whereas, the inbuilt functional groups such as $-NH_2$ or -NH groups present on the wall structure of the carbon nitride could act as stabilizing agent by providing the anchoring and heterogeneous surface for the formation of highly dispersed Au nanoparticles without any agglomeration. It should also be noted that the presence of functional amine groups on the MCNs helps the reduction of the Au nanoparticles inside the nanopores. The reduction of chloro auric salt is further enhanced by the addition of small amount of reducing agent.

The pore-structure ordering of the MCN materials before and after encapsulation of Au nanoparticles along with the parent silica templates was investigated by powder XRD measurements. SBA-15-150 exhibits three well-ordered peaks (100), (110) and (200) that can be indexed on a two-dimensional hexagonal lattice (*p6mm*) (Figure 2a). Both the samples (MCN-150 and Au-MCN) show a sharp peak at lower angle, indicating that the hexagonally ordered porous structure of the MCN remains intact even after the encapsulation and stabilization of Au nanoparticles (Figure 2 b, c). A significant reduction in the intensity of the lower angle peak is observed for MCN loaded with Au nanoparticles. This can be attributed to the pore filling of Au nanoparticles which are formed along the nanochannels of the carbon nitride and also due to the difference on the scattering contrasts of the pores and the walls, confirming that Au nanoparticles are indeed formed inside the nanochannels of the carbon nitride.[30] It should be noted that the unit cell constant of the sample before and after the encapsulation of Au nanoparticles is almost same.

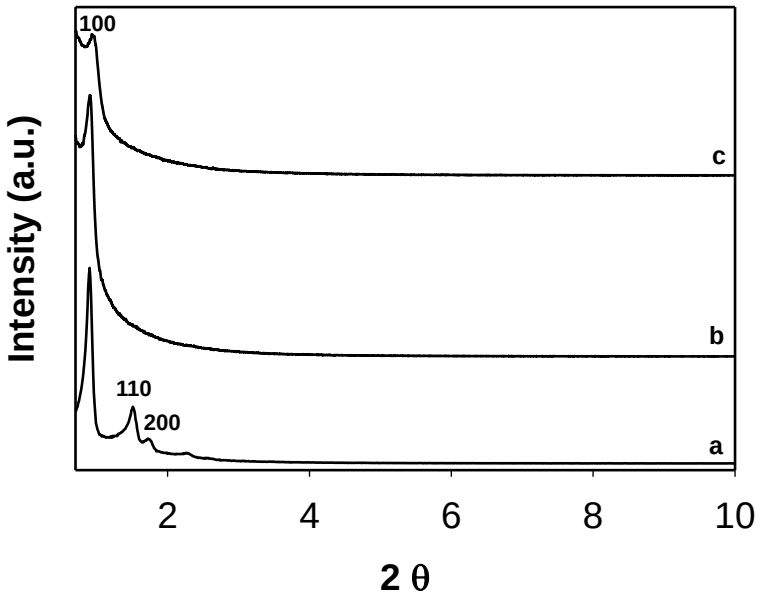


**Figure 2**. Low angle powder XRD patterns of a) SBA-15-150, b) MCN-1-150 and c) Au nanoparticles encapsulated MCN materials.

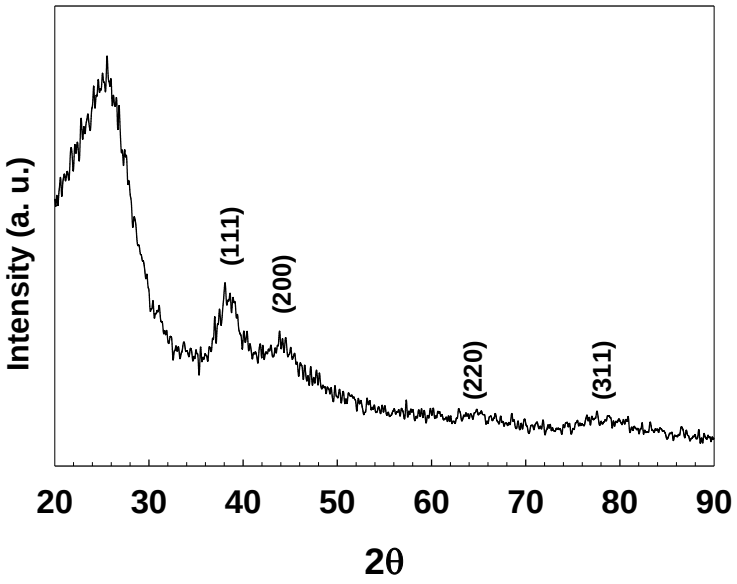


**Figure 3.** Wide-angle powder XRD pattern of Au nanoparticle encapsulated MCN.

The wide-angle X-ray diffraction pattern of the Au nanoparticle loaded MCN exhibits four peaks which could be indexed as the (111), (200), (220) and (311) reflections of the face-centered cubic structure of crystalline Au(0) (Figure 3). Among the peaks observed, the intensity of the (111) peak is the highest, indicating

that (111) plane was the predominant crystal facet. The peaks are very broad and weak, suggesting the formation of the ultra small nanocrystalline Au particles inside the pore channels of carbon nitride. The absence of sharp and intense peaks at higher angles further confirms that no large particles are formed on the external surface of the support. These results reveal the pore size controlled growth of the nanoparticle in the confined matrix.

The structure and the morphology of Au nanoparticles inside MCN were clearly examined from scanning electron microscopy (Figure 4a). White colored dots which correspond to the gold nanoparticles are uniformly distributed and anchored along the heterogeneous nanoporous surface of the carbon nitride (Figure. 4a). It is interesting to note that all the particles are uniform in size and shape and densely packed inside the nanochannels of carbon nitride. The agglomeration of the Au nanoparticles was not observed in the FESEM image, revealing that the inbuilt functional groups in the MCN firmly anchor the formed nanoparticles.

TEM image of the Au nanoparticle encapsulated MCN is shown in Figure 4b. It can be observed from Figure 4b that a regular arrangement of dark spherical spots which correspond to Au nanoparticles is clearly observed along the nanochannels of the support. Interestingly, a linear arrangement of mesochannels which are arranged in a regular interval is also clearly seen, suggesting that mesostructure of the support is stable even after the formation of Au nanoparticles.

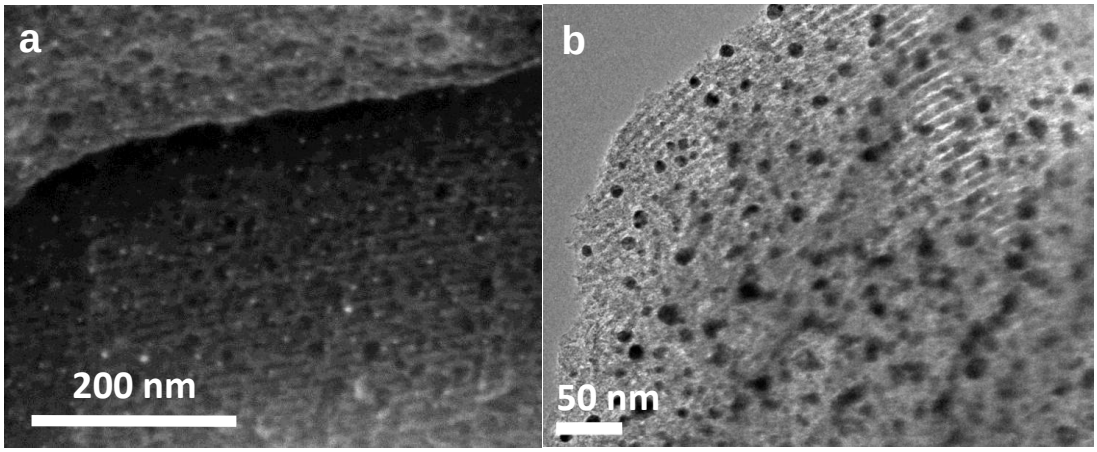


**Figure 4.** (a) Field emission scanning electron microscope (FESEM) and (b) Transmission electron microscope (TEM) image of Au nanoparticles encapsulated MCN.

The average size of the Au nanoparticles obtained from the TEM image is found to be approximately 7 nm. It should be noted that the size of the particles which are formed on the external surface of the support as seen in the TEM image and anchored by the terminal functional groups is slightly larger than that of the particles formed inside the mesochannels.

Figure 5 shows the energy-dispersive X-ray (EDX) pattern and the elemental mapping of the Au nanoparticles encapsulated on the MCN. Peaks for the elements C, N and Au are clearly seen in the EDX spectrum. It should be noted that there is no peak of Cl in the EDX spectrum, indicating the high purity of the Au nanoparticles. The amount of Au present in the sample is 0.05 atomic percent which matches well with results from inductively coupled plasma mass spectroscopy (ICP-MS) analysis report. Elemental mapping revealed that the Au atoms are uniformly distributed in the sample (Figure 5 inset).

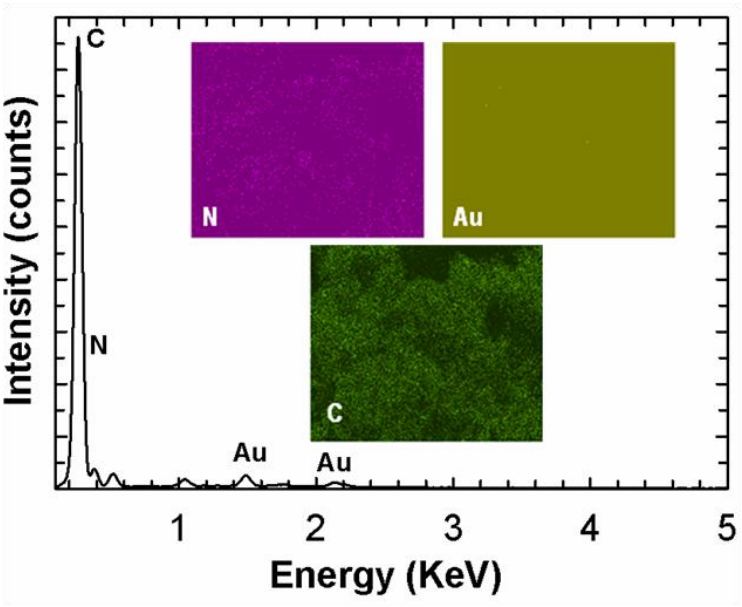


**Figure 5.** EDX pattern of Au nanoparticles encapsulated MCN. Inset shows the elemental mapping of the same sample.

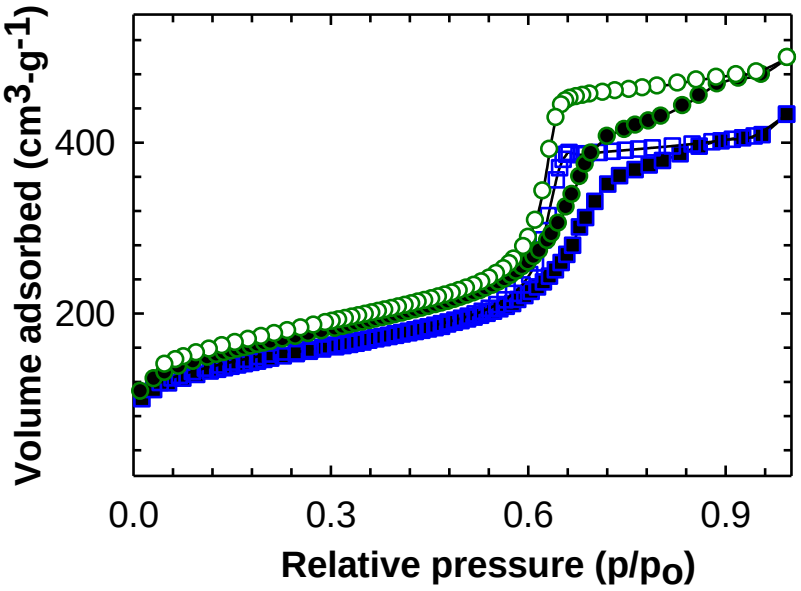


**Figure 6.** Nitrogen adsorption-desorption isotherms of (●) pure MCN and (■) Au nanoparticles encapsulated MCN.

The encapsulation of the Au nanoparticles over the mesochannels of the MCN stabilizer has made a significant change in the textural parameters of the materials. Figure 6 shows the nitrogen adsorption-desorption isotherms of the MCN before and

after the encapsulation of the Au nanoparticles. The isotherms of both the samples are of Type IV with a H1 hysteresis loop, which are typically observed for the mesoporous materials. The pore size distribution for both the samples reveals that the pores are highly ordered and have the narrow pore size distribution (not shown). In addition, the shape of the isotherm and the hysteresis loop of the two samples are almost identical. These results reveal that the highly ordered structure is maintained even after the encapsulation of Au nanoparticles. A little change in the specific surface area and the specific pore volume of the sample after the Au encapsulation is observed. The specific surface area was found to decrease from 580 $m^2/g$ for pure MCN to 508 $m^2/g$ for Au nanoparticle encapsulated MCN whereas, the specific pore volume decreases from 0.74 to 0.63 $cm^3g^{-1}$ for the same samples. This result could be mainly due to the formation of the nanoparticles inside the pores. The absence of an abrupt change in the pore volume and surface area of the support after the Au encapsulation further reveals that pores of the support are not blocked by the Au particles whose size is larger than the pore size of the support, revealing that the inbuilt basic sites or groups on the support materials do not allow the agglomeration of the nanoparticles but instead stabilize or anchor them on the pore wall structure. However, the size of the nitrogen adsorbate molecule is too small which can also penetrate inside the pore channels of the support encapsulated with the metal nanoparticles via the microporous channels connected between the primary mesopores of the support. Thus, it is also possible that the reduction of the textural parameters of the support may be originated from the blockage caused by the encapsulated nanoparticles with the size similar to that of the pore size of the support.

To make it clear the real stabilizing role of the inbuilt amine or basic sites, we have conducted a control experiment with pure mesoporous carbon without any nitrogen atom in the wall structure. Mesoporous carbon CMK-150 with the pore size of 6.5 nm was used as the support for the encapsulation of the Au nanoparticles.

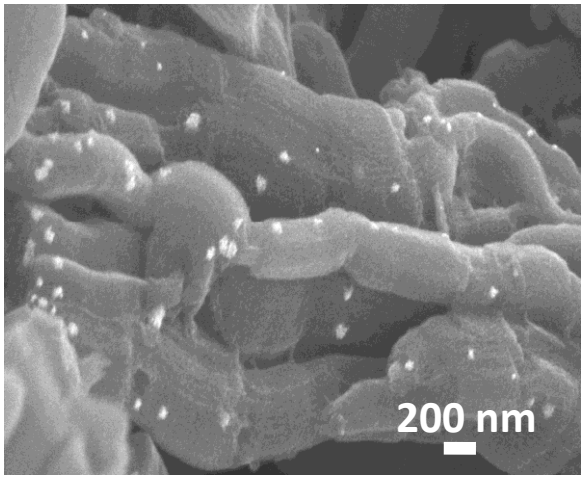


**Figure 7.** FESEM image of Au nanoparticle encapsulated mesoporous carbon without any nitrogen content.

It has been observed that a series of Au nanoparticles, size ranging from 20-140 nm are formed (Figure 7). Most of the particles are formed on the external surface of the mesoporous carbon but not inside the mesoporous channels due to agglomeration. These results reveal the vital role of nitrogen in the MCN matrix in preventing the aggregation of nanoparticles and stabilize the formed nanoparticles inside the mesoporous channels (Scheme 1b).

**Au-MCN catalyzed $A^3$ coupling reactions:**

Herein we used for the first time highly dispersed Au nanoparticle encapsulated over MCN (Au-MCN) stabilizer as the catalyst for the synthesis of propargylamines via $A^3$-coupling reaction. The catalytic efficiency of Au-MCN was tested in three component coupling of aldehyde, amineand alkyne. Initially, benzaldehyde, piperidine and phenylacetylene were mixed with CN-Au-150 (20 mg) in toluene.

Although the reaction proceeded smoothly in toluene at 100 $^{o}$C, a low yield of the product was obtained even after 24 h. Interestingly the yield of the final product significantly increases with increasing the loading of the catalyst from 20 to 50 mg. Hence further experiments were carried out with the catalyst weight of 50 mg for the treatment of benzaldehyde, piperidine and phenyl acetylene.

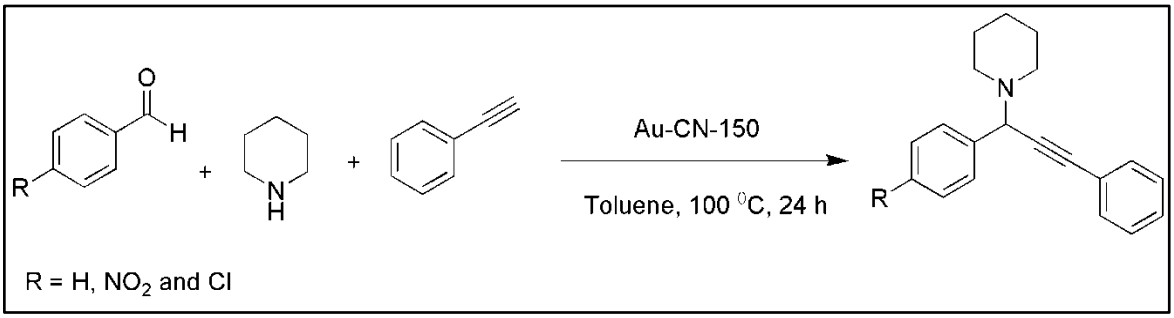


**Figure 8.** Catalytic activity of Au nanoparticle encapsulated MCN in the three component coupling reaction of benzaldehyde, piperidineand phenyl acetylene for the synthesis of propargylamine.

| Substrate | Conversion (%) | | Selectivity (%) | |
|---|---|---|---|---|
| | 12 h | 24 h | 12 h | 24 h |
| benzaldehyde | 63.8 | 96.2 | 79.2 | 64.4 |
| p-nitrobenzaldehyde | 40.7 | 55.6 | 70.3 | 76.7 |
| p-chlorobenzaldehyde | 25.5 | 35.7 | 47.3 | 60.0 |

**Table 1.** Catalytic activity of Au nanoparticle encapsulated MCN in the $A^3$-coupling reaction for the synthesis of propargylamines.

The reaction was completed in 24 h with a yield of the final product of almost 96%, as analyzed by gas chromatography. These results prompted us to study the substituent effects on the aromatic ring. Interestingly, electron deficient aromatic

aldehydes like *p*-nitrobenzaldehyde also gave reasonable conversion under similar conditions. Even, halo substituted benzaldehyde e.g. *p*-chlorobenzaldehyde also furnished the desired product in good yield. The results are summarized in Table 1. It should be noted that no conversion was found in the absence of catalyst or using only pure MCN catalyst under identical conditions. These results clearly signify the importance of the encapsulation of the Au nanoparticles inside the mesochannels of the MCN stabilizer.

## 5.6. Conclusions:

In conclusion, we demonstrate a simple approach for the encapsulation of Au nanoparticles over highly ordered MCN with inbuilt functionalities which acts as stabilizing, reducing and pore-size-controlling agent without addition of any external agent or surface modification of the wall structure of the support. The ultra small Au nanoparticles are highly dispersed and anchored firmly on the functional moieties in the surface of the MCN, which helps the formation of the particle by an in-situ reduction process. We also demonstrated that the Au nanoparticle encapsulated MCN can be used as a highly active, selective and recyclable heterogenous catalyst for coupling benzaldehyde, piperidine and phenyl acetylene for the synthesis of propargylamine. This method is quite simple and the strategy can simply be extended for the fabrication of various other metal and metal oxide nanoparticles over MCN with different structure and pore diameters, which could have many potential applications in separation, hydrogen storage, drug delivery, electrode materials for fuel cells and catalytic organic transformations.

## 5.7. References:


1. M. C. Fuertes, M. Marchena, M. C. Marchi, A. Wolosiuk, G. J. A. A. Soler-Illia, *Small*. **2009**, *5*, 272.
2. a) A. Calvo, M. C. Fuertes, B. Yameen, F. J. Williams, O. Azzaroni, G. J. A. A. Soler-Illia, *Langmuir*. **2010**, *26*, 5559, b) K. E. Geckeler, E. Rosenberg, *Functional Nanomaterials*, **2006**, *American Scientific Publishers*, c) D. Vollath, *Nanomaterials: An Introduction to Synthesis, Properties and Applications*, **2008**, *Wiley-VCH*.
3. L. Zhang, Y. H. Shen, A. J. Xie, S. K. Li, C. Wang, *J. Mater. Chem*. **2008**, *18*, 1196.
4. T. Hasell, L. Lagonigro, A. C. Peacock, S. Yoda, P. D. Brown, P. J. A. Sazio, S. M. Howdle, *Adv. Funct. Mater*. **2008**, *18*, 1265.
5. a) G. Schmid, *Nanoparticles: From theory to Applications*, **2004**, *Wiley-VCH*, b) K. Philippot, B. Chaudret, C. R. Chim. **2003**, *6*, 1019, c) B. Chaudret, *Top. Organomet. Chem.* **2005**, *16*, 233.
6. a) G. J. Hutchings, *Catal. Today*. **2005**, *100*, 55, b) G. J. Hutchings, M. Haruta, *Appl. Catal. A.* **2005**, *291*, 2, c) M. Haruta, *Gold. Bull.* **2004,** *37*, 27.
7. F. L. Didier Astruc, J. R. Aranzaes, *Angew. Chem., Int. Ed.* **2005,** *44*, 7852 and references therein.
8. a) C. T. Campbell, *Science*. **2004**, *306*, 234, b) J. Sun, X. Bao, *Chem. Eur. J*. **2008**, *14*, 7478, c) F. Wen, W. Zhang, G. Wei, Y. Wang, J. Zhang, M. Zhang, L. Shi, *Chem. Mater*. **2008**, *20*, 2144, d) X. Chen, Y. Hou, H. Wang, Y. Cao, J. He, *J. Phys. Chem. C.* **2008**, *112*, 8172.

9. a) C-K. Tsung, W. Hong, Q. Shi, X. Kou, M. H. Yeung, J. Wang, G. D. Stucky, *Adv. Funct. Mater*. **2006**, *16*, 2225, b) M. Schierhorn, S. J. Lee, S. W. Boettcher, G. D. Stucky, M. Moskovits. *Adv. Mater*. **2006**, *18*, 2829.
10. a) X. Huab, S. Dong, *J. Mater. Chem*. **2008**, *18*, 1279, b) R. W. Murray, *Chem. Rev*. **2008**, *108*, 2688.
11. Y-G. Guo, J-S. Hu, L-J. Wan, *Adv. Mater*. **2008**, *20*, 2878.
12. a) J. S. Beck, J. C. Vartuli, W. J. Roth, M. E. Leonowicz, C. T. Kresge, K. D. Schmitt, C. T. W. Chu, D. H. Olson, E. W. Sheppard, *J. Am. Chem. Soc*. **1992**, *114*, 10834, b) D. Zhao, Q. Huo, J. Feng, B. F. Chmelka, G. D. Stucky, *J. Am. Chem. Soc*. **1998**, *120*, 6024.
13. K. Wikander, A. B. Hungria, P. A. Midgley, A. E. C. Palmqvist, K. Holmberg, J. M. Thomas, *J. of Colloid Interface Sci*. **2007**, *305*, 204.
14. V. Hulea, D. Brunel, A. Galarneau, K. Philippot, B. Chaudret, P. J. Kooyman, F. Fajula, *Microporous and Mesoporous Materials*. **2005**, *79***,** 185.
15. a) C-M. Yang, P-h. Liu, Y-f. Ho, C-y Chiu, K-j. Chao, *Chem. Mater*. **2003,** *15*, 275, b) E. Besson, A. Mehdi, C. Reyé, R. J. P. Corriu, *J. Mater. Chem.* **2009**, *19*, 4746.
16. Y. Zhang, F. L-Y. Lam, X. Hu, Z. Yan, P. Sheng, *J. Phys. Chem. C.* **2007**, *111*, 12536.
17. N. Zheng, G. D. Stucky, *J. Am. Chem. Soc***. 2006**, *128*, 14278.
18. W. Huang, J. N. Kuhn, C-K Tsung, Y. Zhang, S. E. Habas, P. Yang, G. A. Somorjai, *Nano Lett.* **2008**, *8*, 2027.
19. M. Boutros, A. D-Nowicki, A. Roucoux, L. Gengembre, P. Beaunier, A. Gédéona, F. Launay, *Chem. Commun*. **2008**, 2920.

20. A. K. Prashar, R. P. Hodgkins, R. Kumara, R. N. Devi, *J. Mater. Chem.* **2008**, *18*, 1765.

21. A. Fukuoka, T. Higuchi, T. Ohtake, T. Oshio, J-i. Kimura, Y. Sakamoto, N. Shimomura, S. Inagaki, M. Ichikawa, *Chem. Mater.* **2006,** *18*, 337.

22. a) A. Vinu, K. Ariga, T. Mori, T. Nakanishi, S. Hishita, D. Golberg, Y. Bando, *Adv. Mater*. **2005**, *17*, 1648, b) A. Vinu, *Adv. Funct. Mater*. **2008**, *18*, 816.

23. Q. Zhang, M. Cheng, X. Hu, B-G. Li, J-X. Ji, *J. Am. Chem. Soc*. **2010**, *132*, 7256.

24. a) C. Cao, Y. Shi, A. L. Odom, *J. Am. Chem. Soc.* **2003**, *125*, 2880, b) S. Kamijo, Y. Yamamoto, *J. Am. Chem. Soc*. **2002**, *124*, 11940, c) A. Domling, I. Ugi, *Angew. Chem*. **2000**, *112*, 3300, d) I. Ugi, A. Domling, B. Werner, *J. Heterocycl. Chem*. **2000**, *37*, 647, e) R. W. Armstrong, A. P. Combs, P. A. Tempst, S. D. Brown, T. A. Keating, *Acc. Chem. Res*. **1996**, *29*, 123.

25. a) A. A. Boulton, B. A. Davis, D. A. Durden, L. E. Dyck, A. V. Juorio, X. M. Li, I. A. Paterson, P. H. Yu, *Drug Dev. Res.* **1997**, *42*, 150, b) M. A. Huffman, N. Yasuda, A. E. DeCamp, E. J. J. Grabowski, *J. Org. Chem*. **1995**, *60*, 1590.

26. a) M. Miura, M. Enna, K. Okuro, M. Nomura, *J. Org. Chem*. **1995**, *60*, 4999, b) A. Jenmalm, W. Berts, Y. L. Li, K. Luthman, I. Csoregh, U. Hacksell, *J. Org. Chem*. **1994**, *59*, 1139, c) B. Nilsson, H. M. Vargas, B. Ringdahl, U. Hacksell, *J. Med. Chem. Soc.* **1992**, *35*, 285, d) M. Konishi, H. Ohkuma, T. Tsuno, T. Oki, G. D. VanDuyne, J. Clardy, *J. Am. Chem. Soc*. **1990**, *112*, 3715.

27. a) G. Dyker, *Angew. Chem*. **1999**, *38*, 1698, b) I. Naota, H. Takaya, S. I. Murahashi, *Chem. Rev*. **1998**, *98*, 2599.

28. a) X. Zhang, A. Corma, *Angew. Chem. Int. Ed.* **2008**, *47*, 4358, b) M. Kidwai, V. Bansal, A. Kumar, S. Mozumdar, *Green Chem*. **2007**, *9*, 742.

29. a) Y. Zhang, A. Thomas, M. Antonietti, X. Wang, *J. Am. Chem. Soc.* **2009**, *131*, 50, b) X. Wang, K. Maeda, A. Thomas, K. Takanabe, G. Xin, J. M. Carlsson, K. Domen, M. Antonietti, *Nat. Mater.* **2009**, *8*, 76, c) X. D. Bai, D. Zhong, G. Y. Zhang, X. C. Ma, S. Liu, E. G. Wang, Y. Chen, D. T. Shaw, *Appl. Phys. Lett.* **2001**, *79*, 1552, d) D. Portehault, C. Giordano, C. Gervais, I. Senkovska, S. Kaskel, C. Sanchez, M. Antonietti, *Adv. Funct. Mater*. **2010**, *20*, 1827, e) M. Kim, S. Hwang, J-S. Yu, *J. Mater. Chem*. **2007**, *17*, 1656, f) A. Thomas, A. Fischer, F. Goettmann, M. Antonietti, J-O. Müller, R. Schlögl, J. M. Carlsson, *J. Mater. Chem*. **2008**, *18*, 4893.

30. C-m. Yang, H-s. Sheu, K-j. Chao, *Adv. Funct. Mater.* **2002**, *12*, 143.

# Chapter 6

# Highly Crystalline and Conductive Nitrogen Doped Mesoporous Carbon with Graphitic Walls and its Electrochemical Performance

## Summary

We present a rational and simple methodology to fabricate highly conductive nitrogen doped ordered mesoporous carbons with the graphitic wall structure by the simple adjustment of the carbonization temperature of mesoporous carbon nitride. By simply controlling the heat treatment temperature, the structural order and the intrinsic properties such as surface area, conductivity, pore volume and the nitrogen content of ordered graphitic mesoporous carbons can be controlled. Among the materials studied, the sample heat treated at 1000 °C shows the highest conductivity which is 32 times higher than that for the samples treated at 800 °C and retains the well ordered mesoporous structure of the parent mesoporous carbon nitride and the reasonable amount of nitrogen in the graphitic framework. Since these materials exhibit high conductivity with the nitrogen atoms in the graphitic framework, we further demonstrate their use as support for the nanoparticle fabrication without the addition of any external stabilizing or size controlling agent, as well as the anode electrode catalysts. Highly dispersed platinum nanoparticles with the size similar to that of the pore diameter of the support can be fabricated as the nitrogen atoms and the well ordered porous structure in the mesoporous graphitic carbon framework act as stabilizing and size controlling agent respectively. Furthermore the Pt loaded nitrogen doped mesoporous graphitic carbon sample with a high conductivity shows much higher anodic electrocatalytic activity than the other materials used in the study.



A paper based on this study has been published in *Chem. Eur. J.* **2011**, *17*, 3390.

## 6.1. Introduction:

Carbon nitrides are remarkable materials, as the incorporation of nitrogen atoms into the carbon matrix can significantly enhance its conductivity, basicity, catalytic activity and gas storage property.[1] Indeed, depending on the amount of nitrogen incorporated the properties of carbon can be altered and often enhanced for a special purpose. These materials also exhibit high thermal and mechanical stability and intercalation ability which attract them in many potential applications mainly in the field of nanoscience and nanotechnology.[2] However, for efficient transport, diffusion, catalysis, storage and fuel cell related applications, porous materials are advantageous over non-porous solids.[3,4] Well-ordered mesoporosity in carbon nitrides was first realized in 2005 by Vinu et al. by introducing the hard templating approach for the fabrication of mesoporous carbon nitrides using mesoporous silica (nano-casting technique) as template through a simple polymerization reaction between carbon tetrachloride and ethylene diamine.[5] It has been found that porous carbon nitrides outsmart non-porous carbon nitrides in many novel applications such as catalysis, metal free activation of $CO_2$, photocatalyst for water splitting, templating ternary metal nitrides, fabrication of low dielectric devices, hydrogen storage and fuel cells.[6,7] Recently Vinu et al. also demonstrated that the mesoporous carbon nitride can be used as metal free basic catalyst for the transesterification of β-keto esters.[8]

On a more fancier note we also explored the capping aspects of mesoporous carbon nitride by fabricating highly dispersed Au nanoparticles on the support which acts as stabilizing, size controlling and reducing agent without the need for any external stabilizing agent.[9] However, mesoporous carbon nitride produced by this route display less crystallinity and poor conductivity which have limited its potential

applications mainly in the fields of fuel cells, solar cells, sensors and electronic devices. Enhancing crystallinity within mesostructured carbon nitride framework is advantageous over amorphous carbons due to a well developed crystalline structure, high electrical conductivity, high thermal stability and satisfactory oxidation resistance at low temperatures.[5-6,10]

There are several ways to control the graphitic nature of the carbon matrix.[11] Till date, most frequently employed methods to catalyze graphitization process are by the usage of transition metal ions and high temperature carbonization treatments.[11] In the former case the main disadvantages are the usage of expensive precursors and removal of metal nanoparticle species encapsulated within carbon framework despite of repetitive washing cycles which often results in low yields and greatly affecting the pore volume and structure.[12] The latter case wherein, high temperatures are vital for increasing crystallinity within carbon network. However, in the case of carbon nitride the thermodynamic stability of nitrogen in the carbon framework is very low and the nitrogen prefers to stay as nitrogen molecule at high temperature.[5] Thermal treatment may lead to significant reduction in nitrogen content which transforms the material towards nitrogen doped graphitic carbon[13] which is also attractive material because doping of nitrogen atom into the graphenic π-framework significantly contributes to its conductivity.[14] Although our mesoporous carbon nitride exhibits high nitrogen content, high thermal stability and excellent textural parameters, the wall structure is amorphous which makes the material less conductive. Hence, one of the challenges in this process is to produce the porous carbon nitride materials with high conductivity, crystalline wall and high nitrogen content, without affecting the structural order and wall structure.

## 6.2. Scope of the present investigation:

Herein we demonstrate a simple experiment to fabricate well ordered arrays of highly conductive nitrogen doped mesoporous carbon from mesoporous carbon nitride prepared from the hard templating approach (Scheme 1). The graphitic and the conductivity of the mesoporous carbon nitride materials have been controlled by treating the material at various carbonization temperatures. The carbonization temperatures chosen in this study are 800, 1000 and 1200 $^{o}$C. Increasing the temperatures from 800 $^{o}$C to 1200 $^{o}$C yields an improvised trend in crystallinity with reduced nitrogen content, pore volume and surface area. Of the temperatures chosen, 1000 $^{o}$C was found to be optimal carbonization temperature for obtaining the material with excellent crystallinity, finest textural characteristics and reasonable nitrogen content. It has been found that the conductivity of the material treated at 1000 °C is more than 32 times higher than the material treated at 800 °C. Furthermore, pore walls are highly graphitic and ordered. These functional pore channels with extremely high conducting walls have been used as nanoreactors for the fabrication of pore-directed growth of Pt nanoparticles. We also investigate the anodic performance of the Pt-loaded mesoporous carbon nitride treated at different temperatures. It has been found that the anodic performance of Pt loaded nitrogen doped mesoporous graphitic carbon treated at high temperature is very high due to nitrogen doping and high conductivity.

## 6.3. Experimental Section:

### (a) Materials:

Pluronic P123, HCl, HF, tetraethylorthosilicate (TEOS), ethylene diamine, carbon tetrachloride, $H_2PtCl_6$, $H_2SO_4$and $NaBH_4$ were purchased at an analytical

pure grade and were used without any further purification. Millipore water and ethanol were used wherever essential.

**(b) Preparation of the nitrogen doped graphitic mesoporous carbon (N-MGC):**

N-MGC materials were prepared by the following method. In a typical synthesis, the calcined SBA-15-100 (0.5 g),[15] prepared at the synthesis temperature of 100 °C was added to a mixture of ethylenediamine (EDA; 1.35 g) and carbon tetrachloride (CTC; 3 g). The resultant mixture was refluxed and stirred at 90 °C for 6 h. Then, the obtained dark-brown-colored solid mixture was placed in a drying oven for 12 h and ground into fine powder. The template-carbon nitride polymer composite was then heat treated in a nitrogen flow of 100 mL per minute at various temperatures such as 800 °C, 1000 $^{o}$C and 1200 $^{o}$C respectively with a heating rate of 5.0 °C per minutefor 5 h to carbonize the polymer. The N-MGC was recovered after dissolution of the silica framework in 5 wt% hydrofluoric acid, by filtration, washed several times with ethanol and dried at 100 °C. The samples were denoted N-MGC-X where X denotes the carbonization temperature.

**(c) Preparation of Pt nanoparticles within N-MGC**:

$H_2PtCl_6$ was used as metallic salt precursor for the preparation of Pt nanoparticles. Typically 20 mg of N-MGC synthesized at various temperatures was dispersed in 2 mL of water by mild sonication for 2 minutes. To this 2 mL of 2 mM $H_2PtCl_6$ solution (4 wt% of Pt with respect to N-MGC) was added followed by the addition of 2 ml 0.l M $NaBH_4$. The obtained mixture was washed thoroughly with distilled water and finally dried at vacuum oven at 60 °C.

**(d) Measurement of Electrochemical Activity:**

Pt nanoparticles supported on N-MGC synthesized at various carbonization temperatures were dispersed into ethanol. The mixture was dried at room temperature in $N_2$ gas flow. Anodic performance of Pt-N-MGC was examined by cyclic voltammetry (CV) using CH760C electrochemical analyzer. The measurements were carried out in an aqueous solution of 0.5 M $H_2SO_4$. Pt foil and calomel electrode were used as counter and reference electrodes, respectively. The electrode materials (3 mg/mL) were suspended into ethanol aqueous solution. The suspension (10 μL) was spread onto the surface of Au electrode using a micro-pipette. After the solvent evaporated, the electrode surface was covered with 5μL of Nafion solution (diluted to 1% solution with $CH_3OH$) and the electrode was dried at 60°C for 1h to evaporate the solvent.

**(e) Measurement of conductivity by two probe method:**

Electrical conductivity of N-MGC-X (where X indicates the carbonization temperatures) samples were measured under ambient laboratory conditions using a standard two-probe method in the total absence of moisture. Two-probe measurements were carried out by using Keithley 4300 Semiconductor Characterization System or Semiconductor Parameter Analyzer (Model 4200-SCS) under clean room (Class 1000) conditions. All measurements were performed on a minimum of three different places to provide consistency in the resistance values. Pellets of N-MGC-X with uniform thickness ($l$=1mm and $A$=1) were fabricated and are sandwiched between two aluminium electrodes to measure electrical conductivity. Conductivity (σ) values are calculated by the following equation where

R is electrical resistance of a uniform specimen of the material, *A* is the cross-sectional area of the specimenand *l* is the length of the piece of material.

$\sigma = l/(R*A)$

## 6.4. Characterization Techniques:

**X-ray Diffraction:**

X-ray diffraction (XRD) patterns of the mesoporous carbon nitride materials were collected on a Rigaku diffractometer using Cu Kα (λ = 0.154 nm) radiation. The diffractograms were recorded in a 2θ range from 0.8 to 10º with a 2θ step size of 0.01 and a step time of 1 s.

**Nitrogen adsorption and desorption isotherms:**

$N_2$ adsorption and desorption isotherms were measured at 77 K on a Quantachrome Autosorb 1 sorption analyzer. All samples were outgassed at 250 ºC for 5 h prior to the nitrogen-adsorption measurements. The specific surface area was calculated using the Brunauer-Emmett-Teller (BET) method. The pore size was obtained from the adsorption branch of the nitrogen isotherms using the Barrett-Joyner-Halenda method.

**Field emission scanning electron microscopy:**

The morphology of the materials prepared at different synthesis conditions was observed on a Hitachi S-4800 field emission scanning electron microscope using an accelerating voltage of 5.0 kV.

**Transmission electron microscopy:**

The preparation of the samples for HRTEM analysis involved sonication of N-MGC-1000 $^{o}$C in ethanol for 2 to 5 min and deposition on a copper grid. The accelerating voltage of the electron beam was 200 kV. The HRTEM images were obtained using

a JEOL-3000F and a JEOL-3100FEF field emission high-resolution transmission electron microscope equipped with a Gatan-766 electron energy-loss spectrometer.

**Measurement of conductivity by two probe method:**

Two-probe measurements were carried out by using Keithley 4300 semiconductor characterization system or semiconductor parameter analyzer (Model 4200-SCS) under clean room (Class 1000) conditions.

**Cyclic voltammetry studies:**

Anodic performance of Pt-N-MGC was examined by cyclic voltammetry (CV) using CH760C electrochemical analyzer.

## 6.5. Results and Discussion:

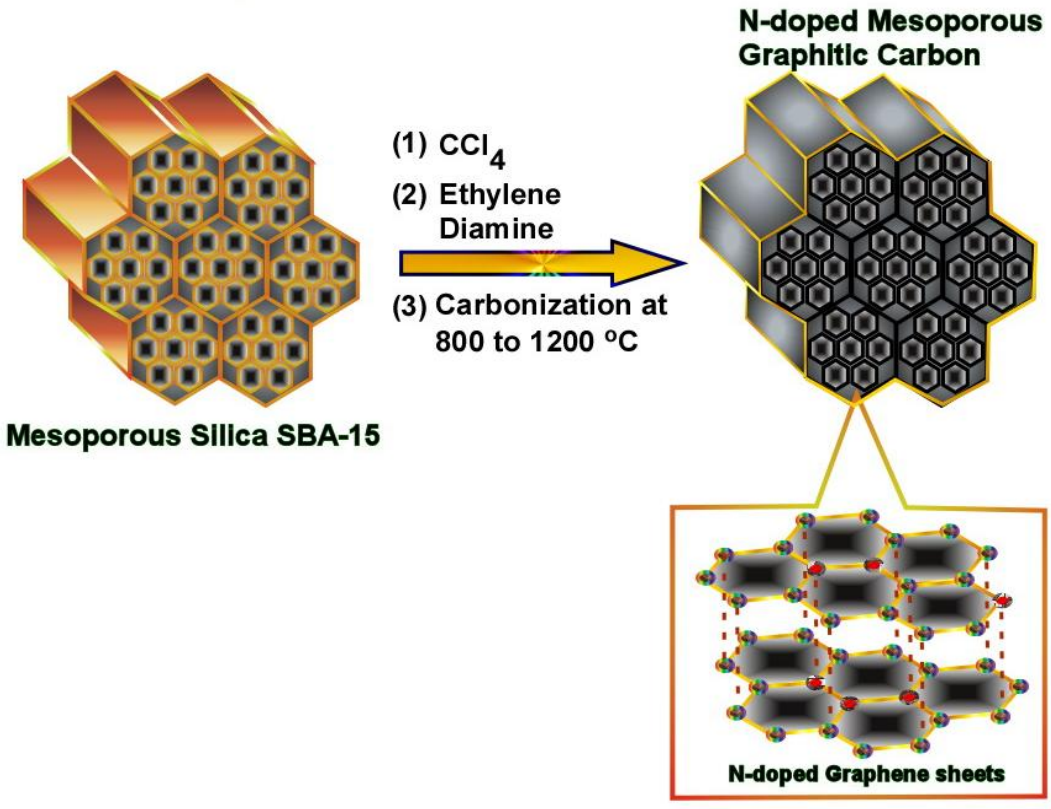


**Figure 1**. Schematic representation of the preparation of N-doped mesoporous graphitic carbons.

Herein, we demonstrate a simple experiment to fabricate well ordered arrays of highly conductive nitrogen doped mesoporous carbon by nanocasting strategy. Firstly, simple polymerization reaction between carbon tetrachloride (carbon source) and ethylenediamine (nitrogen source) within the pores of mesoporous silica (SBA-15) results in carbon nitride polymer encapsulated SBA-15. The obtained composite was subsequently carbonized at 800, 1000 and 1200 $^{o}$C temperatures followed by removal of silica by means of HF to get nitrogen doped ordered mesoporous graphitic carbons. The wall structure is made up of nitrogen doped graphene sheets which is depicted in Figure 1.

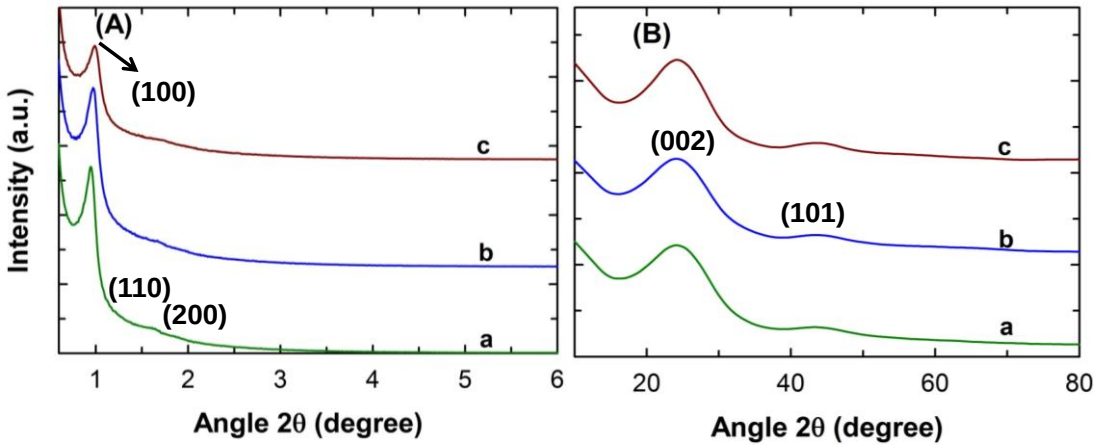


**Figure 2**. (A) Powder XRD patterns of graphitic MCN-1 synthesized at different carbonization temperatures (a) N-MGC-800, (b) N-MGC-1000, (c) N-MGC-1200; (B) Higher angle XRD pattern showing the graphitic peak centered around 25.47$^{o}$ corresponding to an interlayer d-spacing of 0.349 nm.

N-doped mesoporous graphitic carbon (N-MGC) arrays are synthesized by carbonization of mesoporous carbon nitride polymer encapsulated SBA-15 nanocomposite at 800, 1000 and 1200 $^{o}$C. Figure 2A shows the lower angle powder XRD patterns of N-MGC-800, N-MGC-1000 and N-MGC-1200. The low angle powder X-ray diffraction pattern (Figure 2A) of all the samples except N-MGC-1200

show three well ordered peaks, which can be assigned to the (100), (110) and (200) diffractions of a 2D hexagonal mesostructure for space group *p6mm*, confirming well ordered porous structure even after the high temperature treatment up to 1000 °C. However when the carbonization temperature was 1200 °C, only the sharp (100) peak at lower angle is observed and the higher angle reflections such as (110) and (200) are completely disappeared, indicating the loss of structural order in the sample.[16] It should also be noted that the d-spacing and the unit cell constant of the samples decrease with increasing the carbonization temperature which suggests that the contraction of the carbon nitride (CN) framework is increased upon the carbonization temperature due to the orderly arrangement of the CN layers. The unit-cell constants for N-MGC-800, N-MGC-1000 and N-MGC-1200 are calculated to be 9.29, 9.09 and 8.91 nm respectively (Table 1). The crystallinity of the sample treated at different carbonization temperature was obtained by the wide-angle powder XRD measurements. It has been found that all the samples show two peaks centered at $25.47^{o}$ and $43^{o}$ which correspond to (002) and (101) reflections from graphitic pore walls (Figure 2B).

| Sample | $a_o$ (nm) | $A_{BET}$[a] ($m^2 g^{-1}$) | Vp[b] ($cm^3 g^{-1}$) | Dp[c] (nm) | Cond.[d] ($S cm^{-1}$)*$10^{-3}$ |
|---|---|---|---|---|---|
| N-MGC-800 | 9.29 | 714 | 0.97 | 4.76 | 2.5 |
| N-MGC-1000 | 9.09 | 682 | 0.93 | 4.71 | 80 |
| N-MGC-1200 | 8.91 | 650 | 0.88 | 4.44 | 57 |

*[a] BET specific surface area ($A_{BET}$) [b] Specific pore volume (Vp) [c] Pore diameter (Dp) [d] Conductivity (cond.)*

**Table 1**. Textural parameters of the N-MGC samples treated at different carbonization temperatures.

The d-spacing of (002) peak observed at around 0.349 nm in our case is slightly greater than that of pure graphite (0.335 nm)[17] and is relatively close to that of nonporous graphitic carbon nitride spheres, confirming the turbostatic ordering of carbon and nitrogen atoms in the wall structure of the N-MGC.[18] It must be noted that no significant difference in the intensity of the peaks at higher angle was observed for the N-MGC samples treated at different carbonization temperatures.

High resolution transmission electron microscope (HRTEM) images confirmed the ordered mesostructure of N-MGC-1000, substantiating large domains with well ordered arrays of carbon nanorods and pore channels. Figure 3a shows the hexagonal arrays of carbon rods made up of 5 nm in diameter and 4 nm apart, similar to the structure of mesoporous carbon nitride carbonized at 600 $^{o}$C.[5a] The retention of mesostructure can be clearly observed from HRTEM which is quite consistent with the data obtained from low angle XRD (Figure 2A).

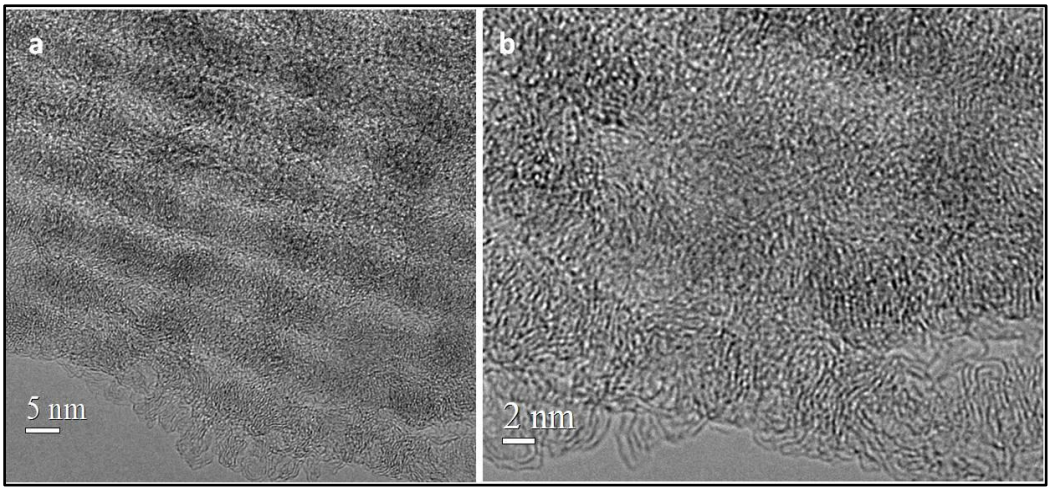


**Figure 3**. TEM images of N-MGC synthesized at 1000 $^{o}$C. (a) showing graphitic pore channels, (b) showing graphitic layers.

Furthermore, careful examination of high temperature treated N-MGC sample shows, many crystalline domains formed by a number of parallel fringes which are

composed of graphene sheets (Figure 3b) aligned perpendicularly to the template walls during synthesis process. HRTEM images also clearly illustrate small crystalline domains with a d-spacing of 0.35 nm which agrees well with the high angle XRD pattern (Figure 2B).

Field emission scanning electron microscope (FESEM) images reveal that heat treatment influences the morphology of the materials. Both the N-MGC-800 and N-MGC-1000 exhibit rod like morphology which is similar to that of the parent mesoporous carbon nitride but a slight deterioration of the morphology is observed for the N-MGC-1200 (Figure 4). These results indicate that high temperature treatment converts the amorphous CN walls of the mesoporous carbon nitride into highly crystalline nitrogen doped carbon framework without affecting the mesostructure order of the parent material.

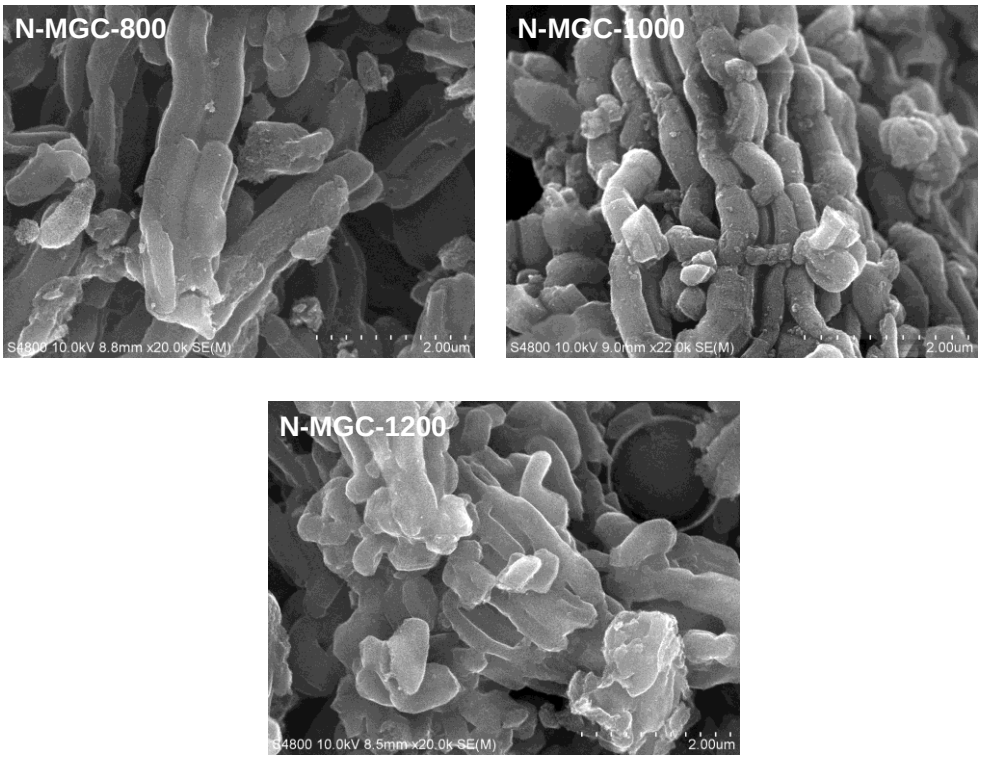


**Figure 4**. FESEM images of N-MGC samples synthesized at various carbonization temperatures.

High temperature treatment also makes a significant influence on the textural parameters of the N-MGC materials such as specific surface area and the specific pore volume. The textural parameters of the sample treated at different carbonization temperature were obtained from nitrogen adsorption-desorption measurement which has been the most reliable probe available for ascertaining textural parameters of mesoporous materials to date. Figure 5 shows the nitrogen adsorption-desorption isotherms of N-MGC-800, N-MGC-1000 and N-MGC-1200. All of the isotherms are of type IV according to the IUPAC classification, with a H1 type hysteresis loop and featured a sharp, capillary condensation at higher relative pressures, which indicates the presence of well-ordered mesopores in all of the heat treated samples. The textural parameters such as the specific surface area and total pore volume of the N-MGC samples are also given in Table 1. Compared to the mesoporous carbon nitride[5a] which is normally prepared at 600 °C, the specific pore volume and the specific surface area are smaller. Increasing the temperature from 800 to 1200 $^{o}$C leads to decrease in specific surface area from 714 $m^2/g$ to 650 $m^2/g$ with a concomitant reduction of the pore volume from 0.97 to 0.88 $cm^3g^{-1}$. In addition the micropore volume of the sample is significantly reduced upon increasing the heat treatment temperature, confirming that the specific surface area is mainly originated from the mesopores in the materials and the contribution by micropores due to the defect sites in the wall structure of the materials is very small. It should also be noted that the specific surface area and the specific pore volume of N-MGC-1000 were found to be 682 $m^2/g$ and 0.91 $cm^3$ $g^{-1}$, respectively. The decrease in the textural parameters upon the heat treatment is not related to the disintegration of pore structure but due to the conversion of the amorphous wall structure into the crystalline porous wall along the mesochannels which makes the surface

homogenous as confirmed by the TEM (Figure 3) and the higher angle XRD data (Figure 2B).

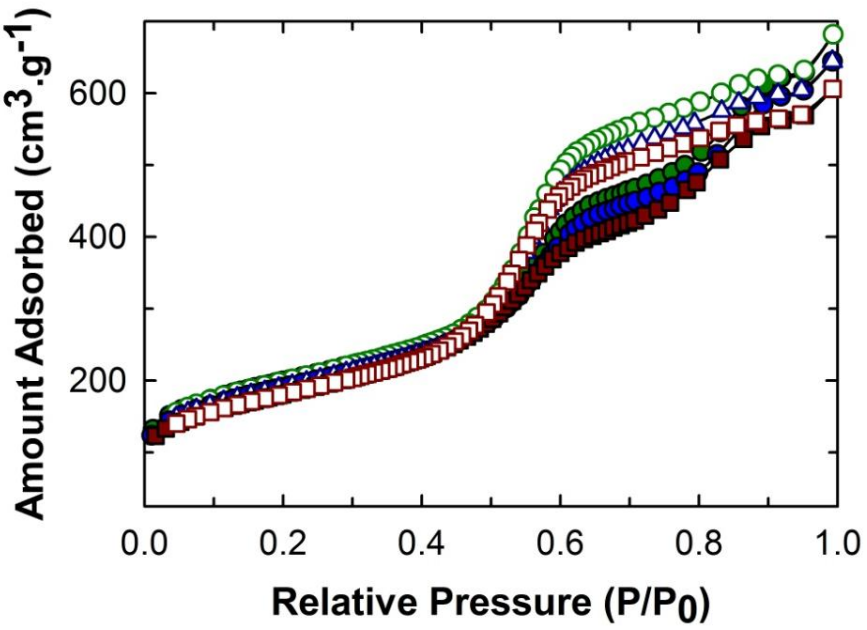


**Figure 5**. Nitrogen adsorption-desorption isotherms of nitrogen doped graphitic mesoporous carbons synthesized at various carbonization temperatures (closed symbols: adsorption; open symbols: desorption; circles: N-MGC-800, triangles: N-MGC-1000 and squares: N-MGC-1200).

The nitrogen content of the mesoporous carbon nitride was significantly affected by the heat treatment which forces us to call the high temperature treated samples as nitrogen doped mesoporous graphitic carbon instead of mesoporous carbon nitride although the final materials were derived from the latter materials. The amount of carbon obtained from CHN analysis raises from 77 to 86 % by increasing carbonization temperature whereas the nitrogen content decreases by a factor of 3 on increasing the carbonization temperature, due to the lower thermodynamic stability of nitrogen in the carbon framework at high temperature and the volatile nature of the amorphous CN framework.[5] It should be noted that all the samples except N-MGC-800 exhibit a small amount of oxygen which mainly comes from the

atmospheric $CO_2$ adsorbed on the basic -NH or -$NH_2$ groups on the wall structure of the sample. The detailed elemental compositions are listed in Table 2.

| Sample | C (mass %) | N (mass %) | Other elements (O, Si, Cl and F) (mass %) |
|---|---|---|---|
| N-MGC-800 | 77.4 | 9.0 | 11.0 |
| N-MGC-1000 | 80.6 | 3.9 | 9.6 |
| N-MGC-1200 | 85.5 | 1.3 | 7.8 |

**Table 2**. Elemental composition of N-MGC materials obtained from CHN analysis

**Pt nanoparticles encapsulated N-MGC:**

Platinum (Pt) based materials have long been investigated as active catalysts for oxygen-reduction reaction. Unfortunately, its high cost and the limited resources made the researchers to find the alternative ways to improve the performance of the anodic catalytic materials.[19] To solve this problem in PEM fuel cells, researchers either used the Pt nanoparticles or encapsulated the Pt catalysts on the high surface area porous supports such as activated or porous carbons as they can offer high surface area which is essential for obtaining the high dispersion of the catalysts.[19,20] However these support materials do not possess much conductivity, as good support materials require not only the excellent textural parameters but also high conductivity for the electron transport. Since N-MGC materials exhibit high crystallinity together with excellent textural parameters, we employed them as the anodic catalytic supports for PEM fuel cells. It is also expected that the N-MGC materials can offer the platform for growing the nanoparticles without the capping,

stabilizing and size controlling agent. The size of the well ordered pores in N-MGC can direct the size of the Pt nanoparticles whereas, the doped nitrogen atoms in the wall structure can offer the capping and the stabilizing effect which is extremely important to avoid the agglomeration of the particles. Based on this concept, Pt nanoparticles were introduced within the nanochannels of N-MGC by bottom up approach. Firstly, chloroplatinic acid was adsorbed onto the N-MGC support by means of sonication and further reduction with $NaBH_4$ yields the generation of Pt nanoparticles. Figure 6 shows the representative XRD pattern and TEM image of Pt nanoparticles encapsulated N-MGC-1000. The wide-angle X-ray diffraction pattern of the Pt nanoparticles within N-MGC-1000 exhibits four peaks which could be indexed as the (111), (200), (220) and (311) reflections of the face-centered cubic structure of crystalline Pt(0). Among the peaks observed the intensity of the (111) peak is the highest indicating that (111) plane was the predominant crystal facet. The peaks are very broad and weak suggesting the formation of the ultra small nanocrystalline Pt particles inside the pore channels of N-MGC. The absence of large and intense peaks at higher angles further corroborates that no large particles are formed on the external surface of the support.

Transmission electron microscope (TEM) image of the Pt nanoparticle encapsulated N-MGC clearly shows a regular arrangement of dark spherical spots which correspond to Pt nanoparticles observed along the nanochannels of the support (Figure 6 b). Interestingly, a linear arrangement of mesochannels which are arranged in a regular interval is also clearly seen suggesting that mesostructure of the support is stable even after the formation of Pt nanoparticles. The average size of the Pt nanoparticles obtained from the TEM image is found to be less than 5 nm and the particles are highly dispersed on the porous channels of the support.

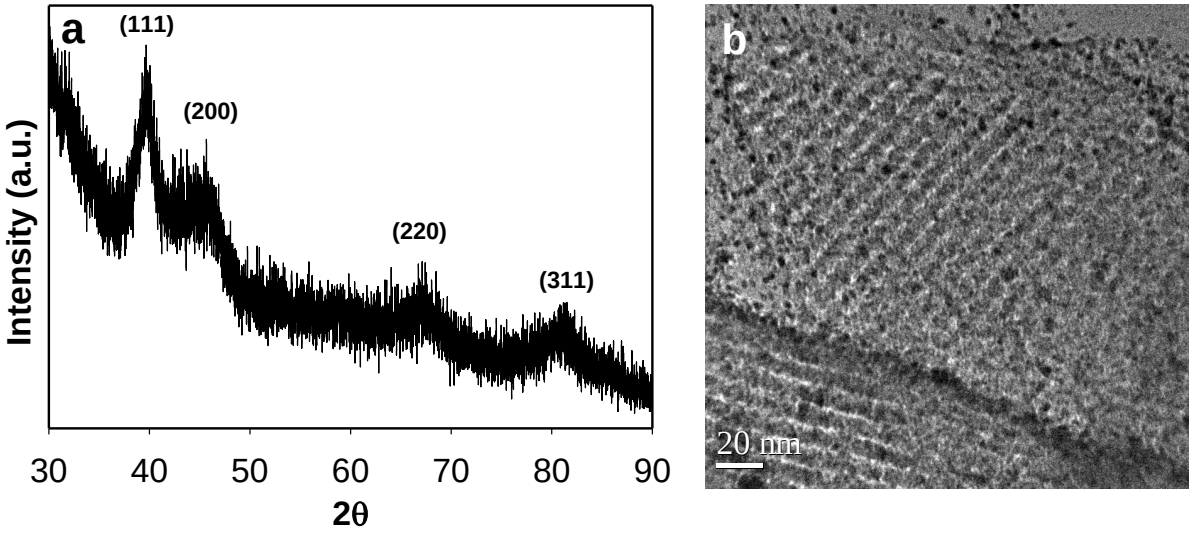


**Figure 6**. (a) Wide angle XRD pattern of Pt nanoparticles encapsulated within N-MGC-1000, (b) corresponding TEM image.

These results reveal the pore size controlled growth of the nanoparticle in the confined matrix and the presence of the nitrogen atom in the graphitic carbon matrix helps the stabilization which limits the agglomeration of the individual Pt nanoparticles. This is also confirmed by the inductively coupled plasma mass spectroscopy (ICP-MS) data that the amount of the Pt on the pore channels of the N-MGC samples decreases with decreasing in the nitrogen content. Among the samples studied N-MGC-800 has the highest Pt content under the similar preparation conditions revealing the capping action of nitrogen atoms in the N-MGC samples (Table 3). It should also be noted that agglomerated Pt particles are found in the case of Pt encapsulated N-MGC-1200 (TEM image not shown) due to its low nitrogen content and inferior textural parameters.

| Sample name | Pt (mass %) |
|---|---|
| Pt-N-MGC-800 | 4.16 |
| Pt-N-MGC-1000 | 3.60 |
| Pt-N-MGC-1200 | 2.81 |

**Table 3**. Elemental composition of Pt nanoparticles within N-MGC obtained from ICP analysis.

| Sample | $A_{BET}$ ($m^2 g^{-1}$) | Pore volume ($cm^3 g^{-1}$) |
|---|---|---|
| N-MGC-800 | 714 | 0.97 |
| N-MGC-1000 | 682 | 0.93 |
| N-MGC-1200 | 650 | 0.88 |
| Pt-N-MGC-800 | 615 | 0.85 |
| Pt-N-MGC-1000 | 644 | 0.88 |
| Pt-N-MGC-1200 | 626 | 0.81 |

**Table 4**. Comparison of BET surface areas and pore volumes before and after stabilizing Pt nanoparticles within N-MGC at various carbonization temperatures.

The textural parameters showed a significant change after the loading of Pt nanoparticles over the mesochannels of the support and the results are shown in Table 4. The specific surface area was found to decrease from 714 $m^2/g$ for pure N-MGC-800 to 615 $m^2/g$ for Pt-N-MGC-800 whereas, the specific pore volume decreases from 0.97 to 0.85 $cm^3g^{-1}$ for the same sample. However, only a little reduction in the specific surface area and the specific pore volume was observed for

the Pt-N-MGC-1000 and Pt-N-MGC-1200 which is mainly due to the difference in the amount of Pt on the samples.

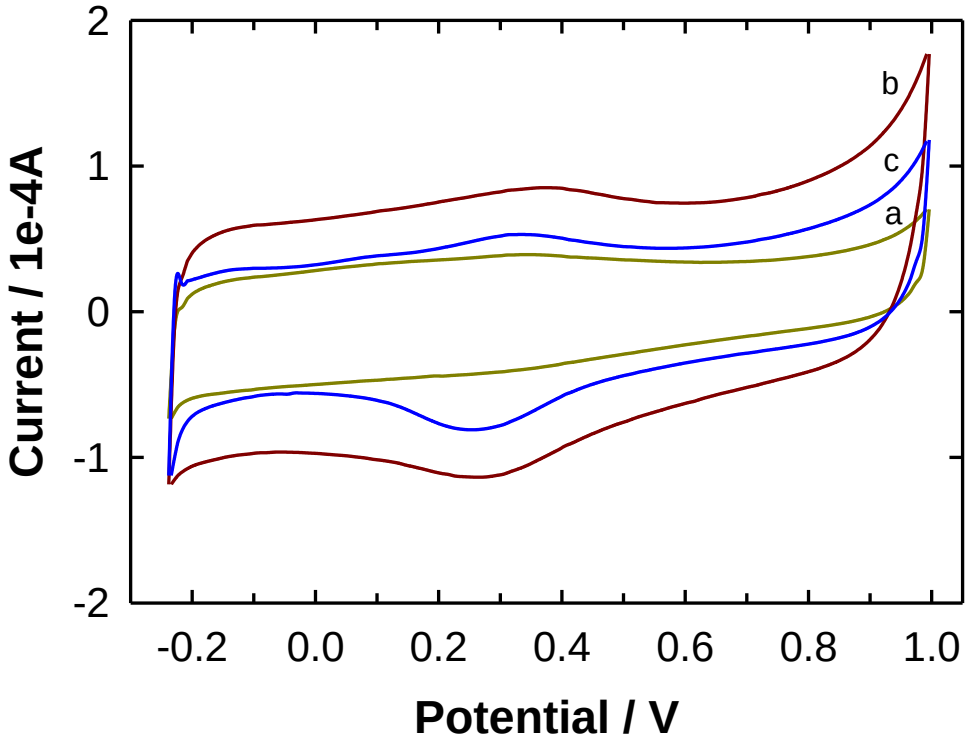


**Figure 7**. Cyclic voltammograms of Pt nanoparticles embedded within N-MGC synthesized at various temperatures: (a) N-MGC-800, (b) N-MGC-1000 and (c) N-MGC-1200.

Furthermore we evaluated the transport characteristics of Pt-N-MGC by conducting cyclic voltammetry (CV) experiment (Figure 7). CV is employed to obtain the amount of the hydrogen desorption for Pt-N-MGC samples treated at different carbonization temperature. It is observed that the double layer thickness and the charge of $H_2$ desorption increase with raise in carbonization temperature from 800 °C to 1000 °C but decrease for Pt-N-MGC-1200 which was heat treated at 1200 °C. Among the samples tested, Pt-N-MGC-1000 showed the maximum performance with the high amount of charge of hydrogen desorption. This could be mainly due to the fact that the perfect combination of the textural parameters and the graphitic

content in the sample. On the other hand, the poor performance of the Pt-N-MGC-800 and Pt-N-MGC-1200 could be due to low crystallinity and poor textural characteristics respectively.

To support these facts we have measured the electrical conductivity of all the samples. Electrical conductivity is an important parameter which improves enormously on moving from less ordered amorphous materials to highly ordered crystalline materials. One such mysterious, two-dimensional form of carbon is named graphene, and it is probably the best-studied carbon allotrope theoretically.[21] Graphene planar, hexagonal arrangements of carbon atoms are the starting point for all calculations on graphite, carbon nanotubes, and fullerenes.[22-23] The remarkable feature of this wonder material is that it is a Dirac solid, with the electron energy being linearly dependent on the wave vector near the vertices of the hexagonal Brillouin zone. It exhibits room-temperature fractional quantum Hall effect[24] and ambipolar electric field effect along with ballistic conduction of charge carriers. Doping of hetero atom within graphene lattice also enhances electrical conductivity significantly.[14a,b] N-MGC which is analogous to nitrogen doped graphene material with additional benefit of high porosity can also serve as good electrical conductivity and electrode material. In order to obtain the electrical conductivity of the samples, N-MGC samples were sandwiched between two aluminum electrodes and the I-V characteristics was measured (Scheme given in Figure 8a). Figure 8c-d show the current-voltage curves of N-MGC samples heat treated at different carbonization temperature which reveal typical ohmic performance. We observed 32 times improvement in conductivity on moving from N-MGC-800 to N-MGC-1000 (Table 1) whereas, 1.4 times decrease in conductivity in the case of N-MGC-1200 (with respect to N-MGC-1000). The observation of high conductivity in N-MGC-1000

could be attributed to the combination of excellent structural order, high specific surface area and pore volume and high crystallinity. These results also give us the proof that the high electronic conductivity originated from the crystalline graphitic framework coupled with the good textural parameters such as high specific surface area and high pore volume is responsible for the highest anodic performance of N-MGC-1000.

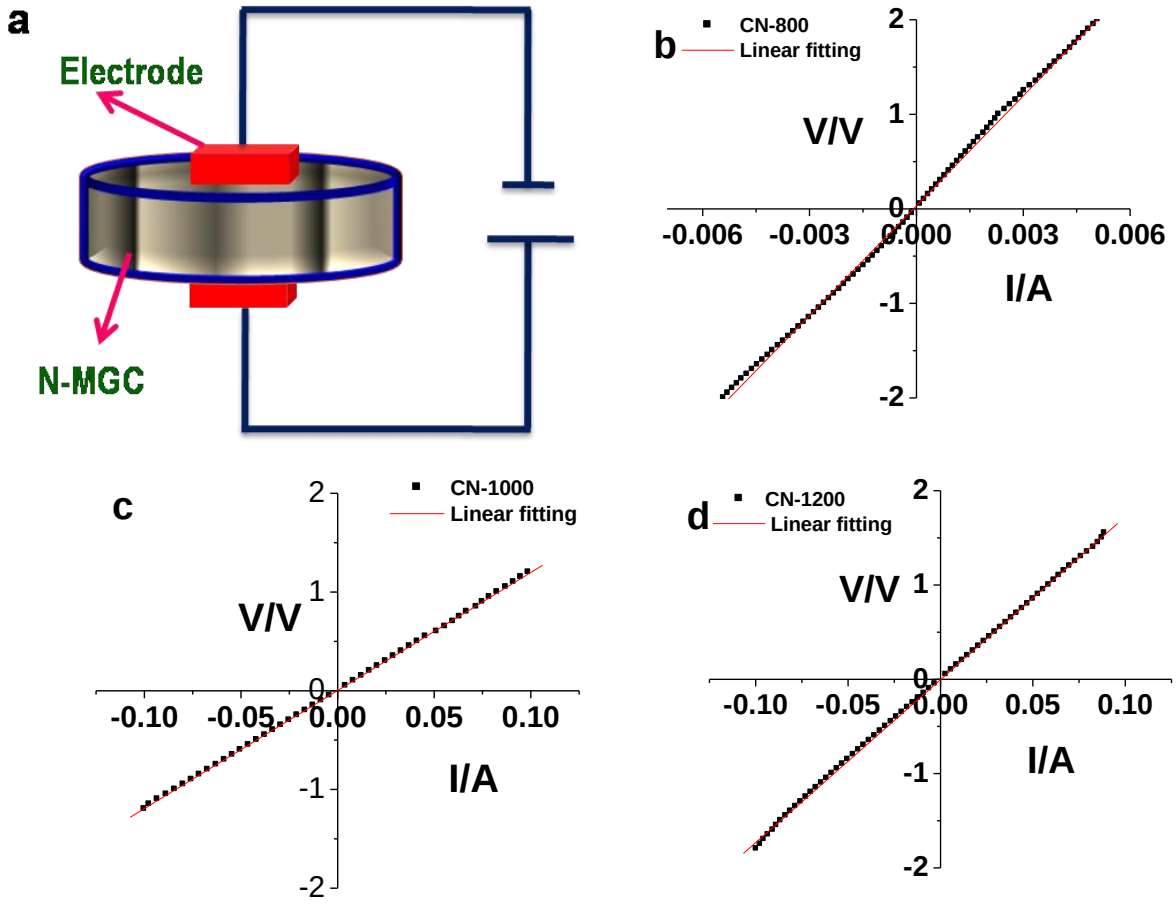


**Figure 8**. (a) Scheme showing the fabrication of graphitic carbon sandwiched between Al electrodes (b-d) I-V plots corresponding to N-MGC's synthesized at various temperatures by semi conductor parameter analyzer.

Although N-MGC-1200 exhibits high conductivity, poor textural parameters, disordered structure and less nitrogen content due to high temperature treatment activate the agglomeration of Pt nanoparticles which is the main cause for its low electrocatalytic activity (Figure 7c). From these results one can conclude that the perfect match of the textural parameters, structural order, nitrogen content and the electrical conductivity in the support materials are required for the design of anodic catalysts for the PEM fuel cells.

## 6.6. Conclusions:

In conclusion, we have successfully demonstrated the preparation of highly conductive, nitrogen doped mesoporous carbon with well-ordered hexagonal type pores along with the graphitic wall structure. Highly crystalline nitrogen doped mesoporous carbon is obtained by simple heat treatment of the mesoporous carbon nitride at carbonization temperature higher than 800 °C. Although the textural parameters and the nitrogen content of the materials decrease with increasing the carbonization temperature due to the atomic rearrangement of the carbon and nitrogen atoms in the wall structure, the ordered mesoporous structure was maintained upto the heat treatment temperature of 1000 °C. We also demonstrated that the conductivity of the material treated at 1000 °C is 32 times higher than that of the samples treated at 800 °C due to its highly crystalline wall structure. The capping aspects of the nitrogen doped ordered nanoporous graphitic carbons were explored by in-situ stabilization of Pt nanoparticles well within the nanochannels of the material without the aid of external stabilizing agent. It has been found that the size of the pores of the nitrogen doped mesoporous materials dictates the particle size and the nitrogen atoms help to avoid the agglomeration of the Pt nanoparticles.

Furthermore, the Pt loaded highly conductive nitrogen doped mesoporous graphitic carbon samples were utilized as the anodic catalysts for the PEM fuel cells. The material with high conductivity together with well ordered porous structure showed much higher anodic electrocatalytic activity than the other materials used in the study. Since these materials exhibit high conductivity, well ordered porous structure and excellent anodic catalytic activity in the PEM fuel cells, they might also find potential applications in the field of solar cells, electronic devices, catalysis, hydrogen storage and photocatalysis.

## 6.7. References:


1. a) L. Hultman, J. Neidhardt, N. Hellgren, H. Sjöström, J-E. Sundgren, *MRS Bull*. **2003**, *28*, 194, b) M. Deifallah, P. F. McMillan, F. Cora, *J. Phys. Chem. C.* **2008**, *112*, 5447, c) T. Kwon, H. Nishihara, H. Itoi, Q-H. Yang, T. Kyotani, *Langmuir*. **2009**, *25*, 11961, d) S. Giraudet, Z. Zhu, X. Yao, G. Lu, *J. Phys. Chem. C.* **2010**, *114*, 8639, e) L. Wang, R. T. Yang, *J. Phys. Chem. C*. **2009**, *113*, 21883, f) E. Kroke, M. Schwarz, *Coord. Chem. Rev*. **2004**, *248*, 493.

2. a) C. M. Lieber, Z. J. Zhang, *Adv. Mater.* **1994**, *6*, 497, b) A. Y. Liu, M. L. Cohen, *Science*. **1989**, *245*, 841.

3. a) M. E. Davis, *Nature*. **2002**, *417*, 813, b) D. R. Rolison, *Science*. **2003**, *299*, 1698, c) J. W. Long, B. Dunn, D. R. Rolison, H. S. White, *Chem. Rev*. **2004,** *104*, 4463, d) E. C. de. Oliveira, C. T. G. V. M. T. Pires, H. O. Pastore, *J. Braz. Chem. Soc.* **2006**, *17*, 16, e) H. Nishihara, H. Itoi, T. Kogure, P-X Hou, H. Touhara, F. Okino, T. Kyotani, *Chem. Eur. J*. **2009**, *15*, 5355, f) A. D. Leonard, J. L. Hudson, H. Fan, R. Booker, L. J. Simpson, K. J. O. Neill, P. A. Parilla, M. J. Heben, M. Pasquali, C. Kittrell, J. M. Tour, *J. Am. Chem. Soc.* **2009**, *131*, 723.

4. a) N. P. Brandon, D. J. Brett, *Phil. Trans. R. Soc. A*. **2006**, *364*, 147, b) A. Kelly, *Phil. Trans. R. Soc. A.* **2006**, *364*, 5.

5. a) A. Vinu, K. Ariga, T. Mori, T. Nakanishi, S. Hishita, D. Golberg, Y. Bando, *Adv. Mater*. **2005**, *17*, 1648, b) A. Vinu, *Adv. Funct. Mater*. **2008**, *18*, 816.

6. a) Y. Zhang, A. Thomas, M. Antonietti, X. Wang, *J. Am. Chem. Soc.* **2009**, *131*, 50, b) X. Wang, K. Maeda, A. Thomas, K. Takanabe, G. Xin, J. M. Carlsson, K. Domen, M. Antonietti, *Nat. Mater.* **2009**, *8*, 76, c) Y-S Jun, W. H. Hong, M. Antonietti, A. Thomas, *Adv. Mater.* **2009**, *21*, 4270, d) X. D. Bai, D. Zhong, G. Y. Zhang, X. C. Ma, S. Liu, E. G. Wang, Y. Chen, D. T. Shaw, *Appl. Phys. Lett.* **2001**, *79*, 1552, e) D. Portehault, C. Giordano, C. Gervais, I. Senkovska, S. Kaskel, C. Sanchez, M. Antonietti, *Adv. Funct. Mater*. **2010**, *20*, 1827, f) M. Kim, S. Hwang, J-S. Yu, *J. Mater. Chem*. **2007**, *17*, 1656.

7. A. Thomas, A. Fischer, F. Goettmann, M. Antonietti, J-O. Müller, R. Schlögl, J. M. Carlsson, *J. Mater. Chem*. **2008**, *18*, 4893.

8. X. Jin, V. V. Balasubramanian, S. T. Selvan, D. P. Sawant, M. A. Chari, G. Q. Lu, A. Vinu, *Angew. Chem. Int. Ed*. **2009**, *48*, 7884.

9. K.K.R. Datta, B. V. S. Reddy, K. Ariga, A. Vinu, *Angew. Chem. Int. Ed.***2010**, *49*, 5961.

10. a) Z. Yang, Y. Xia, R. Mokaya, *J. Am. Chem. Soc*. **2007**, *129*, 1673, b) E. Frackowiak, *Phys. Chem. Chem. Phys*. **2007**, *9*, 1774, c) J. N. Wang, Y. Z. Zhao J. J. Niu, *J. Mater. Chem*. **2007**, *17*, 2251.

11. a) Q. Huo, D. I. Margolese, U. Ciesla, P. feng, T. E. Gier, P. Sieger, R. Leon, P. M. Petroff, F. Schüth, G. D. Stucky, *Nature.* **1994**, *368*, 317, b) T. Hyeon, S. Han, Y. E. Sung, K.W. Park, Y.W. Kim, *Angew. Chem. Int. Ed.* **2003**, *42*, 4352, c) X. Ji, P. S. Herle, Y. Rho, L. F. Nazar, *Chem. Mater*. **2007**, *19*, 374, d) W. H. Zhang, C. Liang, H. Sun, Z. Shen, Y. Guan, P. Ying, C. Li, *Adv. Mater.* **2002**, *14*, 1776, e) Y. Xia, R. Mokaya, *Adv. Mater.* **2004**, *16*, 1553; f)

T-W. Kim, I-S. Park, R. Ryoo, *Angew. Chem. Int. Ed.* **2003**, *42*, 4375, g) B. Y. Xia, J. N. Wang, X. X. Wang, J. J. Niu, Z. M. Sheng, M. R. Hu, Q. C. Yu, *Adv. Funct. Mater*. **2008**, *18*, 1790, h) K. T. Lee, X. Ji, M. Rault, L. F. Nazar, *Angew. Chem. Int. Ed.* **2009**, *48*, 5661, i) C. H. Kim, D-K. Lee, T. J. Pinnavaia, *Langmuir*. **2004**, *20*, 5157.

12. a) A. B. Fuertes, S. Alvarez, *Carbon.* **2004**, *42*, 3049, b) Y. Hanzawa, H. Hatori, N. Yoshizawa, Y. Yamada, *Carbon.* **2002**, *40*, 575.
13. a) A. J. Stevens, T. Koga, C. B. Agee, M. J. Aziz, C. M. Lieber, *J. Am. Chem. Soc.* **1996,** *118*, 10900, b) J. Hu, P. Yang, C. M. Lieber, *Phys. Rev. B.* ***1998***, *57*, 3185.
14. a) D. Wei, Y. Liu, Y. Wang, H. Zhang, L. Huang, G. Yu, *Nano Lett*. **2009**, *9*, 1752, b) J. D. W-Camacho, K. J. Stevenson, *J. Phys. Chem. C*. **2009**, *113*, 19082, c) J. P. Paraknowitsch, J. Zhang, D. Su, A. Thomas, M. Antonietti, *Adv. Mater*. **2009**, *21*, 87, d) R. Liu, D. Wu, X. Feng, K. Müllen, *Angew. Chem. Int. Ed*. **2010**, *49*, 2565.
15. M. Hartmann, A. Vinu, *Langmuir*. **2002**, *18*, 8010.
16. H. J. Shin, R. Ryoo, M. Kruk, M. Jaroniec, *Chem. Commun.* **2001**, 349.
17. F. Tunistra, J. L. Koenig, *J. Chem. Phys.* **1970**, *53*, 1126.
18. a) Y. Qiu, L. Gao, *Chem. Commun*. **2003**, 2378, b) Q. Guo, Q. Yang, L. Zhu, C. Yi, S. Zhang, Y. Xie, *Solid State Commun*. **2004**, *132*, 369.
19. a) M. Winter, R. J. Brodd, *Chem. Rev*. **2004**, *104*, 4245, b) X.W. Yu, S. Y. Ye, *J. Power. Sources*. **2007**, *172*, 145, c) Z. W. Chen, M. Waje, W. Z. Li, Y. S. Yan, *Angew. Chem. Int. Ed*. **2007**, *46*, 4060, d) B. Lim, M. J. Jiang, P. H.

C. Camargo, E. C. Cho, J. Tao, X. M. Lu, Y. M. Zhu, Y. N. Xia, *Science.* **2009**, *324*, 1302.

20. a) A. Eftekhari, *Nanostructured Materials in Electrochemistry*, **2008**, *Wiley-VCH*, b) J. J. Watkins, J. Chen, H. S. White, H. D. Abruña, E. Maisonhaute, C. Amatore, *Anal. Chem*. **2003**, *75*, 3962, c) T. You, O. Niwa, M. Tomita, S. Hirono, *Anal. Chem*.**2003**, *75*, 2080.
21. a) C. N. R. Rao, A. K. Sood, K. S. Subrahmanyam, A. Govindaraj, *Angew. Chem. Int. Ed*. **2009**, *48*, 7752, b) A. K. Geim, K. S. Novoselov, *Nat. Mater*. **2007**, *6*, 183, c) A. K. Geim, *Science* **2009**, *324*, 1530, d) M. J. Allen, V. C. Tung, R. B. Kaner. *Chem. Rev.* **2010**, *110*, 132.
22. M. I. Katsnelson, *Mater. Today*. **2007**, *10*, 20.
23. C. N. R. Rao, K. Biswas, K. S. Subrahmanyam, A. Govindaraj, *J. Mater. Chem*. **2009**, *19*, 2457.
24. K. S. Novoselov, Z. Jiang, Y. Zhang, S. V. Morozov, H. L. Stormer, U. Zeitler, J. C. Maan, G. S. Boebinger, P. Kim, A. K. Geim, *Science*, **2007**, *315*, 1379.

# Chapter 7

## Part A

# Base-Selective Adsorption of Nucleosides to Pore-Engineered Nanocarbon, Carbon Nanocage

## Summary

This part of the chapter deals with the sorption of purine and pyrimidine based nucleosides (adenosine, guanosine and thymidine) onto various porous carbon and silica supports. As compared with mesoporous silica, porous carbons displayed superior adsorptive performance. As serendipitous finding, pronounced selection for purine-based and pyrimidine-based nucleosides by carbon nanocage has been observed. These findings would be highly useful in materials design on adsorption-based separation and column stationary phase for separation of precious and important biomolecules.

A paper based on this study has appeared in *J. Nanosci. Nanotech*, **2011**, *11*, 3959.

## 7.1. Introduction:

Selective molecular recognition has been an essential focus in supramolecular science including host-guest chemistry[1] and self-assembled nanofabrication.[2] Not limited to fundamental science and technology, practical applications such as sensing,[3] drug delivery[4] and biomedical processes[5] often requires efficient and selective molecular recognition. Molecular recognition chemistry started from complex formation between molecules dissolved in solutions.[6] Later, interfacial media such as air-water interface,[7] lipid membrane surfaces[8] and modified electrode surfaces[9] became recognized as effective medium for molecular recognition. Very recently, a concept on mechanical control of interfacial medium to precisely tune selectivity of molecular recognition is also proposed.[10]

Further advanced and practical approaches can be seen in material-based molecular selection. Materials with well designed structures such as metal organic frameworks[11] and mesoporous materials[12] are expected as powerful hosts that can recognize and accommodate target molecules within their precise nanospaces. Mesoporous materials can be easily and economically synthesized and their pore interiors can be easily modified.[13] Main bodies of mesoporous structures are changeable from hydrophilic silica[14] to hydrophobic carbon[15] as well as mixed elemental materials such as carbon nitride[16] and boron nitride.[17] Pore-geometry control of mesoporous materials is also a powerful method to create materials capable of molecular separations. Recently carbon nanocage, has been successfully demonstrated as an ideal material for tea component separation.[18] In addition, it was also realized that assembling mesoporous materials into layered structure is an efficient way to construct sensing devices with sharp molecular discrimination.[19]

Although there are plenty of possibilities in molecular recognition by pore-engineered materials, their application to biomolecules are not fully explored.

## 7.2. Scope of the present study:

In the present study we observed the base selective sorptive properties of carbon nanocage in the discrimination of nucleosides among various nanoporous materials. Nucleosides are strikingly the most important class of biomolecules in comparison with that of amino-acids, carbohydrates and lipids for their participation in the reactions those are central to the continuation and proliferation of life. Owing to their significant biochemical effects, nucleosides and their derivatives are generally employed in manufacturing medicaments.[20] However, there are few reports concerning adsorption and separation of nucleosides onto various supports.[21-23]

The curiosity in this work comes in analyzing how these nucleosides are discriminated within designed carbon nanospace. In such nanospaces, hydrophobic interactions and π-π interactions as well as van der Waals interaction play important roles which must be significantly influenced by highly restricted molecular motion in nanospaces and shape-matching between absorbent and adsorbate surfaces. In this work, we compared adsorption of three nucleosides (adenosine, guanosine and thymidine) onto various mesoporous materials including carbon nanocage, conventional mesoporous carbon (CMK-3), activated carbon and cage-type mesoporous silica (KIT-5). Adenosine and guanosine are purine based while thymidine is pyrimidine based (purine consists of pyrimidine ring fused to imidazole ring). Pronounced selection between purine and pyrimidine-based nucleosides by carbon nanocage has been recognized as serendipitous findings.

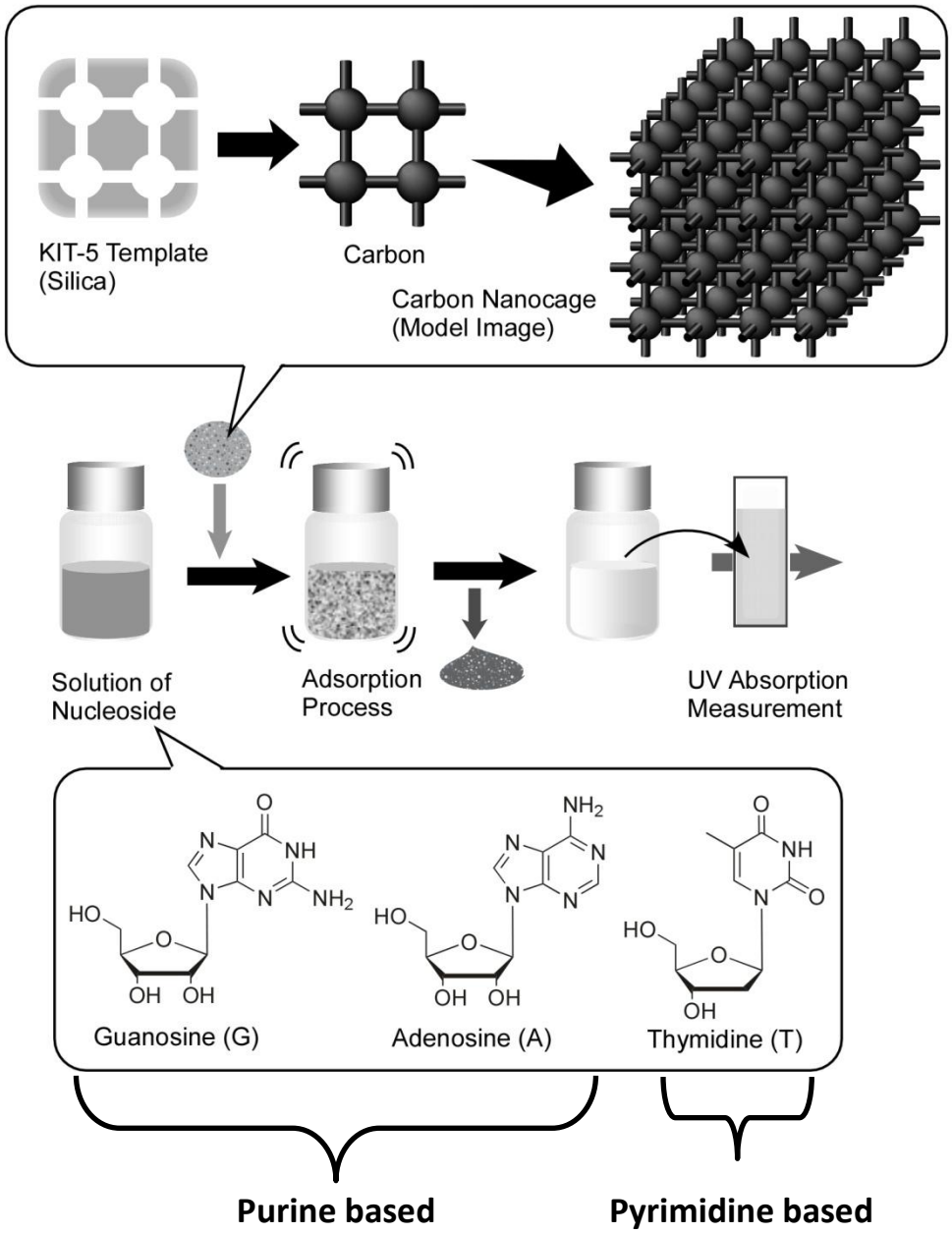


**Figure 1.** Scheme illustrating the synthesis of carbon nanocage and adsorption experiment for nucleosides.

## 7.3. Experimental and related aspects:

### (a) Materials:

Tetraethylorthosilicate (TEOS), triblock copolymers, sucrose, hydrochloric acid, potassium dihydrogen phosphate, sodium hydroxide, activated carbon,

adenosine, guanosine and thymidine were purchased at an analytical pure grade and were used without any further purification. Millipore water and ethanol were used wherever essential.

**Synthesis of mesoporous materials:**

**(b) Synthesis of mesoporous silica KIT-150:**

In a typical synthesis, 2.5 g of F127 was dissolved in 120 g of distilled water and 5.25 g of concentrated hydrochloric acid (35 wt% HCl). To this mixture, 12 g of TEOS was quickly added under stirring at 45 $^{o}$C. The mixture was stirred at 45 $^{o}$C for 24 h for the formation of the mesostructured product. Subsequently, the reaction mixture was heated for 24 h at 150 $^{o}$C under static conditions for hydrothermal treatment. The solid product was then filtered and dried at 100 $^{o}$C without washing. Finally, the samples were calcined at 550 $^{o}$C to remove the template.

**(c) Synthesis of Carbon Nanocage (CNC):**

In a typical synthesis, 1 g of mesoporous silica KIT-150 template was added to a solution obtained by dissolving 0.45 g of sucrose and 0.05 g of sulphuric acid in 2.5 g of water. The obtained mixture was kept in an oven for 6 h at 100 $^{o}$C. Subsequently, the oven temperature was raised to 160 $^{o}$C for another 6 h. In order to obtain fully polymerized and carbonized sucrose inside the pores of the silica template, 0.3 g of sucrose, 0.03 g of sulphuric acid and 2.5 g of water were added to the pre-treated sample and the mixture was again subjected to the thermal treatment described above. The template-polymer composites were then pyrolyzed in a nitrogen flow at 900 $^{o}$C and kept under these conditions for 5 h to carbonize the polymer. The carbon nanocage were recovered after dissolution of the silica

framework in a 5 wt% solution of hydrofluoric acid by filtration, washed several times with ethanol and dried at 120 $^{o}$C.

**(d) Synthesis of SBA-15-150**

In a typical synthesis, 4 g of Pluronic P123 was added to 30 g of water. After stirring for a few hours, a clear solution was obtained. Thereafter, 120 g of 2 M HCl was added and the solution was stirred for another 2 h. Then, 9 g of tetraethylorthosilicate was added and the resulting mixture was stirred for 24 h at 40 $^{o}$C, and subsequently heated for 48 h to 150 $^{o}$C under hydrothermal conditions. The solid product was recovered by filtration, washed several times with water, and dried overnight at 100 $^{o}$C. Finally, the product was calcined at 540 $^{o}$C to remove the template.

**(e) Synthesis of CMK-150:**

In a typical synthesis of mesoporous carbon, 1 g of mesoporous silica material SBA-15 was added to a solution obtained by dissolving 1.25 g of sucrose and 0.14 g of $H_2SO_4$ in 5 g of water, and keeping the mixture in an oven for 6 h at 100 $^{o}$C. Subsequently, the oven temperature was raised to 160 $^{o}$C for another 6 h. In order to obtain fully polymerized and carbonized sucrose inside the pores of the silica template, 0.8 g of sucrose, 0.09 g of $H_2SO_4$ and 5 g of water were again added to the pre-treated sample and the mixture was again subjected to the thermal treatment described above. The template-polymer composites were then pyrolyzed in a nitrogen flow at 900 $^{o}$C and kept under these conditions for 6 h to carbonize the polymer. The mesoporous carbon was recovered after dissolution of the silica framework in 5 wt% hydrofluoric acid, by filtration, washed several times with ethanol and dried at 100 $^{o}$C.

**(f) Nucleoside adsorption:**

A series of standard nucleoside solutions with concentration ranging from 0.5 to 5 g/L was prepared by dissolving different amount of nucleosides in 25 mM buffer solution at a pH 6.5 by using potassium dihydrogen phosphate buffer. In each experiment, 20 mg of the different nanoporous adsorbents were suspended in 4g of the respective nucleoside solution. The resulting mixture was continuously shaken in an agitator bathat 20 ºC until equilibrium was reached (30 minutes). The amount of nucleoside molecule adsorbed was calculated by subtracting the amount found in the supernatant liquid after adsorption from the amount of nucleoside present before addition of the adsorbent by UV absorption at characteristic wavelength maximum of the corresponding nucleoside. Calibration experiments were done separately before each set of measurements with nucleoside solutions of different concentrations in buffer solution. Centrifugation prior to the analysis was used to avoid potential interference from suspended scattering particles in the UV-Vis spectroscopic analysis.

## 7.4. Characterization technique:

**UV-Vis Spectroscopy**: UV-Vis spectroscopic measurements of adsorption of nucleosides to various porous materials were performed with Perkin Elmer Lambda 750.

**Computational details**:

For estimation of molecular size, nucleoside molecules were visualized using VMD (Visual Molecular dynamics)[24] and geometry optimization was done using ADF (Amsterdam Density Functional)[25] programs.

## 7.5. Results and Discussion:

Adsorption isotherms of three nucleosides such as guanosine, adenosine and thymidine onto various mesoporous materials such as carbon nanocage, mesoporous carbon CMK-3, activated carbon and mesoporous silica KIT-5 are summarized in Figures 2, 3 and 4 respectively. As a general tendency, mesoporous silica KIT-5 is basically inert towards all the nucleosides where very poor adsorption capacity was identified, although the molecular size of nucleosides (described later) are reasonably small in comparison with that of the pore size of the KIT-5 (Barret-Joyner-Halenda pore diameter, 5.7 nm; specific surface area, 470 $m^2/g$; specific pore volume, 0.75 $cm^3/g$). This could be due to the absence of hydrophobic interactions and π-π interactions, which unlikely to occur in the case of mesoporous silica.

In the case of nanoporous carbons each isotherm showed a steep initial rise, signifying a high affinity for the guest molecule and then gradually increasing and reaching a plateau at higher final concentration. Overall, the amount of nucleosides adsorbed on the activated carbon is smaller than those of carbon nanocage and CMK-3. Since the size of the nucleoside molecules and the pore size of activated carbon are roughly the same (pore size of the activated carbon on the basis of nonlocal density functional theory (NLDFT), less than 1 nm; specific surface area, 1629 $m^2/g$; specific pore volume, 0.70 $cm^3/g$), the diffusion of nucleosides into the pores for efficient adsorption is greatly suppressed besides having high specific surface area. In contrast, carbon nanocage (Barret-Joyner-Halenda pore diameter, 5.2 nm; specific surface area, 1851 $m^2/g$; specific pore volume, 2.23 $cm^3/g$) and CMK-3 (Barret-Joyner-Halenda pore diameter, 5.4 nm; specific surface area, 1350 $m^2/g$; specific pore volume, 1.60 $cm^3/g$) for their large pores, facilitate the nucleoside

diffusion into the pores and hence the adsorption of nucleosides. Interestingly, detailed adsorption profiles of nucleosides to three carbon materials (carbon nanocage, CMK-3 and activated carbon) show (Figures 2-4) certain dependency on nucleoside molecules.

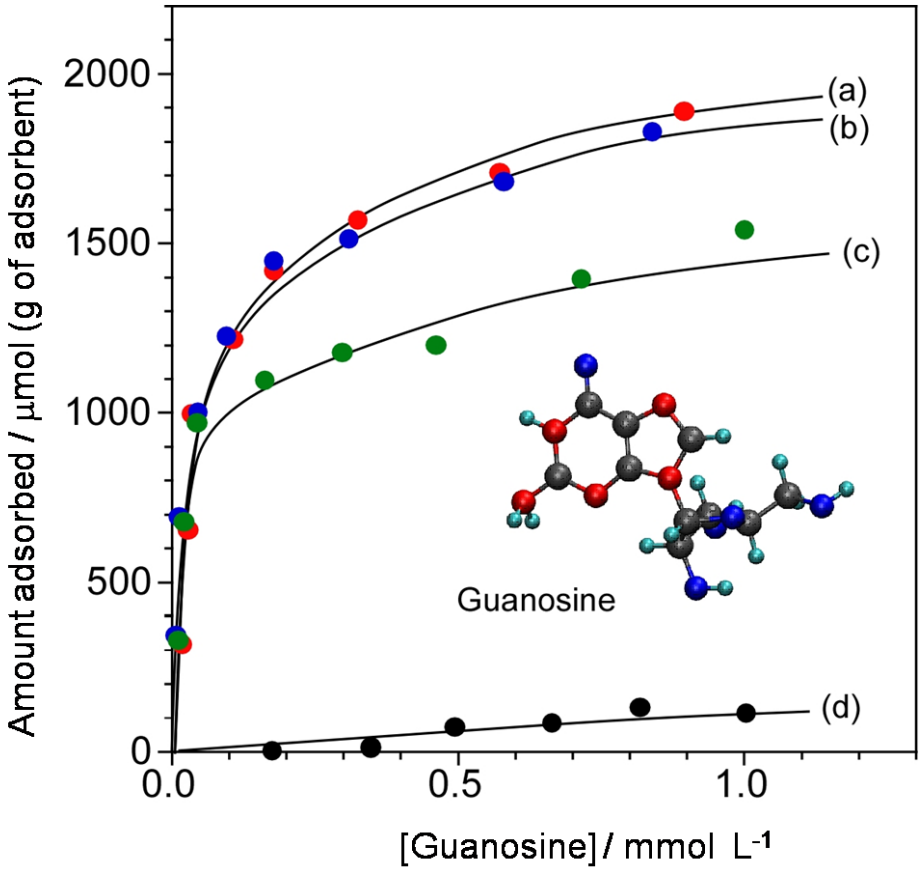


**Figure 2.** Binding isotherms of guanosine to porous materials: (a) carbon nanocage; (b) mesoporous carbon CMK-3; (c) activated carbon; (d) mesoporous silica KIT-5.

Figure 2 summarizes adsorption profiles of guanosine onto porous hosts. Guanosine belongs to purine family having a molecular size of 1 nm which is relatively large amongst all the nucleosides. Carbon nanocage and CMK-3 show very good adsorption capacity to guanosine compared to the microporous activated carbon and hydrophilic mesoporous silica KIT-5.

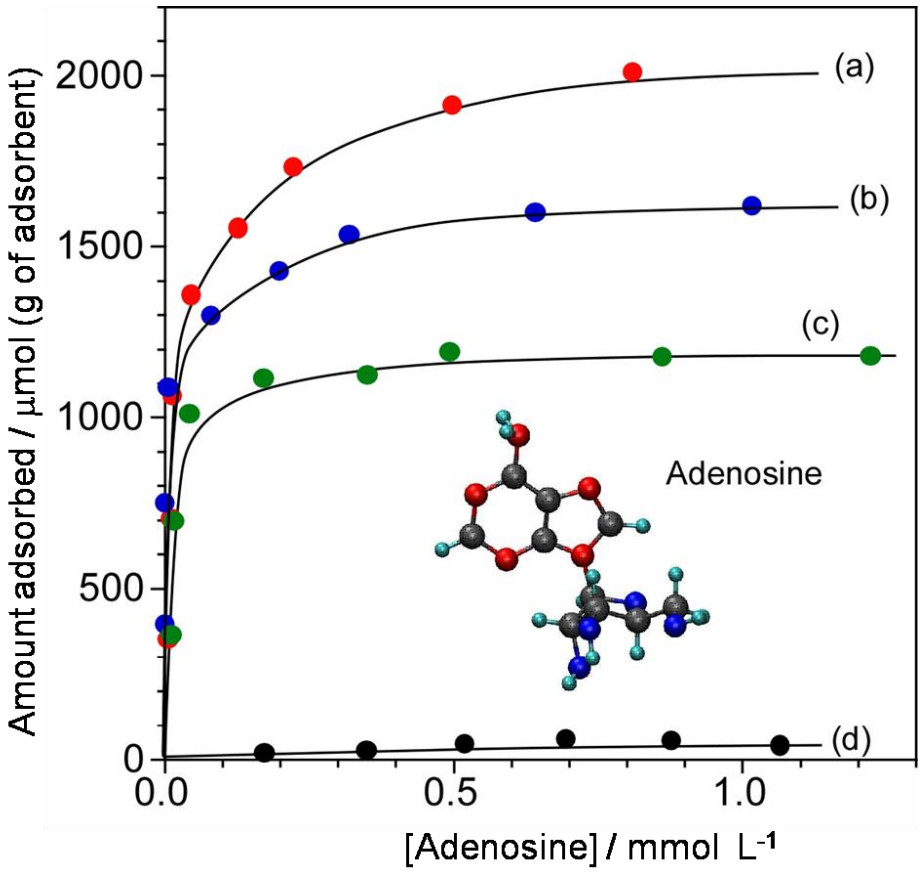


**Figure 3.** Binding isotherms of adenosine to porous materials: (a) carbon nanocage; (b) mesoporous carbon CMK-3; (c) activated carbon; (d) mesoporous silica KIT-5.

In Figure 3, adenosine adsorption on different porous supports is displayed. Adenosine belongs to the purine family with a molecular size of approximately 0.75 nm and is structurally planar. Each isotherm showed a sharp initial rise, suggesting a high affinity between guest molecule and the adsorbent surface and slowly increases and reaches a plateau at higher concentrations. In particular, carbon nanocage displayed maximum adsorption, while CMK-3 showed 17 % lesser adsorptive capacity than carbon nanocage, followed by activated carbon which showed 42 % less adsorption capacity. Poor adsorption capacity of adenosine was again observed in the case of KIT-5.

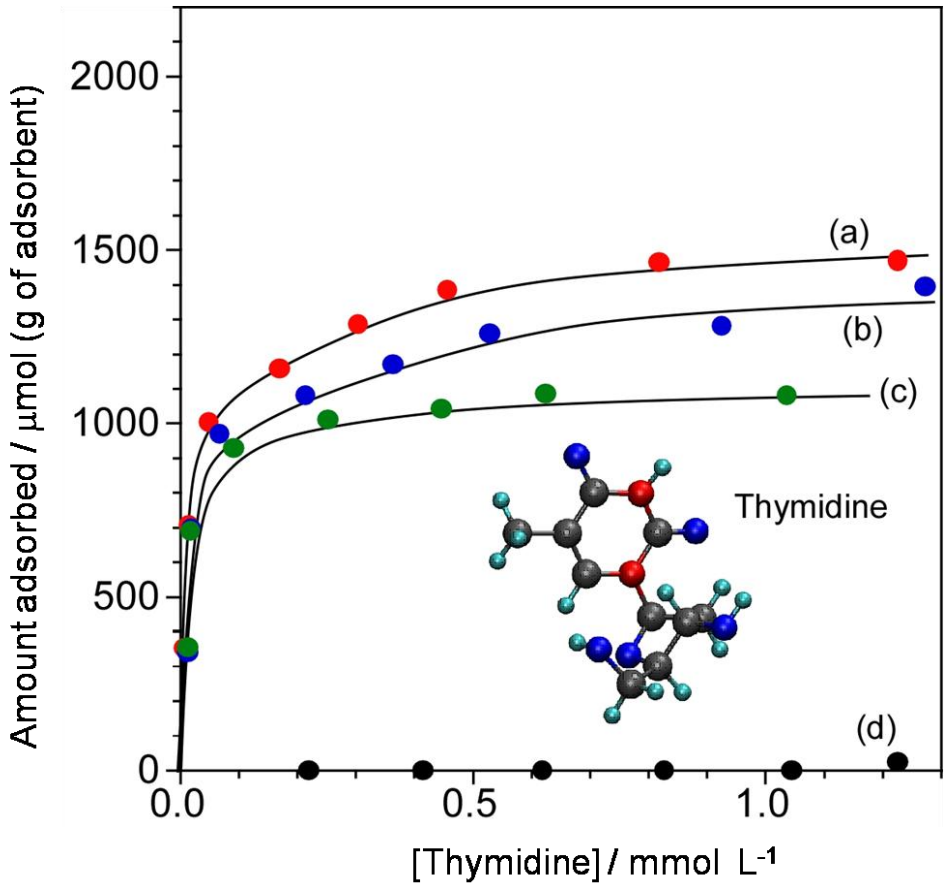


**Figure 4.** Binding isotherms of thymidine to porous materials: (a) carbon nanocage; (b) mesoporous carbon CMK-3; (c) activated carbon; (d) mesoporous silica KIT-5.

Thymidine nucleoside (molecular size of approximately 0.78 nm) is categorized as a pyrimidine family which has a single aromatic ring. From Figures 2, 3 and 4 it can be inferred that all the carbon materials show relatively strong adsorption for purine based nucleosides (adenosine and guanosine) then thymidine. Probably, the large purine ring has strong hydrophobic, π-π and van der Waals interactions with the carbon surface in comparison to pyrimidine ring. In the case of thymidine, carbon nanocage displayed maximum adsorption capacity followed by CMK-3 (Figure 4). Due to the smaller size of the thymidine molecule activated carbon also shows a good adsorptive behaviour although it is 23 % less as compared

to carbon nanocage. KIT-5 due to its hydrophilic nature displayed poor adsorption towards thymidine.

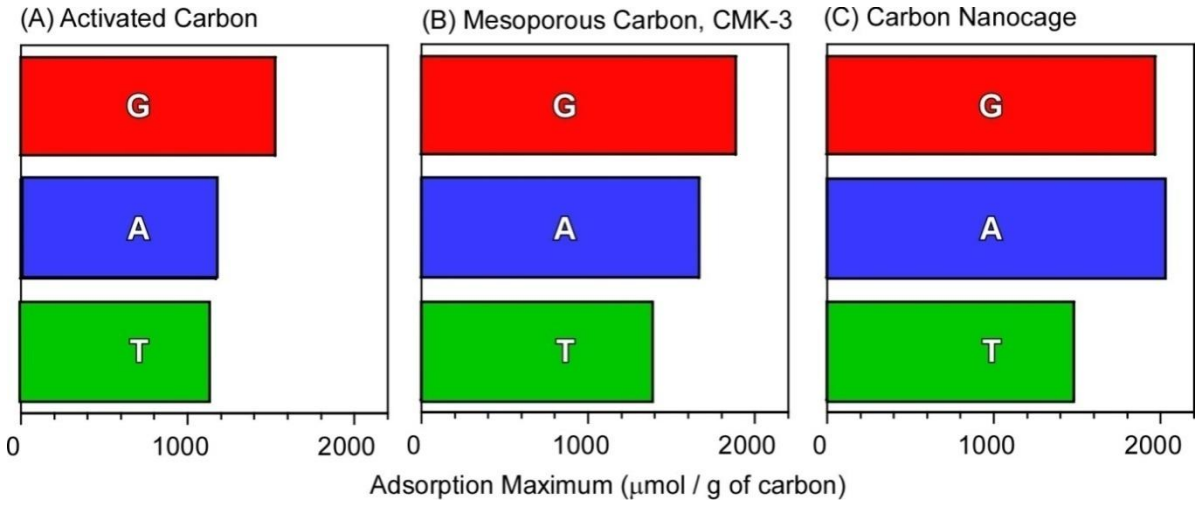


**Figure 5.** Binding selectivity between nucleosides [guanosine (G), adenosine (A), and thymidine (T)]: (A) activated carbon; (B) mesoporous carbon CMK-3; (C) carbon nanocage.

Adsorption selectivity for three nucleosides (adenosine, guanosine and thymidine) over three carbon materials is summarized in Figure 5. As a general trend, guanosine is adsorbed in high selectivity in all the cases while thymidine always shows minimum adsorption. Guanosine has a larger hydrophobic aromatic plane than thymidine, which causes more favourable hydrophobic interaction and π-π interaction. Activated carbon and CMK-3 showed adsorption behaviour for the nucleosides in the following order guanosine > adenosine > thymidine whereas, carbon nanocage has clear discrimination capability between purine family (guanosine and adenosine) and pyrimidine family (thymidine). In order to quantitatively clarify selectivity between purine and pyrmidine bases, binding selectivities (guanosine/thymidine and adenosine/thymidine) are summarized in Figure 6. Binding selectivity to (G/T) is more or less same in all the carbon materials

(Figure 6A). In contrast, binding affinity to adenosine over thymidine is more pronounced in the case of carbon nanocage (Figure 6B).

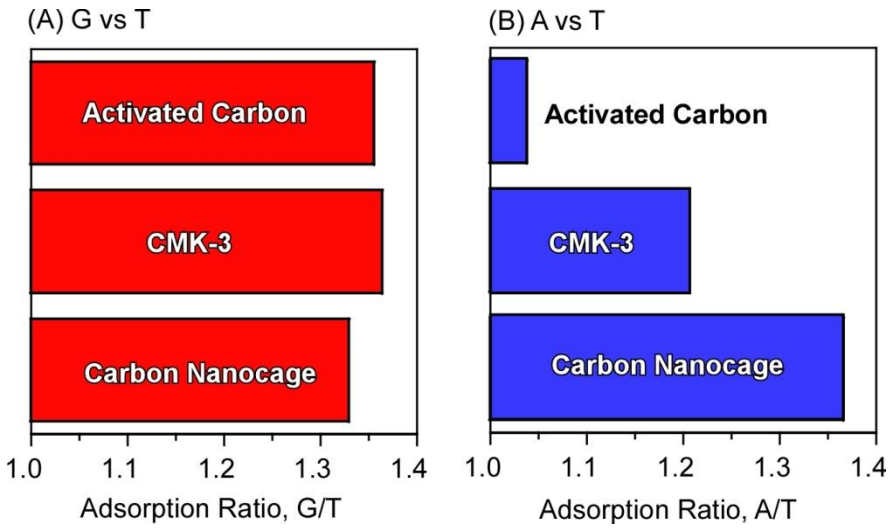


**Figure 6.** Binding selectivity between purine-base and pyrmidine-base nucleosides: (A) guanosine over thymidine; (B) adenosine over thymidine.

These results indicate that carbon nanocage has discrimination capability between purine and pyrimidine nucleosides and is especially a good material to differentiate adenosine and thymidine. Purine bases generally have large aromatic π plane which is advantageous for adsorption over carbon through hydrophobic interaction and π-π stacking. Larger pore volume of carbon nanocage probably allows sufficient freedom of guest (nucleoside) motion, resulting in favourable contact between guest (nucleoside) molecules. Such effects would result in selective binding to purine-base nucleosides.

## 7.6. Conclusions:

We have investigated the adsorption behaviour of various fundamental building blocks central to the origin of life, nucleosides onto various porous carbon

and silica supports. As compared with mesoporous silica, porous carbons displayed superior adsorptive performance. Porous carbons due to its high surface area, pore volume and hydrophobic nature show strong adsorption to nucleosides. Pronounced selection between purine- and pyrimidine-base nucleosides by carbon nanocage has been observed. These pore-engineered materials for the selective sorption would be highly applicable in the separation of precious and important biomolecules.

## 7.7. References:


1. a) F. D. Souza, N. K. Subbaiyan, Y. Xie, J. P. Hill, K. Ariga, K. Ohkubo, S. Fukuzumi, *J. Am. Chem. Soc.* **2009**, *131*, 16138, b) J. P. Hill, M. E. El-Khouly, R. Charvet, N. K. Subbaiyan, K. Ariga, S. Fukuzumi, F. D. Souza, *Chem. Commun.* **2010**, 46, 7933.
2. a) K. Ariga, J. P. Hill, Q. Ji, *Phys. Chem. Chem. Phys.* **2007**, *9*, 2319**,** b) K. Ariga, J. P. Hill, M. V. Lee, A. Vinu, R. Charvet, S. Acharya, *Sci. Technol. Adv. Mater.* **2008**, *9*, 014109, c) S. Mandal, M. V. Lee, J. P. Hill, A. Vinu, K. Ariga, *J. Nanosci. Nanotechnol.* **2010**, *10*, 21, d) K. Ariga, X. Hu, S. Mandal, J. P. Hill, *Nanoscale.* **2010**, *2*, 198, e) K. Ariga, M. Li, G. J. Richards, J. P. Hill, *J. Nanosci. Nanotechnol.* **2011**, *11*, 1, f) E. R-Hitzky, M. Darder, P. Aranda, K. Ariga, *Adv. Mater.***2010**, *22*, 323.
3. a) Q. Ji, I. Honma, S-M. Paek, M. Akada, J. P. Hill, A. Vinu, K. Ariga, *Angew. Chem. Int. Ed.* **2010**, *49*, 9737, b) K. Ariga, G. J. Richards, S. Ishihara, H. Izawa, J. P. Hill, *Sensors.* **2010**, *10*, 6796.
4. a) Q. Ji, M. Miyahara, J. P. Hill, S. Acharya, A. Vinu, S. B. Yoon, J.-S. Yu, K. Sakamoto, K. Ariga, *J. Am. Chem. Soc.* **2008**, *130*, 2376, b) Q. Ji, S. Acharya, J. P. Hill, A. Vinu, S. B. Yoon, J.-S. Yu, K. Sakamoto, K. Ariga, *Adv. Funct. Mater.* **2009**, *19*, 1792.
5. a) K. Ariga, J. P. Hill, Q. Ji, *Macromol. Biosci.* **2008**, *8*, 981, b) K. Ariga, Q. Ji, J. P. Hill, N. Kawazoe, G. Chen, *Expert Opin. Biol. Ther.* **2009**, *9*, 307, c) K. Ariga, Q. Ji, J. P. Hill**,** *Adv. Polym. Sci.* **2010**, *229*, 51.
6. a) J. Smith, K. Ariga, E. V. Anslyn, *J. Am. Chem. Soc.* **1993**, *115*, 362, b) J. P. Hill, A. L. Schumacher, F. D'Souza, J. Labuta, C. Redshaw, M. R. J. Elsegood, M. Aoyagi, T. Nakanishi, K. Ariga, *Inorg. Chem.* **2006**, *45*, 8288, c)

A. Shundo, J. Labuta, J. P. Hill, S. Ishihara, K. Ariga, *J. Am. Chem. Soc.* **2009**, *131*, 9494.

7. K. Ariga, T. Kunitake, *Acc. Chem. Res.* **1998**, *31*, 371.
8. M. Onda, K. Yoshihara, H. Koyano, K. Ariga, T. Kunitake, *J. Am. Chem. Soc.* **1996**, *118*, 8524.
9. a) Y. Okahata, M. Yokobori, Y. Ebara, H. Ebato, K. Ariga, *Langmuir*.**1990**, *6*, 1148, b) Y. Ebara, H. Ebato, K. Ariga, Y. Okahata, *Langmuir*. **1994**, *10*, 2267.
10. a) K. Ariga, T. Nakanishi, J. P. Hill, Y. Terasaka, D. Sakai, J. Kikuchi, *Soft Matter*. **2005**, *1*, 132, b) K. Ariga, T. Nakanishi, J. P. Hill, *Soft Matter*. **2006**, *2*, 465, c) K. Ariga, T. Michinobu, T. Nakanishi, J. P. Hill, *Curr. Opin. Colloid Interface Sci.* **2008**, *13*, 23, d) T. Mori, K. Okamoto, H. Endo, J. P. Hill, S. Shinoda, M. Matsukura, H. Tsukube, Y. Suzuki, Y. Kanekiyo, K. Ariga, *J. Am. Chem. Soc.* **2010**, *132*, 12868.
11. a) S. Bureekaew, S. Shimomura, S. Kitagawa, *Sci. Technol. Adv. Mater.* **2008**, *9*, 014108, b) J. Seo, H. Sakamoto, R. Matsuda, S. Kitagawa, *J. Nanosci. Nanotechnol.* **2010**, *10*, 3, c) A. Phan, C. J. Doonan, F. J. U-Romo, C. B. Knobler, M. O'Keeffe, O. M. Yaghi, *Acc. Chem. Res.* **2010**, *43*, 58.
12. a) M. E. Davis, *Nature*. **2002**, *417*, 813, b) D. R. Rolison, *Science*. **2003**, *299*, 1698, c) J. W. Long, B. Dunn, D. R. Rolison, H. S. White, *Chem. Rev*. **2004**, *104*, 4463, d) A. Vinu, M. Miyahara, K. Ariga, *J. Nanosci. Nanotechnol.* **2006**, *6*, 1510, e) K. Ariga, A. Vinu, J. P. Hill, T. Mori, *Coord. Chem. Rev.* **2007**, *251*, 2562.
13. a) Q. Zhang, K. Ariga, A. Okabe, T. Aida, *J. Am. Chem. Soc.* **2004**, *126*, 988, b) A. Vinu, K. Z. Hossain, K. Ariga, *J. Nanosci. Nanotechnol.* **2005**, *5*, 347, c) W. Otani, K. Kinbara, Q. Zhang, K. Ariga, T. Aida, *Chem. Eur. J.* **2007**, *13*, 1731.

14. a) H. Jin, Z. Liu, T. Ohsuna, O. Terasaki, Y. Inoue, K. Sakamoto, T. Nakanishi, K. Ariga, S. Che, *Adv. Mater.* **2006**, *18*, 593, b) A. Vinu, J. Justus, D. P. Sawant, K. Ariga, T. Mori, P. Srinivasu, V. V. Balasubramanian, S. Velmathi, S. Alam, *Microporous Mesoporous Mater.* **2008**, *116*, 108, c) E. C. de. Oliveira, C. T. G. V. M. T. Pires, H. O. Pastore, *J. Braz. Chem. Soc.* **2006**, *17*, 16.

15. a) A. Vinu, K. Z. Hossian, P. Srinivasu, M. Miyahara, S. Anandan, N. Gokulakrishnan, T. Mori, K. Ariga, V. V. Balasubramanian, *J. Mater. Chem.* **2007**, *17*, 1819, b) P. Srinivasu, A. Vinu, N. Gokulakrishnan, S. Anandan, A. Asthana, T. Mori, K. Ariga, *J. Nanosci. Nanotechnol.* **2007**, *7*, 2913, c) R. Ryoo, S. H. Joo, S. Jun, *J. Phys. Chem. B.* **1999**, *103*, 7743, d) S. Jun, S. H. Joo, R. Ryoo, M. Kruk, M. Jaroniec, Z. Liu, T. Ohsuna, O. Terasaki, *J. Am. Chem. Soc.* **2000**, *122*, 10712.

16. a) A. Vinu, K. Ariga, T. Mori, T. Nakanishi, S. Hishita, D. Golberg, Y. Bando, *Adv. Mater.* **2005**, *17*, 1648, b) Y. Zhang, A. Thomas, M. Antonietti, X. Wang, *J. Am. Chem. Soc.* **2009**, *131*, 50, c) A. Thomas, A. Fischer, F. Goettmann, M. Antonietti, J-O. Müller, R. Schlögl, J. M. Carlsson, *J. Mater. Chem*. **2008**, *18*, 4893.

17. A. Vinu, M. Terrones, D. Golberg, S. Hishita, K. Ariga, T. Mori, *Chem. Mater*. **2005**, *17*, 5887.

18. a) A. Vinu, M. Miyahara, V. Sivamurugan, T. Mori, K. Ariga, *J. Mater. Chem.* **2005**, *15*, 5122, b) A. Vinu, M. Miyahara, T. Mori, K. Ariga, *J. Porous Mater*. **2006**, *13*, 379, c) K. Ariga, A. Vinu, M. Miyahara, J. P. Hill, T. Mori, *J. Am. Chem. Soc.* **2007**, *129*, 11022.

19. a) K. Ariga, A. Vinu, Q. Ji, O. Ohmori, J. P. Hill, S. Acharya, J. Koike, S. Shiratori, *Angew. Chem. Int. Ed.* **2008**, *47*, 7254, b) Q. Ji, S. B. Yoon, J. P. Hill, A. Vinu, J-S. Yu, K. Ariga, *J. Am. Chem. Soc.* **2009**, *131*, 4220, c) K. Ariga, Q. Ji, J. P. Hill, A. Vinu, *Soft Matter*. **2009**, *5*, 3562.

20. L. Jin, X. Ni, X. Liu, M. Wei,*Chem. Eng. Technol.* 2**010**, *33*, 82.

21. A. H. Khairy, G. Davies, H. Z. Ibrahim, E. A. Ghabbour, *J. Phys. Chem.* **1996**, *100*, 2410.

22. K. Fisher K. Huddersman, *New J. Chem.* **2008**, *26*, 1698.

23. a) N. Varghese, U. Mogera, A. Govindaraj, A. Das, P. K. Maiti, A. K. Sood, C. N. R. Rao, *Chem Phys Chem*. **2009**, *10*, 206, b) J. B. Xiao, *J. Appl. Polym. Sci.* **2007**, *103*, 3050.

24. W. Humphrey, A. Dalke, K. Schulten, *J. Molec. Graphics.* **1996**, *14*, 33.

25. G. te Velde, F. M. Bickelhaupt, S.J.A. van Gisbergen, C. Fonseca Guerra, E.J. Baerends, J.G. Snijders, T. Ziegler, *J. Comput. Chem.* **2001**, *22*, 931.

# Chapter 7

## Part B

# Carbon Nanocage: Super-Adsorber of Intercalators for DNA Protection

## Summary

This chapter deals with the adsorption behaviors of two kinds of DNA intercalators, methyl violet and 3,6-diaminoacridine hydrochloride onto various mesoporous materials such as carbon nanocage, mesoporous carbon CMK-3, activated carbon (microporous material) and mesoporous silica SBA-15. Carbon nanocage due to its unique cage type structure shows high adsorption capacity for DNA intercalators as compared to other adsorbents. In addition, competitive adsorption of methyl violet between DNA and mesoporous materials confirmed that carbon nanocage can be very efficient in inhibiting the methyl violet intercalation to DNA.

A paper based on this study has appeared in *J. Nanosci. Nanotech*. **2011**, *11*, 3084.

## 7.1. Introduction:

Preparation of microstructures has been widely explored mainly based on top-down micro-fabrication techniques. These structures are highly useful for advanced electronic devices.[1] However, they are not always good at molecular-based functions such as molecular sensing/recognition,[2] material separation,[3] drug delivery[4] and biomedical applications.[5] Most of these functions require well defined structures with molecular-level precision, which are not easily attained by top-down, micro-fabrication methods. Instead, materials with internal molecular and nano-sized structures can be prepared through bottom-up processes mainly driven by self-assembled phenomena[6] and directed-assembly process such as Langmuir-Blodgett[7] and layer-by-layer[8] assembling techniques. The bottom-up approaches on material fabrication are available in molecular complex formation,[9] molecular array formation,[10] functional micro-assemblies[11] and micron-sized materials with nano-internal structures.[12] Especially, the last category of the materials can be created through materialization of micro- and nano-structures by well-designed methodologies such as structure transcription and template synthesis.[13]

Developing various techniques to design mesoporous carbon materials with regularly arrayed pore structures whose size, geometry, dimensions and internal structures can be tunable has attracted significant interest among various researchers.[14] Various kinds of mesoporous carbons were prepared either by hard templating (mesoporous silica as template) or soft templating (amphiphilic, surfactant molecules) methods.[14] Recently, carbon nanocage[15] comprising of cage-type mesopore arrays with high surface area and pore volume, has been reported using hard templating method (mesoporous silica, KIT-150). This nanocage carbon exhibits very high affinity to aromatic organic compounds and shows unusual

separation of tea-components such as catechin and tannic acid.[16,17] However, their sorption specificity to the biomolecules and aromatic molecules remains largely unexplored.

## 7.2. Scope of the present study:

In the present work, we have paid attention to the removal of DNA intercalators by using carbon nanocage (Figure 1). Intercalating agents or intercalating dye molecules are generally used for the substantial increase in fluorescence intensity for important DNA analyses.[18,19] Intercalation of these compounds dynamically induces changes of space between DNAs base pairs by unwinding, leading often to the inhibition of transcription and replication of DNA. Therefore, most of the intercalators are suspected to be mutagenic and carcinogenic.[20-22] Not limited to intercalators, certain kinds of aromatic compounds such as dye molecules have unavoidable toxicity towards DNA often leading to DNA damage.[23] Materials such as clays, activated carbon, inorganic oxides and mesoporous materials are extensively employed as adsorbents for the removal of hazardous compounds.[24]

Here we study the adsorption behaviors of DNA intercalators, methyl violet and 3,6-diaminoacridine hydrochloride as well as cytosine as a control guest onto various mesoporous materials such as carbon nanocage, mesoporous carbon CMK-3, activated carbon and mesoporous silica SBA-15. In addition, competitive adsorption of methyl violet between DNA and mesoporous materials was examined. The obtained results clearly demonstrated that carbon nanocage is a super-adsorber of the intercalators and suppress their intercalation to DNA.

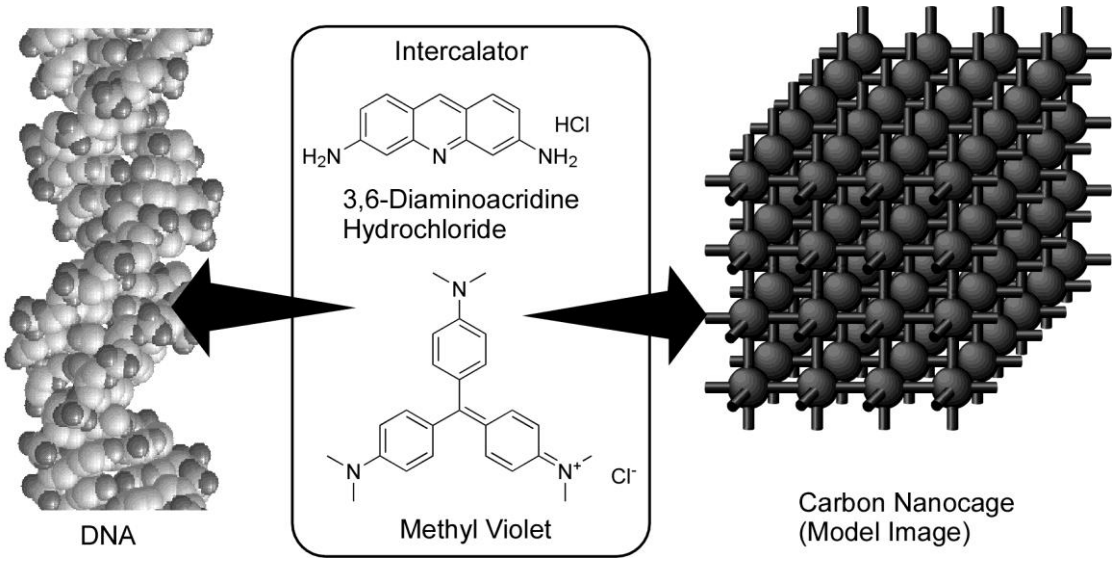


**Figure 1.** Structures of intercalators (3,6-diaminoacridine hydrochloride and methyl violet) that are supposed to intercalate into DNA and adsorb onto carbon nanocage.

## 7.3. Experimental and related aspects:

### (a) Materials:

Tetraethylorthosilicate (TEOS), triblock copolymers, sucrose, hydrochloric acid, potassium dihydrogen phosphate, sodium hydroxide, activated carbon, methyl violet, 3,6-diaminoacridine hydrochloride and cytosine were purchased at an analytical pure grade and were used without any further purification. Millipore water and ethanol were used wherever essential.

### Synthesis of mesoporous materials:

### (b) Synthesis of mesoporous silica KIT-150:

In a typical synthesis, 2.5 g of F127 was dissolved in 120 g of distilled water and 5.25 g of concentrated hydrochloric acid (35 wt% HCl). To this mixture, 12 g of TEOS was quickly added under stirring at 45 $^{o}$C. The mixture was stirred at 45 $^{o}$C for 24 h for the formation of the mesostructured product. Subsequently, the reaction

mixture was heated for 24 h at 150 $^{o}$C under static conditions for hydrothermal treatment. The solid product was then filtered and dried at 100 $^{o}$C without washing. Finally, the samples were calcined at 550 $^{o}$C to remove the template.

**(c) Synthesis of carbon nanocage (CNC):**

In a typical synthesis of carbon nanocage, 1 g of mesoporous silica KIT-150 template was added to a solution obtained by dissolving 0.45 g of sucrose and 0.05 g of sulphuric acid in 2.5 g of water. The obtained mixture was kept in an oven for 6 h at 100 $^{o}$C. Subsequently, the oven temperature was raised to 160 $^{o}$C for another 6 h. In order to obtain fully polymerized and carbonized sucrose inside the pores of the silica template, 0.3 g of sucrose, 0.03 g of sulphuric acid and 2.5 g of water were again added to the pre-treated sample and the mixture was again subjected to the thermal treatment described above. The template-polymer composites were then pyrolyzed in a nitrogen flow at 900$^{o}$C and kept under these conditions for 5 h to carbonize the polymer. The carbon nanocage was recovered after dissolution of the silica framework in a 5 wt% solution of hydrofluoric acid by filtration, washed several times with ethanol and dried at 120 $^{o}$C.

**(d) Synthesis of SBA-15-150:**

In a typical synthesis, 4 g of Pluronic P123 was added to 30 g of water. After stirring for a few hours, a clear solution was obtained. Thereafter, 120 g of 2 M HCl was added and the solution was stirred for another 2 h. Then, 9 g of tetraethylorthosilicate was added and the resulting mixture was stirred for 24 h at 40 $^{o}$C, and subsequently heated at 150 $^{o}$C for 48 h under hydrothermal conditions. The solid product was recovered by filtration, washed several times with water, and dried overnight at 100 $^{o}$C. Finally, the product was calcined at 540 $^{o}$C to remove the template.

**(e) Synthesis of CMK-150:**

In a typical synthesis of mesoporous carbon, 1 g of mesoporous silica material SBA-15 was added to a solution obtained by dissolving 1.25 g of sucrose and 0.14 g of $H_2SO_4$ in 5 g of water, and keeping the mixture in an oven for 6 h at 100 $^oC$. Subsequently, the oven temperature was raised to 160 $^oC$ for another 6 h. In order to obtain fully polymerized and carbonized sucrose inside the pores of the silica template, 0.8 g of sucrose, 0.09 g of $H_2SO_4$ and 5 g of water were added to the pre-treated sample and the mixture was again subjected to the thermal treatment described above. The template-polymer composites were then pyrolyzed in a nitrogen flow at 900 $^oC$ and kept under these conditions for 6 h to carbonize the polymer. The mesoporous carbon was recovered after dissolution of the silica framework in 5 wt% hydrofluoric acid, by filtration, washed several times with ethanol and dried at 100 $^oC$.

**(f) Intercalators adsorption:**

A series of standard methyl violet and acridine (DNA intercalating agents) solutions with concentration ranging from 0.5 to 6 g/L were prepared by dissolving different amount of methyl violet and acridine in 25 mM buffer solution at a pH 6.5 by using potassium dihydrogen phosphate buffer. In each experiment, 20 mg of different nanoporous adsorbents were suspended in 4g of the methyl violet and acridine solutions. The resulting mixture was continuously shaken in an agitator bath at 20 ºC until the equilibrium was reached (around 60 minutes). The amount of DNA intercalator adsorbed on various porous supports was calculated by subtracting the remaining amount found in the supernatant liquid after adsorption, from the amount found in original mixture (before addition of adsorbent). Calibration experiments

were done separately before each set of measurements with methyl violet and acridine solutions of different concentrations in buffer solution. Centrifugation prior to the analysis was used to avoid potential interference from suspended scattering particles in the UV-Vis spectroscopic analysis.

**(g) DNA intercalation experiment:**

Methyl violet with concentration of 2 g/L was prepared in 25 mM buffer solution at a pH 6.5 by using potassium dihydrogen phosphate buffer. A standard DNA solution with concentration of 1 g/L was prepared in 25 mM buffer solution at a pH 6.5 by using potassium dihydrogen phosphate buffer. The DNA solution (1 mL) was mixed with methyl violet solution (2 mL) followed by aging for 1 h. To the above solution, 20 mg of different nanoporous adsorbents were added. The resulting mixture was continuously shaken in an agitator bath at 20 ºC until equilibrium was reached (typically 1 h). DNA intercalation was monitored qualitatively by UV-Vis spectrophotometer. Centrifugation prior to the analysis was used to avoid potential interference from suspended scattering particles in the UV-Vis spectroscopic analysis.

## 7.4. Characterization technique:

**UV-Vis spectroscopy**: UV-Vis spectroscopic measurements of adsorption of intercalators to various mesoporous materials were performed with Perkin Elmer Lambda 750.

## 7.5. Results and Discussion:

Adsorption isotherms of 3,6-diaminoacridine hydrochloride, methyl violet and cytosine are shown in Figures 2, 3 and 4 respectively. In general, carbon

nanocage and CMK-3 have prominent adsorption capability to these guest compounds. Each isotherm shows a sharp initial rise, suggesting a high affinity between dye molecule and the mesoporous carbon adsorbent due to strong hydrophobic interactions in aqueous media as well as π-π stacking. The isotherms reach a first plateau basically obeying type L (Langmuir isotherm) behavior. However, some cases show the second rise indicating multilayer adsorption. The adsorption behaviors for each guest are shown below.

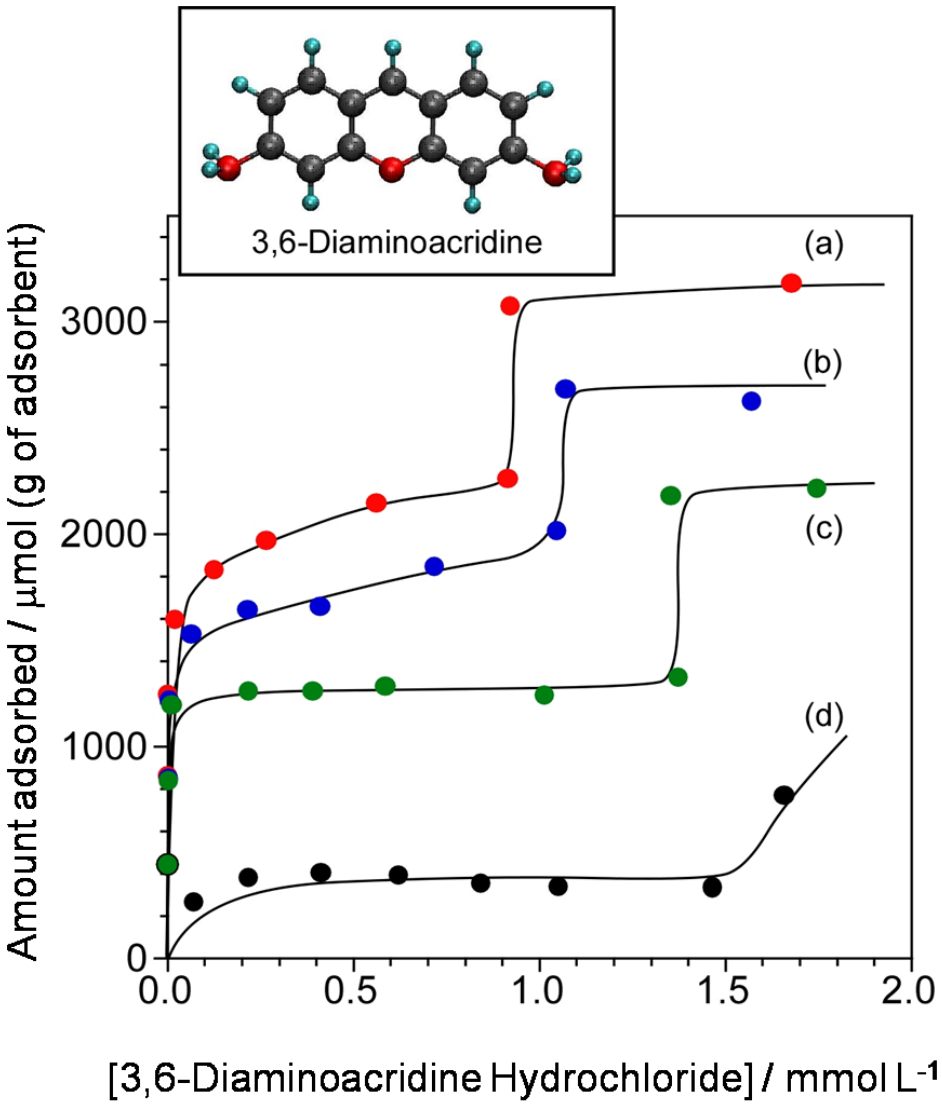


**Figure 2.** Binding isotherms of 3,6-diaminoacridine hydrochloride on (a) carbon nanocage; (b) mesoporous carbon CMK-3; (c) activated carbon; (d) mesoporous silica SBA-15.

Adsorption of 3,6-diaminoacridine hydrochloride onto various porous hosts, displayed two-stepped adsorption mode and greater adsorption at higher concentration (Figure 2). Carbon nanocage exhibited maximum adsorption capacity followed by CMK-3 which showed the similar trend with slightly lesser adsorption capacity. Activated carbon and SBA-15 also show similar trend, a two-stepped adsorption behavior, wherein the plateau region was retained till higher concentration as compared to that of carbon nanocage and CMK-3 adsorbents. The decrease in adsorption capacity in the case of activated carbon can be accounted due to the increased number of micropores which are not accessible to guest molecules. In the case of SBA-15 we observed poor adsorption capacity as compared to the rest of the porous carbon adsorbents which can be due to overall hydrophilic nature of the silica surface. The surface hydroxyl groups of SBA-15 prefer to form hydrogen bonds with water molecules present in the buffer rather than the guest molecule leading to the reduced interaction between guest and the adsorbent surface despite having large pore diameter and high pore volume (Barret-Joyner-Halenda pore diameter, 11.2 nm; specific surface area, 390 $m^2/g$; specific pore volume, 1.10 $cm^3/g$).

In the case of methyl violet all the adsorbents except activated carbon, exhibit two-stepped adsorption behavior with large amount of adsorption at higher concentration (Figure 3). Carbon nanocage again exhibited the largest adsorption capacity, while adsorption at CMK-3 was 28.8 % lower than that of carbon nanocage. Although SBA-15 has inferior adsorption capability due to its hydrophilic nature it also showed two-stepped adsorption behavior. On the other hand, activated carbon despite having high surface area shows poor adsorption as part of its

micropores are not accessible to methyl violet molecules which in turn lead to the pore blockage and aggregation of guest molecules.

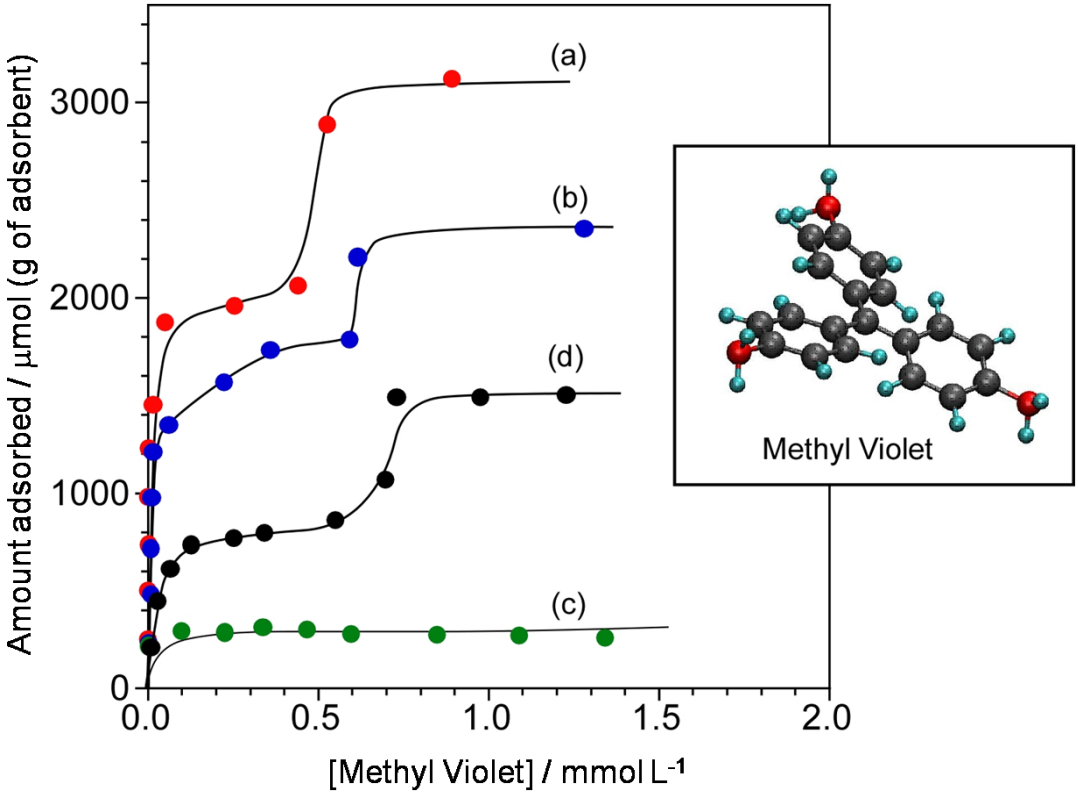


**Figure 3.** Binding isotherms of methyl violet on: (a) carbon nanocage; (b) mesoporous carbon CMK-3; (c) activated carbon; (d) mesoporous silica SBA-15.

Unlike the above-mentioned intercalators, adsorption isotherms of cytosine to carbon nanocage, CMK-3 and activated carbon showed single-step mode (Figure 4). Because cytosine has smaller aromatic ring, guest-guest interaction based upon π-π stacking would not be well pronounced, resulting in absence of multilayer adsorption behavior.

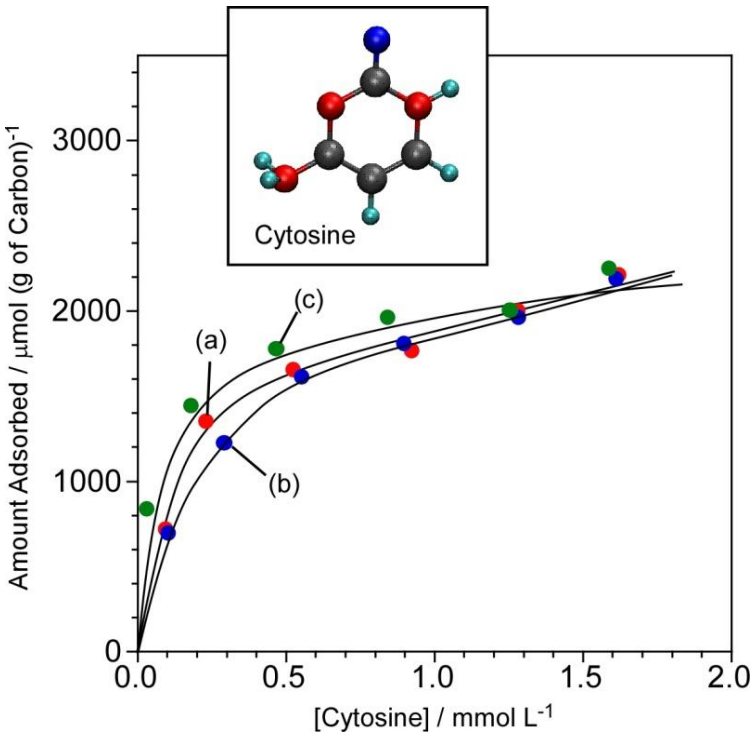


**Figure 4.** Binding isotherms of cytosine on: (a) carbon nanocage; (b) mesoporous carbon CMK-3; (c) activated carbon.

All the results displayed in Figures 2, 3 and 4 indicate superior adsorption capability of carbon nanocage to the DNA intercalator molecules, compared to the conventional carbon adsorbents such as activated carbon and mesoporous carbon.

Adsorption behaviors of carbon nanocage and CMK-3 to the intercalators are further analyzed as shown in Figure 5. First, maximum adsorption amounts ($M_{max}$) of the intercalators are plotted as a function of specific pore volume (Figure 5B). Regardless of adsorbents and adsorbates, the data fit to unified relation. This result indicates that the adsorption capability is basically determined by volume available for the adsorption. Because carbon nanocage (CNC) has high specific pore volume compared to the conventional mesoporous carbon, it has an excellent capacity for the intercalator removal.

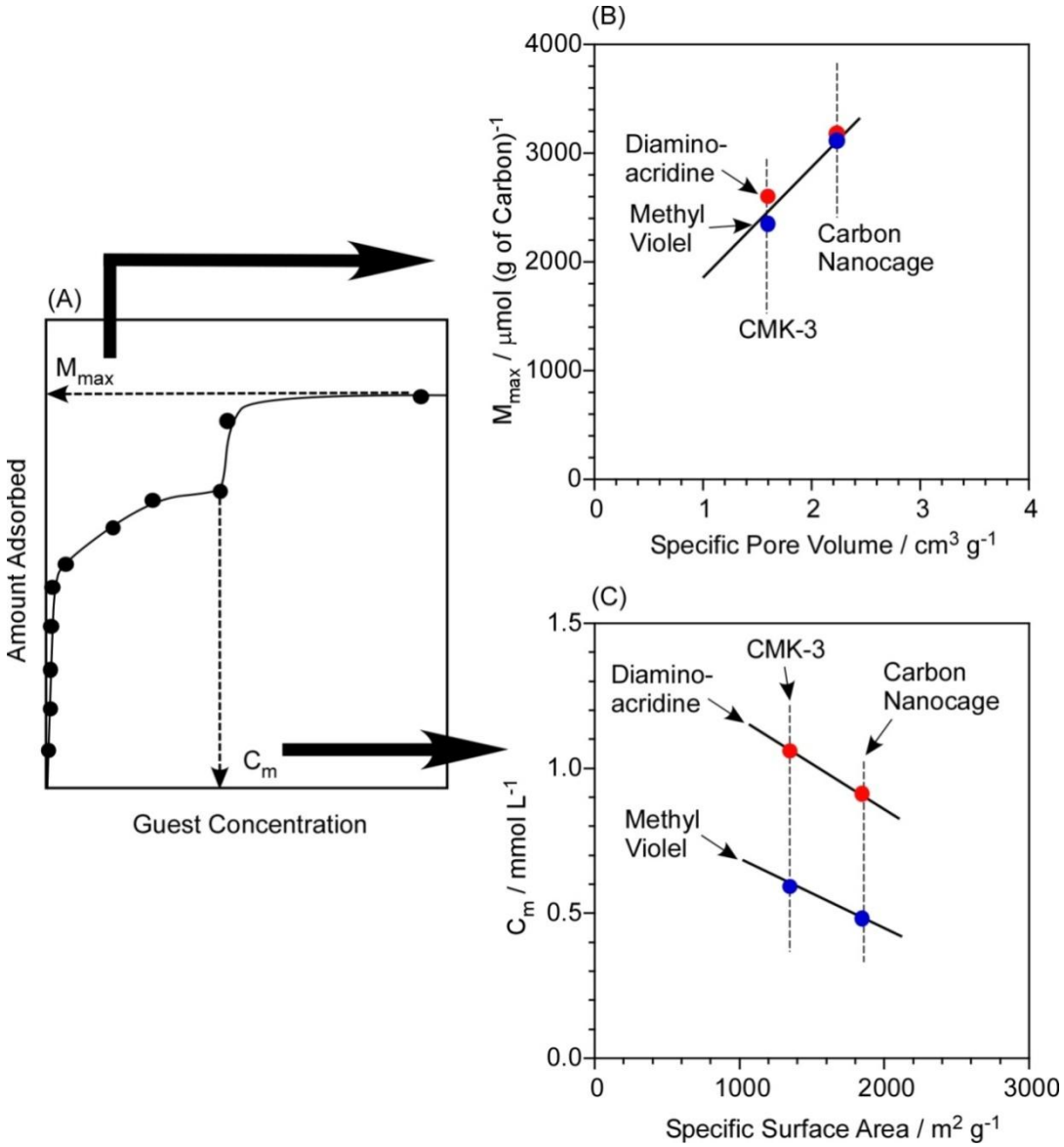


**Figure 5.** Analyses on binding isotherms of methyl violet and 3,6-diaminoacridine to mesoporous carbon materials (carbon nanocage and mesoporous carbon CMK-3): (A) parameters used for analyses; (B) maximum adsorption amount ($M_{max}$) as function of specific pore volume; (C) concentration at initiation of multilayer adsorption ($C_m$) as function of specific surface area. Blue and red plots come from the experimental data of methyl violet and 3,6-diaminoacridine adsorption, respectively.

Next, guest concentrations for starting multilayer adsorption ($C_m$) are plotted as a function of specific surface area (Figure 5C). Since multilayer adsorption occurs after covering the entire surface with monolayer of the guest molecules, one can expect higher $C_m$ values for materials with larger surface area. As opposite to this

expectation, carbon nanocage with large surface area has smaller $C_m$ value. This result suggests that guest-guest interaction for multilayer adsorption is well promoted within the pores of carbon nanocage. Huge pore volume of carbon nanocage probably allows large freedom of guest motion, resulting in favourable contact between guest molecules.

Finally, we examined competitive adsorption of methyl violet to porous adsorbents and DNA (Figure 6). Mixing DNA with methyl violet leads to DNA intercalation, wherein dye molecules slip in between the stacked bases of DNA. We observed a spectral shift ($\lambda_{max}$ shifts from 260 nm to 248 nm) upon an electronic stacking interaction of dye molecules with the base pairs of helix, characteristic of intercalation (Figure 6A).[25,26]

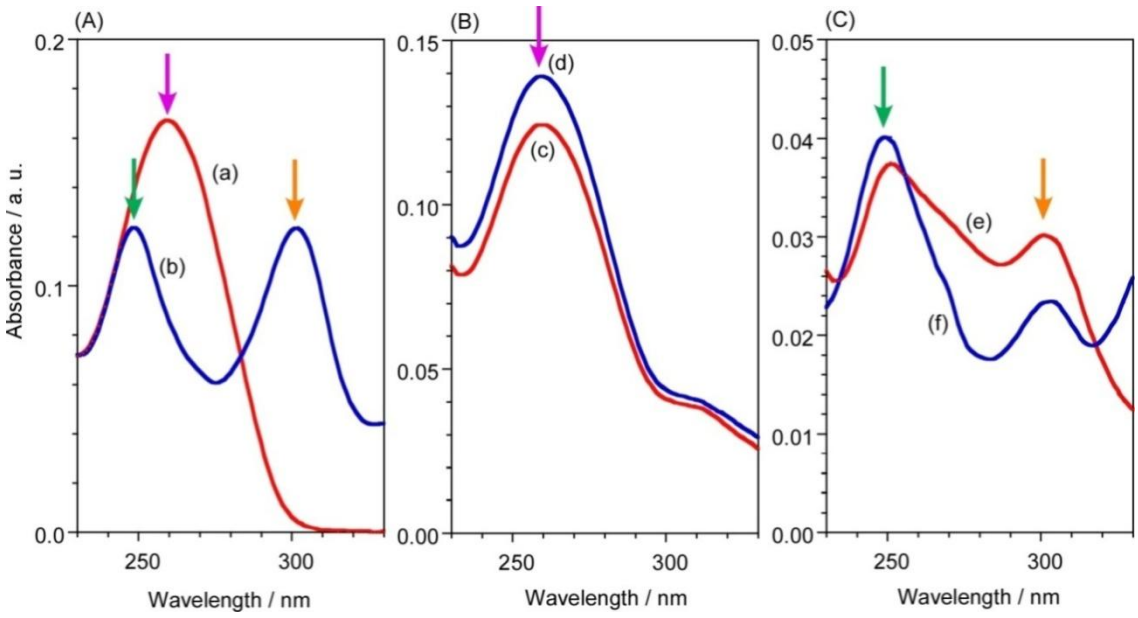


**Figure 6.** UV spectra of DNA with and without methyl violet and adsorbents (see Experimental section for details): (A) (a) DNA alone and (b) DNA + methyl violet; (B) (c) DNA + methyl violet + carbon nanocage and (d) DNA + methyl violet + CMK-3; (C) (e) DNA + methyl violet + activated carbon and (f) DNA + methyl violet + SBA-15. Green arrow represents a peak for native DNA. Violet and orange arrows indicated peaks resulted from intercalation of methyl violet to DNA.

We expect that addition of adsorbents to intercalated DNA selectively adsorbs methyl violet molecules (intercalated in DNA) thus the peak in the UV-Vis absorption reverts back to DNA spectrum ($\lambda_{max}$ = 260 nm). The presence of carbon nanocage and CMK-3 showed retention of DNA peak through removing the dye molecule initially bound to DNA (Figure 6B). In contrast, activated carbon and SBA-15 are not capable of deintercalating the dye molecules from the DNA.

These results indicate the preferential binding ability of carbon nanocage and CMK-3 towards methyl violet and hence its deintercalation from DNA. DNA intercalation process can be repaired or altered by using nanoporous materials such as carbon nanocage that has hydrophobic character along with high surface area, large pore volume and pore size.

## 7.6. Conclusions:

We showed a simplistic approach to adsorb and remove carcinogenic and mutagenic dye molecules like acridine and methyl violet which are responsible for DNA intercalation. Carbon nanocage due to its unique cage type structure shows high adsorption capacity as compared with the other adsorbents like mesoporous carbon CMK-3, activated carbon and mesoporous silica SBA-15. It was also demonstrated that carbon nanocage as well as CMK-3 can inhibit intercalation of methyl violet to DNA. Thus, carbon nanocage is exceptionally good material for removal of DNA intercalators and would be used for entrapment of many harmful aromatic molecules which are considered to be a biggest peril to the modern world.

## 7.7. References:


1. a) R. Waser M. Aono, *Nat. Mater.* **2007**, *6*, 833, b) T. Hino, H. Tanaka, T. Hasegawa, M. Aono, T. Ogawa, *Small.* **2010**, *6*, 1745, c) T. Hasegawa, T. Ohno, K. Terabe, T. Tsuruoka, T. Nakayama, J. K. Gimzewski, M. Aono, *Adv. Mater.* **2010**, *22*, 1831, d) M. Nakaya, S. Tsukamoto, Y. Kuwahara, M. Aono, T. Nakayama, *Adv. Mater.* **2010**, *22*, 1622, e) S. Wu, T. Tsuruoka, K. Terabe, T. Hasegawa, J. P. Hill, K. Ariga, M. Aono, *Adv. Funct. Mater.* **2011**, *21*, 93.
2. a) K. Ariga, A. Vinu, Q. Ji, O. Ohmori, J. P. Hill, S. Acharya, J. Koike, S. Shiratori, *Angew. Chem. Int. Ed.* **2008**, *47*, 7254, b) Q. Ji, S. B. Yoon, J. P. Hill, A. Vinu, J.-S. Yu, K. Ariga, *J. Am. Chem. Soc.* **2009**, *131*, 4220, c) K. Ariga, G. J. Richards, S. Ishihara, H. Izawa, J. P. Hill, *Sensors*. **2010**, *10*, 6796.
3. a) K. Ariga, Y. Okahata, *J. Am. Chem. Soc.* **1988**, *111*, 5618, b) K. Ariga, A. Vinu, J. P. Hill, T. Mori, *Coord. Chem. Rev.* **2007**, *251*, 2562.
4. a) Q. Ji, S. Acharya, J. P. Hill, A. Vinu, S. B. Yoon, J.-S. Yu, K. Sakamoto, K. Ariga, *Adv. Funct. Mater.* **2009**, *19*, 1792, b) Q. Ji, M. Miyahara, J. P. Hill, S. Acharya, A. Vinu, S. B. Yoon, J.-S. Yu, K. Sakamoto, K. Ariga, *J. Am. Chem. Soc.* **2008**, *130*, 2376.
5. a) K. Ariga, J. P. Hill, Q. Ji, *Macromol. Biosci.* **2008**, *8*, 981, b) K. Ariga, Q. Ji, J. P. Hill, N. Kawazoe, G. Chen, *Expert Opin. Biol. Ther.* **2009**, *9*, 307, c) E. R-Hitzky, M. Darder, P. Aranda, K. Ariga, *Adv. Mater.* **2010,** *22*, 323.
6. a) T. Nakanishi, K. Ariga, T. Michinobu, K. Yoshida, H. Takahashi, T. Teranishi, H. Möhwald, D. G. Kurth, *Small.* **2007**, *3*, 2019, b) K. Ariga, J. P. Hill, M. V. P. Lee, A. Vinu, R. Charvet, S. Acharya, *Sci. Technol. Adv.*

*Mater.* **2008**, *9*, 014109, c) K. Ariga, X. Hu, S. Mandal, J. P. Hill, *Nanoscale.* **2010**, *2*, 198, d) K. Ariga, M. Li, G. J. Richards, J. P. Hill, *J. Nanosci. Nanotechnol.* **2011**, *11*, 1.

7. S. Acharya, J. P. Hill, K. Ariga, *Adv. Mater.* **2009**, *21*, 2959.
8. a) N. Fujii, K. Fujimoto, T. Michinobu, M. Akada, J. P. Hill, S. Shiratori, K. Ariga, K. Shigehara, *Macromolecules.* **2010**, *43*, 3947, b) K. Ariga, J. P. Hill, Q. Ji, *Phys. Chem. Chem. Phys.* **2007**, *9*, 2319.
9. a) F. D. Souza, N. K. Subbaiyan, Y. Xie, J. P. Hill, K. Ariga, K. Ohkubo, S. Fukuzumi, *J. Am. Chem. Soc.* **2009**, *131*, 16138, b) J. P. Hill, M. E. El-Khouly, R. Charvet, N. K. Subbaiyan, K. Ariga, S. Fukuzumi, F. D. Souza, *Chem. Commun.* **2010**, *46*, 7933.
10. a) T. Nakanishi, H. Takahashi, T. Michinobu, J. P. Hill, T. Teranishi, K. Ariga, *Thin Solid Films.* **2008,** *516*, 2401, b) J. P. Hill, R. Scipioni, M. Boero, Y. Wakayama, M. Akada, T. Miyazaki, K. Ariga, *Phys. Chem. Chem. Phys.* **2009**, *11*, 6038.
11. a) S. Acharya, S. Kundu, J. P. Hill, G. J. Richards, K. Ariga, *Adv. Mater.* **2009**, *21*, 989, b) R. Charvet, S. Acharya, J. P. Hill, M. Akada, M. Liao, S. Seki, Y. Honsho, A. Saeki, K. Ariga, *J. Am. Chem. Soc.* **2009**, *131*, 18030. c) S. Kundu, J. P. Hill, G. J. Richards, K. Ariga, A. H. Khan, U. Thupakula, S. Acharya, *ACS Appl. Mater. Interfaces.* **2010**, *2*, 2759.
12. a) H. Jin, Z. Liu, T. Ohsuna, O. Terasaki, Y. Inoue, K. Sakamoto, T. Nakanishi, K. Ariga, S. Che, *Adv. Mater.* **2006**, *18*, 593, b) A. Vinu, M. Miyahara, K. Ariga, *J. Nanosci. Nanotechnol.* **2006**, *6*, 1510.
13. a) S. Mandal, M. Sathish, G. Saravanan, K. K. R. Datta, Q. Ji,J. P. Hill, H. Abe,I. Honma, K. Ariga, *J. Am. Chem. Soc.* **2010**, *132*, 14415, b) S. Mandal,

M. V. Lee, J. P. Hill, A. Vinu, K. Ariga, *J. Nanosci. Nanotechnol.* **2010**, *10*, 21.

14. a) F. Schüth, *Angew. Chem. Int. Ed.* **2003**, *42*, 3604, b) T. N. Hoheisel, S. Schrettl, R. Szilluweit, H. Frauenrath, *Angew. Chem. Int. Ed.* **2010**, *49*, 6496, c) C. Liang, Z. Li, S. Da, *Angew. Chem. Int. Ed.* **2008**, *47*, 3696.
15. A. Vinu, M. Miyahara, V. Sivamurugan, T. Mori, K. Ariga, *J. Mater. Chem.* **2005**, *15*, 5122.
16. A. Vinu, M. Miyahara, T. Mori, K. Ariga, *J. Porous Mater.* **2006**, *13*, 379.
17. K. Ariga, A. Vinu, M. Miyahara, J. P. Hill, T. Mori, *J. Am. Chem. Soc.* **2007**, *129*, 11022.
18. W. D. Wilson, R. L. Jones, *Adv. Pharmcol. Chemother.* **1981**, *18*, 177.
19. K. E. Erkkila, D. T. Odom, J. K. Barton, *Chem. Rev.* **1999**, *99*, 2777.
20. H. Ihmels, K. Faulhaber, D. Vedaldi, F. D. Acqua, G. Viola, *Photochem. Photobiol.* **2005**, *81*, 1107.
21. V. Brabec, O. Novakova, *Drug Resist. Updates.* **2006**, *9*, 111.
22. H.-T. Wang, S. Zhang, Y. Hu, M.-S. Tang, *Chem. Res. Toxicol.* **2009**, *22*, 511.
23. T. Lindahl, *Nature*. **1993**, *362*, 709.
24. a) X. Zhuang, Y. Wan, C. Feng, Y. Shen, D. Zhao, *Chem. Mater.* **2009,** *21*,706, b) M. Dogan, M. Alkan, *Chemosphere.* **2003**, *50*, 517, c) M. Dogan, M. Alkan, *Journal of Colloid and Interface Science*. **2003**, *267*, 32.
25. V. A. Bloomfield, D. M. Crothersn, I. Tinoco, in *Physical Chemistry of Nucleic Acids*, **1974**, *Harper and Row*, 432.
26. M. Aslanoglu, *Anal. Sci.* **2006**, *22*, 439.

# List of Publications

***From Thesis:***

1. *Water-Solubilized Aminoclay-Metal Nanoparticle Composites and their Novel Properties,* **K. K. R. Datta**, M. Eswaramoorthy, C. N. R. Rao, ***J. Mater. Chem***. **2007**, *17*, 613-615.

2. *Synthesis of Agarose-Metal/Semiconductor Nanoparticles having Superior Bacteriocidal Activity and their Simple Conversion to Metal-Carbon Composites,* **K. K. R. Datta**, B. Srinivasan, H. Balaram, M. Eswaramoorthy, ***J. Chem. Sci*. 2008**, *120*, 579-586.

3. *Aminoclay: A Permselective Matrix to Stabilize Copper Nanoparticles,* **K. K. R. Datta**, C. Kulkarni, M. Eswaramoorthy, ***Chem. Commun***. **2010**, *46*, 616-618.

4. *Gold Nanoparticles Embedded in a Mesoporous Carbon Nitride Stabilizer for Highly Efficient Three-Component Coupling Reaction,* **K. K. R. Datta**, B. V. S. Reddy, K. Ariga, A. Vinu, ***Angew. Chem. Int. Ed***. **2010**, *49*, 5961-5965.

5. *Base-Selective Adsorption of Nucleosides to Pore-Engineered Nanocarbon, Carbon Nanocage,* **K. K. R. Datta**, A. Vinu, S. Mandal, S. Al-deyab, J. P. Hill, K. Ariga, ***J. Nanosci. Nanotechnol***. **2011**, *11*, 3959-3964.

6. *Carbon Nanocage: Super-Adsorber of Intercalators for DNA Protection,* **K. K. R. Datta**, A. Vinu, S. Mandal, S. Al-deyab, J. P. Hill, K. Ariga, ***J. Nanosci. Nanotechnol.* 2011**, *11*, 3084-3090.

7. *Highly Crystalline and Conductive Nitrogen Doped Mesoporous Carbon with Graphitic Walls and its Electrochemical Performance,* **K. K. R. Datta**, V.V. Balasubramanian, K. Ariga, T. Mori, A. Vinu, ***Chem. Euro. J*. 2011**, *17*, 3390.

8. *Observation of Pore-switching Behaviour in Porous Layered Carbon through Mesoscale Order-Disorder Transformation*, **K. K. R. Datta**, D. Jagadeesan, C. Kulkarni, A. Kamath, R. Datta, M. Eswaramoorthy, ***Angew. Chem. Int. Ed***. **2011**, *50*, 3929.

***Miscellaneous:***

1. *Aminoclay: A Designer Filler for the synthesis of Highly Ductile Polymer-Nanocomposite Film*, G. Johnsy, **K. K. R. Datta**, S. Vallayil, S. Shanmugam, B. Amarinder, M. Eswaramoorthy, ***ACS Applied Materials & Interfaces*****. 2009**, *1*, 2796-2803.

2. *Light-Harvesting Hybrid Hydrogels: Energy Transfer Induced Amplified Fluorescence in Non-Covalently Assembled Chromophore-Organoclay Composites,* K. V. Rao, **K. K. R. Datta**, M. Eswaramoorthy, S. J. George, ***Angew. Chem. Int. Ed***. **2011**, *50*, 1179-1184.

3. *Open-Mouthed Metallic Microcapsules: Exploring Performance Improvements at Agglomeration-Free Interiors*, S. Mandal, M. Sathish, G. Saravanan, **K. K. R. Datta**, Q. Ji, J. P. Hill, H. Abe, I. Honma, K. Ariga, ***J. Am. Chem. Soc.*** **2010**, *132*, 14415-14417.

4. *Honey Derivatized Au and Ag Nanoparticles and Evaluation of its Antimicrobial Activity*, C. Sreelakshmi, **K. K. R. Datta**, J. S. Yadav, B. V. S. Reddy, ***J. Nanosci. Nanotechnol.*** **2011**, *In Press.*